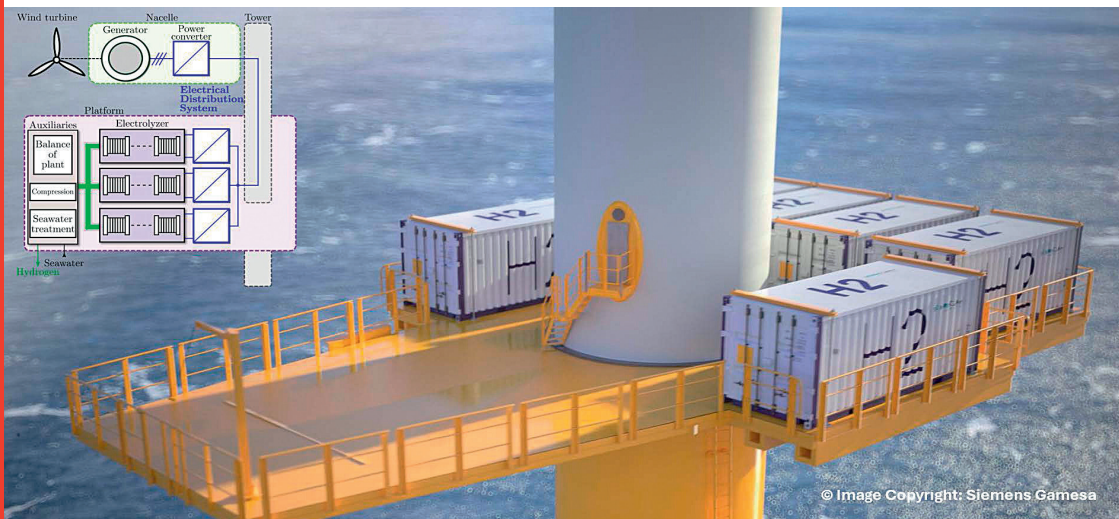
E.ON Energy Research Center | RWTH AACHEN UNIVERSITY

Analysis of Electrolyzer Connections to Offshore Stand-Alone Wind Turbines

Thibaut Runser
Institute for Power Generation and Storage Systems



© Image Copyright: Siemens Gamesa

Analysis of Electrolyzer Connections to Offshore Stand-Alone Wind Turbines

Von der Fakultät für Elektrotechnik und Informationstechnik der Rheinisch-Westfälischen Technischen Hochschule Aachen zur Erlangung des akademischen Grades eines Doktors der Ingenieurwissenschaften genehmigte Dissertation

vorgelegt von
Dipl.-Ing. Thibaut Runser
aus Mulhouse, Frankreich

Berichter:
Univ.-Prof. Dr. ir. Dr. h. c. Rik W. De Doncker,
Professor Dr. Damien Guilbert

Tag der mündlichen Prüfung: 30.06.2026

Diese Dissertation ist auf den Internetseiten der Universitätsbibliothek online verfügbar.

Bibliographische Information der Deutschen Nationalbibliothek
Die Deutsche Nationalbibliothek verzeichnet diese Publikation in der Deutschen Nationalbibliografie; detaillierte bibliografische Daten sind im Internet über https://dnb.dnb.de abrufbar.

D 82 (Diss. RWTH Aachen University, 2026)

Herausgeber:
E.ON Energy Research Center

Institute for Power Generation and Storage Systems (PGS)
E.ON Energy Research Center
Mathieustraße 10
52074 Aachen

E.ON Energy Research Center I 155. Ausgabe der Serie
PGS I Power Generation and Storage Systems

Copyright Thibaut Runser
Alle Rechte, auch das des auszugsweisen Nachdrucks, der auszugsweisen oder vollständigen Wiedergabe, der Speicherung in Datenverarbeitungsanlagen und der Übersetzung, vorbehalten.

Printed in Germany

ISBN: 978-3-948234-69-0
1. Auflage 2026

Verlag:
E.ON Energy Research Center, RWTH Aachen University
Mathieustraße 10
52074 Aachen
Internet: www.eonerc.rwth-aachen.de
E-Mail: post_erc@eonerc.rwth-aachen.de

Herstellung :
Druckservice Zillekens
Rainweg 19
52224 Stolberg
Mail: info@druckservice-zillekens.de

Preface

This dissertation is the result of my work within the Sustainable Energy Systems department at Siemens Energy. First and foremost, I would like to express my deepest gratitude to my PhD advisor, Professor Rik W. De Doncker, for agreeing to supervise my work. His guidance, constructive feedback, constant availability, and generous willingness to share his extensive knowledge have been invaluable throughout this journey.

I would also like to thank Professor Damien Guilbert from Université Le Havre Normandie for his interest in my research and for kindly agreeing to act as the co-examiner during my PhD defense. I am grateful for the time he devoted to carefully reading my dissertation and for his valuable and insightful feedback.

My special thanks go to Sven Schumann, who welcomed me into his team in January 2022 and provided constant guidance and support. His mentorship has been instrumental to the successful realization of this research. I would also like to thank colleagues who supported and guided me throughout my research journey, including Bogdan Craciun, Nils Langenberg, Josef Niedernhuber and Marvin Bendig. Under their mentorship, I have learned how to conduct high-quality research and how to present research results in a comprehensible way.

I am particularly grateful to Sven Schumann and Fabian Herzig for devoting substantial time to reviewing my dissertation and offering invaluable advice. Furthermore, I am thankful to all my office colleagues, particulary Max Layer and Fabian Herzig from the Tuesday's evening contract team, with whom I enjoyed a great working environment and many pleasant moments shared outside of work.

I would also like to extend my thanks to all of my students, whose excellent work and contributions significantly complemented my research.

Finally, I want to express my deepest gratitude to my family for their constant encouragement and support throughout my life. A very special thank you goes to my girlfriend, Laura, for her unconditional love and for always believing in me.

Nürnberg, in July 2026

Thibaut Runser

Contents

1 Introduction **1**
- 1.1 Introduction to the Topic . . . 3
- 1.2 State of Knowledge . . . 9
  - 1.2.1 Coupling of Electrolyzers to Stand-Alone Offshore Wind Turbines . 9
  - 1.2.2 Power Supply for Electrolyzers . . . 11
  - 1.2.3 Plant Sizing Optimization . . . 16
- 1.3 Research Objectives and Outline of this Work . . . 17

2 Requirements Specification for the Power Electronics Interface **19**
- 2.1 Modeling and Requirements of Offshore Wind Turbines . . . 19
  - 2.1.1 Wind Turbine Aerodynamics . . . 19
  - 2.1.2 Wind Turbine Electrical Drivetrain . . . 23
  - 2.1.3 Power Electronics Converter Architecture . . . 26
  - 2.1.4 Requirements Specification for Wind Turbine Electrical Drivetrains 28
- 2.2 Modeling and Requirements of Electrolysis . . . 33
  - 2.2.1 Electrolysis Fundamentals . . . 33
  - 2.2.2 Electrolysis Plant . . . 41
  - 2.2.3 Requirements Specification for Electrolysis Power Supply . . . 45

3 System Architecture and Design **48**
- 3.1 Balancing Power Dynamics . . . 48
- 3.2 Modularity and Power Allocation Strategy . . . 52
- 3.3 Electrical Distribution Systems Considered[1] . . . 54
  - 3.3.1 MVAC . . . 56
  - 3.3.2 AC1 . . . 58
  - 3.3.3 DC1 . . . 59
  - 3.3.4 DC2 . . . 60

4 High-Power Isolated DC-DC Converter **62**
- 4.1 Three-Phase Dual Active Bridge Fundamentals[2] . . . 62
- 4.2 Configuration Optimization of ISOP Connection of DABCS[2] . . . 64
  - 4.2.1 DABCS Sizing . . . 65
  - 4.2.2 Submodule Sizing . . . 66
  - 4.2.3 Semiconductor Losses . . . 68

[1] Parts of this section have been published in Runser *et al.* [162]
[2] Parts of this section have been published in Runser *et al.* [180]

4.2.4 Semiconductor Cooling . . . 70
4.2.5 DC-Link Capacitance . . . 72
4.2.6 Medium Frequency Transformer . . . 73
4.2.7 Cost and Reliability Assessment . . . 76
4.2.8 Pareto Optimization . . . 78
4.2.9 Trade-Off Analysis under Varying Conditions . . . 81
4.3 Configuration Optimization of IPOP and IPOS Connections of DABCS . . 81
4.3.1 IPOP connection . . . 82
4.3.2 IPOS connection . . . 84

5 Life Cycle Cost Analysis[3] 87
5.1 Plant Conditions . . . 87
5.2 EDS Components Evaluation . . . 90
5.2.1 Component Losses . . . 90
5.2.2 Cost, Volume, Mass and Availability of EDS Components . . . 96
5.3 LCOH Calculation . . . 97
5.4 Comparative Analysis of EDS . . . 102

6 Comprehensive Parametric Analysis 105
6.1 Sensitivity Analysis . . . 105
6.1.1 Economical Parameters . . . 105
6.1.2 Plant Conditions . . . 106
6.2 DABCS Efficiency . . . 110
6.2.1 Operation at Lower Switching Frequencies . . . 110
6.2.2 Parallel and Series Connection of Semiconductors . . . 111
6.2.3 Employment of Wide-Bandgap Semiconductors . . . 112
6.3 Plant Sizing Optimization[4] . . . 115
6.3.1 Plant Capacity Factor . . . 115
6.3.2 Electrolyzer Specific Energy Consumption . . . 116
6.3.3 Power Electronics Efficiency . . . 117
6.3.4 Plant CapEx . . . 118
6.3.5 LCOH . . . 119
6.4 Achieving Competitive LCOH . . . 120

7 Conclusions and Outlook 121
7.1 Contributions . . . 121
7.2 Future Work . . . 123

A Characteristics of Considered Semiconductors 125

B Calculation of Semiconductor Junction Temperature Under DAB Operation 126

List of Abbreviations and Acronyms 127

List of Symbols 129

List of Figures 139

[3]Parts of this chapter are published in Runser *et al.* [162]
[4]Parts of this section have been published in Runser *et al.* [222]

List of Tables **140**

Bibliography **159**

Curriculum Vitae **160**

1 Introduction

Recently, water electrolysis has received much attention as a promising technology to produce hydrogen (di-hydrogen, H_2) without direct greenhouse gases (GHG) emissions. Water electrolysis (hereafter simply referred to as electrolysis) involves splitting water molecules into hydrogen and oxygen using electricity in an electrolyzer cell. The only by-products of this process are oxygen, water and heat [1]. A simplified representation of an electrolysis plant comprising the power supply, the auxiliaries and the electrolyzer cells connected in series and regrouped in so-called stacks is shown in Fig. 1.1.

The electrolysis process at an industrial scale has existed for a long time, with alkaline electrolyzers being the initial and preferred solution in the past decades [2]. Although they have reached a mature stage and are comparably less expensive with longer lifetimes than other technologies, alkaline electrolyzers have some disadvantages, such as slow dynamic response and bulky designs due to low current densities [3, 4]. In contrast, proton exchange membrane (PEM) electrolyzers are more recent and have reached a commercial stage on an industrial scale in the mid-2010s. Despite a higher initial cost due to the use of expensive materials, PEM electrolyzers have become competitive with their counterparts due to advantages such as higher output pressure, high dynamic capabilities, fast start-up/shut-down time and greater hydrogen purity [3]. Lastly, in the early 2020s, solid oxide electrolyzer cells have developed further from laboratory scale to industrial applicability and are characterized by high-temperature requirements ($> 700\,°C$) as well as the potential for reduced electrical energy consumption [5].

If the electrolysis plant is powered by renewable energy sources (RES), the resulting hydrogen is commonly referred to as green hydrogen. However, as illustrated in Fig. 1.2a, nearly all of the 97 million tons (Mt) of hydrogen produced worldwide in 2023 was derived from natural gas reforming without carbon capture utilization and storage (CCUS), coal gasification and as a by-product of naphtha reforming at refineries. This production released equivalent emissions of 920 Mt of CO_2 during that year [6]. To put this into

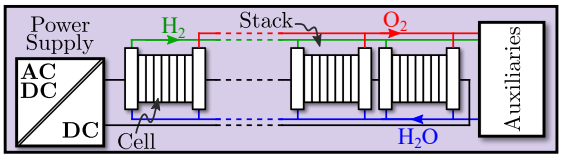
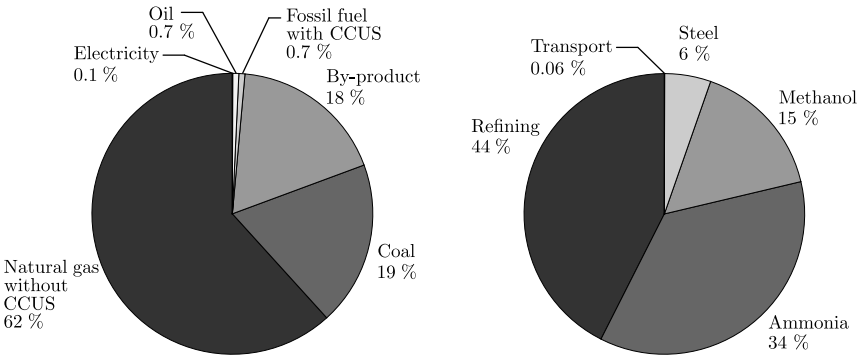


Figure 1.1: Simplified representation of an electrolysis plant.



(a) Production (b) Demand

Figure 1.2: Breakdown of global production and demand for 97 Mt of hydrogen in 2023 [6].

perspective, if hydrogen production were considered a country, it would rank as the sixth most emissive country in the world. As depicted in Fig. 1.2b, most of the hydrogen produced is used in refineries and to make other chemicals such as ammonia and methanol. Under these circumstances, policymakers are developing roadmaps and implementing programs to support the expansion of green hydrogen production, aiming to decarbonize current hydrogen usage and create opportunities for decarbonizing hard-to-abate sectors such as long-haul transportation and heavy industry.

At the end of 2023, the global installed electrolyzer capacity for hydrogen production reached almost 1.4 GW (expressed in electrical power input), representing almost double the capacity recorded at the end of 2022 [6], indicating a growing interest in this production method. Nevertheless, despite clear signs of growth, electrolysis still accounts for just 0.1 % of today's global hydrogen production. Replacing existing hydrogen production from fossil fuels with electrolysis-based production would require deploying about 730 to 940 GW of electrolysis capacity [7]. To put this into perspective, this would necessitate the installation of an additional quarter of the total installed capacity of RES worldwide [8]. This substantial increase in installation underscores the imperative need for significant grid and RES capacity expansion within a short timeframe.

The primary challenge hindering the widespread adoption of green hydrogen production is its cost. In 2023, the cost of hydrogen derived from electrolysis ranged from 3.6 to 12 USD/kg, whereas hydrogen from fossil fuels varies between 0.8 and 5.7 USD/kg, depending on fossil fuel prices [6]. As the electrolysis process is energy-intensive, requiring around 45 to 60 kWh per kg of hydrogen produced, electricity expenses constitute a significant portion of the green hydrogen production costs, ranging from 50 to 85 % of the total production costs, depending on electricity costs and the plant's capacity factor [9]. In parallel, RES can be situated far from consumer centers like cities and industrial areas and transmitting the energy via electricity requires significant electrical transport infrastructure. However, current indications suggest that electrical grids are becoming a bottleneck for further expansion and integration of RES. Delays are accumulating for many reasons, such as aging grid infrastructure, connection queues, outage costs, grid congestion, generation curtailment and timelines for grid development [10].

1.1 Introduction to the Topic

A promising approach to address the challenges associated with scaling up green hydrogen production without extensive grid expansion is the connection of the electrolysis plant to RES. This type of connection, known as an off-grid or stand-alone operation, exclusively relies on RES for the operation of the electrolysis plant, without any connection to the grid infrastructure [11–15]. This approach could increase efficiency and cost effectiveness compared to grid-connected electrolysis plant, as it has the potential to reduce not only transmission and conversion losses but also investments in grid infrastructure [16–20].

Compared to electrolysis connected to the grid, which could result in emissions depending on the grid electricity mix, hydrogen produced from plants coupled to stand-alone RES can unequivocally be labeled as green hydrogen. Numerous studies have conducted research on the connection of electrolysis plants with different stand-alone RES, including solar energy from photovoltaic (PV) panels or concentrated solar power, wind energy from either onshore or offshore wind turbines, hydroelectricity from dams and thermal energy from biomass or geothermal power plants to name a few [11, 21]. Nevertheless, the focus of research and project development has primarily been on wind and PV due to their declining costs over the years, high availability, and fewer geographical limitations compared to other RES [19, 22].

In this thesis, the focus is solely on offshore wind energy due to its proximity to abundant free water resources and higher capacity factors compared to onshore wind energy and PV, making it an ideal RES for competitive green hydrogen production [7, 23, 24]. The potential for combining hydrogen with offshore wind energy offers a solution to address challenges of the high cost of electrical transmission systems and transmission losses [19]:

- Traditional high voltage alternating current (HVAC) transmission cables experience conduction losses of 6.7 %/1000 km, whereas more recent high voltage direct current (HVDC) technology reduces losses to less than 3.5 %/1000 km but requires the use of converter stations at each end of the transmission line, leading to additional costs and conversion losses [25].

- The grid infrastructure (converters, transformers and transmission cables) between the wind farm and the shore, whether HVAC- or HVDC-based, increases the overall system initial investment cost and can account for up to 18 % of offshore wind projects [26].

By coupling electrolysis plants to stand-alone offshore wind farms, the need for expensive, long-distance grid connections is eliminated. This approach enables energy from remote offshore sites with abundant resources (high average annual wind speeds), previously deemed too costly or inefficient to access, to be transmitted to shore in the form of hydrogen through low-cost pipelines with limited losses:

- The cost of energy transmission per delivered MWh has been reported to be up to eight times lower for offshore hydrogen pipelines than for transmission cables [27].

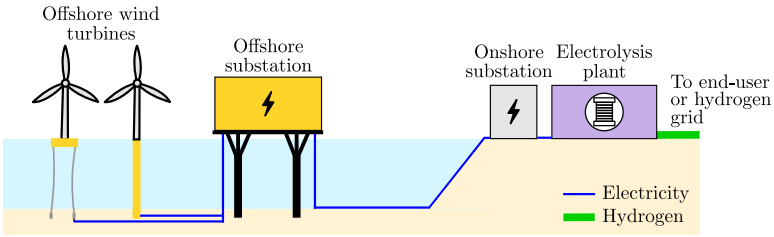
- Pipelines have a lifetime of 40 to 80 years and experience minimal energy losses, except for the energy requirements of the compressor, if required [28].

In the literature, the coupling of electrolysis plants to stand-alone offshore wind energy is mainly categorized into three different connection schemes based on the location of the electrolysis plant:

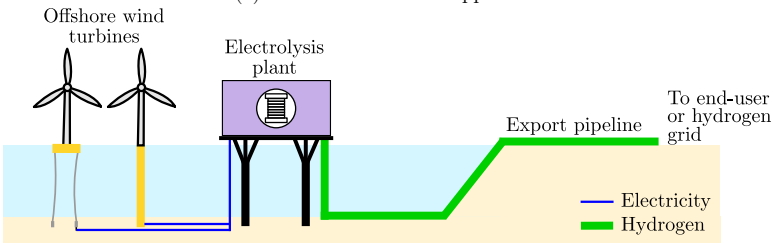
Centralized onshore as depicted in Fig. 1.3a, consists of centralizing the electrolysis plant onshore and connecting the wind farm via a standard electrical connection (HVAC or HVDC, depending on the distance from the shore). One significant challenge of this approach is the need for expensive and low-efficient grid infrastructure, as previously described, along with the requirement of onshore areas, which can lead to high land costs. Nevertheless, the main advantage of this connection scheme lies in its flexibility. If the electrolysis plant is located near an existing grid coupling point, it can be as well connected to the main grid. In this scenario, the operator can control the amount of power sold to the grid or fed into the electrolysis plant, depending on the most economically viable choice [29]. Electricity can be purchased from the grid during periods of low electricity prices to combine with volatile energy from the offshore wind farm to produce hydrogen at a constant load. This approach achieves higher capacity factors, but does not guarantee 100 % carbon-free hydrogen production [30]. The electrolysis plant may also be used to "peak shave" the offshore wind energy if required by the grid operator, thus avoiding curtailment of green electricity [31]. Moreover, electrolysis plants are expected to enhance the grid flexibility by providing frequency control ancillary services, including virtual inertia and primary and secondary frequency response [32, 33]. Additionally, this approach enables the consolidation of the electrolysis plant in one onshore location, thereby facilitating installation and maintenance work. Despite the potential for improved flexibility and capacity factors, the capital expenditures (CapEx) of the transmission infrastructure to the shore may hinder the connection to far offshore locations.

Centralized offshore as illustrated in Fig. 1.3b, involves centralizing the electrolysis plant on a single offshore platform within or in proximity to the wind farm. The electricity generated by the wind turbines is transmitted over a shorter distance via regular subsea array cables and collected at the offshore platform. Hydrogen is then produced, compressed to the desired pipeline input pressure if required, and transported to the shore via the export pipeline, which could also serve as a potential storage facility. The offshore platform can be a retrofitted oil and gas platform, a new platform, or in the form of an energy island [34]. This approach capitalizes on the lower cost of pipelines, as mentioned previously, but still requires the use of array cables and an expensive dedicated offshore platform. However, the construction and maintenance costs, as well as technical challenges, are significantly higher compared to the onshore approach due to potential rough sea conditions. Moreover, one undesired environmental impact arising from the consolidation of the electrolysis plant is the concentration of brine discharge resulting from the desalination of seawater [23, 35].

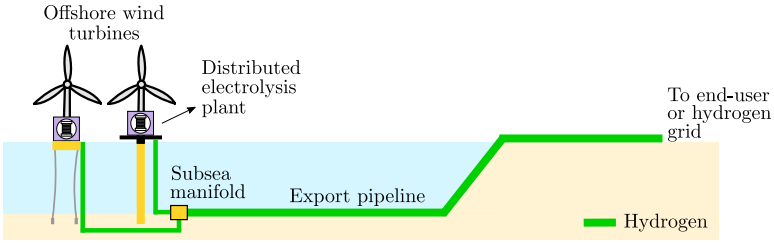
Decentralized offshore as illustrated in Fig. 1.3c, the electrolysis plant is distributed at each wind turbine. The electrolysis plant, of smaller capacity and size compared to the previous approaches, can be accommodated on both bottom-fixed and floating wind turbines [36]. This approach leverages at most the advantages of pipelines over transmission cables, as hydrogen is produced directly at each wind turbine and



(a) Centralized onshore approach.



(b) Centralized offshore approach.



(c) Decentralized offshore approach.

Figure 1.3: Three different connection schemes of coupling of electrolysis to stand-alone offshore wind energy.

is exported via a relatively small dimension pipeline to a subsea collection manifold, which receives the hydrogen produced by each turbine, to finally be exported to the shore using a larger diameter pipeline. Thus, all power transmission infrastructure is replaced with hydrogen pipelines, reducing dependence on transmission infrastructure, power transmission losses and investment costs of subsea cable. Directly producing at the wind turbine eliminates as well the need for a centralized offshore platform. Moreover, decentralized production yields the advantages of increased production flexibility, as hydrogen production can easily continue at other turbines if one wind turbine or electrolysis plant fails. Nevertheless, decentralizing the electrolysis plants across multiple locations result in each plant requiring its own set of smaller auxiliaries (desalination, cooling, compression,etc.) which might incur higher overall CapEx compared to the centralized schemes previously discussed.

Each connection scheme possesses its own set of advantages and disadvantages. Numerous studies have conducted economic comparisons of the three different approaches by

evaluating the production cost of hydrogen within each approach. Singlitico *et al.* presented a techno-economic assessment of the three different connection schemes in the North Sea [37]. Centralized offshore was highlighted as the most competitive approach, with a production cost as low as 2.4 € per kg of hydrogen, comparable to current costs of hydrogen produced with fossil fuels. However, for all connection schemes, electricity and hydrogen cogeneration is considered in the study, consequently requiring both grid and pipeline infrastructure. Similarly, D. Jang *et al.* conducted a techno-economic analysis of the three approaches, focusing solely on hydrogen production. Their findings indicated that in this case, the decentralized offshore approach emerged as the most competitive due to the absence of expensive HVDC infrastructure [38]. Eventually, Rogeau *et al.*, highlighted that there is no single optimal solution for all situations as the competitiveness of each connection scheme is influenced by various factors, including distance from the shore and water depth [16]. Considering various timeframes and assuming decreasing costs of wind turbines and electrolyzers over the years, it was found that before 2030, the centralized option is preferable for shallow waters located far from the shore (≥ 50 - 100 km), whereas the decentralized option is favored for deep waters (≥ 100 m). However, in the 2050 scenario, decentralized offshore connection schemes are preferred in nearly all situations, except in nearshore and shallow waters, as the scaling effect of installing small electrolyzers diminishes.

From an industry perspective, as detailed in Table 1.1, numerous large-scale projects have been announced worldwide for the next decade, with some already progressing through initial trial phases. There appears to be a predominant interest in either centralized onshore or decentralized offshore approaches. The preference for the former may be attributed to the established technology and design, as well as to the reduced risk and easier installation due to the onshore location of the electrolysis plant. The enhanced flexibility may instill confidence among stakeholders and mitigate the plant's exposure to volatile offshore energy conditions. Additionally, there is considerable interest for the decentralized offshore connection scheme, likely due to the smaller initial plant size and lower project costs. This modular approach does not require an offshore platform to install triple digit megawatt capacity and can be readily expanded. The distribution of hydrogen production at multiple wind turbines also mitigates the risk of a single point of failure that could disrupt production across the entire field.

Considering the potential competitiveness in the near future in nearly all offshore scenarios, as highlighted in [16] and the widespread adoption in industrial projects, this thesis focuses only on the decentralized offshore connection scheme, hereafter referred to as decentralized wind-to-hydrogen plant. Despite its promise in bypassing extensive grid infrastructure while enabling scalable hydrogen production, the decentralized approach remains underexplored in several critical aspects. While the electrolysis process and the capture of offshore wind energy are two mature technologies individually, their close integration demands a detailed examination of the requirements for both systems in combination. From an electrical perspective, an electrolyzer is a variable load with low-voltage (LV) and high-current demands. For example, an industrial-scale PEM electrolyzer in the megawatt range typically requires a voltage of a few hundred volts and an output current in the kiloampere range [49]. To bridge the gap in electrical disparities between a wind turbine and an electrolyzer, one or several stages of power converters are used to match the variable AC power output of the generator to the specific DC voltage and current

Table 1.1: Summary of most relevant offshore hydrogen production projects around the world.

Connection scheme	Project name	Country	Capacity and year deployed (or estimated)	Description
Centralized onshore	TOKYO	Japan	110 MW by 2030	Scheduled to begin operation by 2030, the plant will produce up to roughly 550 tons of hydrogen a year [39].
	Holland Hydrogen I	Netherlands	200 MW in 2026	Announced as the largest green hydrogen production plant in Europe, the plant located in the port of Rotterdam aims to produce up to 60 tons per day. It will be linked to a 759 MW wind farm situated 18.5 km off the coast [40].
	SeaH2Land	Netherlands	1 GW in 2030	1 GW electrolysis plant connected to a 2 GW offshore wind farm. The initial phase will encompass 500 MW of electrolyzer capacity, with a planned expansion to 1 GW in the second phase [41].
	NortH2	Netherlands	GW-scale by 2030	Industrial consortium planning to produce hydrogen offshore at GW scale [42].
Centralized offshore	Sealhyfe	France	1 MW in 2022	Announced as the world's first offshore green hydrogen production facility. The electrolyzer located on a floating platform is powered by a nearby floating wind turbine. After a successful 14-month trial phase, Lhyfe has announced plans to scale up the capacity to 10 MW by 2026 as part of the HOPE project [43, 44].
	PosHYdon	Netherlands	1 MW in 2024	Production of 400 kg/day of hydrogen on an operating offshore gas platform located 13 km off the coast. Neptune Energy has reported successful initial onshore tests, with the next phase focusing on offshore testing [45].
Decentralized offshore	OYSTER	United Kingdom	MW-scale in 2024	Scheduled to begin production by the end of 2024 and will be installed on an offshore wind turbine base platform [46]. No updates provided as of 2025.
	AquaVentus initiative	Germany	5 MW in 2025 300 MW in 2035 10 GW planned	RWE plans to have hydrogen production at the base of a 15 MW wind turbine by 2025 and extend the concept with a commissioning scheduled for mid-2030. The project aims to produce 1 Mt of green hydrogen per year by 2035 [47].
	Dolphyn	United Kingdom	10 MW before 2030 GW scale by 2030s	Announced as the largest floating decentralized offshore hydrogen production, the electrolysis plant will be located on the deck of a floating wind turbine [48].

requirements of the electrolyzer.

In the context of an electrolysis plant directly connected to RES, particularly to an offshore wind turbine, the requirements for the power converters interfacing the electrolyzer units to the wind turbine generator are not defined in the literature. Moreover, no previous studies specifically addressing power converters and operation strategies for decentralized wind-to-hydrogen plants have been found in the existing literature. The sole coupling of electrolysis with offshore wind power introduces a range of new challenges due to constrained environments, variable power supply, rapid power ramp rates and changing operational conditions over the lifetime of the plant. Electrical components located between the wind turbine generator and the electrolyzer units, along with operation strategies, are key factors in the electrical integration of the electrolysis plant with decentralized stand-alone offshore wind turbines. Research is needed to develop a holistic methodology for designing, evaluating and optimizing the electrical integration of electrolyzers within decentralized wind-to-hydrogen plants. Such a methodology must consider technical challenges arising from fluctuating renewable power and variable operating conditions, with the goals of maximizing operational performance, enhancing reliability, and reducing overall costs. Therefore, this thesis focuses on establishing a methodology to comprehensively compare different electrical connection schemes and operating strategies, thereby providing robust insights for the design and optimization of decentralized wind-to-hydrogen plants.

1.2 State of Knowledge

1.2.1 Coupling of Electrolyzers to Stand-Alone Offshore Wind Turbines

Although the wind turbine and the electrolysis plant in a wind-to-hydrogen plant are based on well-known and thoroughly tested technologies, they are placed into a new context. Usually, electrolysis plants are connected to the main grid and designed for a constant production load [50]. The dispersion of the electrolysis plant at each wind turbine and the disconnection from strong grid lines expose the plant to the volatile power of the wind. One of the inherent drawbacks of wind power, although offshore sites typically experience faster and more consistent winds than onshore areas, is the intermittency of wind velocity, on a second-by-second, hourly, daily and even seasonal basis [51]. Consequently, the electrolyzer operation becomes intermittent, with highly variable power input. Although electrolysis is a mature technology, the sole coupling with offshore wind power amplifies the consideration of the specific requirements of electrolysis. Therefore, further investigation is required to fully explore the potential and limitations of such a coupling of the electrolysis plant with a decentralized stand-alone wind turbine.

Fluctuating Power / Dynamic Loading

Several studies have investigated the impacts of fluctuating power profiles on the electrolysis process. While the electrical dynamic response of an electrolyzer has been reported to have a minor influence, the slower dynamic requirements introduced by temperature and pressure management were highlighted as playing a more important role [52]. Fluctuating power input could result in operating temperatures and pressures deviating from nominal ranges, leading to lower efficiencies of the electrolysis process [4, 53, 54]. In the case of alkaline electrolyzers, Fang *et al.* pointed out that the fluctuating power mainly converts into heat [55], whereas Gambou *et al.* showed that alkaline electrolyzers can respond quickly to dynamic load changes and are therefore capable of integration with RES [56]. Conversely, there is a consensus favoring the use of PEM electrolyzers when coupling with RES, partly due to their superior dynamic capabilities [57]. The differences in response time, start-up/shutdown time (minutes for alkaline vs. seconds for PEM under warm conditions) and load response (a factor of 10 to 20 faster in favor of PEM), are the main differentiating factors between alkaline and PEM electrolyzers [53, 58]. Alternatively, a hybrid of PEM and alkaline electrolyzers is also suggested to take advantage of the fast dynamics of the former and the lower cost of the latter [59].

The degradation of electrolysis performance under dynamic loading over the lifetime of the electrolyzer is of particular concern, especially at offshore sites where access is constrained. Across various electrolyzer technologies, degradation occurs at the electrolyzer cell level and is typically enhanced with current density and temperature [60]. Dynamic loading has been shown to greatly reduce degradation compared to operation at constant full loading, as it allows reversible parts of the degradation process to recover, resulting in substantially reduced degradation per amount of hydrogen produced [61, 62]. However, although the dynamic operation has demonstrated improved performance on a short-term basis, long-term degradation remains a concern and further electrolyzer cell optimization is anticipated to be required [63].

Minimum Load Requirement

An essential safety consideration relates to the minimum load requirement. Under nominal operation, hydrogen and oxygen are produced and released at the cathode and anode, respectively, without gas mixing. However, as the load decreases, the concentration of hydrogen in oxygen on the anode side increases due to gas cross-permeation [64]. This situation can potentially create hazardous conditions inside the electrolyzer. The lower flammability limit of hydrogen in oxygen is about 4 % and to prevent the formation of potentially flammable mixtures, commercial units are generally designed to trigger a safety shutdown when the hydrogen content in oxygen reaches 1.5 to 2 % [54, 57]. Depending on the operating pressure, temperature and other structural parameters, this level is typically reached when operating at power loads below 10 to 40 % of the rated power, with PEM electrolyzers having lower minimum load requirements than alkaline electrolyzers [4]. Though this requirement may not be as restrictive in a conventional grid application due to the typically high power availability, it must be carefully considered when connected solely to a wind turbine, as the power may be highly variable and the lower operating limit may be reached frequently, leading to potential repeated shutdowns of the plant [53]. This could potentially affect the capacity factor and economics of the plant, as well as accelerate the degradation of the electrolyzer [65].

Dutton *et al.* performed measurements on an electrolyzer powered by a wind turbine under varying overload, partial load, shutdown and dynamic conditions over a four-day period [66]. On six occasions, the safety limit was exceeded, resulting in the subsequent shutdown of the electrolyzer. The study highlighted that the purity of the hydrogen as well as the efficiency of the hydrogen production was reduced due to rapid load fluctuations. To address these challenges, several control strategies have been suggested in the literature. Some consist of extending the conventional wind turbine control algorithm with an additional loop to accommodate the electrolyzer requirements [67, 68]. Others have proposed to integrate additional energy storage systems (ESS) such as batteries, fuel cells or supercapacitors to smooth out fluctuations in wind power and develop a modular adaptive control strategy [55, 69]. However, the employment of ESS entails additional expenses and requires space in an already constrained offshore environment. Muyeen *et al.* proposed to segment the electrolysis plant into several electrolyzer units of smaller size and developed a power allocation strategy to enhance the full-load condition of individual units, thereby increasing their service life [70]. Additionally, Ursúa *et al.* proposed allowing the electrolyzer to operate below the lower operating limit for a certain period of time, but this approach did not consider the safety risk associated with the potential build-up of explosive mixtures [50].

Overall, the limitations encountered when operating under fluctuating power are mainly due to the operating limits of the electrolyzer, especially with respect to the minimum operating limit required for safe operation. In this context, intermittency rather than variability of the power source plays a more significant role in constraining the integration of electrolysis plants with stand-alone offshore wind turbines. As highlighted, studies predominantly focused on exploring the addition of ESS, segmenting the electrolysis plant into several smaller units and employing control strategies, to extend the operating hours of the electrolyzer units and enhance the integration of electrolysis plants with wind power. However, these proposals have not been comprehensively studied regarding their impact on the plant from technical and economic perspectives. For instance, an electrolyzer

exhibits a decreasing efficiency and accelerated degradation with increasing load [3]. The underlying assumption that the electrolyzer units need to maximize their service life by operating at full load can then be questioned. Therefore, there is a need for a holistic approach that considers plant efficiency, safety, capacity factor, electrolyzer degradation and overall cost altogether when evaluating different control strategies.

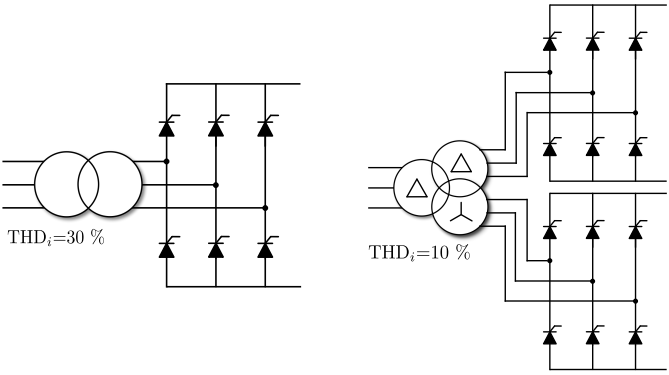
1.2.2 Power Supply for Electrolyzers

Scientific publications have mainly focused on reviewing different power converter topologies for grid-connected electrolyzers and are therefore first summarized in the following [71–74].

Power Supply for Grid-Connected Electrolyzers

In this context, the main challenges are to deliver a high DC current with minimized current ripple, while ensuring high AC power quality by reducing harmonic content emitted to the grid and minimizing reactive power consumption. In addition, the power supply should be cost-optimized as it can account for 15 to 30 % of the overall electrolysis plant CapEx [75, 76]. Early methods involved using diode rectifiers in conjunction with regulating auto-transformers equipped with on-load tap changer (OLTC), step-down transformers and saturable reactors [77]. These methods have a limited output voltage range and rely on the OLTC for relatively large voltage adjustments. The introduction of thyristor semiconductors allowed for faster current regulation and increased controllability, eliminating the need for high-loss saturable reactors [77]. Thyristor rectifiers can smoothly vary their output voltage by adjusting the firing angle. However, the natural commutation of thyristors introduces several drawbacks, such as a relatively high harmonic content and reactive power consumption on the grid side, as well as a relatively low-frequency current ripple on the electrolyzer side, all of which are exacerbated at low load conditions. The harmonics produced by a 6-pulse thyristor rectifier, as shown in Fig. 1.4a, can be costly to filter out due to their low frequency and high amplitude [73]. A higher pulse system, such as a 12-pulse rectifier system illustrated in Fig. 1.4b, is typically employed to reduce harmonic content emitted to the grid. This involves the use of a three-phase three-winding transformer with a specific windings connection to introduce a natural phase shift of 30° between the secondary voltages, supplying two 6-pulse rectifiers. If necessary, the system can be extended to a 24-pulse rectifier system by incorporating a second three-winding transformer, resulting in a total of four 6-pulse rectifiers. These rectifiers can supply several independent electrolyzer units, be connected in parallel to increase output current, or be in series to increase output voltage. AC power quality can be further improved by using additional equipment on the AC side, such as a static compensator (STATCOM) and/or passive filters, but introduces additional losses and increases the CapEx of the overall system [78].

However, the natural commutation of thyristors impacts not only the grid side but also the electrolyzer side. To reduce the volume and cost of such rectifiers, the output DC smoothing inductance is usually omitted, leading to a high ripple in the output current [79]. Studies have shown that increasing current ripple and decreasing ripple frequency correlate with an increase in specific energy consumption (SEC) of the electrolyzer, meaning that less hydrogen is produced for the same amount of input energy. This phenomenon



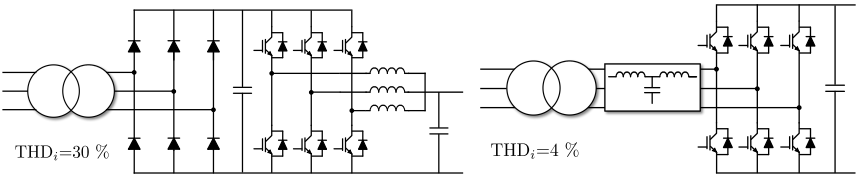
(a) 6-pulse. (b) 12-pulse.

Figure 1.4: Thyristor rectifier topologies commonly used in industrial-scale electrolyzer power supplies.

has been observed in both alkaline [80–82] and PEM electrolyzers [83]. Furthermore, the current ripple imposes dynamic operation on a millisecond time scale for the electrolyzer cells, which may accelerate their degradation [84].

Insulated Gate Bipolar Transistor (IGBT) rectifiers, such as DC chopper rectifier and active front end (AFE) rectifiers, as illustrated in Fig. 1.5a and Fig. 1.5b respectively, emerged later in the industrial landscape. Thanks to their active turn-off capabilities, they can operate at higher switching frequencies than the grid frequency and the input-side AC currents can be controlled to be sinusoidal. In addition, the phase shift of the AC currents relative to grid voltage can be manipulated by adjusting the modulation signal of the converter. This offers several operational benefits over diode or thyristor rectifiers, including a higher power factor, lower harmonic generation, reduced output ripple, greater speed and accuracy of controls [77]. Although IGBT rectifiers experience more semiconductor losses compared to thyristor rectifiers, the reduced harmonic content decreases transformer losses and the reduced current ripple improves the SEC of the electrolyzer [85]. Indeed, improved power quality by IGBT-based power supplies has been reported to decrease the SEC of alkaline electrolyzers by 14 and 9 % compared to 6-pulse and 12-pulse thyristor rectifiers, respectively [82]. Ultimately, under a RES power profile, the IGBT rectifier could achieve a 2.1 % lower annual energy consumption for the electrolyzer compared to a 6-pulse thyristor rectifier [73].

Despite the advantages of IGBT rectifiers over their counterparts, thyristor rectifiers have been most common and are still widely used in the power supply of industrial-scale electrolyzers, due to their maturity, proven reliability, comparably high current capabilities, high semiconductor efficiency, small footprint and low capital cost [74,86]. Moreover, due to the lower current capability of IGBT (about a maximum of 3.6 kA for commercially available IGBT devices versus 6.5 kA for thyristor devices), several IGBT devices or converter units need to be parallelized, thereby decreasing the reliability of the overall power supply. Previous studies have not adequately considered the reliability impact of having multiple IGBT devices or converters connected in parallel. Characteristics of power



(a) DC chopper rectifier. (b) AFE rectifier.

Figure 1.5: IGBT rectifier topologies commonly used in industrial-scale electrolyzer power supplies.

supply systems, such as efficiency, power quality, CapEx and footprint, are typically compared separately. There is no comprehensive methodology in the literature that allows for a holistic comparison of different power supply systems.

Power Supply for RES-Connected Electrolyzer

Between the wind turbine generator and the electrolyzer units, a certain distance is expected, ranging from a few meters to several hundred meters, depending on the location of the electrolyzer units. All the electrical components in between are referred to as the electrical distribution system (EDS), as highlighted in blue in Fig. 1.6. In the context of an electrolysis plant directly connected to a RES, particularly to an offshore wind turbine, the requirements for the EDS interfacing the electrolyzer units to the wind turbine generator are not defined in the literature.

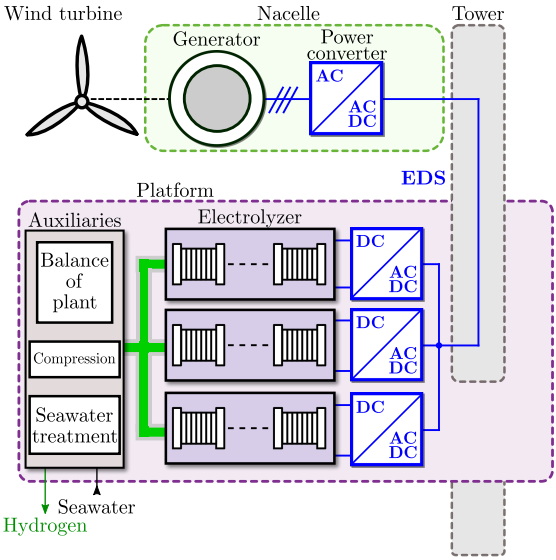


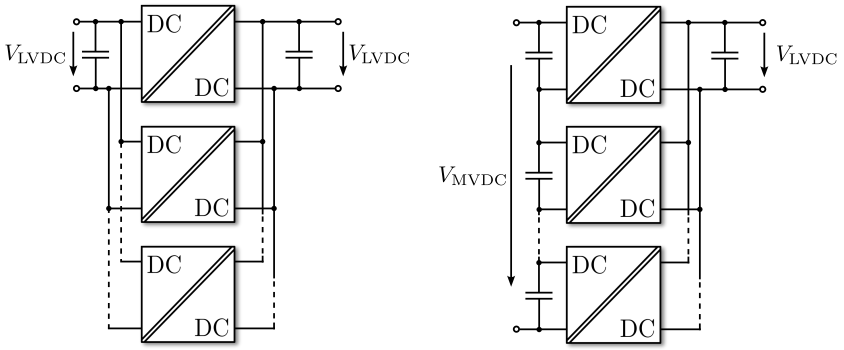
Figure 1.6: Simplified representation of a decentralized wind-to-hydrogen plant comprising three independent electrolyzer units.

On the one hand, several papers provide a comprehensive overview and describe the requirements for wind turbine converter systems [87,88]. Wind turbine generators typically produce AC power at a variable frequency, which needs to be converted to a fixed grid frequency through a back-to-back converter and then stepped up in voltage via a line-frequency transformer (LFT) to connect to the AC collector grid, typically ranging from 33 to 66 kV. Additionally, several studies have emphasized the connection of wind turbines to a DC collector grid by using an isolated DC-DC converter after the generator's rectifier to step up the relatively low DC voltage to the DC collector grid voltage [89,90].

On the other hand, several papers provide an overview and describe the requirements for EDS interfacing electrolyzers mainly with PV systems, highlighting different DC-DC converter topologies [15,22]. However, no previous studies specifically addressing power supply for decentralized wind-to-hydrogen plants have been found in the existing literature. Since the electrolyzer units in a decentralized wind-to-hydrogen plant are not connected to any grid, traditional grid code requirements do not apply to the EDS. The production of hydrogen in a decentralized approach presents new and complex challenges, due to constrained offshore environments, variable power supply, and changing operational conditions of the electrolyzer over its lifespan. This application comprises interrelated requirements that need to be identified and assessed. These specific requirements have not been adequately addressed in the existing literature.

Employing a DC bus configuration between stand-alone RES and the electrolyzer has been recognized as a promising interface, particularly in PV applications, but can also be applied in wind turbines if a DC bus is implemented after the generator's rectifier [91]. Furthermore, the use of an isolated DC-DC converter as the power converter between the electrolyzer and the DC bus has been highlighted as an advantageous converter topology due to its high voltage gain at high energy efficiency [92]. The higher switching frequency compared to grid frequency results in a potential reduction in space and mass requirements of passive elements and the converter dynamics are typically faster. However, the considered electrolyzer loads were limited to only laboratory-scale applications (a few kilowatts maximum). To deliver several kiloamperes from the DC bus to an LV/high-current electrolyzer, multiple DC-DC converter submodules connected in parallel, as shown in Fig. 1.7a, should be employed to overcome the current limitations of semiconductor switches and to share the load. Conversely, depending on the DC voltage of the DC bus, several submodules can be connected in series on the input side to share the voltage, resulting in an input-series output-parallel (ISOP) connection of DC-DC converters as illustrated in Fig. 1.7b [93]. However, in addition to the LV/high current requirements, electrolyzers exhibit variable voltage characteristics due to factors such as loading and aging. This aspect necessitates further consideration when designing the DC-DC converters operating limits and components, an area that has not yet been explored in the existing literature.

Moreover, the voltage class of the semiconductor switches employed in the submodules can significantly influence the overall DC-DC converters efficiency and power density. Previous research has investigated the trade-offs involved in cascading converter cells, specifically for cascaded H-bridge cells in high-power AC-DC solid-state transformers [94]. Higher efficiencies were observed with the use of a high number of cells in series with low-blocking voltage semiconductor switches for a grid voltage of 10 kV. However, the DC side was



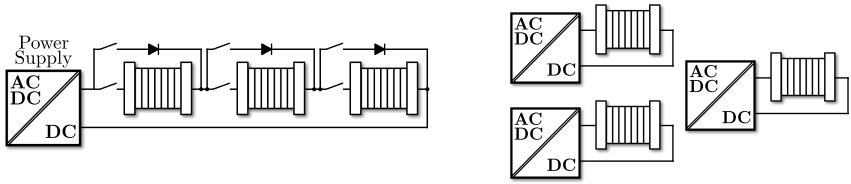
(a) Input-parallel output-parallel (IPOP) connection.

(b) ISOP connection.

Figure 1.7: Modular connection of isolated DC-DC converter submodules.

modeled as DC current sources and the impact of using a higher number of lower-rated medium-frequency transformers (MFTs) was not considered. Therefore, open questions remain regarding the design and implementation of isolated DC-DC converters for optimal connection of large-scale electrolyzers to DC buses.

In the context of coupling with RES, a modular configuration of the electrolysis plant, has been highlighted in the literature for its potential advantages in energy management [4]. As depicted in Fig. 1.8a, stacks can be connected in series and the use of additional bypass semiconductor switches can theoretically enable the disconnection of faulty electrolyzer stack(s) to deviate the current to the remaining healthy stacks, ensuring continuity of service [71]. Stacks can also be connected in parallel, each individually interfaced by a dedicated power converter, as illustrated in Fig. 1.8b [95,96]. Therefore, the modularity of the electrolyzer is enabled by power electronics, but no studies have holistically evaluated the impact of implementing more power electronics components in the electrolysis plant.



(a) Series connection of stacks with the use of bypass switches as proposed in [71].

(b) Parallel connection of stacks with the use of dedicated power supplies.

Figure 1.8: Modular connection of electrolyzer stacks.

1.2.3 Plant Sizing Optimization

Another important area of research is the relative sizing of the electrolysis plant in relation to the wind turbine. Optimizing the electrolyzer capacity involves both technical and economic considerations, as it affects interrelated characteristics such as the electrolyzer capacity factor, SEC and CapEx, all of which collectively influence the economic viability of the plant.

Several studies have focused on determining the optimal sizing of the electrolyzer capacity for wind-to-hydrogen plants that are also connected to the grid (referred to as "grid-assisted"). For example, García Clúa *et al.* aimed to minimize the reliance on grid support to ensure GHG-free hydrogen production, suggesting that the optimal electrolyzer capacity should be approximately 40 % of the wind turbine-rated power [97]. Other studies have aimed to achieve the lowest levelized cost of hydrogen (LCOH) as the primary objective. In these cases, a trade-off between maximizing RES utilization and minimizing hydrogen production costs is found to be optimal when the electrolysis capacity is between 80 and 90 % of the installed capacity of the wind farm [98–100]. However, these studies mainly considered centralized systems that are also connected to the grid. It was often assumed that the electrolysis plant could not be oversized relative to the wind turbine, since no additional energy could be captured and thus no economic benefit could be gained. Nevertheless, these studies overlooked the fact that an electrolyzer has a variable efficiency that increases with decreasing load [3]. Hofrichter *et al.* considered this fact in their study for a centralized connection scheme with grid connection and an optimal sizing in terms of LCOH was then found with a 44 % oversized electrolyzer capacity, striking a trade-off between increasing electrolyzer efficiency and the associated increase in CapEx for the electrolysis plant [101].

When performing sizing optimization of the electrolyzer, it is important to consider not only its rated capacity but also its modularity. Modularity refers to the ability of electrolyzer units to be operated independently in parallel. This feature is particularly relevant in plants connected to RES due to the enhanced flexibility it provides [102]. A higher number of small-rated power electrolyzers compared to a single-unit approach can lead to a reduction in the minimum load of the plant, as depicted in Fig. 1.9, and ensure continued operation in a degraded state if one of the electrolyzer units fails, potentially contributing to a higher capacity factor [103].

Embracing a modular design, as opposed to a single-unit approach, has been suggested to result in a 33 % increase in hydrogen production due to the higher capacity factor and operation of units at optimal efficiency levels [104]. Furthermore, electrolyzer modularity and the implementation of a specific power allocation strategy have been highlighted as methods to mitigate the rate of electrolyzer degradation [105]. Nevertheless, the use of a larger number of smaller electrolyzer units can potentially contribute to higher CapEx of the plant, partly because each unit requires its own smaller auxiliary systems and additional power electronics components or converters, as previously discussed. The implications of having more power electronics in an electrolysis plant, as opposed to a single-unit approach, need to be studied from efficiency and reliability perspectives. For decentralized offshore plants, there is a lack of research evaluating the sizing and modularity of the electrolyzer while considering factors such as the electrolyzer

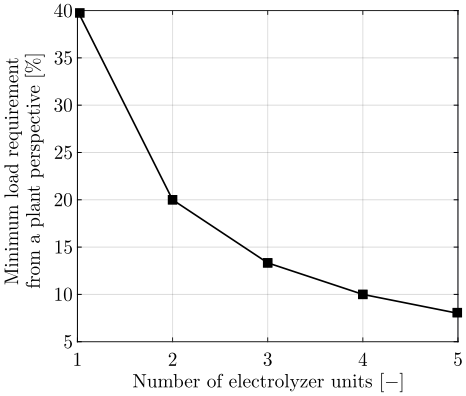


Figure 1.9: Evolution of the minimum load requirement from a plant perspective for different number of units[1].

CapEx, efficiency, capacity factor and power electronics efficiency.

1.3 Research Objectives and Outline of this Work

Based on the identified research gaps in the literature, the objectives of this thesis are to:

- Compile the specific requirements of both electrolysis and offshore wind turbine systems that need to be considered for the power allocation strategy and for the design of EDS interfacing wind turbine generators with electrolyzer units.
- Conduct an in-depth design study of the EDS, with a particular focus on emerging topologies such as modular DC-DC converters that are subject to optimization in their modularity to enhance key performance parameters such as efficiency, power density, reliability and cost.
- Develop a methodology to holistically compare different EDS configurations by taking into account factors such as fluctuating power supply and changing electrolyzer conditions.
- Propose a sizing optimization of the electrolysis plant in terms of capacity and modularity by considering the impact of implementing additional power electronics components.

In order to achieve the set goals and provide knowledge to the research gaps, the investigative approach of this thesis follows the structure depicted in Fig. 1.10.

[1] Assuming a 40 % minimum load requirement on the electrolyzer cell.

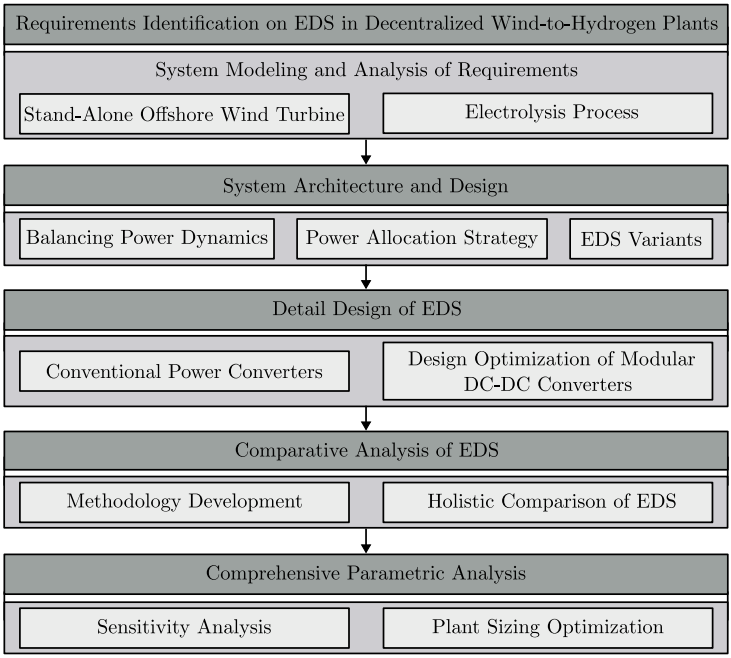


Figure 1.10: Schematic structure of the thesis.

2 Requirements Specification for the Power Electronics Interface

An important research gap, identified in the introduction, is the absence of requirements specification for the EDS interfacing the electrolyzer units with the wind turbine generator in a decentralized wind-to-hydrogen plant. The key performance metrics of the EDS, such as efficiency, reliability, volume, mass and cost, are strongly tied to the electrical requirements and parameters of both the wind turbine and the electrolyzers [106]. Thus, it is essential to understand the requirements of both systems before comparing different EDS configurations. This chapter aims to comprehensively identify the specific requirements of both systems to ensure the efficient, reliable, safe and stable operation of the wind-to-hydrogen plant. Firstly, the modeling of each system is described and the electrical characteristics of the electrolysis plant and the wind turbine are extracted. Secondly, based on these extracted characteristics and supplemented by a thorough literature review, the specific requirements applying to the EDS are identified and consolidated.

2.1 Modeling and Requirements of Offshore Wind Turbines

2.1.1 Wind Turbine Aerodynamics

The theoretical available power in the wind P_w represented by a mass of air with a density ρ, moving at normal velocity v through a cross-sectional area A, is expressed as

$$P_\mathrm{w} = \frac{1}{2}\rho A v^3. \tag{2.1}$$

The power in the wind increases with the cube of the wind speed, meaning that doubling the wind speed results in an eightfold increase in power. This principle motivates the placement of wind turbines in areas with high annual wind speeds, e.g. those exceeding 10 m/s. Since wind power is proportional to the swept area of the wind turbine blades, doubling the diameter leads to an increase in power by a factor of 4, justifying the scaling of offshore wind turbine blades. However, the mechanical power P_m extracted by the wind turbine is limited by the power coefficient C_p of the wind turbine, which is a function of both the tip-speed ratio (TSR) λ and the pitch angle of the blades β, such as

$$P_\mathrm{m} = \frac{1}{2}\rho A \cdot C_\mathrm{p}(\lambda, \beta) v^3. \tag{2.2}$$

The TSR is defined as the ratio between the linear speed of the blade tip to the wind speed v and is given by

$$\lambda = \frac{\omega_{\mathrm{m}} R_{\mathrm{blade}}}{v} \tag{2.3}$$

with ω_{m} the angular rotor speed and R_{blade} the turbine blade length. C_{p} represents the ratio of the actual mechanical power captured by the wind turbine blades to the theoretical available wind power flowing through the blades, and can be modeled by the following empiric formula

$$C_{\mathrm{P}} = c_1 \left(\frac{c_2}{\lambda_i} - c_3 \beta - c_4 \right) \exp\left(- \frac{c_5}{\lambda_{\mathrm{i}}} \right) + c_6 \lambda \tag{2.4}$$

$$\text{with } \frac{1}{\lambda_{\mathrm{i}}} = \frac{1}{\lambda + 0.08\beta} - \frac{0.035}{\beta^3 + 1}, \tag{2.5}$$

where the parameters c_1 to c_6 define the shape of the C_{p} curve of a generic three-blade turbine [107]. The dependence of C_{p} on λ and β is shown in Fig. 2.1a. As the pitch angle of the blades increases, the angle of attack also increases, causing more wind to be shed and resulting in reduced energy capture by the turbine. The original derivation for the maximum power that a turbine can extract from the wind is credited to Albert Betz, who first formulated the relationship in 1919 [108]. According to Betz, the theoretical maximum C_{P} of a wind turbine is 0.593. The empirical equations described in (2.5) represent a wind turbine capable of approaching 80 % of that theoretical limit, achieving a C_{P} of approximately 0.48 under optimal operating conditions ($\lambda = 8.1$ and $\beta = 0°$).

Fig. 2.1b illustrates the performance of the considered wind turbine by representing its mechanical power as a function of the rotor rotational speed for various wind speeds and a blade pitch angle $\beta = 0°$. In this study, the wind turbine model is based on a 15 MW

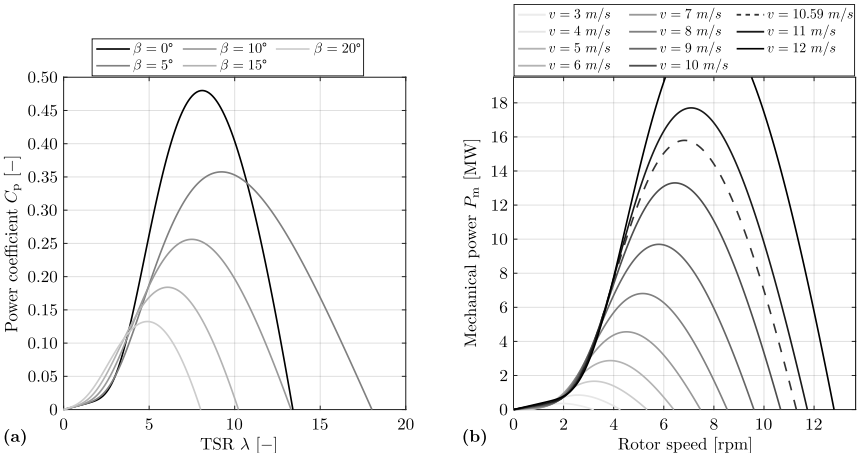


Figure 2.1: (a) Power coefficient C_{p} for variable TSR and different pitch angles β. (b) Wind turbine mechanical power P_{m} for different wind speed.

Table 2.1: Parameters of the 15 MW Wind Turbine [109].

Parameters	Value	Unit
Rated power	15	MW
Cut-in wind speed	3	m/s
Rated wind speed	10.59	m/s
Cut-out wind speed	25	m/s
Design TSR	9.0	–
Minimum rotor speed	5.0	rpm
Maximum rotor speed	7.56	rpm
Maximum tip speed	95	m/s
Rotor diameter	240	m
Rotor inertia	3.5×10^8	kg·m^2
Hub height	150	m

definition from the International Energy Agency, with the key parameters listed in Table 2.1 [109]. Opting for the ratings of the largest commercially available offshore wind turbine enables a significant reduction in the number of units required in a wind farm. This is advantageous as the total installation and maintenance costs of a single high-power wind turbine are lower than those of a cluster of low-power wind turbines [87, 110]. Additionally, the increased inertia of larger turbines may also facilitate the coupling of the comparatively slow operation of the electrolyzer with the faster dynamics of the wind [111], a topic further discussed in Section 3.1.

The wind turbine under consideration operates at variable rotor speeds and is pitch-controlled. The averaged power curve of an exemplary 15 MW wind turbine model, along with the power coefficient C_p, the blade pitch angle, the rotor speed and the TSR, are depicted in Fig. 2.2. Practical considerations impose four wind speed limits on turbine operation, dividing the wind turbine control into five operating regions which are as follows:

Region I: At wind speeds below the minimum wind speed, the so-called cut-in wind speed, the rotor cannot overcome friction in the drive train and/or the generated electrical power may not be sufficient to offset the power required for turbine operation.

Region II: Above the cut-in wind speed, the wind turbine control ensures the minimum rotor speed is maintained, resulting in a suboptimal TSR. The blade pitch controller imposes a minimum positive pitch angle based on the wind speed estimates to capture maximum power while maintaining the minimum rotor speed. This minimum rotor speed constraint is to avoid 3-period interference with the tower/monopile natural frequency [109].

Region III: Once the TSR reaches the designed TSR of the turbine at a wind speed of 6.98 m/s (2.3), the pitch angle is set to 0° and the rotor torque control regulates that rotor speed increases with the wind speed to maintain a constant TSR. The turbine designed TSR is slightly above the optimal TSR of 8.1 as shown in Fig. 2.1a. This suboptimal design point results from a trade-off between power production and

design constraining loads [109]. The operation in the region II and III is commonly referred to as Maximum Power Point Tracking (MPPT) operation since the power coefficient is maximized for each instantaneous wind speed.

Region IV: At above-rated wind speeds, the blade pitch angle is adjusted to shed the wind and regulate the rotor to operate at its maximum speed, reducing the power coefficient and maintaining the power extraction at the rated power of the turbine.

Region V: When the wind speed exceeds the maximum wind speed of the turbine, the so-called cut-out wind speed, the pitch angle is set to 45°, resulting in no power being produced and avoiding risking the mechanical integrity of the wind turbine. Some wind turbines incorporate a particular generator and pitch control strategy to introduce a soft cut-out by producing power at a reduced load for wind speed above the cut-out wind speed, often referred to as a High Wind Ride Through (HWRT) cut-out strategy [112], but is not considered in this thesis.

Wind turbines are designed according to wind classes defined by the IEC 61400-1 standard. Given that this thesis focuses on offshore locations, the wind class I has been selected as it poses the highest wind speed requirement, specifically an average wind speed of 10 m/s (considered in this thesis at the hub height). Since the wind speed is not constant

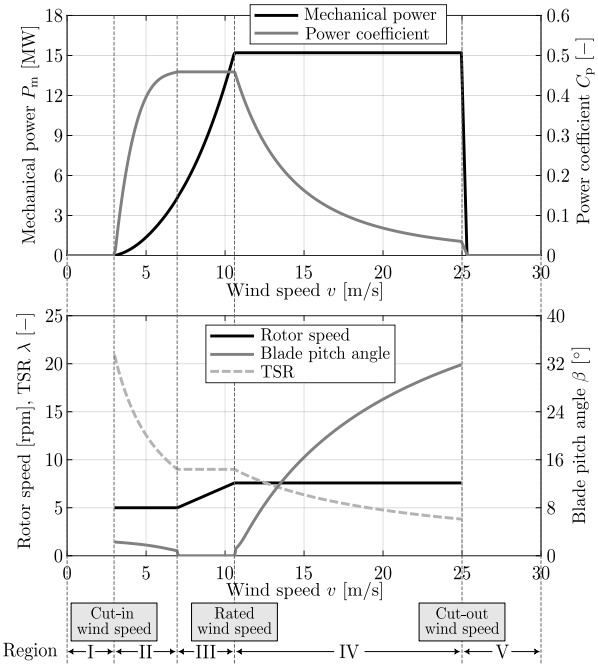


Figure 2.2: Power curve of the considered wind turbine and evolution of the power coefficient, blade pitch angle, rotor speed and TSR with wind speed.

throughout the year at a given site, it is typically represented using a probability density function, such as the Weibull distribution function as follows

$$f_{\text{Weibull}}(v) = \frac{k}{c}\left(\frac{v}{c}\right)^{k-1} \exp\left(-\left(\frac{v}{c}\right)^{k}\right) \tag{2.6}$$

where k is the shape parameter and c is the scale parameter. In this thesis, an exemplary wind speed distribution characterized by an annual average wind speed of 10 m/s, with Weibull parameters $k = 2.0$ and $c = 11.6$, is chosen to represent typical offshore conditions rather than those of a specific site. The resulting wind speed distribution is illustrated in Fig. 2.3a. Assuming that the wind turbine operates with an availability of 100 %, the output power distribution is calculated based on the wind speed distribution and the power curve of the wind turbine, and is depicted in Fig. 2.3b with a discretized power interval of 2.5 %. It can be observed that 43 % of the time the wind turbine will produce power at rated power (operating in region IV) and that 7 % of the time no power will be produced (regions I and V). This underscores the importance of designing the wind-to-hydrogen plant not only for nominal operation but also for operation at partial load, which accounts for 50 % of the load distribution. Still assuming the ideal scenario where the wind turbine operates with an availability of 100 %, approximately 80 GWh per year could be theoretically generated. This yields a theoretical capacity factor $C_{\text{F,WT}}$ of 60.8 % under the considered wind conditions and wind turbine power curve.

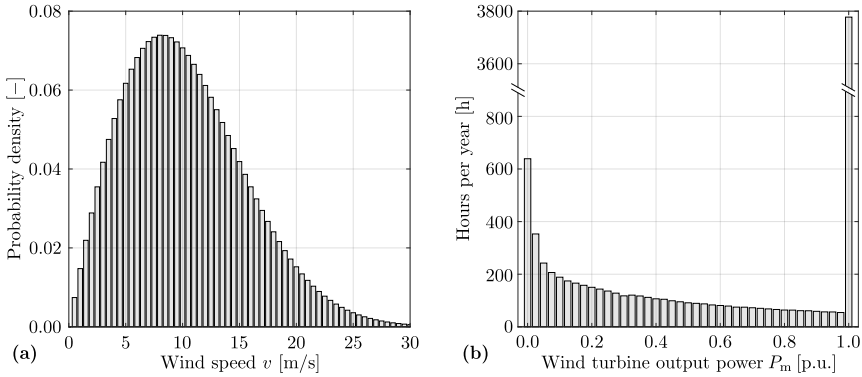


Figure 2.3: (a) Probability density function of wind speed and (b) corresponding hours per year at different wind turbine output power.

2.1.2 Wind Turbine Electrical Drivetrain

Although this thesis focuses solely on stand-alone wind turbines (i.e. without a grid connection), the typical configuration of the electrical drivetrain of an offshore grid-connected wind turbine and its control scheme, both illustrated in Fig. 2.4, are first described in the following to provide a foundational understanding of wind turbine electrical drivetrain and to highlight challenges that arise when operating in stand-alone.

The generator is directly driven by the wind turbine, eliminating the need for a gearbox. This offers several advantages over geared drivetrains, including reduced maintenance

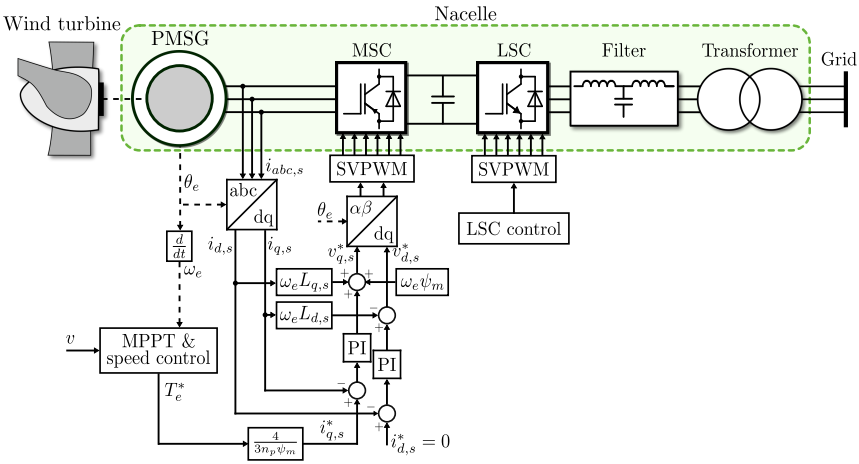


Figure 2.4: Standard full-scale converter and its control scheme typically used in offshore wind turbines connected to the grid [118].

requirements, lower conversion losses, decreased CapEx, and enhanced overall system reliability [113]. Low rotational speed (e.g. < 30 rpm) generators such as direct-driven multi-pole permanent magnet synchronous generator (PMSG) are widely employed, accounting for above 50 % of market shares in recent years [114]. Permanent magnet generators provide higher power density, reduced size and weight compared to other generator technologies. Moreover, the absence of an external excitation circuit results in higher efficiency, greater reliability and lower maintenance costs [115]. However, the direct coupling of the generator at low speeds also leads to larger physical dimensions and higher mass of the generator, which may pose challenges in transport, assembly, and servicing [116].

The variable speed operation of the generator, necessary to allow the wind turbine to operate at the optimal TSR for any wind speed in region III, translates to a variable electrical frequency. The high number of poles (n_p = 200 [109]) elevates the low rotational speed to an electrical frequency ranging between 8.3 to 12.6 Hz, depending on the generator rotational speed. Hence, the electrical drivetrain of offshore grid-connected wind turbines typically consists of bidirectional back-to-back (BTB) voltage source converters to convert the variable frequency to the fixed grid frequency of 50 or 60 Hz [117]. The BTB converter comprises a machine-side converter (MSC), a DC link and a line-side converter (LSC). The MSC acts as a rectifier and is in charge of PMSG torque management, while the LSC operates as an inverter, managing the DC-link voltage and reactive power exchange.

PMSG Side

Considering that the three-phase PMSG has a sinusoidal back-electromotive force (EMF), the electrical model of the PMSG is derived in its rotating dq synchronous reference frame with angular velocity ω_e using the Park-Clarke transform. The phase equations of the

stator are given by [118]

$$v_{\mathrm{d}} = R_{\mathrm{s}} i_{\mathrm{d,s}} + L_{\mathrm{d,s}} \frac{d}{dt} i_{\mathrm{d,s}} - \omega_{\mathrm{e}} L_{\mathrm{q,s}} i_{\mathrm{q,s}} \tag{2.7}$$

$$v_{\mathrm{q}} = R_{\mathrm{s}} i_{\mathrm{q,s}} + L_{\mathrm{q,s}} \frac{d}{dt} i_{\mathrm{q,s}} + \omega_{\mathrm{e}} L_{\mathrm{d,s}} i_{\mathrm{d,s}} - \omega_{\mathrm{e}} \psi_{\mathrm{m}} \tag{2.8}$$

where R_{s} is the stator resistance, $L_{\mathrm{d,s}}$ and $L_{\mathrm{q,s}}$ are inductance in the d- and q-axis, respectively, $i_{\mathrm{d,s}}$, $i_{\mathrm{q,s}}$, $v_{\mathrm{d,s}}$ and $v_{\mathrm{q,s}}$ are the d- and q-axis stator currents and voltages, respectively, ω_{e} is the PMSG electric angular speed ($\omega_{\mathrm{e}} = n_{\mathrm{p}} \cdot \omega_{\mathrm{m}}$), and ψ_{m} is the constant magnet flux-linkage. The representation of the control variable in the synchronous reference dq frame has the advantage of transforming sinusoidal currents and voltages to DC quantities, which can be controlled with a proportional integrator (PI) regulator without steady state error. The mechanical system of the PMSG can be simply modeled with the one-mass model such as,

$$\frac{d}{dt}\omega_{\mathrm{m}} = \frac{1}{J_{\mathrm{m}}}(T_{\mathrm{m}} - T_{\mathrm{e}} - B \cdot \omega_{\mathrm{m}}) \tag{2.9}$$

where J_{m} is the total moment of inertia of the wind turbine drive train, T_{m} is the turbine mechanical torque ($P_{\mathrm{m}}/w_{\mathrm{m}}$), T_{e} is the electromagnetic torque and B is the total rotation friction coefficient. The electromagnetic torque T_{e} exerted on the rotor consists of two parts, the permanent magnet torque and the reluctance torque that is generated in the machine, and is given by

$$T_{\mathrm{e}} = \frac{3}{4} n_{\mathrm{p}} \Big[\underbrace{\psi_{\mathrm{m}} i_{\mathrm{q,s}}}_{\text{perm. mag.}} + \underbrace{(L_{\mathrm{d,s}} - L_{\mathrm{q,s}}) i_{\mathrm{d,s}} i_{\mathrm{q,s}}}_{\text{reluctance}} \Big]. \tag{2.10}$$

The electromagnetic torque is a linear function of the reactive current when the direct component is controlled to zero. Thus, the MSC control scheme as depicted in Fig. 2.4, involves controlling the PMSG torque via the quadrature current component $i_{\mathrm{q,s}}$, while regulating the direct component at zero. This control strategy is commonly known as the vector control strategy [118]. The q-axis current reference $i^*_{\mathrm{q,s}}$ is derived from the speed controller, which adjusts its control strategy based on the wind speed. In regions II and IV, the generator torque is regulated by a constant rotor speed reference, whereas in region III, the speed controller tracks the optimal TSR to maximize the captured power, i.e. MPPT operation. The differences between the references and measured currents are fed into two PI controllers, resulting in dq-axis reference voltages.

The PMSG's voltage equations demonstrate cross-coupling between the dq-axis voltages through the terms $\omega_{\mathrm{e}} L_{\mathrm{q}} i_{\mathrm{q,s}}$ and $\omega_{\mathrm{e}} L_{\mathrm{d}} i_{\mathrm{d,s}}$. These coupling terms are compensated in the current controller to obtain two independent decoupled circuits, which are easier to control and more accurate. Subsequently, the space vector pulse width modulation (SVPWM) approach is employed as the modulation strategy to generate the six gate signals required to control the semiconductor devices of the MSC. The SVPWM generates less harmonic distortion in the output stator voltages/currents and provides more efficient use of the DC supply voltage than the conventional sinusoidal pulse width modulation [119].

Line Side

The usual control scheme of the grid-connected LSC involves a control loop to stabilize the DC link voltage and another to control the reactive power exchanged with the grid.

However, due to the decentralized offshore connection scheme operating in a stand-alone manner, the wind turbine is not connected to any grid. The LSC operates as a grid-forming converter rather than a grid-following one. The detailed control of the converter, which is fed by the MSC (the LSC in the case of grid-connected wind turbines), depends on the exact EDS employed. This includes whether a subsequent converter is used and whether the EDS is AC- or DC-based. Therefore, the control of the subsequent converter is detailed in Section 3.3.1, as it inherently depends on the EDS configuration employed.

Step Up Transformer

To minimize conduction losses in the collection system of the wind farm, an LFT is employed to elevate the relatively low voltage output of the electrical drivetrain to the collection system level, typically ranging from 33 to 66 kV. The placement of the LFT depends on the wind turbine design, with options including installation in the nacelle or at the tower base. Although LFT requires a relatively large volume and add weight requirements, their high reliability makes them preferred for nacelle placement, reducing the length of low-voltage cabling in the tower, potentially lowering conduction losses and costs [120].

Offshore wind turbine LFTs are usually of dry type due to reduced maintenance needs, lower fire hazards and environmental benefits from the absence of oil leaks. The LFT short circuit impedance shall be designed to be in the range of 8 % according to the IEC 60076-16 and supports the LCL filter to mitigate harmonics. Furthermore, the transformer enhances protection of the electrical drivetrain against lightning strikes by providing galvanic isolation between the collection system and the wind turbine electrical drivetrain [121].

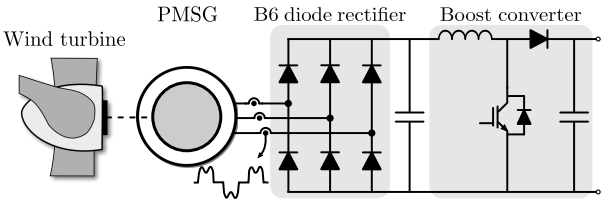
2.1.3 Power Electronics Converter Architecture

The power converter topology employed as the BTB converters in electrical wind turbines with direct-driven multipole PMSG highly depends on the rated voltage and power of the PMSG. The classification is carried out based on active versus passive rectification, and LV versus medium voltage (MV) operation.

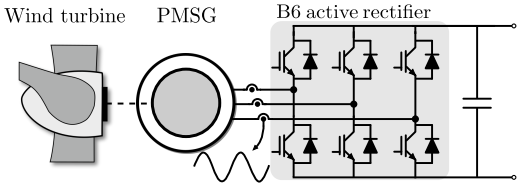
Passive Versus Active Rectification

In wind turbines, the active power flow is unidirectional, from the generator to the grid. To reduce system cost and complexity while enhancing reliability, passive rectification (e.g. three-phase bridge (B6) diode rectifier) could be considered as an alternative to active rectification [118]. However, this approach presents several challenges, which are discussed below.

Technically, B6 diode rectifier can be employed as MSC for PMSG as the machine inherently provides its own rotor flux through permanent magnets, eliminating the need for magnetizing current. While a four-quadrant converter can inject reactive power to compensate for voltage drops across the generator's internal reactance, a diode rectifier cannot control the d-axis current to zero, leading to a decreasing PMSG terminal voltage as rotational speed increases [118]. Consequently, the generator has to be designed to be over-excited so that under full load, the induced stator voltage (back EMF) is higher



(a) Passive rectification.



(b) Active rectification.

Figure 2.5: Passive and active rectification in wind turbine electrical drivetrain.

than the terminal voltage. In a PMSG, this leads to lower machine efficiency, increased magnet usage and higher costs [122]. This also means that the converter has to be rated for the higher terminal voltage at low loads and that in the event of a sudden power loss, the terminal voltage would jump to the no-load voltage [123].

Hence, in practice, a B6 diode rectifier as the MSC is typically supplemented, as shown in Fig. 2.5a, with a boost converter on the DC link to maintain a constant DC link voltage and ensure correct operation of the LSC across the full wind speed range. High-power setup often consists of several interleaved boost converters. However, the use of a diode rectifier results in distorted stator current waveforms, increasing generator losses and causing torque ripple [124]. While diode-bridge rectifiers were commonly employed in lower-scale wind turbines in the past, they are no longer used in modern megawatt-scale applications partly because low-frequency torque pulsations and high total harmonic distortion become detrimental to the generator [113]. Therefore, this thesis excludes the use of diode-bridge rectifiers as the MSC, opting instead for active rectification through AFE rectifiers, as illustrated in Fig. 2.5b.

LV Versus MV Converter Architecture

Double-digit megawatt PMSG are reported with varying rated voltages depending on the manufacturer [125]. The operating voltage for commercial offshore wind generators ranges from a few hundred volts (typically 690 V) to a few thousand volts (e.g., 3300 V). Depending on the power and voltage ratings of the system, the BTB converters can consist of a multitude of LV two-level (2L) voltage source converters which are parallelized or a few MV converters such as three-level (3L) neutral point clamped converters [117].

The 2L BTB converter configuration is a well-established solution for LV power conversion systems in commercial wind turbine electrical drivetrains [87]. The power rating

of a single LV 2L BTB converter is limited to a few megawatts by the current ratings of the semiconductor devices. A multi-MW PMSG, as shown in Fig. 2.6a, typically consists of multiple windings that can feed parallel-connected BTB 2L converters, thereby avoiding the need to parallelize semiconductor devices within a single converter.

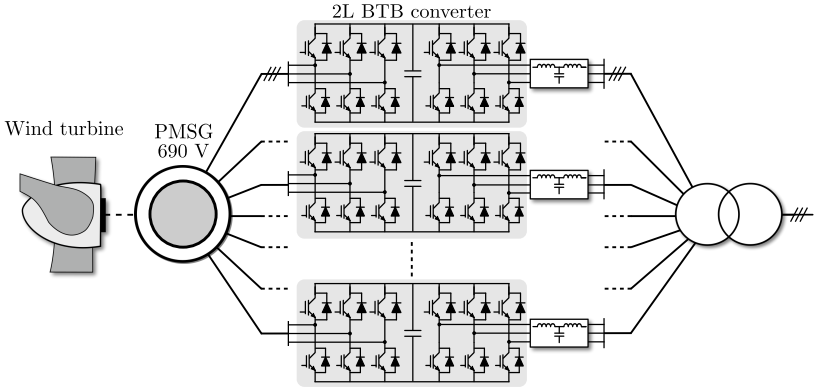
Although a multi-winding generator entails higher design cost, this configuration has found practical application due to several advantages [118, 126]:

- The total generated power can be delivered through several standard 2L voltage source converters of lower-rated power, which can be mass-produced, benefiting from economies of scale.
- The parallelized BTB converters are insulated from each other through the stator windings, eliminating the possibility of circulating currents among the converters and preventing converter power derating. The outputs of the parallelized converters can be connected to the same transformer winding.
- With proper phase-shifting of the carrier waveforms of each BTB converter, the output harmonic performance of the system can be further improved, allowing the use of smaller-size filters with reduced costs, weight and losses [127, 128].
- In the event of a converter failure, the faulty converter module can be isolated from the generator and the other converters by opening disconnectors. The wind turbine can still supply a share of the rated power or even the full rated power if the remaining converter can handle the increased current. This results in a significantly lower loss of produced energy in case of a converter fault.
- The number of active converter modules can be varied based on the power level, potentially operating all converters at an optimal load, resulting in improved power electronics efficiency.

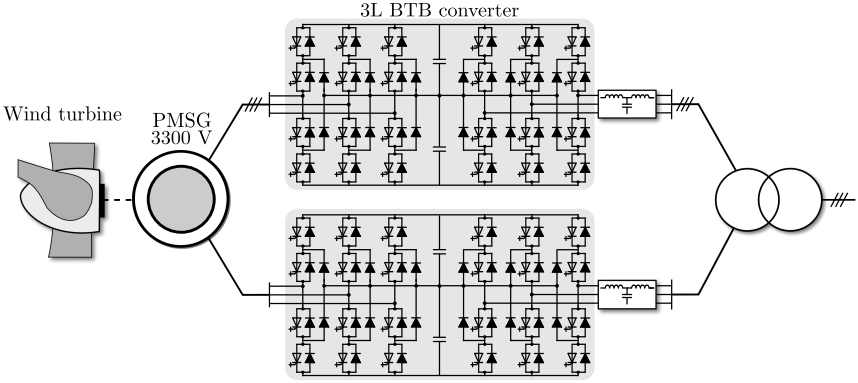
Conversely, at high power levels, the use of MV converters, such as 3L converter as depicted in Fig. 2.6b, offers an efficient, economical, and promising alternative to LV converters [88]. The MV operation of wind turbine electrical drivetrains, shows promise for achieving higher power ratings with lower currents, thereby improving power conversion efficiency and reducing the size of passive components, including inductors, transformers, generators, and cables. The adoption of MV configuration has been shown to lead to CapEx reduction in the wind turbine electrical drivetrains, with larger cost savings for larger systems [129]. Although 3L converters in wind turbine BTB converters often consist of integrated gate commutated thyristor (IGCT) devices, which are inherently more reliable than IGBT devices [130], MV operation results in fewer converter units (one to three for a 15 MW study case [131]), leading to lower redundancy and potentially lower availability of the wind turbine.

2.1.4 Requirements Specification for Wind Turbine Electrical Drivetrains

The design of a power converter system in a wind turbine for stand-alone offshore operation must address several key requirements. The requirements can be divided into two categories: general offshore requirements and electrical considerations specific to wind turbines, and are outlined in the following.



(a) LV configuration with several parallel 2L BTB converters.



(b) MV configuration with two 3L BTB converters.

Figure 2.6: Examples of common topologies used in the wind turbine electrical drivetrain, depending on the voltage level [88].

Offshore Specific Requirements

Due to the remote and harsh operating environments, the maintenance of offshore wind turbines presents a unique set of challenges. Accessibility is a primary concern, as turbines are often located far from shore, requiring specialized vessels and equipment for transportation and maintenance activities. Adverse weather conditions, including high winds, rough seas, and extreme temperatures, can further complicate access and safety, limiting the windows of opportunity for maintenance work. Long repair times are often compounded by additional delays caused by waiting times during the winter seasons [132]. Maintenance costs have been reported to account for up to 30 % of the cost of energy produced [133]. These factors collectively contribute to higher operational costs, underscoring the need for solutions to keep manned maintenance to the absolute minimum.

According to IEC 61400-1, the design lifetime for offshore wind turbines shall be at least 20 years. Recent reports on wind turbine faults indicate that generators and power converters have the highest failure rates, averaging between 30 and 35 % of overall failures [132]. Power converter faults, in particular, significantly increase turbine downtime and overall energy costs. For these reasons, equipment should be designed for long maintenance intervals—or ideally, no maintenance at all—and with high reliability. A maximum of one planned maintenance per year is considered in this thesis. Power converters should feature modular structures, with redundant components in critical systems, and fault-tolerant capabilities to ensure continued operation even under faulty conditions [134].

The advanced technology and high reliability required for power converters, including extensive redundancy, can significantly increase their initial costs. Power converters account for approximately 7 to 12 % of the overall wind turbine cost [88]. Although this may seem like a small portion, non-negligible cost savings can be accomplished and favorably impact the cost of energy. While CapEx is a significant consideration, the financial impact of an unmanned offshore plant being unable to produce hydrogen, such as due to a failure of a non-redundant converter, can potentially far exceed the cost of implementing a redundant converter. This includes lost production and the expenses associated with unscheduled maintenance. Therefore, ensuring high availability is considered in this thesis as one of the top priorities considered in the design philosophy.

Additionally, components should be protected from the corrosive marine environment, which accelerates wear and tear on exposed parts. The harsh and variable conditions, including constant exposure to salt air, wind, and water, require equipment to be either located indoors or housed in sealed enclosures [135]. To protect against harsh offshore environments, all essential wind turbine components such as generators, power converters, and control systems, are housed within the nacelle and tower. Given the limited available space, the footprint, volume, and weight of these components must be carefully considered to ensure structural integrity, operational efficiency, and ease of installation. Components should be as compact as possible to minimize overall size and weight, while also allowing for ease of maintenance and accessibility. Additionally, housing equipment indoors requires reduced insulation levels and isolation clearances, which means the distribution voltage in the EDS should be kept as low as possible while balancing practical considerations.

The intermittent nature of offshore wind energy can result in periods without power generation, thus necessitating reliable backup systems or energy storage solutions to maintain auxiliary power during low wind periods. Ensuring a continuous and reliable power supply for critical auxiliary systems, such as control systems, heating systems (to prevent freezing), and safety equipment, is vital for the operational integrity and survival of the wind turbine. While IEC standards specify guidelines for electrical network outages (not applicable in this case), they do not specifically address low wind periods, as these are site-specific. In this case study, a continuous period of 72 hours shall be considered as the extreme condition for planning and designing auxiliary power systems [136].

Wind Turbine Specific Electrical Requirements

Ensuring the high efficiency of power converters in offshore wind turbines is a key factor for maximizing energy output and reducing the overall cost of energy. To achieve this, power converters must operate at the highest levels of efficiency across a wide range of operating conditions (voltage and power wise), including not only full-load but also part-load scenarios, as in this study case the wind turbine operates half of the time at partial load. At the multi-megawatt scale, even a 1 % loss in conversion or transmission can result in several hundred kilowatts of heat to dissipate. Minimizing power losses requires the use of efficient switching devices, optimal power converter topologies, and sophisticated control schemes. Reducing the losses at each conversion step—or preferably reducing the number of power conversion steps—is essential for enhancing overall system performance. Additionally, given the tower height of 150 meters, the relatively long tower cables can lead to significant conduction losses depending on the voltage employed in the EDS. According to IEC 60204-1, which applies to the design of wind turbine electrical drivetrains, the corresponding voltage drop shall not exceed 5 % of the nominal voltage under normal operating conditions. This factor has also to be considered with the aim of minimizing both tower cable costs and conduction losses as much as possible.

As discussed in the introduction, one of the inherent drawbacks of wind power is the intermittency of wind velocity. This leads to potential power fluctuations, which can be categorized based on their duration. Long-term fluctuation arises from weather patterns and can be approximated by a Weibull distribution. In contrast, short-term fluctuations are caused by different factors, such as wind turbulence, tower shadowing effects and drivetrain resonances [137].

Wind turbulence, as categorized in IEC 61400-1, follows a stochastic behavior that can be represented by a Gaussian probability distribution function. The tower shadowing effect, as the name suggests, occurs when a rotor blade passes in front of the tower, causing a temporary reduction in the torque produced by that blade. This results in a potential power dip that repeats at a frequency three times the rotational frequency of the rotor in three-blade wind turbines. Lastly, drivetrain resonances occur when the wind turbine operates at one of the eigenfrequencies of the drivetrain, potentially leading to power fluctuations. The resonances with the 3-period interference and with the drivetrain can be mitigated by imposing a minimum rotational speed of the rotor within a specific wind speed range, such as in region II. In addition, as highlighted in [137], the magnitude of wind speed fluctuation due to the tower shadowing effect is much lower compared to wind turbulence, resulting in power oscillations on the generator side caused by the tower shadowing significantly smaller than those caused by turbulent wind. Therefore, only wind turbulence is considered in this work.

Wind variations can be modeled as a step increase or decrease of the wind speed as illustrated in Fig. 2.7a. Though positive gradients can be compensated by the pitch control, a negative gradient will result inevitably in decrease power production. A decrease in wind speed from rated to cut-in speed, corresponding to a deliberately conservative negative decrease of 70 % in wind speed, is considered. In accordance with the wind turbine dynamic model governed by (2.9), the wind turbine mechanical torque responds based on the rotor inertia J_{m}, which in turn influences the PMSG output power response. As depicted in Fig. 2.7b, the higher the rotor inertia J_{m}, the slower the change in wind

turbine output power. Given the relatively high rotor inertia considered in this thesis for large-scale offshore wind turbines (see Table 2.1), the overall rate of change of power is averaged at 13 %/s while the instantaneous rate of change of power peaks at 22 %/s as shown in Fig. 2.7c.

In addition to the PMSG torque management to maximize energy capture in region III by providing reactive power control and meeting limited torque ripple requirements, the wind turbine electrical drivetrain should incorporate overvoltage protection to protect the semiconductor devices employed in the power converters from any harmful voltages. The relatively fast dynamics in the power output of the PMSG could result in a power mismatch with the electrolysis plant. Moreover, sudden power flow interruptions such as faults or tripped loads should be considered as worst-case scenarios. High-power PMSGs are characterized by high leakage reactance compared to other machine types. This characteristic can lead to an exponential rise in the DC link voltage when surplus energy is generated [138]. In the event of a sudden interruption in power flow, such as when the load (particularly the electrolysis plant in this study) is tripped, the output power from the generator must be dissipated or curtailed. This involves reducing the generator current from its prevailing value to zero, necessitating the application of sufficient volt-seconds to the generator reactance to stop the current flow. Consequently, the terminal voltage of the generator has to be greater than the internal back-EMF of the generator.

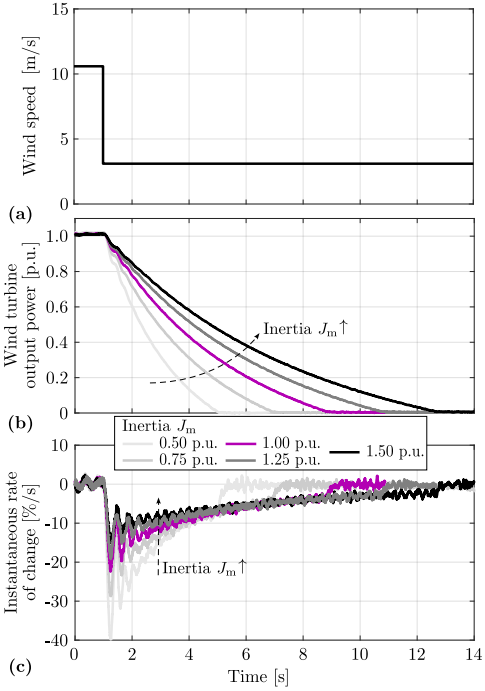


Figure 2.7: (a) Wind speed variation with negative gradient, (b) corresponding response in wind turbine output power according to the rotor inertia and (c) the instantaneous rate of change in output power.

2.2 Modeling and Requirements of Electrolysis

The combination of high dynamic capabilities, rapid startup and shut-down times, compact size, absence of chemical usage, low operating temperature and low maintenance requirements makes PEM electrolysis more suitable than its counterparts for connection to a stand-alone wind turbine [3]. Due to these factors, this thesis exclusively focuses on PEM electrolysis. The electrical behavior of an electrolyzer can be characterized by the aggregated model of individual electrolytic cells. This section aims to provide a comprehensive understanding of the electrical behavior of the cell and its specific requirements before delving into the broader plant level and its corresponding needs. Subsequently, the requirements for the power supply of the electrolyzer and for the electrolysis system are described.

2.2.1 Electrolysis Fundamentals

As illustrated in Fig. 2.8, a PEM electrolyzer cell comprises two electrodes—an anode and a cathode—immersed in water and separated by a solid polymer membrane. The membrane acts as the electrolyte, allowing only hydrogen protons to pass from the anode to the cathode, closing the electric circuit while electronically isolating the electrodes and preventing the mixing of hydrogen and oxygen gases. The anode and cathode are connected to bipolar plates, which feature water and gas flow channels through each side. The two electrodes are connected through an external voltage source for electron flow.

When a DC voltage and heat are applied, two half-reactions occur: an oxidation at the anode and a reduction at the cathode. At the anode, water molecules are oxidized releasing oxygen, electrons and hydrogen protons. The positively charged protons are attracted to the cathode and migrate through the membrane, while the electrons are directed through an external power circuit, providing the energy required for the reaction. At the cathode, the protons that have migrated through the membrane combine with the electrons in a reduction reaction, producing gaseous hydrogen [5].

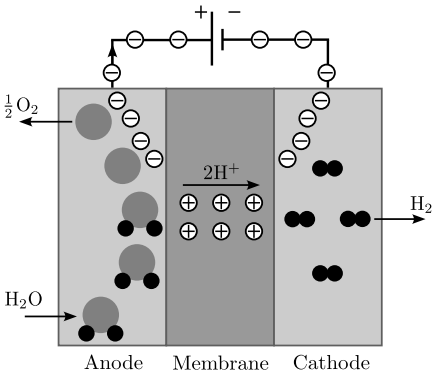


Figure 2.8: Schematic of the basic operating principle of a PEM electrolysis cell.

Thermodynamics of PEM electrolysis

The PEM electrolysis process consists of two half-reactions at the anode and cathode and can be written as follows [139]

$$\text{Anode reaction}: \mathrm{H_2O} \longrightarrow \frac{1}{2}\mathrm{O_2} + 2\mathrm{H^+} + 2\mathrm{e^-} \tag{2.11}$$

$$\text{Cathode reaction}: 2\mathrm{H^+} + 2\mathrm{e^-} \longrightarrow \mathrm{H_2}. \tag{2.12}$$

Thus, the overall electrochemical reaction is

$$\mathrm{H_2O(l)} + 237.2\ \mathrm{kJ_{el.}/mol} + 48.6\ \mathrm{kJ_{heat}/mol} \longrightarrow \mathrm{H_2(g)} + \frac{1}{2}\mathrm{O_2(g)}. \tag{2.13}$$

Given that the hydrogen generated requires two-electron transfer, the hydrogen production rate (mol/s) is proportional to the supplied current according to Faraday's law as follows

$$\dot{n}_{\mathrm{H_2}} = \eta_{\mathrm{F}} \frac{I_{\mathrm{cell}}}{2F} \tag{2.14}$$

where η_F is the Faraday efficiency (also known as the current efficiency), I_{cell} the current applied to the cell, and F the Faraday constant. The amount of hydrogen gas produced in one hour (kg/h) is given by

$$\dot{M}_{\mathrm{H_2}} = 3600 \cdot \dot{n}_{\mathrm{H_2}} v_{\mathrm{m}} d_{\mathrm{H_2}}(T_{\mathrm{cell}}, p_{\mathrm{H_2}}) \tag{2.15}$$

$$\text{with } v_{\mathrm{m}} = \frac{R \cdot T_{\mathrm{cell}}}{p_{\mathrm{H_2}}} \tag{2.16}$$

where $d_{\mathrm{H_2}}(T_{\mathrm{cell}}, p_{\mathrm{H_2}})$ is the hydrogen density dependent on the cell temperature T_{cell} and the hydrogen partial pressure $p_{\mathrm{H_2}}$, v_{m} is the molar volume of hydrogen and R is the universal gas constant [139].

Under constant standard ambient conditions (298.15 K and 101.325 hPa), the enthalpy of the overall electrochemical reaction is 285.9 kJ/mol, which is the minimum amount of energy that has to be supplied electrically (237.2 kJ/mol) and thermally (48.6 kJ/mol) to split water into hydrogen and oxygen gases. When thermal energy is provided externally, the theoretical voltage required between electrodes to initiate the water electrolysis is known as reversible voltage and can be calculated as

$$V_{\mathrm{rev}}^0 = \frac{\Delta \mathrm{G}}{2F} = \frac{237.2\ \mathrm{kJ/mol}}{2\ \mathrm{x}\ 96485\ \mathrm{C/mol}} = 1.23\ \mathrm{V} \tag{2.17}$$

with ΔG the Gibbs free energy at standard ambient conditions. Conversely, if the thermal energy is supplied by the electrical source (common practice in commercial electrolyzers), the minimum reversible voltage is referred to as the thermoneutral voltage and is calculated as

$$V_{\mathrm{th}}^0 = \frac{\Delta \mathrm{G}}{2F} = \frac{285.9\ \mathrm{kJ/mol}}{2\ \mathrm{x}\ 96485\ \mathrm{C/mol}} = 1.48\ \mathrm{V}. \tag{2.18}$$

The former value corresponds to the lower heating value, while the latter value represents the higher heating value in standard ambient conditions [140].

Cell Voltage

In practice, the voltage required to sustain the electrolysis process is higher than the minimum thermoneutral voltage due to various voltage losses from internal electrical resistances, kinetic overvoltages known as activation potentials, and mass transport losses. The electrolyzer cell voltage is approximated as the sum of the open circuit voltage and overvoltages as follows [140]

$$V_{\text{cell}} = V_{\text{oc}} + V_{\Omega} + V_{\text{act}} + V_{\text{trans}}. \tag{2.19}$$

The different components of the electrolyzer cell voltage are illustrated in Fig. 2.9 and are described in the following. The open circuit voltage V_{oc} (defined as the cell voltage when there is no current flow) is equal to the thermoneutral voltage V_{th}^{0} at standard conditions and varies as a function of cell operating temperature and partial pressures, as described by the Nernst equation:

$$V_{\text{oc}} = V_{\text{th}}^{0} + \frac{RT_{\text{cell}}}{2F} \ln\left(\frac{p_{\text{H}_2} \cdot \sqrt{p_{\text{O}_2}}}{p_{\text{H}_2\text{O}}}\right) \tag{2.20}$$

with p_{O_2} and $p_{\text{H}_2\text{O}}$ the partial pressures of oxygen and water, respectively.

The ohmic overpotential V_{Ω} is caused by non-zero resistances to electron and proton conduction. The proton resistance R_{ion} (i.e., from the membrane) is much larger than other ohmic resistances present in the cell conductors (bipolar plates, electrode current collectors, etc.). Therefore, the ohmic overpotential of the cell can be approximated by considering only the ionic component and can be approximated as an electrical resistance [141]:

$$\lambda_{\text{m}} = 0.08533 \cdot T_{\text{cell}} - 6.77632 \tag{2.21}$$

$$\sigma_{\text{m}} = (0.005139 \cdot \lambda_{\text{m}} - 0.00326) \exp\left[1268\left(\frac{1}{303} - \frac{1}{T_{\text{cell}}}\right)\right] \tag{2.22}$$

$$R_{\text{ion}} = \frac{\phi_{\text{m}}}{A_{\text{m}}\sigma_{\text{m}}} \tag{2.23}$$

$$V_{\Omega} = R_{\text{ion}} J \tag{2.24}$$

where σ_{m} is the ionic conductivity that depends on water content and cell temperature T_{cell}, with λ_{m} the membrane humidification ratio, ϕ_{m} the membrane thickness, A_{m} the active cell area and J the current density.

Activation losses originate from the molecular bonds that electrons have to overcome to initiate the reaction. A portion of the applied voltage is lost in transferring electrons to or from the electrodes during chemical reactions at the electrodes. The activation overpotential can be determined separately for the anode (2.25) and the cathode (2.26) using the Butler-Volmer equation

$$V_{\text{act,an}} = \frac{RT_{\text{cell}}}{\alpha_{\text{an}}F} \cdot \sinh^{-1}\left(\frac{J}{2J_{0,\text{an}}}\right) \tag{2.25}$$

$$V_{\text{act,ca}} = \frac{RT_{\text{cell}}}{\alpha_{\text{ca}}F} \cdot \sinh^{-1}\left(\frac{J}{2J_{0,\text{ca}}}\right) \tag{2.26}$$

where α_{an} and α_{ca} are the charge transfer coefficients, and $J_{0,an}$ and $J_{0,ca}$ the exchange current densities at anode and cathode, respectively. The charge transfer coefficients represent the fractions of the electrostatic potential energy that influence the kinetic rate of the reactions [142]. The exchange current density parameters refer to the current flowing at the surface of the electrodes at equilibrium and depend on the operational conditions and structure of the electrodes. As shown in Fig. 2.9, the activation overpotential at the anode remains relatively constant at current densities above 0.5 A/cm^2 and is the most significant component of cell voltage at low current densities. However, once the current density exceeds 1 A/cm^2, the ohmic overpotential, characterized by a linear relationship, becomes more predominant.

Mass transport losses (also referred to as concentration losses) result from limited water flow on the anode and restricted gas diffusion on the cathode, causing deviations in concentrations at the electrodes and suboptimal usage of electrode surfaces. The mass transport overpotential can be estimated as

$$V_{trans} = -\frac{RT_{cell}}{2F} \cdot \ln\left(1 - \frac{J}{J_{lim}}\right) \tag{2.27}$$

where J_{lim} is the maximum current density. Mass transport losses have an almost minimal effect at low current densities and theoretically approach infinity at J_{lim}, defined in this thesis at 3 A/cm^2. Consequently, the contribution to cell voltage is almost negligible at moderate current densities between 0 and 2 A/cm^2, which is the typical operating range for PEM electrolysis cells [3].

The electrolyzer cell voltage exhibits a non-linear positive correlation with the current density due to electrochemical losses occurring within the cells, as illustrated by the polarization curve in Fig. 2.9. Polarization curves are commonly employed to evaluate cell performance. The lower the cell voltage at a given current density, the lower the overpotential losses and the more efficient the cell is.

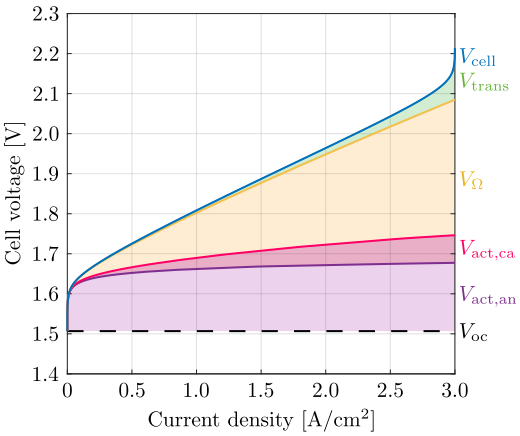
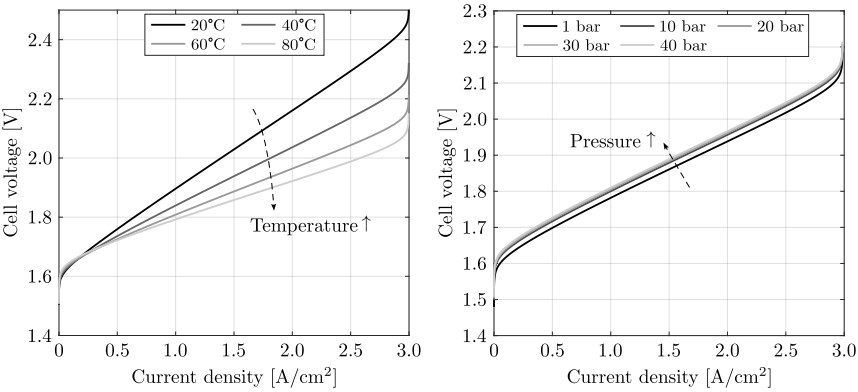


Figure 2.9: Breakdown of the voltage of a generic PEM electrolysis cell operating at a pressure of 35 bar and T_{cell} = 60 °C (adapted from [143]).



(a) For different T_{cell} at a pressure of 35 bar. (b) For different cell pressure at $T_{\text{cell}} = 60\,°\text{C}$.

Figure 2.10: PEM cell polarization curves under variant operating conditions.

The cell voltage is influenced by both temperature and pressure, as depicted in Fig. 2.10a and Fig. 2.10b, respectively. Operating at higher temperatures is favorable as the conductivity of the membrane increases, reducing the ohmic overvoltage within the cell. However, high-temperature operation (> 70 °C-80 °C) requires the use of expensive materials and accelerates the degradation of the electrolyzer cell [63]. Conversely, operating at higher pressure results in higher cell voltage, although the reduction in external compression can balance the electrolysis efficiency decrease to a certain limit.

Cell Efficiency

At the cell level, efficiency can be computed as the ratio of the ideal applied electrical power to the actually applied power ($V_{\text{cell}} I_{\text{cell}}$). The ideal power is defined as the product of the open circuit voltage and the current that corresponds to the actual hydrogen output. The discrepancy between the ideal and applied current is attributed to the loss current I_{loss}, which represents the portion of the current that does not contribute to hydrogen production at the cathodic gas outlet. The cell efficiency can be written as follows [144]

$$\eta_{\text{cell}} = \frac{V_{\text{oc}}(I_{\text{cell}} - I_{\text{loss}})}{V_{\text{cell}} I_{\text{cell}}} \tag{2.28}$$

$$\eta_{\text{cell}} = \underbrace{\left(\frac{V_{\text{oc}}}{V_{\text{cell}}}\right)}_{\eta_{\text{V}}} \cdot \underbrace{\left(1 - \frac{I_{\text{loss}}}{I_{\text{cell}}}\right)}_{\eta_{\text{F}}} \tag{2.29}$$

with η_V the voltage efficiency and η_F the Faraday efficiency. The voltage efficiency at a given current density is defined as the ratio of the open circuit voltage to the actual cell voltage required to drive the reaction at the desired current density. The differences arise from electrochemical internal losses, as previously discussed. As the current density increases, the cell voltage rises due to higher activation and ohmic losses. Consequently, the voltage efficiency decreases with current density, as shown by Fig. 2.11a.

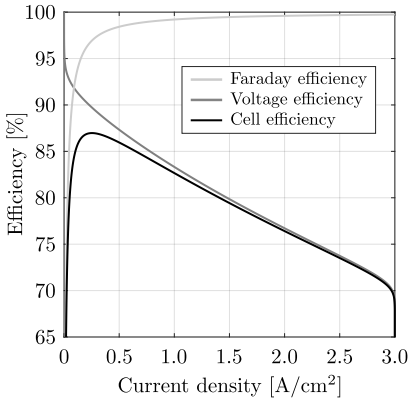
The Faraday efficiency is expressed as the ratio of the ideal electric current to the actual electric current required for the production of a given amount of hydrogen. Faradaic losses occur when electrons or hydrogen protons participate in unwanted side reactions, leading to heat and/or chemical byproducts. For instance, on the anode side, the oxidation of water can result in hydrogen peroxide production, thereby diverting a fraction of the applied current. In a PEM cell, the main causes for faradaic losses arise from gas crossover current, where the produced hydrogen and oxygen can permeate through the membrane and mix with each other, rather than being collected separately [145]. A portion of the applied current is wasted in producing mixed gases rather than pure hydrogen and oxygen. Due to the higher permeation of hydrogen at low current densities, the Faraday efficiency decreases significantly at lower current densities, as shown by Fig. 2.11a.

The SEC is commonly used to represent the electrolyzer cell efficiency, by quantifying the amount of electrical energy required to produce one kg of hydrogen gas, and is given by [146]

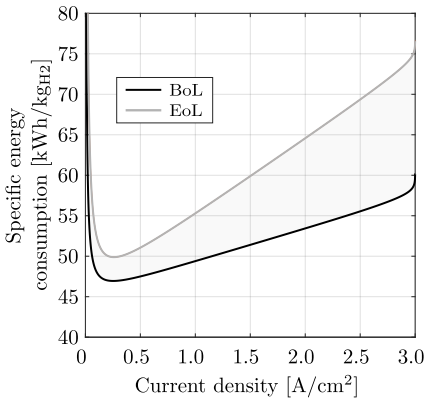
$$E_{\mathrm{SEC}} = \frac{\int_0^t V_{\mathrm{cell}} I_{\mathrm{cell}}\ dt}{\int_0^t \dot{M}_{\mathrm{H_2}}\ dt}. \tag{2.30}$$

Fig. 2.11b depicts a typical SEC curve of a PEM electrolyzer cell. Due to overvoltages, the SEC increases nearly linearly with increasing current density. Consequently, a PEM electrolyzer cell exhibits peak cell efficiency in partial load operation.

In addition, as in every electrochemical system, the cells degrade during operation, leading to lower efficiency and an increased required voltage at a given current density over their lifetime. Thus, the electrolyzer cell is characterized by two polarization curves, one at the beginning-of-life (BoL) and one at the end-of-life (EoL).



(a) Faraday, voltage and cell efficiency of PEM cell at BoL.



(b) SEC for different agings of the cell.

Figure 2.11: Different cell efficiencies at 35 bar and T_{cell} = 60 °C of an exemplary PEM cell (adapted from [143]).

The definition of the EoL depends on several factors. Commercially available PEM electrolyzer cells are expected to reach a lifetime of 60000 operating hours [3]. The specific maximum operating hours can be optimized based on the operating costs (OpEx), the replacement costs and cooling system costs.
On the one hand, enabling a longer maximum operating hours results in:

- lower cell efficiency at EoL, ultimately increasing OpEx to produce the same hydrogen amount.
- larger cooling systems, leading to higher CapEx and OpEx to dissipate the additional heat.

On the other hand, limiting the maximum operating hours results in more frequent cells replacement:

- increasing the number of cells needed over the plant lifetime, potentially raising overall cells CapEx.
- increasing the logistics demand (particularly challenging and expensive offshore), potentially resulting in overall longer downtime.

In this work, cells are considered to have reached their EoL when the overall cell efficiency has decreased by 10 % relative to their initial value, a reduction that corresponds to a 15 % increase in SEC.

Minimum Load Requirements

As discussed, the produced hydrogen can permeate through the membrane and mix with oxygen on the anode side, a process commonly referred to as hydrogen crossover or permeation. The gas crossover reduces the purity of the produced gases and can potentially lead to explosive mixtures of hydrogen in oxygen on the anode side. The permeation rate of hydrogen can be approximated as follows [147],

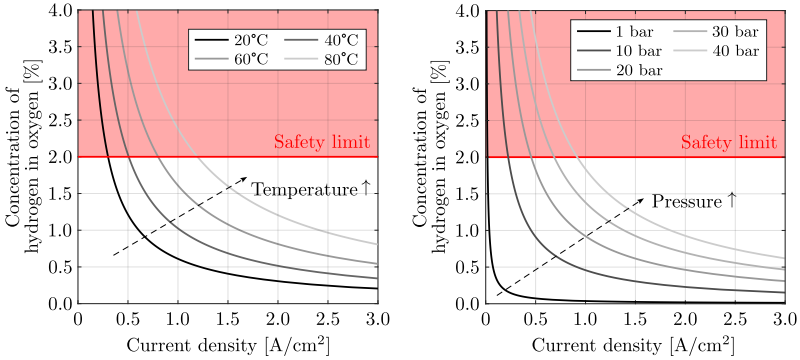
$$\dot{n}_{\mathrm{H_2}}^{\mathrm{perm}} = K_{\mathrm{P}}^{\mathrm{T_{ref}}} \exp\left[\frac{E_{\mathrm{A}}}{R}\left(\frac{1}{T_{\mathrm{ref}}} - \frac{1}{T_{\mathrm{cell}}}\right)\right]\frac{p_{\mathrm{H_2}}}{\phi_{\mathrm{m}}} \tag{2.31}$$

with $K_{\mathrm{P}}^{\mathrm{T_{ref}}}$ the permeability coefficient at the reference temperature T_{ref} , E_{A} the activation energy. The concentration of hydrogen in oxygen can be calculated as,

$$C_{\mathrm{H_2/O_2}} = \frac{\dot{n}_{\mathrm{H_2}}^{\mathrm{perm}}}{\dot{n}_{\mathrm{H_2}}^{\mathrm{perm}} + \dot{n}_{\mathrm{O_2}}^{\mathrm{evo}}} \tag{2.32}$$

with $\dot{n}_{\mathrm{O_2}}^{\mathrm{evo}}$ the evolved oxygen flow. Due to the decreasing oxygen evolution at lower current densities, the concentration of hydrogen in oxygen increases in a hyperbolic manner as current density decreases. As illustrated in Fig. 2.12a and Fig. 2.12b, this phenomenon is amplified with increasing temperature and pressure, especially at low current densities, due to increasing hydrogen solubility and diffusion coefficient, as well as possible induced membrane hot spots and tears [147].

To prevent the formation of potentially flammable mixtures at relatively low current densities, a minimum load requirement is imposed on the electrolyzer range. While the



(a) For different cell temperature at a pressure of 35 bar.

(b) For different cell pressure at $T_{\text{cell}} = 60\,°\text{C}$.

Figure 2.12: Concentration of hydrogen in oxygen on the anode side for different operating conditions in an exemplary PEM cell design (adapted from [147]).

lower explosive limit for hydrogen in oxygen is around 4 % by volume, a more conservative around 2 % is commonly applied as a safety margin due to factors such as unknown precise locations of highest hydrogen concentration within the cell, time delays between hydrogen permeation and detection by gas sensors, as well as dynamic operating conditions and gas mixing effects. Thus, as shown in Fig. 2.12a and Fig. 2.12b, the minimum load requirement can range from near zero up to half the rated current, depending on the operating conditions and cell structure.

The minimum load requirement is a steady-state operational constraint to maintain safety during normal operation. However, the electrolyzer unit can and must operate below this limit during transient phases such as start-up and shut-down, when the cell temporarily runs at low loads. During these phases, additional safety protocols and monitoring are typically applied.

Cell Degradation

In the context of this thesis, cell degradation is a key aspect when comparing different EDS, since degradation results in a higher cell voltage and thus alters the load conditions over the lifetime of the electrolyzer. Degradation mechanisms in PEM electrolyzer cells primarily originate from increased ohmic resistance, decreased exchange current density, and contamination by cation impurities. Ohmic resistance increases due to the passivation of the anode side, exacerbated by high anode overpotentials. The exchange current density decreases over time due to contamination of the anode layer [148, 149]. Widely different degradation rates are reported (0 to 200 µV/h) in the literature, depending on catalyst type, loading and operating conditions [62]. Accelerated stress testing is commonly employed in the literature to evaluate the cell degradation rate for different operating profiles, such as constant current, constant voltage, different temperatures and current cycling. Key factors influencing degradation include:

Temperature: when the cell is operated at a low temperature ($\leq 60\,°\text{C}$), the ohmic

part of the impedance remains stable or may tend to decrease during aging tests, possibly due to the membrane thinning. Conversely, operating at high temperatures ($\geq$ 80-90 °C) accelerates cell degradation due to passivation processes, leading to increased gas crossover and reduced durability [63, 150].

Power profile: while no degradation was observed to occur at low current densities ($\leq$ 1 A/cm^2), the degradation rate is highest at elevated and constant current densities ($\geq$ 2 A/cm^2) due to increased gas bubble formation, mechanical impact on electrode layers, and accelerated accumulation of contaminants [61]. Therefore, long and uninterrupted periods of operation at 2 A/cm^2 or above should be avoided. However, degradation consists of both reversible and irreversible components, with the irreversible components being predominant. In [148], it was observed that approximately 60 % of the total voltage increase is attributed to reversible degradation phenomena, since a buildup of ohmic losses was recovered when the cell current was interrupted. Current density switching has been highlighted to have a positive impact on cell degradation, as it allows reversible parts of degradation to recover, resulting in a substantially reduced degradation per mole of hydrogen produced. Negative degradation rates were even observed, explained by a reduction in total ohmic resistance [63]. Although fewer and longer current interruptions are preferred over more frequent and shorter interruptions.

Water quality: cations impurities present in the water were shown to agglomerate in the membrane, reducing ionomer conductivity and electrode performance. The cation impurities mostly originate from improperly treated feed water or from components in the electrolysis plant, including piping and water tanks [148, 151].

Shutdown periods: lower degradation rates were observed when the cell voltage is maintained at a certain minimum (1 to 1.3 V) during idle/shutdown periods [152, 153]. Loss of ion conductivity and partial reduction of the anode catalyst are both mitigated by applying a small current to keep the cell voltage above a certain minimum. Current reversals can also occur during shutdown periods due to operation in fuel cell mode by the consumption of the remaining heat and gases (H_2 and O_2), which may cause the catalyst to be carried away from the cathode layer into the membrane. Maintaining a minimum current load (e.g., below 1 % of the rated current), for example via the utilization of ESS, can enhance the durability and performance of PEM electrolyzer cells when connected to RES.

2.2.2 Electrolysis Plant

Configuration

The plant configuration initially considered in this thesis comprises three independent PEM electrolyzer units, as in Fig. 1.6, each with a capacity of 5 MW, designed to produce hydrogen at a pressure of 35 bar and a temperature of 60 °C. The main characteristics of the electrolyzers are detailed in Table 2.2. The division of the electrolysis plant into three distinct electrolyzers is driven by the aim to minimize the relative minimum load of the plant, as discussed in Section 1.2.3, and to mitigate the risk of a single point of failure. The choice of a relatively low operating temperature is motivated by the significant degradation rates observed at higher temperatures. Conversely, the relatively high-pressure operation

Table 2.2: Characteristics Considered for the 5 MW PEM Electrolyzer Units Depending on Cell Aging.

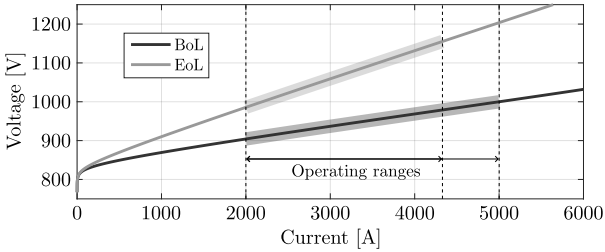
Parameters	Value	Unit
Operating temperature	60	°C
Operating pressure	35	bar
Number of cells	510	[–]
Active cell area	2500	cm^2
Rated current density	2	A/cm^2
Minimum current	40	% of rated current
Minimum load	1.81 — 1.97	MW
Voltage at 5 MW	1000 — 1152	V
Current at 5 MW	5000 — 4340	A
SEC at 5 MW	53.7 — 61.9	kWh/kg_{H_2}
Hydrogen production at 5 MW	93 — 81	kg_{H_2}/h
Maximum applicable ramp rate	± 20	%/s

is considered to eliminate the requirements of compressing the hydrogen offshore, although it necessitates a lower minimum current density of 0.8 A/cm^2 to ensure safe operation. Moreover, the maximum current density is limited to 2 A/cm^2 to limit the degradation rate and avoid significant internal cell losses at higher current densities.

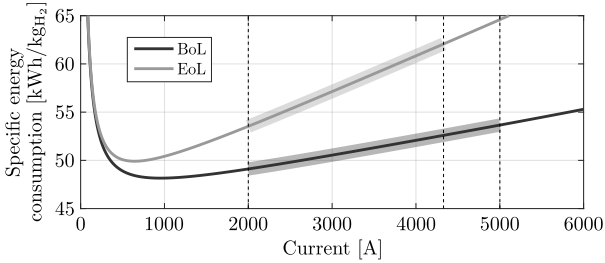
Fig. 2.13a illustrates the polarization curves of the consider electrolyzer unit and were generated using the equations described in Section 2.2.1 based on the aforementioned electrolyzer parameters. The minimum current requirement is equal to 2 kA, while the current at 5 MW depends on the aging of the cells. Indeed, assuming a constant maximum power input of 5 MW throughout the electrolyzer lifespan, the electrolyzer current required for a given power decreases as the electrolyzer cells age. Consequently, the hydrogen production at rated load decreases by approximately 13 % over the cells' lifetime.

The polarization curves are crucial for the design of the electrolyzer power supply, as they determine the operating ranges of the converter and the extremum points at which it needs to operate. For instance, the power supply should be designed to deliver the maximum current of 5 kA at BoL and a maximum voltage of 1152 V at EoL. Keeping the maximum electrolyzer voltage below 1500 V allows for the classification into LV equipment [154]. Exceeding the LV threshold entails significantly higher efforts and expenses for equipment and personnel safety. Moreover, limiting the number of cells in series reduces shunt currents that escape from the main cell flow to low electrical resistance paths (such as water inlet and outlet), thereby resulting in higher Faraday efficiency compared to electrolyzer with a higher number of cells in series [155].

A 15 MW PEM electrolysis plant is projected to occupy an area ranging from 525 to 750 m^2, demonstrating a footprint that is for example two to three times smaller than that of an alkaline electrolysis system [135]. All components are housed in containers to protect against harsh offshore environments. The PEM electrolyzer lifetime is shorter than other parts of the wind-to-hydrogen plant, such as the wind turbine itself, thus requiring to be replaced at least once over the full plant lifetime. Considering the footprint



(a) Polarization curves for different agings of the cells.



(b) SEC for different agings of the cells.

Figure 2.13: Generated characteristic curves of the considered 5 MW PEM electrolyzer.

and maintenance requirements of the electrolysis plant, the electrolyzer units are located on a platform that is mechanically supported by the transition piece of the wind turbine, about twenty meters above sea level.

Auxiliaries

Figure 2.14 gives an overview of the auxiliaries employed in the plant. Each electrolyzer is equipped with its own balance-of-stack (BoS) to enable independent operation. The BoS comprises various auxiliary components and systems necessary for the operation of the electrolyzer stacks, such as the gas separators, the high-pressure pumps, the heat exchangers, the water refinement and the control systems. Moreover, to prevent fuel cell operation and limit cell degradation, as discussed in the previous section, a smaller DC source known as a polarization rectifier is typically employed in addition to the main DC source [156]. This rectifier applies a relatively small current to the electrolysis cell after the main DC source is shut down, keeping the cell voltage above a certain value.

In addition, the platform hosts the balance-of-plant (BoP) and the seawater treatment. The BoP includes several systems necessary for the plant operation such as gas drying, cooling unit, nitrogen generation and safety features. Due to the high salinity of seawater, direct usage in PEM electrolysis is not feasible. Therefore, a seawater treatment system is employed to deliver water with low conductivity ($< 1\,\mu S/cm$ at $25\,^{\circ}C$), high purity and free from impurities that could negatively impact the performance and longevity of the

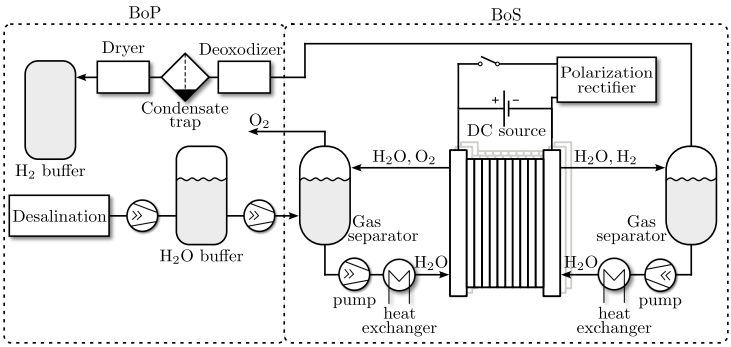


Figure 2.14: Simplified representation of a PEM electrolysis plant [75, 157].

electrolyzers. The seawater is desalinated, deionized, heated, and then pumped in the PEM electrolyzers at the operating pressure and temperature. The desalination system can utilize different processes, such as thermal (multi-effect distillation), reverse osmosis and electrode ionization to ensure high water quality.

Lastly, the electrolysis plant typically encompasses an uninterruptible power supply (UPS) with a suitable battery-buffered power supply. The UPS is provided not for maintaining hydrogen production, but to ensure reliable power delivery to critical systems of the plant after a loss of the main power. In addition to enabling a safe and controlled shutdown, the UPS must also be sized to support critical systems such as communications, instrumentation, control, and when necessary, heaters and pumps to prevent freezing, during power outages up to a period of 72 hours as mentioned in Section 2.1.4.

Thus, the electrolysis process involves more than just the electrolyzer cells as it includes several auxiliaries necessary for its operation. From an electrical perspective, these auxiliaries primarily consist of pumps, heaters and compressors, which have considerably lower energy demands compared to the electrolyzer cells. For instance, the energy demand for the desalination process can be estimated to be within the range of a few kWh per cubic meter, depending on factors such as feed water salinity, pump efficiency, and brine discharge [36]. Assuming a deliberately high consumption of 10 kWh/m^3 due to the combination of several desalination processes, the power consumption for producing approximately 10 L of water per kg of hydrogen results in less than 30 kWh per hour at full load operation, representing less than 0.2 % of the electrolysis consumption. Desalination is expected to be a large consumer of energy among the auxiliaries. Given its relatively low overall consumption, it can be inferred that the energy demands of other auxiliary systems will be minimal compared to the dominant consumption of the electrolyzer cells. However, when determining the overall efficiency of the plant in this thesis, the overall auxiliary components consumption will be estimated to be constant and equivalent to 1 % of the overall plant rated consumption.

Dynamics Requirement

Product specifications from manufacturers often omit details regarding operational flexibility, such as start/stop times, load range, and ramp rates [158]. Studies on PEM electrolyzers have shown a wide variation in allowable power ramp rates from the minimum load to the full load, ranging from 1 %/s to 250 %/s [3, 159]. For example, certain PEM cells have demonstrated the ability to ramp from zero to full load within 0.1 s for ramp-up, and 0.2 s for ramp-down, exhibiting a reaction time of just 13 ms for a 1 % change in current in both directions [160]. However, the majority of reported ramp rates fall within the more moderate spectrum of 10 to 100 %/s, with lower rates often associated with grid-connected electrolyzers and higher rates with units optimized for dynamic operation [161]. Despite the near-instantaneous electrochemical reaction times of the cells, the auxiliaries processes, including water supply and gas management, introduce longer time constants to the plant. Excessive ramp rates can lead to membrane dehumidification and pressure variations. Therefore, more limited ramp-up and ramp-down rates are required to ensure safe operation [57]. In this work, a maximum ramp rate of ± 20 %/s is considered for the electrolyzer units.

In addition to response time and ramp rates, the start-up and shut-down times of the electrolysis plant must be considered to determine how a unit can participate in demand response. When starting from a cold state, the electrolyzer have to be heated up to reach its optimal operating temperature, as hydrogen production efficiency and safe operation depend on attaining this temperature. Thanks to their compact design and low thermal capacity, PEM electrolyzers typically have short heat-up times, ranging from 5 to 10 minutes for cold start-up depending on the current applied, and as short as 2 to 4 s for warm start-up to reach full load [135]. Heating the electrolyzer through internal losses is constrained in part by the maximum current and voltage that the DC power source can provide, as well as by the risk of corrosion at high cell voltages [3]. During start-up, the power supply becomes a limiting factor as the low initial temperature results in higher cell voltage compared to the nominal operating temperature.

2.2.3 Requirements Specification for Electrolysis Power Supply

The design of the power supply of an electrolyzer coupled to a wind turbine in stand-alone offshore operation must address several key requirements. The requirements can be divided into two categories: general electrolysis requirements and electrical considerations specific to the offshore stand-alone operation, and are outlined in the following.

Electrolysis Specific Requirements

The main bottleneck preventing hydrogen from becoming a mainstream fossil-fuel alternative is currently the cost of its production. Therefore the overall cost of produced hydrogen over the lifetime of the system, monitored by the LCOH, should be as low as possible to further enhance the competitiveness of green hydrogen production plants. To achieve low lifetime costs, the power supply has to have low CapEx, high efficiency and high reliability.

- The CapEx of the power supply in typical electrolysis plants, which consists of step-down transformers and rectifiers, often constitutes a significant portion of the

overall plant CapEx, ranging from 15 to 30 % [75,76]. The LCOH in grid-connected electrolysis plants is primarily influenced by relatively high electricity costs, resulting in an OpEx-dominated process. Conversely, in stand-alone offshore, the off-grid nature shifts the cost dynamics to a CapEx-driven context. To reduce the LCOH, it is essential to optimize the cost of every component, making the power supply CapEx a critical factor when comparing different solutions.

- Amortizing the plant CapEx is achievable by maximizing hydrogen production. The power supply of the electrolyzer has to deliver relatively high current at low voltages, and any power losses during conversion directly impact the overall plant efficiency.

  Assuming no power losses between the wind turbine generator and the three electrolyzer units, and considering the electrolyzer SEC at BoL specified in Fig. 2.13b, the total hydrogen production during the first year of operation can be calculated. Although the wind turbine operates 50 % of the time at partial load (see Fig. 2.3b), the majority of the hydrogen is produced when the wind turbine is running at full load of the wind turbine, as illustrated in Fig. 2.15. Consequently, the electrolyzer power supply should be designed for maximum efficiency at full load. However, partial load efficiency should not be overlooked, as 30 % of the hydrogen can be produced in this operating range, necessitating relatively high efficiency in this condition as well.

  Moreover, the power supply can impact the electrolysis efficiency through the DC current ripple fed to the electrolyzer. The ripple should be minimized as the AC component likely does not contribute to the hydrogen flow rate and increases the SEC of the cells [82, 83]. Furthermore, the presence of current ripple could also potentially accelerate the degradation of the electrolyzer cells [84]. Therefore, optimizing the efficiency of the electrolyzer power supply and minimizing current ripple are crucial considerations for maximizing the efficiency and longevity of the plant.

- Due to the maximum DC current demand of 5 kA per electrolyzer unit, employing IGBT devices in the electrolyzer power supply requires the use of parallel devices or converter units. A modular structure is essential not only to handle the high current but also to enhance reliability. High reliability in the power supply minimizes downtimes and maximizes hydrogen production. In this thesis, a plant lifetime of 25 years with a maximum of one planned maintenance per year is considered. To prevent interruptions, redundant topologies guaranteeing fault-tolerant operation should be implemented.

Additionally, to accommodate the required modularity in the electrolysis plant in order to reduce the overall minimum load, each electrolyzer unit should be supplied by a separate galvanic power supply. Ground currents between electrolyzer units, which may potentially decrease the lifetime of electrolyzer cells, can be mitigated by providing galvanic isolation [155]. For instance, if only a portion of the electrolyzer units are in operation, galvanic isolation would limit the propagation of ground currents to the units that are shut down.

Offshore Stand-Alone Operation Requirements

The placement of the electrolysis plant on a platform at the wind turbine tower introduces several unique requirements. The harsh environmental conditions necessitate that all equipment to be housed in protective containers of either 20 (roughly 33 m^3) or

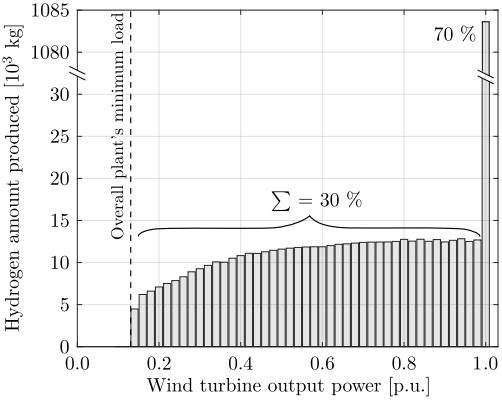


Figure 2.15: Distribution of the possibly theoretical amount of hydrogen produced during the first year of operation at different wind turbine output power (considering no power losses in the EDS) and no downtime in the plant.

40 ft (roughly 66 m^3). Additionally, weight and size, which are typically not primary concerns in electrolysis plants, become critical factors. These parameters must be carefully monitored and considered when comparing different solutions, especially given the limited space offshore and the challenging and costly logistics associated with transporting voluminous and heavy equipment.

3 System Architecture and Design

Building upon the insights from the previous chapters, the operation of an electrolyzer is subject to restrictive constraints, such as minimum load requirements and maximum ramp rates. In addition, the significance of the power allocation strategy and the EDS configuration in addressing these constraints were underscored. This chapter aims to provide the framework for comparison of different power allocation strategies and EDS configurations in decentralized wind-to-hydrogen plant. Firstly, this chapter introduces and explores strategies designed to enhance the integration of electrolyzers with a stand-alone offshore wind turbine. Secondly, different power allocation strategies that adhere to the operational requirements outlined previously, are compared. Finally, the different EDS configurations considered in this work are presented.

3.1 Balancing Power Dynamics

When wind speed changes rapidly, the wind turbine output power may exceed the electrolyzer ramp rate limitation, resulting in a power mismatch. In Fig. 2.7, although the wind speed variation may not be realistic, an instantaneous change from the wind turbine rated wind speed to the cut-in wind speed is deliberately considered as design worst-case scenario, resulting in a conservative negative decrease of 70 % in wind speed. This scenario results in the instantaneous rate of change in the wind turbine output power exceeding the electrolysis plant maximum ramp rate of ± 20 %/s. The dynamic response discrepancy leads to power and energy mismatch, potentially causing frequent shutdowns.

To prevent this, dynamic balancing of power between the wind turbine and the electrolysis plant is required. While blade pitch angle control can mitigate positive wind speed gradients, it cannot influence negative gradients. For this case, several methods have been proposed [68]:

- Release of stored energy from ESS.
- Operation at suboptimal pitch blade angles.
- Power balancing using rotor inertia.

The first option involves releasing energy stored in ESS during power mismatches. This can be achieved by storing the power mismatch during a positive wind speed gradient and/or temporarily storing a portion of the power produced during nominal operation. The stored energy can then be released during output power gradients exceeding ± 20 %/s,

effectively smoothing out power fluctuations. However, this solution entails relatively high CapEx and large volume requirements, especially at multi-megawatt power levels [68].

The second option involves operating with a non-zero blade pitch angle in the MPPT region. Operating at a non-zero pitch angle reduces the power coefficient C_p, thereby decreasing the power extracted from the wind. During a rapid decline in wind speed, the pitch angle would be reduced to temporarily increase C_p and extract additional power from the wind. However, this approach results in suboptimal power production during steady-state operation. Additionally, this method assumes that the control reaction and action of the blade pitch actuators are instantaneous. In reality, during a significant wind speed drop, the negative wind speed gradient may be greater than the variation in rotor speed due to rotor inertia. This causes the TSR to increase to values above 9.5 and under these conditions, the decrease in pitch angle further worsens C_p, as shown in Fig. 3.1.

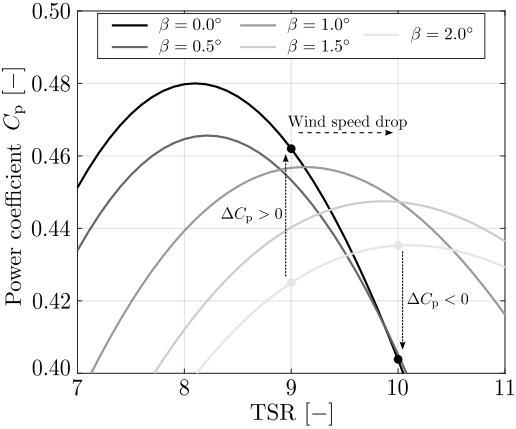


Figure 3.1: Power coefficient C_p for variable TSR and different pitch angles β.

The third option entails using the wind turbine rotor to store additional rotational energy. By operating at a higher rotational speed than nominal, extra energy can be stored and released by the rotor when needed. To assess this approach, the maximum rate of change of power is evaluated by simulating an instantaneous drop in wind speed from the rated to cut-in wind speed (c.f. Fig. 3.2a), for a fixed total moment of inertia and four different nominal TSRs. Figure 3.2b displays the variation in wind turbine output power with four different nominal TSRs and Fig. 3.2c shows the corresponding instantaneous rate of change of power. The results show that higher nominal TSR correspond to lower maximum ramp-down rates during negative wind speed gradients, which is attributed to the increased rotor rotational energy. For instance, Fig. 3.2c indicates that the instantaneous rate of change of power peaks at −22.4 %/s for a TSR of 9.0, compared to −15.4 %/s for a TSR of 9.5. Given the relatively large rotor inertia considered in this work, the rotor speed only needs to be increased by 2 % to meet the maximum ramp-down rate requirement of −20 %/s. Nevertheless, operating at a higher TSR results in a larger deviation from the optimum point, reducing the power captured from the wind.

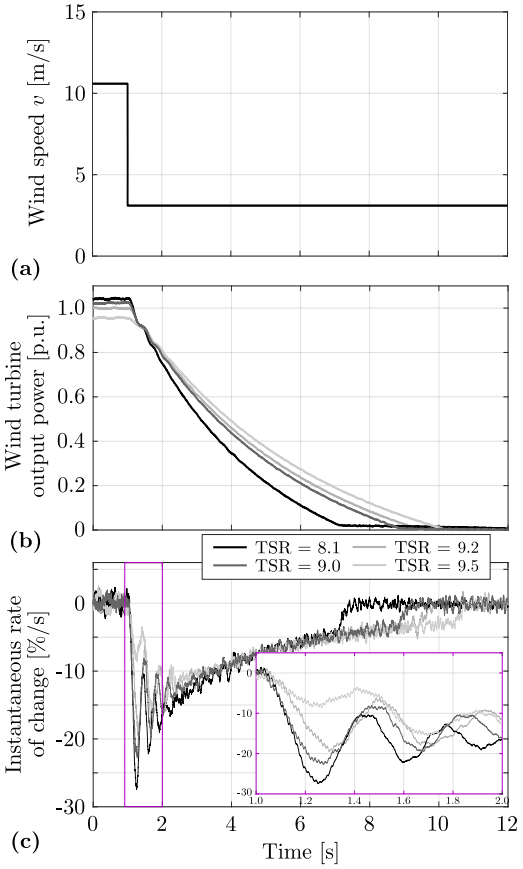


Figure 3.2: (a) Wind speed variation with negative gradient, (b) corresponding response in wind turbine output power according to the wind turbine TSR and (c) the instantaneous rate of change in output power.

Figure 3.3 shows the power extracted from the wind as a function of rotor speed for varying wind speeds. Power curves for each considered TSR are presented, illustrating the distinct operating regions of the wind turbine. At first, the rotor speed is held at a minimum of 5 rpm (region II) and once the nominal TSR is reached, the rotor speed increases with the wind speed to keep the TSR constant (region III). As can be seen, the higher the TSR, the lower the wind speed at which the nominal TSR is reached and the lower the extracted power at a given wind speed. As highlighted in Fig. 3.2c, the rotor speed must be increased by 2 % such that the maximum ramp-down rate requirement of −20 %/s is not exceeded during the considered wind speed negative gradient. This results in a 2 % reduction in the power extracted at the rated wind speed of 10.59 m/s (point C in Fig. 3.3). As listed in Table 3.1 and illustrated in Fig. 3.3, to compensate for the drop in power coefficient and reach the nominal power of the turbine (similar rated power as

point B) at the increased TSR of 9.2, the turbine would need to operate at point C' with a wind speed 0.6 % higher than rated, resulting in a rotational speed 3 % higher than rated.

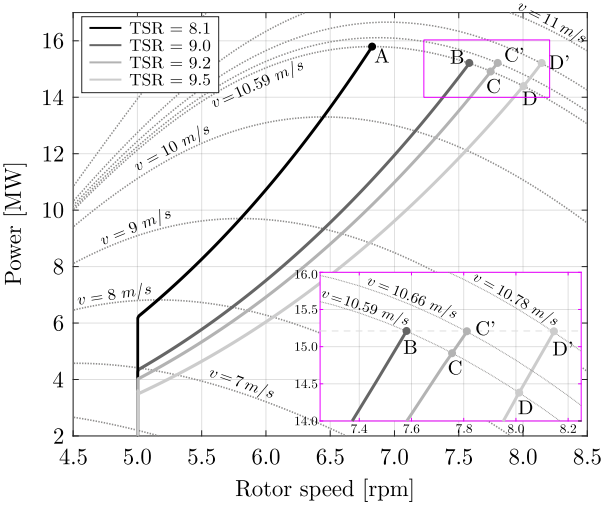


Figure 3.3: Power extracted from the wind according to rotor speed and for different wind speed v.

Table 3.1: Impact of TSR on Rotor Speed, Power Extraction, and Maximum Instantaneous Rate of Change of Power.

Point	A	B	C	D
Rated TSR [–]	8.1	9.0	9.2	9.5
Rotor speed at rated wind speed v = 10.59 m/s [p.u.]	0.90	1.00	1.02	1.06
Power extracted at rated wind speed [p.u.]	1.04	1.00	0.98	0.95
Maximum instantaneous rate of change of power [%]	-27.5	-22.4	-19.5	-15.4
Rotor speed to reach rated power [p.u.]	0.89	1.00	1.03	1.08
Wind speed to reach rated power [p.u.]	0.99	1.00	1.01	1.02

By considering the wind speed distribution shown in Fig. 2.3a, the shift in the wind turbine power curve when operating at a rated TSR of 9.2 results in a theoretical maximum capacity factor of 60.5 %. Although this operational adjustment incurs a decline of 0.3 % in capacity factor relative to the operation at a TSR of 9.0, the choice to operate at a TSR of 9.2 is strategically selected for the remainder of this work. This aims to reduce the possibility of frequent shutdowns of the plant, which could potentially lead to even larger losses in energy production. By storing energy in the form of rotational energy, no additional components are required, potentially avoiding extra CapEx. However, operating the wind turbine at a higher rotational speed than it was designed for increases the stress on the rotor and may lead to reliability issues.

3.2 Modularity and Power Allocation Strategy

The wind turbine's maximum theoretical capacity factor of 60.5 % mentioned in the previous section, is determined by the ratio of the actual electrical energy delivered to the hypothetical electrical energy that would be delivered if the turbine operated at its rated power capacity uninterruptedly throughout the year. It is important to note that the calculation of the maximum theoretical capacity factor does not account for any losses incurred in the EDS or any operational downtime experienced by the plant.

The electrolyzer units are subject to a minimum current requirement that imposes a minimum load constraint of 1.81 MW at BoL and 1.97 MW at EoL for a single unit. Given that the wind turbine output power can vary from nearly zero up to its rated capacity of 15 MW, this minimum load corresponds to approximately 12 to 13 % of the turbine's rated power. Consequently, this requirement may restrict the electrolysis plant's ability to operate at the wind turbine's peak theoretical capacity factor, thereby impacting the overall energy utilization efficiency.

As depicted in Fig. 1.9, the modularity in the electrolysis plant enables a reduction in the overall minimum load requirement from a plant perspective. When connected to RES, such as the considered stand-alone offshore wind turbine, this allows the electrolysis plant to capture a greater amount of energy. Given that the considered electrolysis plant consists of three electrolyzer units, the distribution of the power to these units according to the wind turbine power level, referred to here as the power allocation strategy, can follow different approaches. Three main conventional strategies are depicted at BoL in Fig. 3.4 and described as follows:

- **Equal Load Sharing**: all electrolyzer units are operated synchronously, with the power allocated equally to each unit. While this approach may simplify operation, it leads to a relatively high minimum load requirement at the plant level, because the minimum load of each unit effectively adds up. As a result, the total minimum load for the plant can be equivalent to that of a single larger electrolyzer unit. This compounded minimum load requirement ultimately lowers the plant's capacity factor.

- **Daisy Chain Allocation**: the power is allocated sequentially from one unit to the next. Each unit is brought into operation one by one, with the previous electrolyzer reaching its rated power before the next one starts. The first electrolyzer unit receives all the power from the wind turbine until it reaches its rated capacity, after which the subsequent unit is brought into operation with the minimum load, causing the first unit's power to decrease. As the power continues to increase, it is equally shared between the two units until the first unit returns to its rated capacity. This cycle repeats until all units are at rated power or the available power is fully allocated.

- **Optimal Efficiency Allocation**: this method capitalizes on the higher efficiency of PEM electrolyzers at lower loads. In a plant with multiple independent electrolyzer units, it is beneficial to operate each unit at the lowest feasible load by evenly distributing the wind turbine output power at any given time. A first electrolyzer starts hydrogen production once the wind turbine power exceeds the electrolyzer

minimum load. Subsequently, when the power of the wind turbine exceeds twice the minimum load, a second electrolyzer enters into operation, with both electrolyzers sharing the load equally. The same principle applies as the load increases to a level where the third electrolyzer can begin hydrogen production.

To prevent disproportionate wear on any single unit, the sequence in which units are activated at lower wind speeds can be alternated for the latter two strategies.

Figure 3.5 illustrates the variation in the electrolysis plant efficiency at BoL with wind turbine output power under the three different power allocation strategies. By using the power distribution shown in Fig. 2.3, the average operating electrolysis efficiency over a year can be determined by weighting the efficiency curves according to the operating time at each efficiency level throughout the year. The results for the three different power allocation strategies are presented in Table 3.2.

While the Daisy Chain Allocation and Optimal Efficiency Allocation strategies initiate hydrogen production at comparatively low wind speeds, the latter has the advantage of resulting in an overall higher averaged electrolysis efficiency. The Daisy Chain Allocation results in the lowest overall plant efficiency because it often leads to one or more

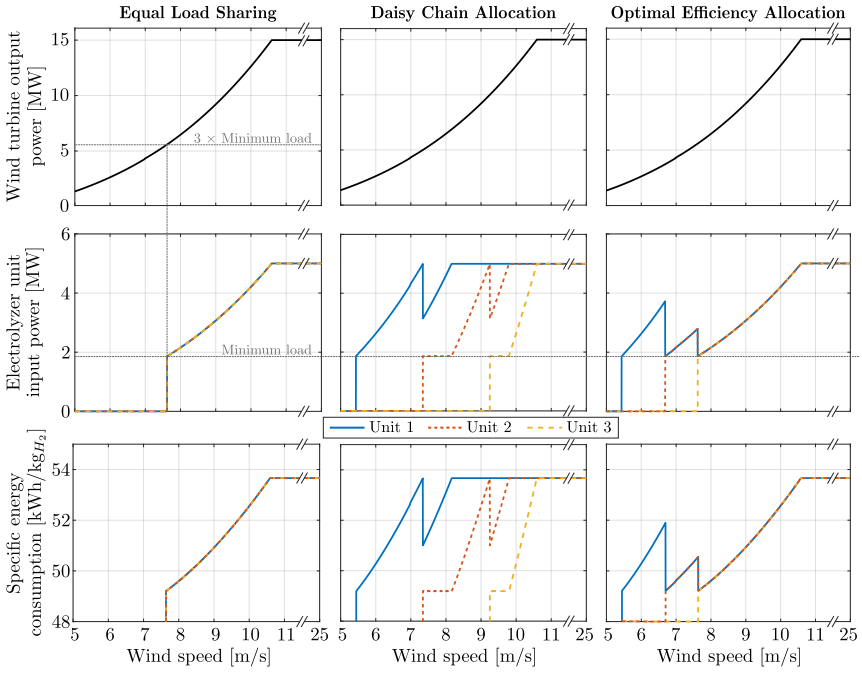


Figure 3.4: Power allocation strategies according to the wind turbine output power represented at BoL. Note that in this figure, the auxiliaries consumption and the losses in the EDS are not considered.

electrolyzer units operating at the highest available load, condition at which the electrolysis efficiency decreases, lowering therefore the average plant electrolysis efficiency. In contrast, Optimal Efficiency Allocation maximizes overall electrolysis efficiency by operating all units at the lowest feasible load, ensuring that each electrolyzer is utilized effectively particularly during partial load conditions. Additionally, due to a more frequent operation of the electrolyzer units at lower loads, the degradation of the units may be reduced [105]. For these reasons, this work exclusively considers the Optimal Efficiency Allocation strategy for power distribution within the electrolysis plant.

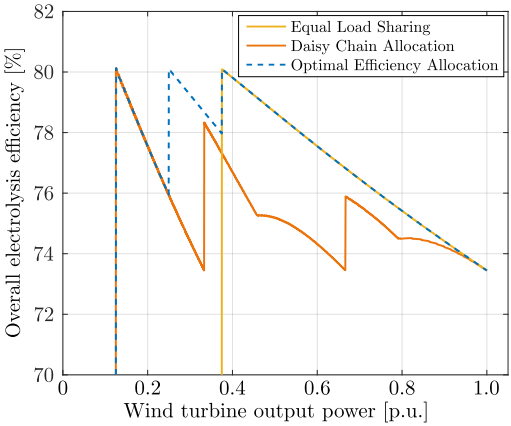


Figure 3.5: Overall electrolysis efficiency at BoL for different power allocation strategies. Note that in this figure, the auxiliaries consumption and the losses in the EDS are not considered.

Table 3.2: Maximum theoretical plant capacity factor and averaged electrolysis efficiency for different power allocation strategies at BoL[1].

Power allocation strategy	Capacity factor [%]	Averaged electrolysis efficiency [%]
Equal Load Sharing	56.0	74.6
Daisy Chain Allocation	59.8	74.5
Optimal Efficiency Allocation	59.8	75.4

[1] Assuming no downtime and EDS losses in the wind-to-hydrogen plant.

3.3 Electrical Distribution Systems Considered[2]

The operational characteristics of the PMSG and the electrolyzer units reveal a significant mismatch in the voltage profiles as shown in Fig. 3.6 through the power and voltage of the

[2] Parts of this section have been published in Runser *et al.* [162]

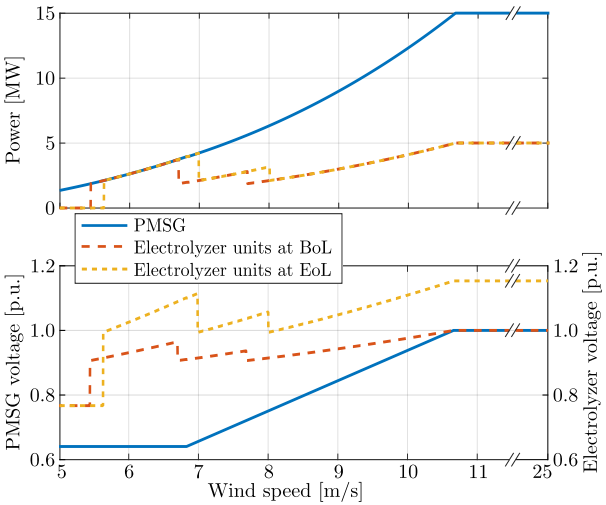


Figure 3.6: Output power and voltage according to the rotational speed of the wind turbine PMSG, as well as the power and voltage of the electrolyzer units under different cell aging. The base electrolyzer voltage is defined at BoL rated load such that it is 1000 V, while the base rms PMSG voltage is set at full load, which is equal to 690 V when LV is considered, or 3300 V when MV is considered for the PMSG.

PMSG's rectifier output and of the electrolyzer at different cell aging. On the one hand, due to the minimum rotational speed requirement of the turbine, the PMSG voltage is reduced and constant at wind speeds below 7 m/s before increasing and stabilizing at its rated value above the rated wind speed of the turbine. On the other hand, the applied power allocation strategy results in power cycling of the electrolyzer units. As illustrated in Fig. 3.6, even if the generator rated voltage is specifically chosen, the voltage characteristics of the PMSG and the electrolyzer voltage do not align. This indicates that direct coupling of the PMSG's rectifier to the electrolyzer units would limit the operational bandwidth and fail to meet the requirements of both systems.

In addition, with a hub height of 150 meters, a 200-meter cable connection is assumed between the nacelle and the electrolyzer units on the platform, thus requiring careful consideration of the power distribution in the EDS. Depending on the EDS configuration employed, the distribution voltage can be dependent on the PMSG rated voltage and can potentially impact considerably the conduction losses in the EDS. Consequently, two distinct line-to-line rms rated voltages for the PMSG are evaluated, one in the LV range at 690 V and the other in the MV range at 3300 V.

To meet these challenges, power conversion by the EDS is required to match the PMSG output with the voltage and power input requirements of the electrolyzers. In the following, four different EDS configurations are described, as illustrated in Fig. 3.7, to optimize power distribution and ensure efficient and safe operation of both the PMSG and the electrolyzer units.

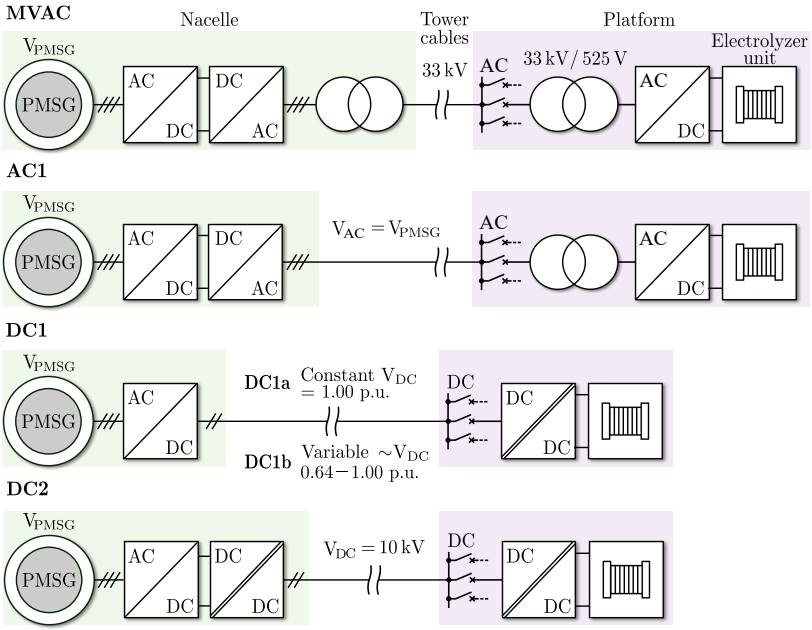


Figure 3.7: EDS considered in this work.

3.3.1 MVAC

The Medium-Voltage Alternating Current (MVAC) configuration is derived from standard electrical installations in grid-connected wind turbines. Existing wind turbines could be retrofitted with low additional engineering effort and all components are available off-the-shelf. The 33 kV distribution voltage level results in negligible conduction losses in the tower cables and low copper usage but requires a relatively high number of conversion steps.

In this configuration, the LSC operates as a grid-forming converter, meaning that the inverter controller regulates instantaneous terminal voltages without needing to track an externally regulated voltage. The main topology and control scheme of the wind turbine electrical drivetrain are shown in Fig. 3.8. Compared to the previously described control strategy in Section 2.1.2, the DC link voltage under grid-forming control can be regulated by either the LSC or the MSC. However, as the MSC is decoupled from line disturbances, it offers better performance in fault conditions when the DC link voltage is controlled by the MSC [163]. This is particularly advantageous for achieving island operation or black start of the wind turbine, as the DC link voltage can be independently regulated by the MSC [164]. Consequently, an outer loop controls the DC link voltage through the stator current q-axis component and adopts the previously discussed voltage-current double closed-loop control strategy.

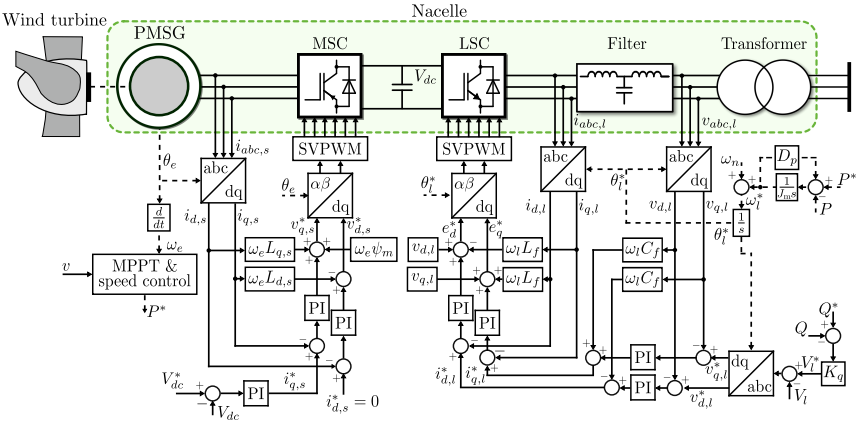


Figure 3.8: Wind turbine electrical drivetrain and its control scheme employed in the MVAC configuration [118].

The LSC implements grid-forming control to support the line frequency and manage both active and reactive power transmission by controlling the magnitude V_l and phase θ_l of the line voltage. This grid-forming control, often referred to as virtual synchronous generator control, includes two outer loops: an active power loop that adjusts the angular phase reference θ_l^* and a reactive power loop that adjusts the output voltage [165]. In addition, a voltage-current inner loop control is implemented with cross-decoupling terms through the filter inductance L_f and capacitance C_f to manage line currents $i_\mathrm{d,l}$, $i_\mathrm{q,l}$ and the line voltages $v_\mathrm{d,l}$,$v_\mathrm{q,l}$. The active power reference is regulated by the MPPT and speed control of the turbine. Active power control is based on droop control to provide frequency regulation and inertial support to improve frequency stability through the inertia coefficient J_m [165]. The power increment varies inversely with the frequency change, with a magnitude determined by the droop coefficient D_p.

To manage the independent power distribution for each electrolyzer unit on the platform while providing galvanic isolation between each unit, an LFT with an AFE rectifier is used to first step down the distribution voltage and convert it to DC. An active rectification enables the independent control of the amount of power distributed to each electrolyzer unit.

A thyristor rectifier is not considered for the electrolyzer rectifier as the harmonics emitted by thyristor rectifiers can result in overvoltages, low-frequency resonances and stability issues in relatively small installations such as the MVAC configuration [166, 167]. Small installations, often referred to as weak AC grids, are typically characterized by relatively low inertia, low regulation capability, low damping, and poor reactive power support [168]. Thyristor rectifiers rely on the line voltage to activate the commutation process from one switch to another and consequently require a strong AC grid to maintain voltage stability during disturbances (power variation and harmonics) and to operate properly [169, 170].

Conversely, voltage source converters are better suited for connection to islanded grids due to their robust vector current control strategy and their ability to quickly and

accurately track power and voltage [171]. Considering a 10 % margin for voltage drop, line voltage fluctuation, and operational reliability [172], the distribution voltage is precisely stepped down to 525 V. This ensures that the minimum DC rectified voltage ranges between 810 and 820 V, which is just below the minimum electrolyzer voltage. As a result, the electrolyzer rectifier can consistently deliver the required voltage across the entire current span.

The AFE rectifier comprises an inductance L_e, a DC link capacitor and six active switches, such as IGBTs. Due to the high phase currents generated by the electrolyzer, which exceed the current ratings of a single IGBT module currently available in the market, multiple AFE rectifier units may be connected in parallel to distribute the load effectively. Figure 3.9 illustrates the control scheme based on the voltage-oriented control method of a three-phase AFE rectifier unit. It primarily consists of an outer control loop that regulates the active power consumption of the electrolysis unit according to the power generated by the wind turbine, providing the reference for the d-axis component of the current. The reactive power is controlled by the q-axis component of the current and the unity power factor can be achieved by setting the value to zero. Similarly, decoupling terms through the inductance L_e are added into the control scheme to enhance dynamic performance [173].

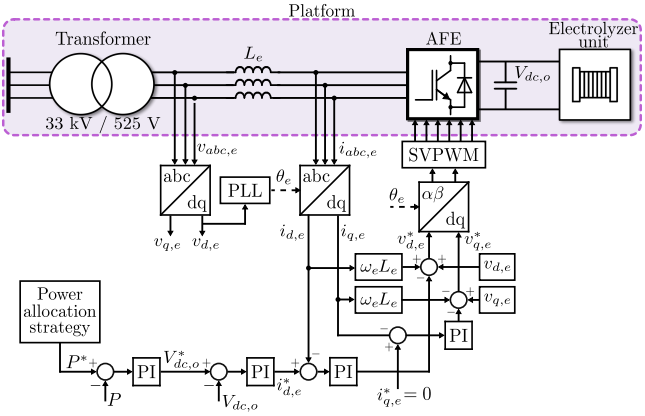


Figure 3.9: Electrolyzer power supply and its control scheme employed in the MVAC configuration (adapted from [173]).

3.3.2 AC1

Given the 200-meter cable length between the nacelle and the electrolyzer, the necessity of a step-up LFT in the nacelle needs to be evaluated. Such transformers are typically used in wind farm collection systems and contribute to higher CapEx and installation costs due to their substantial weight and size. For instance, a 15 MVA transformer generally weighs between 33 to 36 tons and occupies a volume of 40 to 42 cubic meters [174]. Locating this transformer in the nacelle, at a height of 150 meters, increases the weight and volume of the nacelle, imposing considerable additional mechanical constraints on the tower. Each

kilogram added to the nacelle raises the stress on the tower design, leading to a more expensive design.

For these reasons, the single-transformer (AC1) configuration draws from the MVAC configuration and eliminates the LFT in the nacelle, considerably reducing the nacelle's weight and footprint. The control schemes remain equivalent to those in the MVAC configuration. However, since no LFT is employed in the nacelle, the distribution voltage is considered to be constant over the wind speed span and equal to the rated voltage of the PMSG. Depending on the rated voltage employed for the PMSG (690 or 3300 V), the elimination of the LFT may lead to significant increase in conduction losses and copper usage.

3.3.3 DC1

The single-stage DC (DC1) configuration leverages the fact that the electrolyzer is a DC load and eliminates all AC stages in the distribution system. DC distribution reduces copper usage compared to the AC1 configuration but may still suffer from elevated conduction losses in the tower cables depending on the nominal PMSG voltage. Operation at the lowest possible DC voltage is desirable to minimize the switching losses of the hard-switched generator's rectifier. However, to ensure proper operation of the converters, the DC-link voltage has to be for LV systems 10 % above the natural DC-link voltage (defined as the DC voltage if the transistors are not operating and their free-wheeling diodes operate as a standard B6 diode rectifier) to account for voltage variation and voltage drop. For MV systems this margin is usually set at 15 % [175]. Consequently, the expected rated DC distribution voltage is approximately 1.1 kV for 690 V PMSG rated voltage and 5.4 kV for 3.3 kV PMSG rated voltage.

An isolated DC-DC converter is employed to convert the distribution DC voltage to the electrolyzer voltage and ensures galvanic isolation towards the power source. Given the high current requirements from the electrolyzer units, multiple DC-DC converter submodules connected in parallel should be employed to share the load. If the DC distribution voltage is 1.1 kV, several converter submodules can be connected in parallel on the input side as well as on the electrolyzer side, resulting in an IPOP connection, as illustrated in Fig. 1.7a. Conversely, if the distribution voltage at rated load is 5.4 kV, several submodules can be connected in series on the input side to share the voltage, resulting in an ISOP connection of DC-DC converters, as shown in Fig. 1.7b. Both modular approaches offer several advantages:

- By dividing the electrolyzer power among the submodules, each submodule only has to provide a portion of the total power. This effectively reduces the voltage and current stress on the switching devices, allowing for the utilization of commercially available components and eliminating the need for series or parallel connections of individual switches.
- Interleaving the submodules significantly facilitates the current ripple filtering by effectively decreasing the output current ripple magnitude and increasing its frequency.
- Implementing redundancy becomes more straightforward and cost-effective, as

additional submodules of a share of the total power can be readily incorporated into the topology, ensuring that the submodules can continue to operate at nominal power even if one submodule becomes non-functional.

However, this configuration necessitates additional effort on the control aspects, particularly concerning capacitor voltage balancing and potential mismatches in transformer parameters [176–178].

Two versions of the control strategy are considered:

DC1a: In this version, the voltage between the PMSG's rectifier output and the isolated DC-DC converter input is maintained constant at approximately 1 p.u. (1.1 kV for LV PMSG or 5.4 kV for MV PMSG). The voltage can be controlled by the MSC, while the reference power for the isolated DC-DC converter follows the power allocation strategy employed [179].

DC1b: This version allows the generator's rectifier to deliver a variable voltage, that follows the generator rotational speed, ranging from 0.64 p.u. to 1.00 p.u. (0.7 to 1.1 kV for LV PMSG or 3.5 to 5.4 kV for MV PMSG). Since the rectifier typically operates under hard-switching, a variable output voltage due to the operation at a constant modulation index can significantly reduce switching losses at partial loads. However, as shown in Fig. 3.10, this approach leads to a wider operating range for the isolated DC-DC converter. Additionally, it may result in higher conduction losses between the nacelle and the electrolyzer's platform.

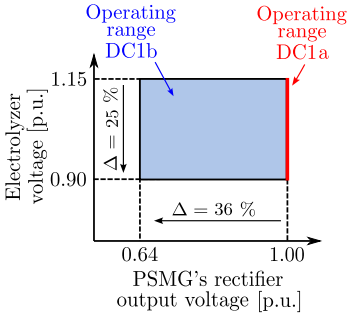


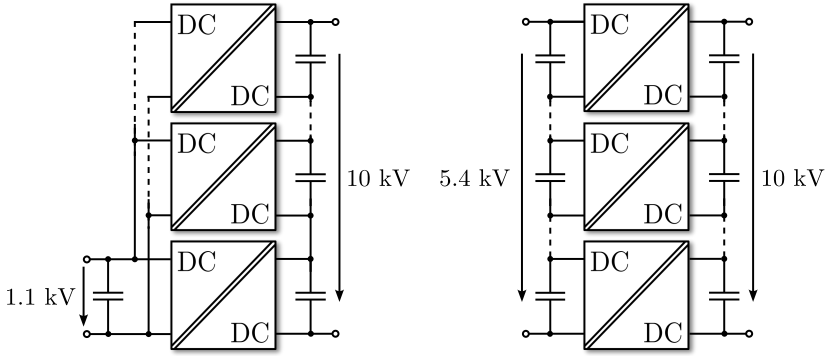
Figure 3.10: Operating ranges of the isolated DC-DC converter in DC1a and DC1b configurations.

3.3.4 DC2

The double-stage DC (DC2) configuration extends the DC1 concept by using an additional isolated DC-DC converter in the nacelle to increase the rectified generator voltage in the nacelle to 10 kV. To meet the step-up requirement of this additional converter, if an LV PMSG is employed, a modular configuration of submodules connected in Input-Parallel Output-Series (IPOS), as illustrated in Fig. 3.11a, is considered. Conversely, if a MV PMSG is used, a modular configuration of submodules connected in Input-Series

Output-Series (ISOS), as illustrated in Fig. 3.11a, is considered.

Maintaining a constant 10 kV voltage between the nacelle and the electrolyzer platform reduces conduction losses in the tower cables, facilitates easier voltage gain and segments the voltage conversion across two isolated DC-DC converters. However, this configuration also results in a relatively large number of conversion steps between the PMSG and the electrolyzer units.



(a) IPOS connection. (b) ISOS connection.

Figure 3.11: Modular connection of isolated DC-DC converter submodules employed in the DC2 EDS to increase the rectified generator voltage to 10 kV.

4 High-Power Isolated DC-DC Converter

This chapter aims to provide a detailed focus on high-power isolated DC-DC converters, as their modularity in terms of the number of submodules employed, can be subject to optimization to enhance key performance parameters such as efficiency, power density, reliability and cost of the converter. For instance, in an ISOP connection, one implementation option involves using High-Voltage (HV) blocking semiconductor switches (e.g. 3.3 kV, 4.5 kV, 6.5 kV) on the primary side bridges and high-current capability semiconductor switches on the secondary side bridges, resulting in a few required number of submodules. Alternatively, employing semiconductor switches with lower blocking voltage (e.g. 1.2 kV, 1.7 kV, 2.3 kV) on the primary side bridges can increase the number of submodules and reduce the load per submodule, potentially allowing for easier submodule design and increased modularity in the converter system.

In the following, first, the topology of the DC-DC isolated converter considered in this study is discussed. Then, the methodology to holistically compare different modularity in the converter system is presented using as an exemplary case the ISOP connection considered in the DC1a EDS with a 5.4 kV input voltage. Finally, the methodology is repeated for the other type of modular connection considered in this work to study the trade-offs under different conditions.

4.1 Three-Phase Dual Active Bridge Fundamentals[1]

In this study, although bidirectional power flow is not required, the three-phase version of the dual active bridge (DAB) is considered as the isolated DC-DC converter. This choice is driven by the proven suitability of DAB for high-power applications, attributed to its wide voltage range, high efficiency and power density [181]. Compared to a unidirectional converter such as the single active bridge (SAB), the DAB offers several advantages, including superior power density and enhanced controllability [182]. Moreover, high-current applications limit the use of resonant-based converters, as the relatively large capacitors in the resonant tank are prone to degradation under high currents, compromising the overall converter reliability [183]. The three-phase variant of the DAB is solely considered because, in contrast to single-phase DAB, the star connection of the transformer results in only 2/3 of the DC-link voltage being applied across the windings, leading to a reduced peak flux linkage. This leads to better transformer utilization and less demanding

[1] Parts of this section have been published in Runser *et al.* [180]

requirements for core design. In addition, the lower DC current ripple of three-phase topologies requires lesser demands on input and output filtering capacitors.

The three-phase DAB as introduced in [184] and depicted in Fig. 4.1a, is a DC-DC power converter topology consisting of two fully controllable two-level three-phase bridges coupled back-to-back via a galvanically isolating MFT. In the single-phase-shift (SPS) modulation, each active switch in one phase leg operates with a 50 % duty cycle and the legs within one bridge exhibit a 120° phase shift, leading to the generation of a six-level mode output voltage generated at each bridge. Furthermore, corresponding phases in both bridges are phase-shifted by the so-called load-angle φ (cf. Fig. 4.1b) to control the amount of power transfer across the series inductance between the two bridges. For a more compact design, the series inductance is usually integrated into the transformer design through the utilization of the leakage inductance L_s between windings. Under SPS modulation, the amount of power transfer across the series inductance L_s between the two bridges in dependency of the load angle φ is as follows

$$P_\mathrm{SPS} = \frac{d\,V_p^2}{2\pi f_\mathrm{sw} L_s} \cdot \left(\frac{2\varphi}{3} - \frac{\varphi^2}{2\pi}\right) \quad \text{for } 0 \le \varphi \le \frac{\pi}{3} \tag{4.1}$$

where $d = n_\mathrm{tr} \cdot V_\mathrm{s}/V_\mathrm{p}$ denotes the voltage ratio, V_p and V_s the primary bridge input voltage and secondary bridge output voltage respectively, n_tr the turns ratio of the transformer and f_sw the switching frequency [184].

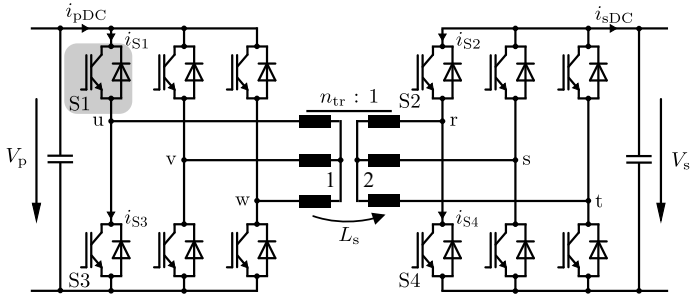
Inherent zero-voltage switching (ZVS) can be achieved over a relatively wide range of operating voltages and power levels. The soft turn-on switching boundaries of the three-phase DAB are expressed by [186]:

$$P_\mathrm{soft-sw,in} = \frac{V_\mathrm{p}\left(n_\mathrm{tr}^2 V_\mathrm{s}^2 - V_\mathrm{p}^2\right)}{9 L_\mathrm{s} f_\mathrm{sw} n_\mathrm{tr} V_\mathrm{s}} \qquad \text{for } n_\mathrm{tr} V_\mathrm{s} > V_\mathrm{p} \tag{4.2}$$

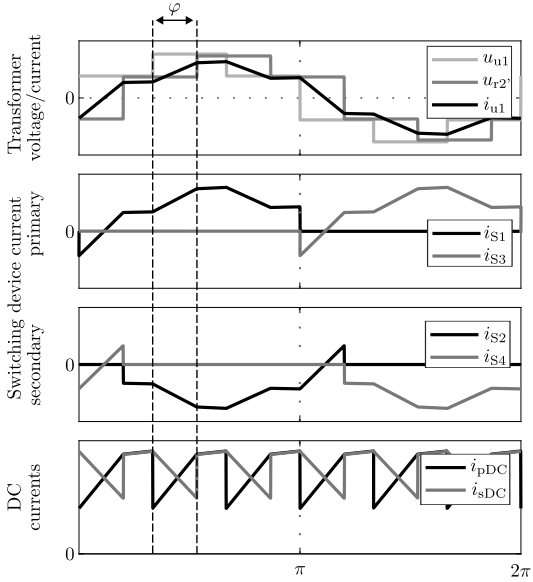
$$P_\mathrm{soft-sw,out} = \frac{n_\mathrm{tr} V_\mathrm{s}\left(V_\mathrm{p}^2 - n_\mathrm{tr}^2 V_\mathrm{s}^2\right)}{9 L_\mathrm{s} f_\mathrm{sw} V_\mathrm{p}} \qquad \text{for } V_\mathrm{p} > n_\mathrm{tr} V_\mathrm{s}. \tag{4.3}$$

To limit reactive power flow, the rated and maximum load angle in this work is restricted to $\varphi_\mathrm{max} = \pi/6$. Given that the switching frequency f_sw remains fixed during operation, the soft switching area is determined solely by the series inductance L_s and the transformer ratio n_tr. These two parameters also define the maximum power that can be transmitted at the rated load angle φ_max. A lower series inductance L_s reduces the reactive power transfer between bridges, which allows for smaller cross sections of the MFT windings and higher efficiencies of the DAB at rated load. Nevertheless, this also results in a narrower ZVS operating area [186].

In a modular connection of DAB converters, often referred to as dual active bridge converter system (DABCS) [187], the soft-switching boundaries are defined in relation to the main DC input and output voltages. The sizing of the submodule series inductance $L_\mathrm{s,SM}$ and turns ratio $n_\mathrm{tr,SM}$ is first performed at the DABCS level, treating the DABCS as a single equivalent converter. Then, the equivalent series inductance $L_\mathrm{s,DABCS}$ and turn ratio $n_\mathrm{tr,DABCS}$ is equally distributed across individual submodules based on the specific arrangement of the DABCS.



(a) Schematic of the three-phase DAB.



(b) Voltages and current waveforms under SPS modulation with a positive load angle φ.

Figure 4.1: Topology and typical waveforms of the three-phase DAB [185].

4.2 Configuration Optimization of ISOP Connection of DABCS[2]

This section outlines the methodology, as depicted in Fig. 4.2, which is implemented to design the main components of the DABCS, based on the switching devices employed on the primary and secondary sides. The methodology is applied to the ISOP connection

[2]Parts of this section have been published in Runser *et al.* [180]

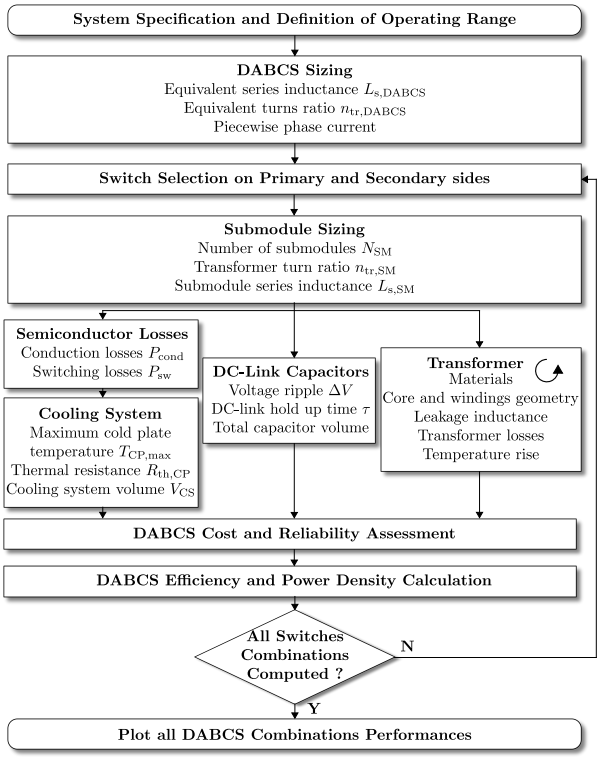


Figure 4.2: Flowchart of the employed design procedure of the DABCS for different switch combinations.

considered in the DC1a EDS between the constant 5.4 kV DC distribution voltage and a 5 MW electrolyzer unit (cf. Table 2.2).

4.2.1 DABCS Sizing

For a given input voltage and electrolyzer polarization curves, $n_{tr,DABCS}$ establishes the voltage ratio d of the DABCS. An operation near $d = 1$ is generally desirable as it ensures ZVS operation even at low loads and reduced reactive power flow. However, due to the naturally varying electrolyzer voltage, maintaining operation near $d = 1$ at any given load is infeasible. The DABCS is thus sized by optimizing both the equivalent DABCS turns ratio $n_{tr,DABCS}$ and the equivalent DABCS series inductance $L_{s,DABCS}$ such that two specific conditions are met. The first set condition is to transfer the maximum rated current of 5000 A at BoL with the rated load angle. The second one is to ensure ZVS operation across the entire electrolyzer operating range throughout its lifetime. This objective is achieved by solving (4.2) and (4.3) to ensure that the primary side soft-switching boundary exceeds the power/voltage curve at EoL while the secondary side soft-switching

boundary is below the minimum load at BoL. By sizing the ZVS area to start at or above the minimum load of the electrolyzer unit, the overall ZVS area is reduced. This approach, favoring higher load conditions, enhances efficiency at the rated load, aligning with the requirement discussed in Section 2.2.3.

Considering a fixed switching frequency of 1 kHz and a constant input voltage of 5.4 kV, the optimized equivalent series inductance $L_{\mathrm{s,DABCS}}$ is 263 μH and the transformer ratio $n_{\mathrm{tr,DABCS}}$ is equal to 5.5. Figure 4.3 illustrates the corresponding soft turn-on switching boundaries of the DABCS, along with the operating curves of the electrolyzer under study. Hard switching on the secondary bridge is observed outside the operating range of the electrolyzer when operating at low load, i.e. below 35 to 40 % of the rated power depending on the aging of the cells.

Alternative modulation techniques, such as the asymmetrical duty-cycle control, could be employed to extend the soft-switching range by adjusting the duty cycles and the load angle between the bridges under light-load conditions [188]. Nevertheless, since during the start-up of the electrolyzer, operation below the minimum load is typically quickly transitioned through to prevent the build-up of potentially explosive gas mixtures on the oxygen side, hard-switching operation at low load is deemed an acceptable operational choice.

4.2.2 Submodule Sizing

The minimum required number of submodules $N_{\mathrm{SM,min}}$ in the DABCS primarily depends on the switching devices ratings. In light of the high current demands and to examine the implications of utilizing different voltage classes of switching devices, this work focuses on

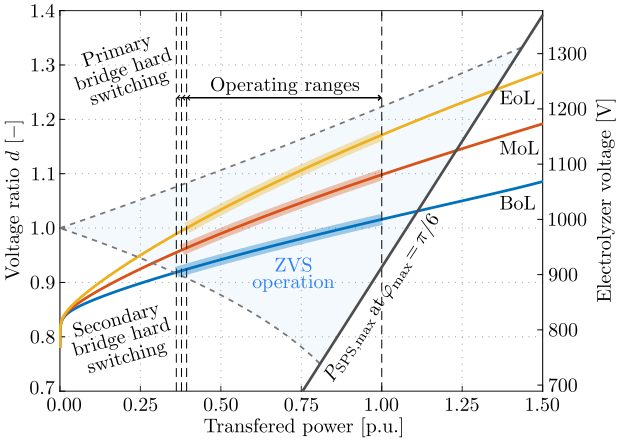


Figure 4.3: Normalized soft-switching area of the DABCS and the polarization curves of the electrolyzer at different cells aging. An additional operating condition, denoted as middle-of-life (MoL), is introduced by assuming a linear degradation of the electrolyzer throughout its lifetime.

Table 4.1: Commercially Available IGBT Power Modules Considered.

Description	DC voltage $V_{\mathrm{DC,IGBT}}$ [V]	Nominal Current I_{nom} [A]	IGBT thermal resistance [K/kW]	Diode thermal resistance [K/kW]
1.2 kV (FZ3600R12HP4)	800	3600	14.5	20.7
1.7 kV (FZ3600R17HP4)	1200	3600	13.5	20
2.3 kV (FF1800R23IE7P)	1500	1800	28.1	54.7
3.3 kV (FZ2400R33HE4)	2100	2400	9.8	15.7
4.5 kV (FZ1800R45HL4)	2900	1800	10.8	18.0
6.5 kV (FZ750R65KE3)	3800	750	17.5	32.5

commercially available IGBT high-power modules from Infineon, as outlined in Table 4.1. These modules were selected because they offer the highest current ratings available within their respective voltage classes, making them suitable candidates for high-current applications. The power modules incorporate IGBT chips as well as anti-parallel diode chips inside the same package. To ensure reliable operation, manufacturers typically specify lower DC operating voltages for IGBTs in comparison to their maximum blocking voltages, to account for voltage transients during switching and cosmic ray impacts. As for the current rating, a maximum DC collector current is given in the datasheet which is limited by the operating temperature.

The DC voltage rating of the IGBT module $V_{\mathrm{DC,IGBT}}$ employed on the primary side determines the required number of series-connected submodules on the primary side $N_{\mathrm{SM,p}}$ (4.4). Care is taken to ensure that the maximum positive value of the switching device current i_{S1} (cf. Fig 4.1b) complies with the device current rating I_{nom}. Thus, since the peak phase current is exceeding 1 kA, the 6.5 kV IGBT module is deemed unsuitable for primary-side application due to its low current rating. Similarly, given its low DC voltage rating, the 1.2 kV IGBT module is not considered suitable for the secondary side, as electrolyzer voltages can reach up to 1150 V. Although series or parallel connections of individual IGBT modules could potentially enable their use, such configurations would increase the complexity of the switching cell and reduce submodule reliability. Within this chapter, the series and parallel connections of individual switches is not considered. In the given application, i.e. assuming only unidirectional power flow from primary to secondary side, the IGBT mainly carries the switching device current i_{S1} on the primary side, whereas on the secondary side the anti-parallel diode handles the larger share of i_{S2} (cf. Fig. 4.1b). Consequently, the current rating of the anti-parallel diode employed on the secondary side governs the number of parallel-connected submodules on the secondary side $N_{\mathrm{SM,s}}$ (4.5). Finally, the minimum number of required submodules $N_{\mathrm{SM,min}}$ of the DABCS is the greater of the two values, as indicated in (4.6).

$$N_{\mathrm{SM,p}} = \lceil V_{\mathrm{MVDC}} / V_{\mathrm{DC,IGBT}} \rceil \tag{4.4}$$

$$N_{\mathrm{SM,s}} = \lceil \max\left(|i_{\mathrm{S2}}^{-}|\right) / I_{\mathrm{nom}} \rceil \tag{4.5}$$

$$N_{\mathrm{SM,min}} = \max\left(N_{\mathrm{SM,p}}, N_{\mathrm{SM,s}}\right) \tag{4.6}$$

The voltage ratio d and the normalized ZVS boundaries as illustrated in Fig. 4.3 are kept constant regardless of the number of submodules, by scaling both the submodules' turns

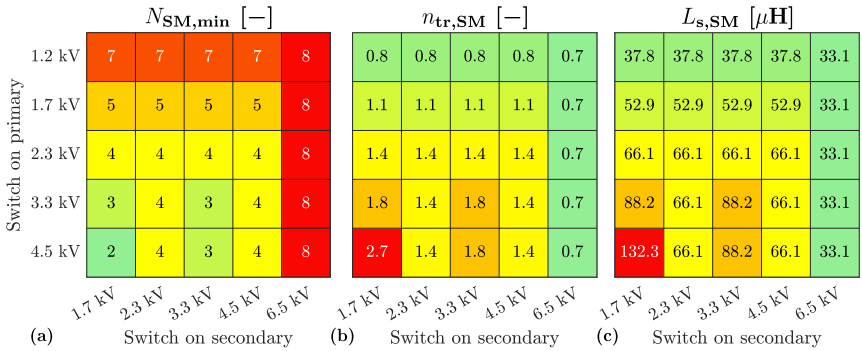


Figure 4.4: (a) Number of submodules employed in the DABCS, (b) submodules' turns ratio, (c) submodules' phase inductance.

ratio n_{SM} and phase inductance $L_{\mathrm{s,SM}}$ according to the number of submodules as follows

$$L_{\mathrm{s,SM}} = L_{\mathrm{s,DABCS}}/N_{\mathrm{SM,min}} \tag{4.7}$$

$$n_{\mathrm{tr,SM}} = n_{\mathrm{tr,DABCS}}/N_{\mathrm{SM,min}}. \tag{4.8}$$

As illustrated in Fig. 4.4a, the use of a HV IGBT module on the primary side and a LV IGBT module with high current capability on the secondary side, significantly reduces the required number of submodules. This results in a higher turns ratio and higher phase inductance per submodule, cf. Fig. 4.4b and Fig. 4.4c.

4.2.3 Semiconductor Losses

The power losses of the semiconductors can be estimated after the selection of the IGBT modules. They are calculated at a switching frequency of 1 kHz and full load operation of the MoL condition of the electrolyzer (cf. Fig. 4.3). Assuming that the electrolyzer voltage gradually increases over its lifetime, evaluating losses at MoL provides an average operating point, thus providing an estimate of the typical losses of the converter throughout the electrolyzer lifetime. Conduction and switching losses are estimated by using the output characteristics in the datasheets provided by manufacturers (cf. Appendix A). The collector-emitter voltage as a function of collector current $v_{\mathrm{ce}} = f(i_{\mathrm{c}})$, and the forward voltage as a function of forward current $v_{\mathrm{f}} = f(i_{\mathrm{f}})$, are given for various junction temperature T_{j}. A worst-case scenario in which a constant T_{j} of 125 °C is maintained, irrespective of the IGBT module pairs employed, is considered. Given the symmetry of the three-phase DAB topology, estimating the losses solely for switching devices $S1$ and $S2$ is sufficient (cf. Fig 4.1). In both devices, the positive portion of the phase current is conducted by the IGBT, whereas the negative portion is conducted by the diode. The conduction losses per submodule on the primary and secondary are then calculated as follows

$$P_{\mathrm{cond,p,SM}} = \frac{6}{T_{\mathrm{sw}}} \int_0^{T_{\mathrm{sw}}} \left[v_{\mathrm{ce}}(i^+_{\mathrm{S1}}) \cdot i^+_{\mathrm{S1}}(t) + v_{\mathrm{f}}(i^-_{\mathrm{S1}}) \cdot i^-_{\mathrm{S1}}(t) \right] dt \tag{4.9}$$

$$P_{\mathrm{cond,s,SM}} = \frac{6}{T_{\mathrm{sw}}} \int_0^{T_{\mathrm{sw}}} \left[v_{\mathrm{ce}}(i^+_{\mathrm{S2}}) \cdot i^+_{\mathrm{S2}}(t) + v_{\mathrm{f}}(i^-_{\mathrm{S2}}) \cdot i^-_{\mathrm{S2}}(t) \right] dt \tag{4.10}$$

where the factor 6 comes from the fact that there are six switching devices per bridge. The overall primary and secondary conduction losses of the DABCS are thus obtained by multiplying by the number of submodules $N_{\mathrm{SM,min}}$ employed.

The switching losses (4.14) can be estimated with the switching energies function (4.11 - 4.13) given in the datasheet according to the switched current.

$$E_{\mathrm{on}} = f\left(I_{\mathrm{c,on}}\right) \tag{4.11}$$
$$E_{\mathrm{off}} = f\left(I_{\mathrm{c,off}}\right) \tag{4.12}$$
$$E_{\mathrm{rr}} = f\left(I_{\mathrm{f,off}}\right) \tag{4.13}$$
$$E_{\mathrm{sw}}\left(I_{\mathrm{c,on}}, I_{\mathrm{c,off}}, I_{\mathrm{f,off}}\right) = E_{\mathrm{on}} + E_{\mathrm{off}} + E_{\mathrm{rr}} \tag{4.14}$$

The switching losses per submodule are then obtained by scaling the switched energy E_{sw} from the measured voltage in the datasheet V_{B} to the DC voltage applied to the IGBT module and by multiplying by the switching frequency

$$P_{\mathrm{sw,p,SM}} = 6\frac{V_{\mathrm{MVDC}}}{N_{\mathrm{SM,min}} V_{\mathrm{B}}} \cdot E_{\mathrm{sw}}\left(I^{+}_{\mathrm{S1,on}}, I^{+}_{\mathrm{S1,off}}, I^{-}_{\mathrm{S1,off}}\right) \cdot f_{\mathrm{sw}} \tag{4.15}$$

$$P_{\mathrm{sw,s,SM}} = 6\frac{V_{\mathrm{EL,MoL}}}{V_{\mathrm{B}}} \cdot E_{\mathrm{sw}}\left(I^{+}_{\mathrm{S2,on}}, I^{+}_{\mathrm{S2,off}}, I^{-}_{\mathrm{S2,off}}\right) \cdot f_{\mathrm{sw}}. \tag{4.16}$$

In the same manner, the overall primary and secondary switching losses of the DABCS are thus obtained by multiplying by the number of submodules $N_{\mathrm{SM,min}}$ employed. The primary $P_{\mathrm{p,DABCS}}$ and secondary $P_{\mathrm{s,DABCS}}$ semiconductor losses are obtained by summing the conduction and switching losses.

Although LV IGBT modules inherently exhibit lower conduction losses, as shown in Fig. 4.5a, their implementation on the primary side of the DABCS results in increased conduction losses on the primary side (cf. Fig. 4.5b), due to the elevated number of submodules in series carrying the phase current. Conversely, as depicted in Fig. 4.5c, employing HV IGBT modules on the primary side increases switching losses. This is attributed to the combination of higher inherent switching losses and increased switching energies caused by the elevated voltage due to the lower submodule count.

The use of LV IGBT modules on the secondary side effectively reduces conduction losses on that side, owing to their lower on-state resistance as shown in Fig. 4.5e. Note that the 2.3 kV IGBT module has been optimized by its manufacturer for inverter operation (larger IGBT chip than the diode) and exhibits therefore considerable secondary side conduction losses due to lower diode performances (cf. Appendix A). It can be seen that for the same IGBT module on the secondary side, employing LV IGBT module on the primary side, i.e. a higher number of submodules, leads to decreased conduction losses on the secondary side. This can be explained by the fact that conduction losses are quadratic with the current (cf. Appendix A). An increase in the number of submodules up to less than double the current decline due to parallelizing, results in a reduction in conduction losses. The switching losses on the secondary side of the DABCS follow a similar pattern as on the primary side, they increase with higher blocking voltage IGBT modules due to their inherently higher switching losses (cf. Fig. 4.5f). However, these losses marginally decrease with higher blocking voltage IGBT modules on the primary side due to the lower number of submodules. This can be again attributed to the non-linear nature of switching

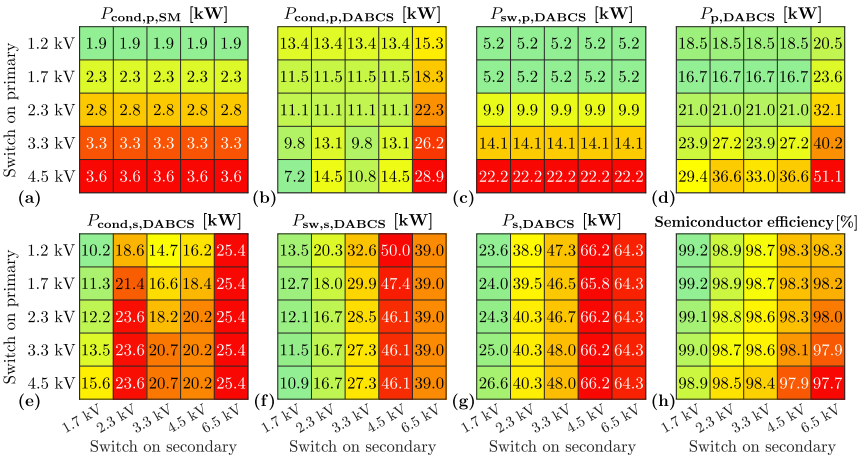


Figure 4.5: DABCS losses at switching frequency of 1 kHz under full load operation at MoL of the electrolyzer according to the pair of IGBT modules employed on the primary and secondary side: (a) Submodule conduction losses on the primary side, DABCS primary side (b) conduction losses, (c) switching losses, and (d) overall semiconductor losses. DABCS secondary side (e) conduction losses, (f) switching losses, and (g) overall semiconductor losses. (h) DABCS overall semiconductor efficiency.

losses with respect to the switched current (cf. Appendix A).

Fig. 4.5d and Fig. 4.5g provide a comprehensive summary of the semiconductor losses on the primary and secondary sides, respectively. As anticipated, conduction losses predominate in designs relying on LV IGBT modules, whereas switching losses prevail when employing HV IGBT modules. The implementation of the lowest blocking voltage IGBT module on the secondary appears as a straightforward choice, as it effectively reduces semiconductor losses on both sides. As for the primary side, the utilization of 1.7 kV IGBTs offers an optimized compromise between conduction and switching losses on both primary and secondary sides.

Fig. 4.5h shows the semiconductor efficiency of the DABCS. It can be observed that the use of LV IGBT modules on both sides, particularly the 1.7 kV IGBT module, results in the highest semiconductor efficiencies. However, the difference in efficiency based on the switch used on the primary side is not pronounced. This highlights the need for further analysis to ensure the selection of an optimal configuration.

4.2.4 Semiconductor Cooling

The heat generated by semiconductor losses must be dissipated by means of a cooling system. In the context of electrolysis plants, substantial electrolysis losses—approximately 20 to 40 % at nominal power, depending on the age of the electrolyzer cells—are prevalent (cf. Fig. 2.13b). Consequently, these plants incorporate extensive de-ionized water

cooling systems [189]. Leveraging this infrastructure, the power electronics can be effectively cooled by liquid-cooled cold plates. Thus, it is assumed that each switching device is equipped with one liquid-cooled cold plate, with its thermal resistance designed to handle the operating point with the highest power losses, whether they occur in the IGBT or the anti-parallel diode of the switching device. As the dynamic voltage d increases over the lifetime of the cells, maximum semiconductor losses are observed on the primary side at the BoL nominal power, whereas on the secondary side, they occur at the EoL nominal power [190].

As previously discussed, a T_j of 125 °C is considered irrespective of the IGBT modules employed, to allow comparability among the different switching devices. By considering the thermal resistances from junction to heatsink listed in Table 4.1 for individual semiconductor devices (IGBT and diode) $R_{\mathrm{th,JH,i}}$, along with the power losses per power device $P_{\mathrm{loss,i}}$, the maximum temperature and the thermal resistance of the cold plate required to dissipate the semiconductor losses at a T_j of 125 °C are as follows

$$T_{\mathrm{CP,max}} = \min_i \left(T_\mathrm{j} - P_{\mathrm{loss,i}} \cdot R_{\mathrm{th,JH,i}}\right) \tag{4.17}$$

$$R_{\mathrm{th,CP}} = \frac{T_\mathrm{j} - T_{\mathrm{cooling}} - \max\limits_i \left(P_{\mathrm{loss,i}} \cdot R_{\mathrm{th,JH,i}}\right)}{\sum\limits_i P_{\mathrm{loss,i}}} \tag{4.18}$$

where T_{cooling} represents the temperature of the cooling medium and is assumed to be 40 °C as this temperature is commonly found in industrial electrolyzer cooling systems [191]. As can be observed in Fig. 4.6a and Fig. 4.6b, the 2.3 kV IGBT module demands considerably lower cold plate temperature than its counterparts. This can be attributed to the half-bridge configuration of the IGBT module and the smaller diode chip (cf. Table 4.1). For the other IGBT modules, it can be seen that the higher the losses per three-phase DAB submodules the lower the maximum allowable temperature of the cold plate.

Figure 4.6d and Figure 4.6e show the required volume of the cooling system on the primary and secondary sides of the entire DABCS, based on the cooling system performance index (CSPI) and the cold plate thermal resistance (4.19) [192]. Although the use of a cold plate considerably reduces the size of the cooling interface with the semiconductor in comparison to forced-air cooling methods, the addition of pumps and pipes of the cooling system increases the overall volume. Therefore, a CSPI value of 5 $\mathrm{W/(K\,dm^3)}$ is typically taken for water cooling [192], and the volume of the cooling system can be calculated as follows

$$V_{\mathrm{CS}} = \frac{1}{\mathrm{CSPI} \cdot R_{\mathrm{th,CP}}}. \tag{4.19}$$

The use of LV IGBT on both sides of the DABCS enables the lowest overall cooling system volume due to a combination of lower power losses and thermal resistances. It can be seen that on the primary side, the 2.3 kV IGBT module requires a low temperature drop between the cold plate and the cooling medium but does not lead to a substantial large cooling system volume. This can be attributed to the comparatively low losses on the primary side, counterbalanced by the high thermal resistance of the IGBT module.

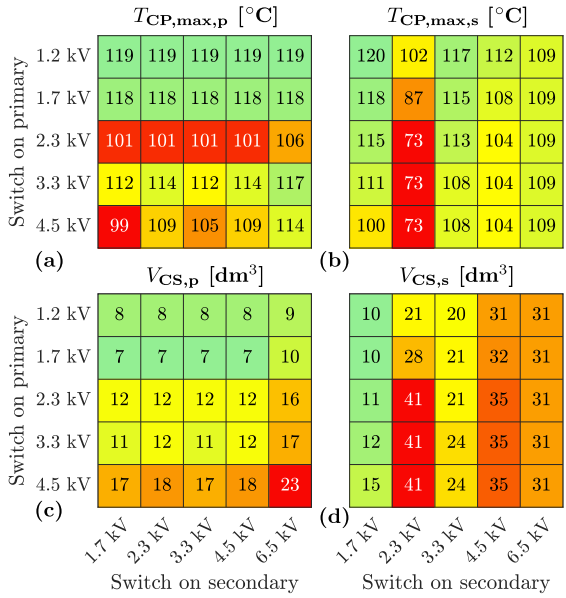


Figure 4.6: Liquid-cooled cold plate maximum temperature allowed on the cold plate (a) on the primary and (b) on the secondary side. The volume of the liquid cooling system for the semiconductor in the entire DABCS (c) on the primary and (d) secondary side.

4.2.5 DC-Link Capacitance

As illustrated in Fig. 1.7b, each submodule on the primary side is equipped with a DC-link capacitor. Conversely, the secondary side features a shared DC-link capacitor to leverage from the interleaving operation of the submodules in the ISOP connection of the DABCS.

Three factors are generally considered for determining the minimum required capacitance $C_{\min}$: the voltage ripple requirement ΔV, the DC-link hold-up time τ and the rms current requirements [193]. Although a hold-up time of 1 ms has been selected for the input side, the secondary side does not necessitate any specific hold-up time requirement owing to the pronounced capacitive behavior of electrolyzer cells [194]. On the secondary side, considering the influence of power electronics-induced current ripple on electrolyzer performance and degradation as discussed previously in Section 2.2.3, a maximum electrolyzer current ripple requirement of 1 % has been chosen for the entire loading and lifetime of the electrolyzer. Leveraging the ISOP connection, the control signal period for each submodule is phase-shifted relative to the subsequent submodule by $\pi/(3N_{\mathrm{SM,min}})$. Given that the polarization curve at the BoL displays the smallest voltage slope in relation to current, it essentially dictates the minimum possible voltage ripple for a specific current ripple. As a result, the current ripple requirement is converted into a voltage ripple requirement utilizing the BoL polarization curve. The capacitor voltage ripple requirement ensures that the secondary-side capacitance is sufficient to absorb and release appropriate charge to limit the voltage ripple below the specified threshold.

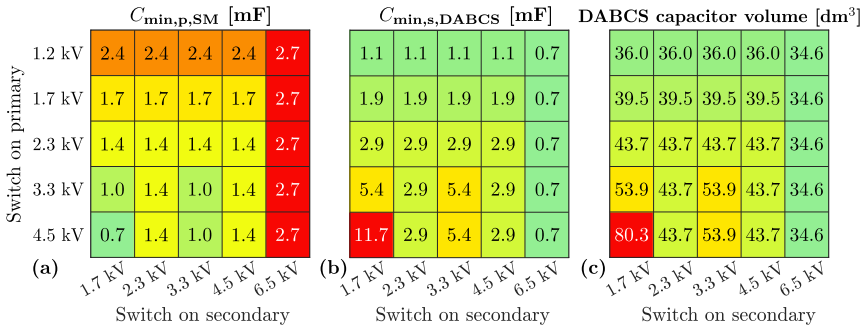


Figure 4.7: (a) Minimum required capacitance on the primary side submodules, (b) minimum required capacitance on the secondary side of the DABCS, and (c) the total capacitor volume of the DABCS according to the different switches combinations and for a switching frequency of 1 kHz.

In practical applications, large-scale electrolyzers typically feature extended conductors (cables and/or busbars) connecting the power electronics to the electrolyzer cells, introducing a non-negligible inductance that tends to diminish current ripple [189]. However, in this work, the stray inductance associated with these conductors is not taken into account. This omission is deliberate to maintain a more conservative design approach.

Figure 4.7a shows that configurations with a high number of submodules result in an elevated capacitance requirement on the primary side. In contrast, configurations with a lower number of submodules necessitate a higher capacitance on the secondary side due to diminished interleaving capabilities as depicted in Fig. 4.7b. The total capacitor volume employed in the DABCS is estimated in Fig. 4.7c, derived from the capacitance value and the capacitor DC voltage, assuming a constant volume per stored energy of 6.3 cm^3/J [94]. The total capacitor volume employed in the DABCS is primarily influenced by the number of submodules. The total capacitor volume increases as the number of submodules decreases due to the reduced interleaving capability and the resulting higher requirements in capacitance.

4.2.6 Medium Frequency Transformer

The MFT configuration considered is based on a dry-type three-phase three-limb core, utilizing silicon steel as the core material and featuring aluminum foil as windings. The chosen core material has been characterized in [195] and employed in a 5 MW DAB [196]. The MFT design procedure employed, outlined in Fig. 4.8a, unfolds as a multi-variable, multi-objective optimization process that builds upon existing and proven methodologies [197, 198]. The design process begins with the specification of material parameters and the definition of electrical and thermal constraints. Subsequently, MFT electrical requirements such as phase current, turn ratio, voltages, operating frequency, and leakage inductance are derived from the DABCS design procedure.

A design variables vector as listed in Table 4.2, containing parameters that influence the MFT geometry (cf. Fig. 4.8b) and performance, is established with initial values. In

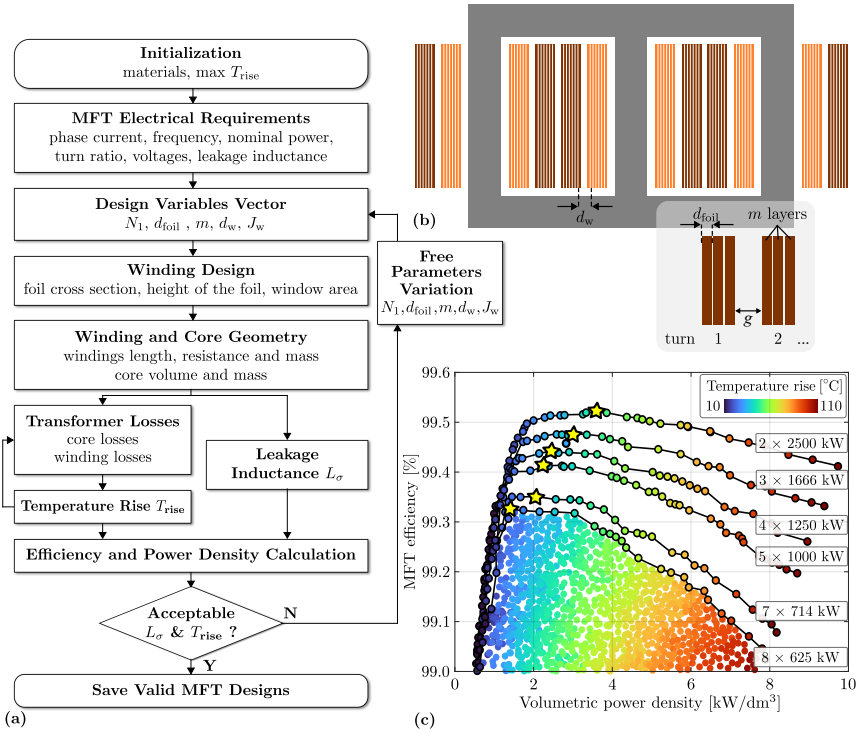


Figure 4.8: (a) Flowchart of the employed design procedure of the MFT design procedure (based on [197,198]). (b) Three-phase transformer core shape geometry and winding schematics. (c) Comparison of Pareto-optimal MFT designs for various DABCS configurations and an operating frequency of 1 kHz. For the case of 8 submodules of 625 kW, all sets of designs and the Pareto front are represented, while other configurations are represented only by their Pareto fronts. The selected efficiency-optimized designs are represented with yellow stars.

this high-current application, aluminum foil windings with a thin thickness d_{foil} as conductors have been opted for to mitigate resistance increase from skin and proximity effects. Determining the required winding cross-section based on maximum current levels, current density and inter-foil spacing gap g, the use of parallel layers m adjusts the winding window height and length. Given the foil's cross-sectional area and the number of turns, the overall area required for the windings on primary on secondary can be ascertained. The distance between the primary and secondary windings d_{w} serves as a lever to meet the leakage inductance requirement, while insulation distances are designed with respect to DC input and maximum electrolyzer EoL voltages, as well as air dielectric strength. All MFT designs are developed with the same maximum flux density of 1 T, which means that the number of turns and the core cross-section are adjusted proportionally. Subsequently, these allow for the calculation of the necessary conductor length needed to wind around the core.

Table 4.2: Range Sweep of Design Variables in the MFT Design Procedure.

Description	**Variable**	**Ranges**
Number of turns on primary	N_1	$1:1:150$
Foil thickness	d_{foil}	$0.2:0.1:3$ mm
Number of layers	m	$1:1:20$
Inter-winding distance	d_{w}	$d_{\text{w,min}}:5:200$ mm
Current density	J_{w}	$0.5:0.1:7$ A/mm^2

Upon determining core dimensions and winding resistances, losses at an operating frequency of 1 kHz can be calculated. Transformer losses originate from core losses (hysteresis and eddy current losses) and AC winding losses. Core losses are computed using improved general Steinmetz equations accounting for harmonics, while AC winding losses are calculated using the Dowell method to consider the reduction in conduction area due to skin and proximity effects at higher frequencies. With core dimensions and losses in hand, temperature rise is estimated, adhering to a 40 °C ambient air temperature and a selected maximum rise of 110 °C, aligning with class F standards [199]. Designs meeting leakage inductance and temperature criteria are saved, and the iterative design procedure continues with new values of the design variables until all possibilities are explored.

Figure 4.8c illustrates the various feasible MFT designs resulting from the design procedure for DABCS configurations with varying submodule counts. Indeed, the characteristics of the MFT are exclusively associated with its rated power, since in the considered methodology the MFT electrical requirements scale in proportion to the submodule count within the DABCS. For a specific DABCS configuration, the selection of transformer designs involves striking a balance between efficiency and power density. In this study, the maximum achievable MFT efficiency was chosen as the selection criterion. Note that if MFT power density were sought-after, the decline in efficiency with higher number of submodules would be even more pronounced as seen in Fig. 4.8c.

Figure 4.9 shows the detailed values of the design variables corresponding to the designs that have been optimized for efficiency. These designs consistently choose the thinnest possible foil to reduce the skin effect, thereby maximizing efficiency across all configurations. The current density in the optimized designs is relatively low compared to the maximum value allowed in the range of design variables listed in Table 4.2, resulting in larger designs. As the number of submodules decreases, N_1 is increased to handle the higher flux linkage and d_{w} is also lengthened to satisfy the requirements for larger leakage inductance.

The Pareto fronts in Fig. 4.8c reveal a decrease in MFT efficiency and power density as the number of submodules increases. This trend can be primarily attributed to the variation in material usage: fewer MFTs for an equivalent DABCS rated power lead to a reduced overall MFT material requirement. In addition, each MFT must provide galvanic isolation from the main input DC voltage of 5.4 kV, irrespective of the number of submodules. As the number of submodules rises, the overall volume required for insulation also increases. This leads to higher material usage (cf. Fig. 4.9), further diminishing efficiency and power density.

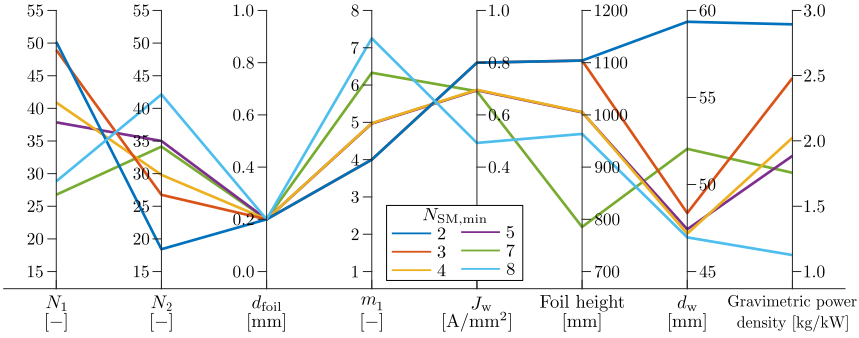


Figure 4.9: Characteristic of the selected efficiency-optimized MFT designs.

As a result, although employing HV IGBT modules on the primary side may not achieve optimal semiconductor efficiencies, the decrease in MFT losses from a reduced submodule count can provide a favorable balance between semiconductor and transformer losses.

A configuration with fewer submodules tends to exhibit higher power density, primarily because the MFT is the largest component of the DABCS. However, depending on the submodule reliability, even configurations with a relatively low submodule count may require redundant submodules to ensure converter system reliability. Adding redundant submodules can significantly increase the total installed power for configurations with a low submodule count. Therefore, to fairly evaluate the power density of different DABCS configurations, it is essential to ensure that all configurations achieve equivalent reliability.

4.2.7 Cost and Reliability Assessment

The cost estimation for each DABCS is derived from the methodology outlined in [200] and is explained as follows. The costs for semiconductors, wiring, cabinets, and control systems are estimated to be 3.5 € per kVA of installed switching power P_{switch}.

$$P_{switch} = N_{semi} \cdot U_{block} \cdot I_{nom} \tag{4.20}$$

where N_{semi} is the number of semiconductor devices, U_{block} the blocking voltage of the devices and I_{nom} the rated device current. A specific cost of 400 €/kJ is considered for the DC link capacitance [200]. Finally, the cost of the magnetic components within the different converter systems is approximately:

$$C_{mag} = A_p \cdot 723 \text{ k€} + N_{SM,min} \cdot 4 \text{ k€} \tag{4.21}$$

where A_p is the area product, defined as the product of the winding window and cross-section of the magnetic core.

For the reliability calculation of the DABCS, first the reliability of a single DAB submodule R_{SM} is assessed. Although there is no specific literature available on the reliability of DAB converters in offshore wind applications, extensive surveys have been conducted

on a wide range of wind turbines worldwide to assess the reliability of BTB converters in wind turbines [201, 202]. The most recent study reports a failure rate of 0.37 per year for the overall converter system, with failures considered as events specifically requiring on-site repair and the use of spare parts or other materials.

A DAB converter is essentially composed of two active bridges (equivalent to a BTB converter) interfaced via a transformer. The distinction in semiconductor operation arises from the soft-switching operation of DAB converters, resulting in higher efficiency than conventional BTB converters. While the efficiency of a BTB wind converter stands at around 98 % at full load (cf. Section 5.2.1), a DAB converter can achieve a semiconductor efficiency of approximately 99 % at 1 kHz under rated load (cf. Fig 4.5h). Assuming an identical cooling system, if the semiconductors of the BTB wind converter are expected to operate at a junction temperature of 125 °C, the DAB operation due to the 1 % difference in semiconductor efficiency would result in a junction temperature of roughly 82.5 °C only (see Appendix B for detailed calculation).

The failure rate of the conventional BTB wind converter λ_{BTB} can be adjusted for DAB operation by using a temperature-dependent stress factor π_{T}. The temperature dependence of a failure rate is described by an empirical model based on the Arrhenius equation [203], as follows

$$\pi_{\mathrm{T}} = \exp\left(\frac{E_{\mathrm{a1}}}{k_0}\left(\frac{1}{T_{\mathrm{ref}}} - \frac{1}{T_{\mathrm{op}}}\right)\right) \tag{4.22}$$

with E_{a1} the activation energy, k_0 the Boltzmann constant, T_{ref} the reference junction temperature and T_{op} the actual junction temperature. As illustrated in Fig. 4.10, operation at a junction temperature of 82.5 °C instead of 125 °C results in a $\pi_{\mathrm{T}} = 0.25$, meaning that the semiconductors failure rate in a DAB is four times lower than that of the BTB wind converter. The failure rate of a single DAB submodule is then calculated as follows

$$\begin{aligned}\lambda_{\mathrm{SM}} &= \lambda_{\mathrm{BTB}} \cdot \pi_{\mathrm{T}} + \lambda_{\mathrm{LFT}} \\ &= 0.37 \cdot 0.25 + 0.025 = 0.12 \text{ yr}^{-1}\end{aligned} \tag{4.23}$$

with λ_{LFT} the failure rate of a conventional LFT [204] and by assuming that it is equivalent in DAB operation.

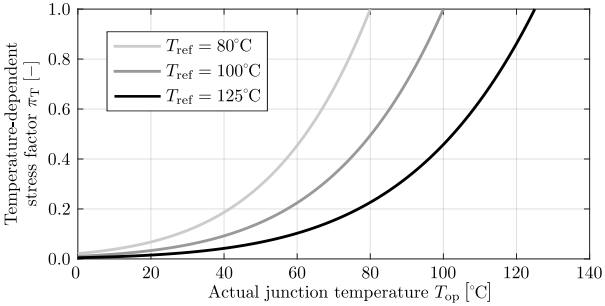


Figure 4.10: Temperature-dependent stress factor π_{T} according to actual junction temperature T_{op} for different reference junction temperature T_{ref}.

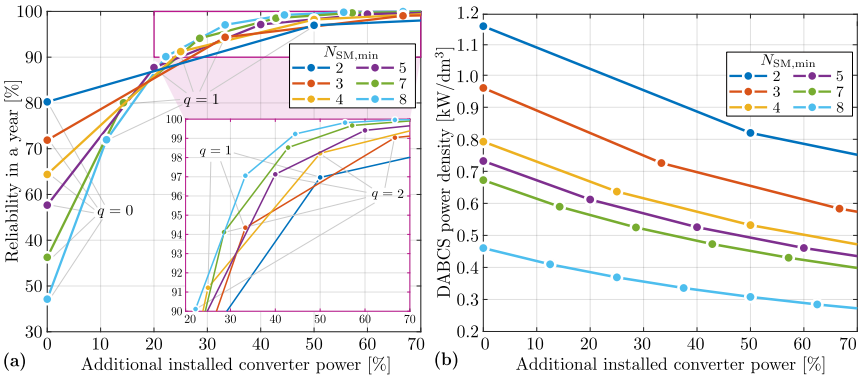


Figure 4.11: DABCS (a) reliability in a year and (b) power density according to the additional installed converter power for different minimum number of submodules required $N_{SM,min}$.

However, a DABCS comprises several DAB converter submodules, leading to the failure rate of the DABCS being equal to $N_{SM,min}$ times the individual submodule failure rate. The advantage of modular topologies, such as the DABCS, lies in the ease and cost-effectiveness of implementing redundancy. Additional submodules of a share of the total converter power can be seamlessly integrated into the topology to enhance reliability without compromising efficiency, by incorporating redundant submodules in a standby fashion [94]. Subsequently, the reliability of the overall DABCS, considering redundant submodules, can be determined using the k-out-of-n model, expressed as [173]

$$R_{DABCS} = \sum_{i=k_{SM}}^{N_t} \binom{N_t}{i} \cdot R_{SM}^{i} \cdot (1 - R_{SM})^{N_t - i} \quad \text{with} \quad R_{SM} = e^{-\lambda_{SM} \cdot T_M} \tag{4.24}$$

where N_t is the total number of submodules, k_{SM} the minimum number of submodules required to remain operational (i.e., $k_{SM} = N_{SM,min}$) and T_M the time period over which the reliability is evaluated. The number of redundant submodules employed is given by $q = N_t - k_{SM}$. With a failure rate of 0.12 yr^{-1} per DAB submodule and with the adoption of a preventative maintenance interval of one year, an oversizing of the total number of submodule around 30 to 50 % is required, depending on the DABCS configuration, to achieve a reliability in a year of around 95 % (cf. Fig 4.11a). This oversizing mechanically results in a reduction in power density, as illustrated in Fig 4.11b.

4.2.8 Pareto Optimization

Upon evaluating the volume and efficiency aspects of semiconductors, DC-link, cooling system, and MFT, the DABCS efficiency, power density and specific cost at a switching frequency of 1 kHz are summarized in Fig. 4.12. Note that the power density and specific cost calculation takes into account the required number of additional redundant submodules to reach a reliability in a year above 95 % for all configurations. In addition, a volume utilization factor of 3 from components volume to the converter system volume is considered [205]. This factor accounts for auxiliary equipment (such as control cabinets) and the inevitable empty spaces required in practical assemblies (overhead, assembly

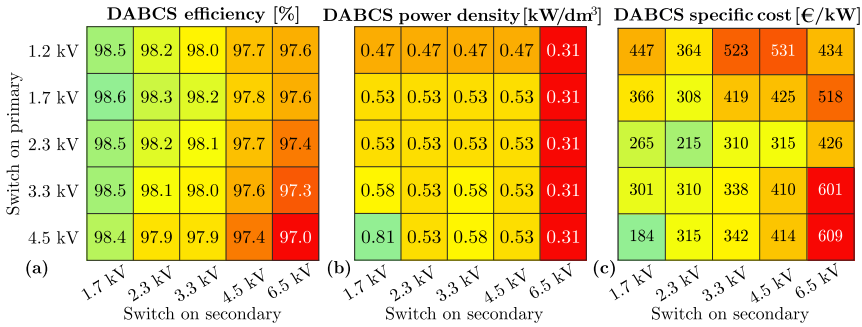


Figure 4.12: DABCS efficiency under full load operation at MoL of the electrolyzer, (b) DABCS power density and (c) specific cost according to the employed switch combination for a switching frequency of 1 kHz.

structure, isolation distances).

While employing 1.7 kV IGBT modules on the secondary side is a straightforward decision, the optimal choice for the primary side IGBT modules does not exhibit a clear optimum. Though the selection of the 4.5 kV module on the primary side provides the highest converter power density and lowest specific cost, it does not provide the highest converter efficiency. The specific cost is minimized because the decreased number of submodules in this configuration results in the lowest installed switching power and lowest MFT material requirements. To enlarge the scope of the results, the switching frequency deliberately kept fixed needs to be swept to perform a Pareto optimization of efficiency versus power density for different DABCS configurations [206]. Nevertheless, only configurations using the 1.7 kV IGBT module on the secondary side are considered as no discernible advantages in terms of semiconductor losses have been established with higher voltage class IGBT modules on the secondary side. The methodology introduced in Fig. 4.2 is thus repeated for various switching frequencies, maintaining the same boundary conditions and materials (semiconductors, core and winding materials), but resulting in different design parameters such as series inductance, power losses and current ripple. Similarly to in Fig. 4.8c, the transformer designs with highest efficiency is selected and each DABCS design is represented by a point in the resulting dataset.

Figure 4.13 illustrates the efficiency and power density along with the Pareto fronts of the considered configurations for switching frequencies ranging from 200 Hz to 3 kHz. The emphasis on efficiencies exceeding 98.5 % aligns with the high-efficiency requirements for converters in hydrogen applications. In this efficiency range, utilizing the 4.5 kV IGBT module on the primary side, i.e. the configuration with the lowest number of submodules, exhibits the most favorable performances in terms of power density and efficiency. Additionally, as listed in Table 4.3, this configuration results as well in the lowest specific cost.

The power density of the DABCS increases with switching frequency, as a higher frequency allows for a reduction in the volume of passive elements. However, this reduction in volume is constrained by thermal considerations. As demonstrated in Fig. 4.14, above a switching frequency of 1.5 kHz, the temperature rise requirement limits the reduction in the MFT volume with increasing switching frequency.

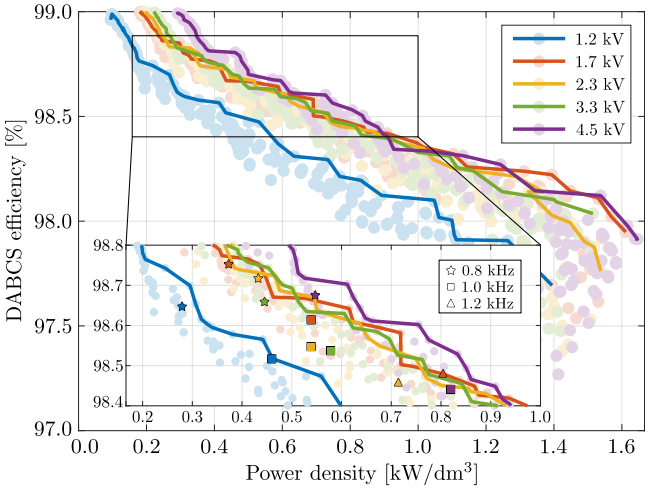


Figure 4.13: Results of the efficiency versus power density Pareto optimization considering the use of the 1.7 kV IGBT module on the secondary side and different IGBT modules on the primary side.

Table 4.3: Comparative Analysis of Different DABCS Configuration Achieving an Efficiency of 98.5 %.

Switch on primary	$N_{\mathbf{SM,min}}$ [–]	q [–]	$L_{\mathbf{s,SM}}$ [μ**H**]	$f_{\mathbf{sw}}$ [**kHz**]	**Semi-conductor eff.** [%]	**MFT eff.** [%]	**Power density** [**kW/dm^3**]	**Specific cost** [**€/kW**]
1.2 kV	7	3	37.8	1000	99.1	99.4	0.47	447
1.7 kV	5	2	49.8	1180	99.1	99.4	0.71	366
2.3 kV	4	2	58.7	1120	99.0	99.5	0.73	265
3.3 kV	3	2	85.6	1030	99.0	99.5	0.73	301
4.5 kV	2	1	147.8	890	98.9	99.6	0.83	184

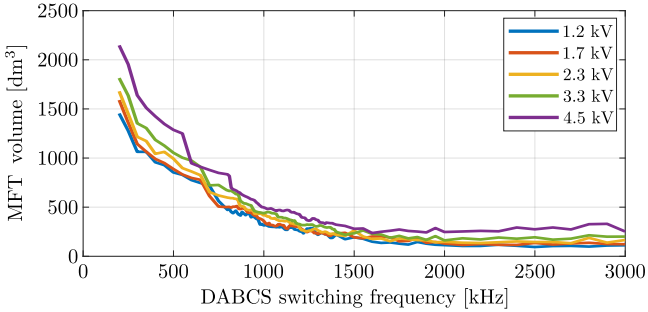


Figure 4.14: Single MFT volume versus switching frequency for different IGBT modules on the primary side.

4.2.9 Trade-Off Analysis under Varying Conditions

This section aims to examine the results of the Pareto optimization for various DC input voltages. The Pareto optimization of the described DABCS design methodology can be iterated for input voltages beyond the previously considered 5.4 kV. The electrolyzer rating is kept constant, while the input voltage is varied, thereby scaling the required number of submodules. However, again in this iteration, the secondary switches exclusively consider the use of 1.7 kV IGBT modules.

Fig. 4.15a depicts the Pareto fronts of DABCS configurations employing different voltage class IGBT modules on the primary side and for different input voltages. Note that the use of the 6.5 kV IGBT module is also considered once the current on the primary side adheres to the switch current rating. While utilizing the 4.5 kV IGBT module on the primary side offers a limited advantage compared to the other configuration at input voltages below 10 kV, as the input voltage increases the use of the 6.5 kV IGBT module stands out more prominently compared to the other DABCS configurations. This can be explained by the relatively small number of submodules required by this DABCS configuration to withstand the elevated DC input voltages as illustrated in Fig. 4.15b.

It can be observed that the DABCS power density decreases for higher DC input voltages due to a higher number of submodules and higher insulation requirements. However, the overall DABCS efficiency remains relatively consistent across varying input voltages. This can be attributed to the fact that semiconductor losses decrease with higher input voltage and balance the efficiency decline of the MFT. The semiconductor losses decrease due to the quadratic relation of conduction losses with the current. Moreover, switching losses on both sides remain constant regardless of the input voltage as the input voltage on the primary side and the phase current on the secondary side are proportionally divided by the number of submodules. The DABCS switching losses are the sum of individual submodule switching losses, thereby canceling out the effect of the number of submodules. Note that if the MFT power density was prioritized instead of the MFT efficiency, the decrease in MFT efficiency would become more pronounced with a higher number of submodules (cf. Fig. 4.8c) and would lead to a DABCS efficiency decrease with higher DC bus voltages.

Eventually, the employment of the lowest number of submodules, by means of the highest possible blocking voltage IGBT modules on the primary side, results for all considered input voltages in the best efficiency, power density and cost.

4.3 Configuration Optimization of IPOP and IPOS Connections of DABCS

This section aims to extend the analysis to other types of modular DABCS connections considered in the different EDS configurations, specifically the IPOP connection in DC1a with a 1.1 kV input voltage and the IPOS connection in DC2 between the PMSG and the 10 kV line voltage. This analysis will determine whether employing the minimum number of submodules, as discussed in the previous section, achieves the optimal balance between power density and efficiency for various modular connections.

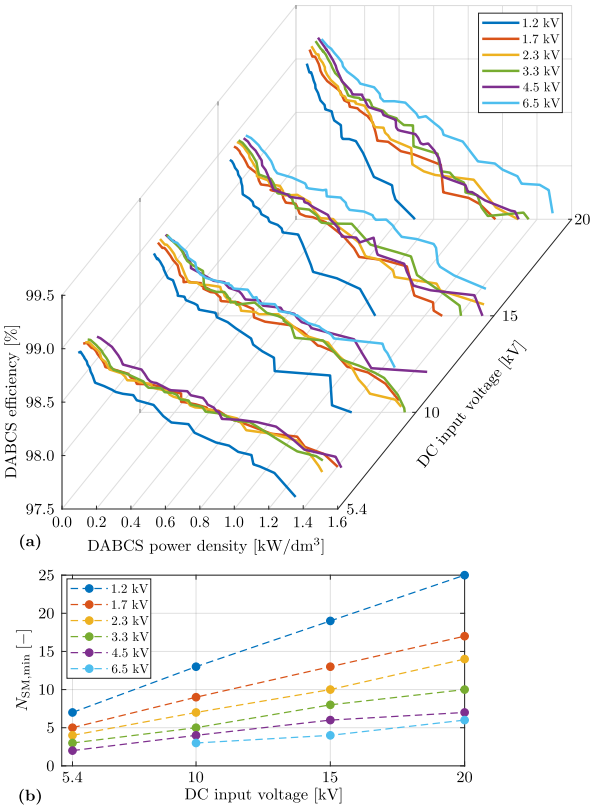


Figure 4.15: (a) Results of the Pareto optimization and (b) number of submodules of the different DABCS configurations employing 1.7 kV IGBT modules on the secondary side and various voltage class IGBT modules on the primary side for different input voltages.

4.3.1 IPOP connection

The same methodology as depicted in Fig. 4.2 for ISOP connection is employed for the DABCS in IPOP connection in the DC1a, between the 1.1 kV and the 5 MW electrolyzer. However, few key differences in the methodology need to be highlighted:

1. The 1.2 kV IGBT module is not considered on either the primary or secondary side of the DABCS due to its insufficient DC voltage ratings and the exclusive use of parallel connections of submodules on both sides of the DABCS.

2. In the IPOP connection, the submodule series inductance $L_{s,SM}$ is obtained by multiplying the DABCS equivalent series inductance $L_{s,DABCS}$ by the number of parallel-connected submodules $N_{SM,min}$.

3. The submodule turns ratio $n_{tr,SM}$ is equal to the DABCS equivalent turns ratio $n_{tr,DABCS}$.

Due to the LV on both sides and high current requirements, using LV IGBT modules on both sides enables the lowest minimum number of submodules in the DABCS for the IPOP connection, as shown in Fig. 4.16a. This configuration also results in the highest semiconductor efficiency, as illustrated in Fig. 4.16b for a switching frequency of 1 kHz, due to the inherent low conduction and switching losses of LV IGBT modules.

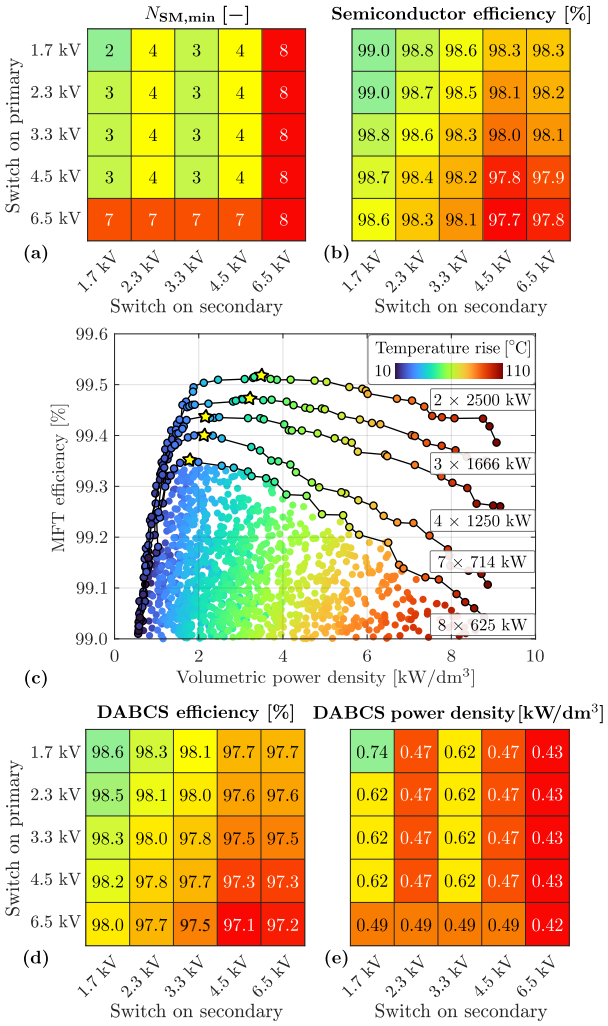


Figure 4.16: (a) Number of submodules employed in the DABCS in IPOP connection. (b) DABCS overall semiconductor efficiency. (c) Comparison of Pareto-optimal MFT designs for various number of submodules. DABCS (d) efficiency under full load operation at MoL of the electrolyzer and (e) power density according to the employed switch combination for a switching frequency of 1 kHz.

Regarding the MFT, the same methodology as in Fig. 4.8a is employed. Figure 4.16c illustrates the various feasible MFT designs resulting from the MFT design procedure for DABCS configurations with varying submodule counts. Similar to the ISOP connection, the Pareto fronts reveal again a decrease in MFT efficiency and power density as the number of submodules increases. However, in the case of the IPOP connection, the efficiency delta is lower than in the ISOP connection. For instance, between two and seven submodules in the DABCS, the MFT efficiency delta is around 0.15 % for the ISOP connection, while in the IPOP connection, it is around 0.10 %. This can be primarily explained by the reduced insulation voltage level compared to the series connection. The difference in MFT efficiency between various submodule counts in the IPOP connection comes from the overall difference in the quantity of materials used.

The combination of high semiconductor efficiency and high MFT efficiency with the employment of LV IGBT modules on both sides results in the highest DABCS efficiency, as shown in Fig. 4.16d. Although not detailed in this section, the volume of the DC link capacitors and the cooling system is identically computed and considered in the DABCS power density estimation, as illustrated in Fig. 4.16e. In addition, due to the parallel connection, the loss of one or several submodules does not lead to a complete DABCS failure, allowing for less stringent reliability requirements. Nevertheless, the DABCS still includes redundant submodules to ensure again a reliability within a year of over 95 %. Therefore, the use of LV IGBT on both sides, such as the 1.7 kV IGBT module, i.e. the configuration with the lowest submodule count results in the highest DABCS efficiency and power density. In this case, a Pareto optimization is not necessary to highlight the superiority of the configuration with the lowest submodule count.

4.3.2 IPOS connection

The methodology is again applied for the 15 MW DABCS in IPOS connection considered in the DC2 EDS between the LV rectified PMSG voltage and the 10 kV line voltage. However, a few key differences in the methodology need to be highlighted:

1. The 1.2 kV IGBT module is not considered on the primary side of the DABCS due to its insufficient DC voltage ratings and the 6.5 kV IGBT module is not considered on the secondary side due to its insufficient current ratings.

2. In the IPOS connection, the submodule series inductance $L_{\mathrm{s,SM}}$ is obtained by multiplying the DABCS equivalent series inductance $L_{\mathrm{s,DABCS}}$ by the number of parallel-connected submodules $N_{\mathrm{SM,min}}$ on the primary side.

3. The submodule turns ratio $n_{\mathrm{tr,SM}}$ is equal to the product of the DABCS equivalent turns ratio $n_{\mathrm{tr,DABCS}}$ and of the number of series-connected submodules $N_{\mathrm{SM,min}}$.

Figure 4.17 represents the soft turn-on switching boundaries of the DABCS and of the voltage ratio across the DABCS in relation to the power transferred. Since in DC2 the output of the PMSG's rectifier is not considered to be regulated at a constant value and that the output voltage of the DABCS is maintained at 10 kV, the increasing PMSG's rectifier output voltage with the power results in a variable voltage ratio d across the DABCS. When the PMSG operates at its minimum rotational speed, typically below wind speeds of approximately 7 m/s (see Fig. 3.6), the voltage ratio remains constant

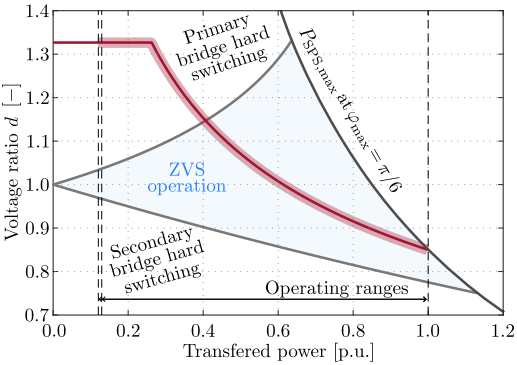


Figure 4.17: Normalized soft-switching area of the step-up DABCS considered in the DC2 EDS and the voltage ratio across the DABCS in relation to the transferred power.

above $d = 1.3$ for power levels below 27 %. As power continues to increase, the rising voltage from the PMSG results in a higher DC output voltage from the generator's rectifier, causing the voltage ratio across the DABCS to decrease with increasing power. The sizing of the equivalent DABCS turns ratio $n_{\mathrm{tr,DABCS}}$ such that the voltage ratio d is lower than 1 at rated transferred power is a result of a trade-off between high efficiency at rated load and ensuring operation under soft switching across the widest possible operating range. Additionally, it is important to highlight that the soft-switching boundaries differ from those in the ISOP connection (cf. Fig. 4.3). This is explained by the fact the DABCS in the IPOS connection in DC2 operates with a variable input voltage, whereas in DC1a, the DABCS in ISOP connection operates with a variable output voltage. The side of the DABCS where the variable voltage is applied exhibits a quadratic behavior with the voltage of the soft-switching boundary on that side (see Eq. 4.2 and 4.3).

The IPOS connection shares a structural similarity with the ISOP connection, as both involve submodules connected in series to meet the voltage requirement on one side and in parallel to cope with the current demands on the other side. The key difference lies in which sides the high and low voltages are applied. Due to this structural resemblance, the IPOS connection demonstrates comparable performance trends to those of the ISOP connection. For instance:

$N_{\mathrm{SM,min}}$: the minimum number of submodules is achieved when employing HV IGBT modules on the high voltage side and LV IGBT modules with higher current capabilities on the low side, as illustrated in Fig. 4.18a.

Semiconductor efficiency: as shown in Fig. 4.18b, similar to the ISOP connection, the use of LV IGBT modules on both sides of the DABCS enables optimal semiconductor efficiency.

MFT efficiency and power density: the principle of non-scaling of insulation distances in the MFT with respect to the number of submodules also applies to the IPOS connection. Consequently, minimizing the number of MFTs in the DABCS achieves similarly the highest MFT efficiency and power density.

DABCS efficiency and power density: the configuration with the lowest number of submodules results similarly in the highest power density, although at a same switching frequency, its efficiency is lower than that of configurations using LV IGBT modules on both sides (see Fig. 4.18c and Fig. 4.18d). As discussed in Section 4.2.8, a Pareto optimization can reveal that employing the minimum number of submodules in the DABCS—specifically using 1.7 kV IGBT modules on the primary side and 3.3 kV IGBT modules on the secondary side—yields the highest DABCS power density and efficiency.

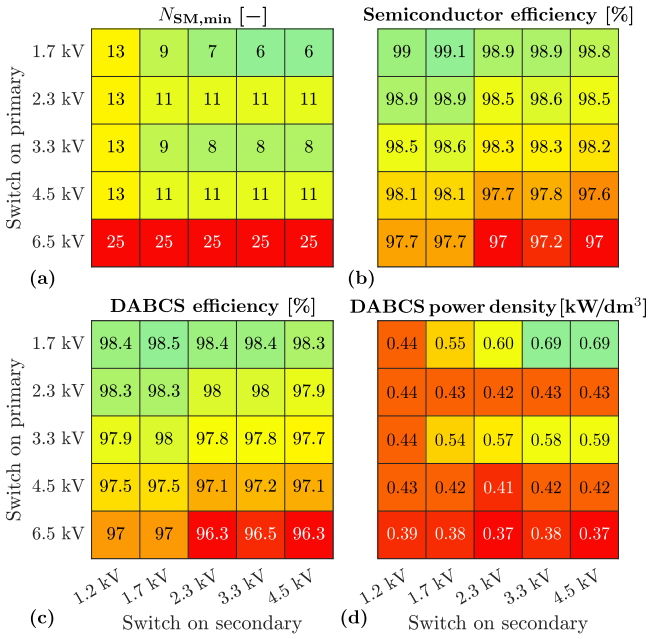


Figure 4.18: (a) Number of submodules employed, (b) overall semiconductor efficiency, (c) DABCS efficiency under rated load operation at MoL and (d) power density according to the employed switch combination in IPOS connection for a switching frequency of 1 kHz.

5 Life Cycle Cost Analysis[1]

Given the wind fluctuations, the wind turbine produces power at different load levels. In addition, as the electrolyzer ages, the voltage increases over its lifetime, resulting in continuously different load conditions. To account for the variability of the power source and the evolving load conditions of electrolyzers over the lifetime of the plant, a life cycle cost analysis (LCCA), as shown in Fig. 5.1, is conducted to comprehensively compare the different EDS discussed in Section 3.3. The LCCA offers a comprehensive assessment method for evaluating the total cost of ownership of the wind-to-hydrogen plant over its entire lifespan. This includes all relevant costs such as initial CapEx, OpEx, replacement costs, but also energy losses and downtime in the plant. By employing an LCCA in the evaluation of different EDS, a holistic view of the long-term techno-economic aspects of each variant is provided.

5.1 Plant Conditions

First, the wind turbine output power is computed based on the equations detailed in Section 2.1.1 and the exemplary 15 MW wind turbine parameters listed in Table 2.1. By considering the wind speed distribution, which in this case study follows a Weibull distribution approximating an average wind speed of 10 m/s, the power output distribution of the wind turbine can be calculated (cf. Fig. 2.3).

Next, the polarization curve and the SEC of the electrolyzer unit for the year $n = 1$ can be established based on equations presented in Section 2.2.1. The minimum load is determined by calculating the power needed to reach 40 % of the electrolyzer rated current, which subsequently increases with the aging of the electrolyzer cells.

Following this, using the selected power allocation strategy discussed in Section 3.2 and the wind turbine output power distribution, the number of hours in operation at various load levels can be assessed. This allows for the calculation of the capacity factor and the degradation encountered for the year. The electrolyzer degradation encountered during the year can be determined by the number of hours it operates under partial and full load. As outlined in Section 2.2.1, the literature reports widely varying degradation rates, which depend on factors such as catalyst type, loading, and operating conditions. To address this, the current EU targets for the 2020s decade, as presented in the report from the

[1] Parts of this chapter are published in Runser *et al.* [162]

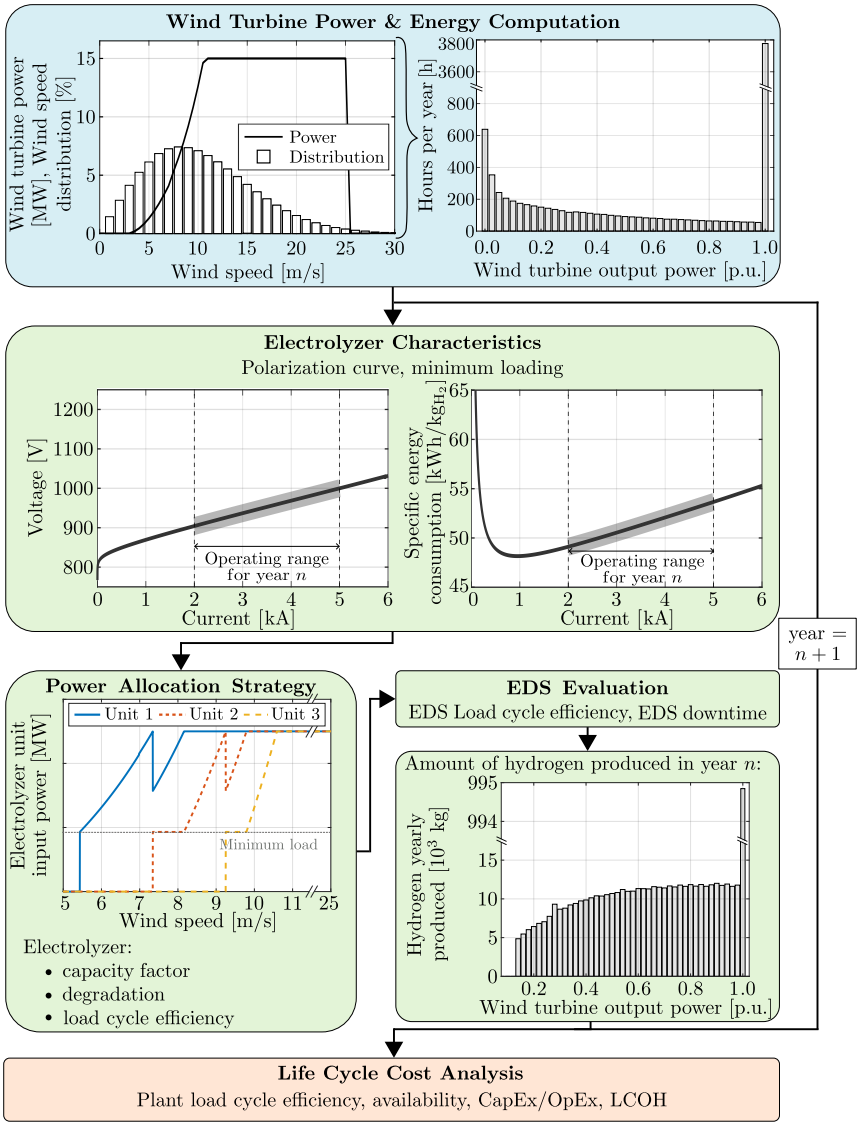


Figure 5.1: Methodology employed for evaluating and comparing the different EDS.

Fuel Cells and Hydrogen 2 Joint Undertaking, are used in this work [207]. Specifically, a degradation between 1 and 2 % per year for PEM electrolyzers is specified. The former value is considered for operation at half-rated load, while the latter value is considered for operation at full load, in line with the discussion in Section 2.2.1 that degradation occurs at a higher rate under full load. In practice, degradation occurs continuously, however,

as the Weibull distribution is approximated on a yearly basis, the methodology simplifies the evaluation to an annual timeframe. Thus, the voltage degradation for year $n+1$ is computed according to the operating conditions of year n as follows

$$\Delta_{V_{n+1}} = h_{pl,n} \cdot d_{pl} + h_{fl,n} \cdot d_{fl} \tag{5.1}$$

with $h_{pl,n}$ and $h_{fl,n}$ representing the hours under partial load and full load in year n, respectively, and d_{pl} and d_{fl} denoting the corresponding degradation rates as listed in Table 5.1. The methodology is then repeated for every year of the plant lifetime and with the assumption that all electrolyzer units degrade identically.

Based on the considered wind turbine output power profile, degradation rate parameters and definition of cell EoL (15 % increase in cell SEC), the electrolyzer cells accumulate approximately 70000 operating hours before reaching their EoL. As illustrated in Fig. 5.2, this implies a need for cell replacement every nine years. These figures are slightly higher than the state-of-the-art for grid-connected PEM electrolyzers. However, they align with expectations since the wind-to-hydrogen plant capacity factor is lower (around 60 %) compared to grid-connected electrolyzers. In addition, the variable nature of the wind profile does not maintain constant operation at full load, which is beneficial in terms of degradation. Moreover, Fig. 5.2 shows that cell degradation (indicated by increases in electrolyzer voltage and SEC) slows down over the lifetime of the cells. This trend is due to the increase in minimum load level with degradation, thereby reducing the number of operating hours at partial load in favor of increased hours in idle time. As a result, the electrolyzer unit operates fewer hours during the year, which in turn leads to a slower overall rate of degradation.

Table 5.1: Degradation rates.

Degradation rates	**Value** [µV/h]
d_{fl}	9
d_{pl}	$d_{fl} \cdot \sum_{i=1}^{u} P_i \cdot t_i \;/\; \sum_{i=1}^{u} t_i$

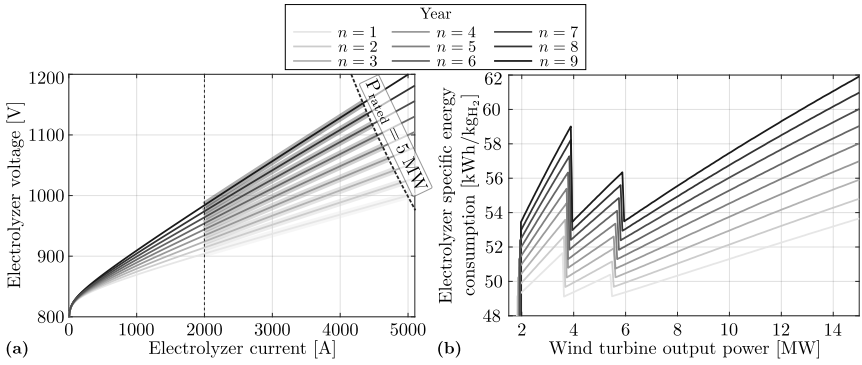


Figure 5.2: (a) Electrolyzer polarization curves over the nine years of operation and (b) the corresponding SEC of the electrolyzer according to the considered power allocation strategy.

5.2 EDS Components Evaluation

Once the plant conditions are set, the losses, cost, volume, mass and reliability of the principal components of the EDS, including rectifiers, inverters, transformers, DABCSs and tower cables can be thoroughly assessed.

5.2.1 Component Losses

Figure 5.3a illustrates the efficiency curves of three-phase BTB converters in wind turbines. Due to their hard-switched operation, the efficiency is primarily influenced by switching losses, which are dictated by the voltage ratio $r = V_{DC}/V_{AC,pk}$ with V_{DC} the DC link voltage and $V_{AC,pk}$ the peak AC voltage. Since in the MVAC and AC1 EDSs the DC link voltage of the BTB converter is considered to be regulated at a constant value, the increasing PMSG voltage with the power results in a variable voltage ratio such as $r = V_{DC}/V_{PMSG,pk}$. As shown in Fig. 5.3b, this leads to a lower efficiency of the BTB's rectifier stage at reduced loads compared to the BTB's inverter stage as the latter is considered to operate with a constant voltage ratio of $r = 1.10$ for LV PMSG and $r = 1.15$ for MV PMSG.

The efficiency curves of the electrolyzer rectifier, which is based on IGBT modules, are derived in the same manner, except that only half of the BTB converter is considered. The electrolyzer rectifier is also hard-switched and the voltage ratio r depends on the electrolyzer loading and aging. As illustrated in Fig. 5.4a and Fig. 5.4b, while r peaks at 1.35 at BoL it reaches its maximum of 1.55 at EoL, resulting in the efficiency of the electrolyzer rectifier at rated load to decrease from approximately 98 % at BoL to 97 % at EoL.

The LFT efficiency curves adhere to the EU Ecodesign directive [208], which outlines minimum peak efficiency and maximum load and no-load losses for different ratings. Figure 5.4c illustrates that higher LFT ratings correspond to improved efficiency and that the transformer efficiency decreases for higher operating points.

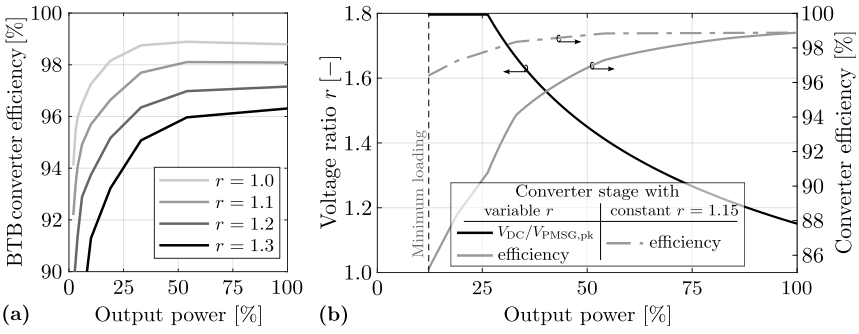


Figure 5.3: Efficiency curves of (a) BTB converter based on the voltage ratio r and (b) corresponding efficiency curves of the BTB converter stage (rectifier or inverter) according to the PMSG variable voltage versus operation at a constant voltage ratio $r = 1.15$.

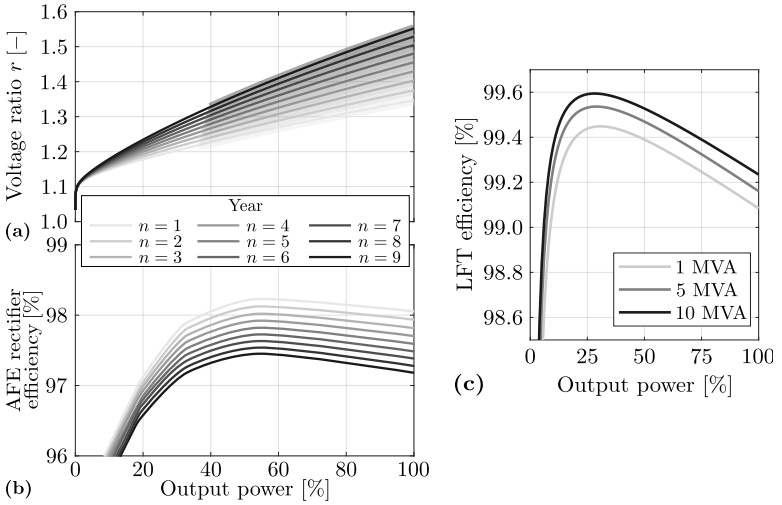


Figure 5.4: (a) Voltage ratio curves across the electrolyzer rectifier for different aging conditions and (b) corresponding electrolyzer rectifier efficiency. (c) Efficiency curves of LFT according to its ratings.

The tower cables are designed considering copper and are dimensioned to meet a nominal current density of 1.5 A/mm^2 to restrict the temperature rise [209]. Detailed cable characteristics for each EDS considered are listed in Table 5.2.

Table 5.3 summarizes the detailed specifications for all DABCSs configurations employed in the DC1 and DC2 EDSs, differentiated by whether an LV or MV PMSG is considered. For each DABCS, the IGBT modules are selected to minimize the number of submodules required, thereby ensuring both optimal efficiency and power density as concluded in Chapter 4. The switching frequency is chosen to achieve precisely 98.5 % efficiency at rated load at MoL, while the number of additional redundant submodules q is determined to ensure an annual reliability exceeding 95 %.

Table 5.2: Tower Cables Characteristics.

EDS	**Voltage [kV]**	**Current ratings [A]**	**Cable configuration**	**Copper mass [kg][2]**	**Rated power losses [%/km][3]**
MVAC	33	262	175 mm^2 x 3 phases	941	0.15
AC1	0.69	12550	250 mm^2 x 33 x 3 ph.	44983	7.34
AC1	3.3	2624	250 mm^2 x 7 x 3 ph.	9406	1.53
DC1	1.1	13636	9090 mm^2 x 2 ph.	32582	5.31
DC1	5.4	2778	1860 mm^2 x 2 ph.	6666	1.08
DC2	10	1500	1000 mm^2 x 2 ph.	3584	0.58

[2] copper mass density: 8960 kg mm^{-3}
[3] specific resistance of copper: $1.95 \times 10^{-2}\,\Omega\,\mathrm{mm}^2\,\mathrm{m}^{-1}$, current density: 1.5 A mm^{-2}

Table 5.3: DABCSs Specifications.

Distribution system	**DC1**	**DC1**	**DC2**	**DC2**	**DC2**
PMSG voltage [kV]	0.69	3.3	0.69	3.3	n.a.
Input voltage [kV]	1.1	5.4	1.1	5.4	10
Connection scheme	IPOP	ISOP	IPOS	ISOS	ISOP
Rated power [MW]	5	5	15	15	5
$N_{\mathrm{SM,min}}$ [–]	2	2	6	5	3
Redundant submodule q [–]	1	1	2	2	1
IGBT on primary	1.7 kV	4.5 kV	1.7 kV	1.7 kV	6.5 kV
IGBT on secondary	1.7 kV	1.7 kV	3.3 kV	3.3 kV	1.7 kV
f_{sw} [Hz]	1050	890	850	850	950
$n_{\mathrm{tr,SM}}$ [–]	1.07	2.73	0.55	0.46	3.37
$L_{\mathrm{s,SM}}$ [µH]	21.4	147.0	22.4	18.7	325.8
Volumetric power density [kW/dm^3]	0.78	0.68	0.47	0.46	0.58
Gravimetric power density [kW/kg]	0.88	0.87	0.74	0.73	0.83
Specific cost [€/kW]	158	184	160	141	189

Figure 5.5a illustrates the efficiency map of the DABCS connected in ISOP considered in the DC1a EDS. Additionally, the voltage ratio curves across the DABCS at BoL and EoL of the electrolyzer are depicted for the DC1a case.

The detailed breakdown of the power losses of the DABCS according to the transferred power at BoL and EoL are illustrated in Fig. 5.5b and Fig. 5.5c. It can be seen that the MFT losses and conduction losses remain constant throughout the electrolyzer lifetime, while the primary- and secondary-side switching losses change according to the cell aging. This behavior can be attributed to the impact of the voltage ratio d on switching losses. When $d > 1$, switching losses on the primary side decrease due to reduced turn-off current, while on the secondary side, they increase due to higher turn-off current [190]. Conversely, for $d < 1$ the opposite occurs. As depicted in Fig. 5.5a, the operation mainly occurs below 1 at BoL and gradually shifts towards voltage ratios above 1 throughout the electrolyzer cells lifetime. Consequently, the main share of switching losses transitions from the primary to the secondary side as the cells degrade. As a result, the primary side experiences the highest losses during BoL operation, whereas the secondary side incurs the maximum losses at EoL operation. Since the secondary side employs 1.7 kV IGBT modules, which have inherently lower switching losses than the 4.5 kV IGBT modules on the primary side, the overall losses decrease towards EoL operation, resulting in improved efficiencies than at BoL.

Regarding DC1b variant, the significant voltage variation across the DABCS, as shown in Fig. 5.5d is attributed to the combination of the applied power allocation strategy resulting in power cycling on the electrolyzers and a variable output voltage of the PMSG's rectifier, which remains constant until the output power reaches roughly 25 % of the wind turbine rated power (cf. Fig. 3.6).

Figures 5.5e and 5.5f provide the detailed breakdown of the power losses of the DABCS in

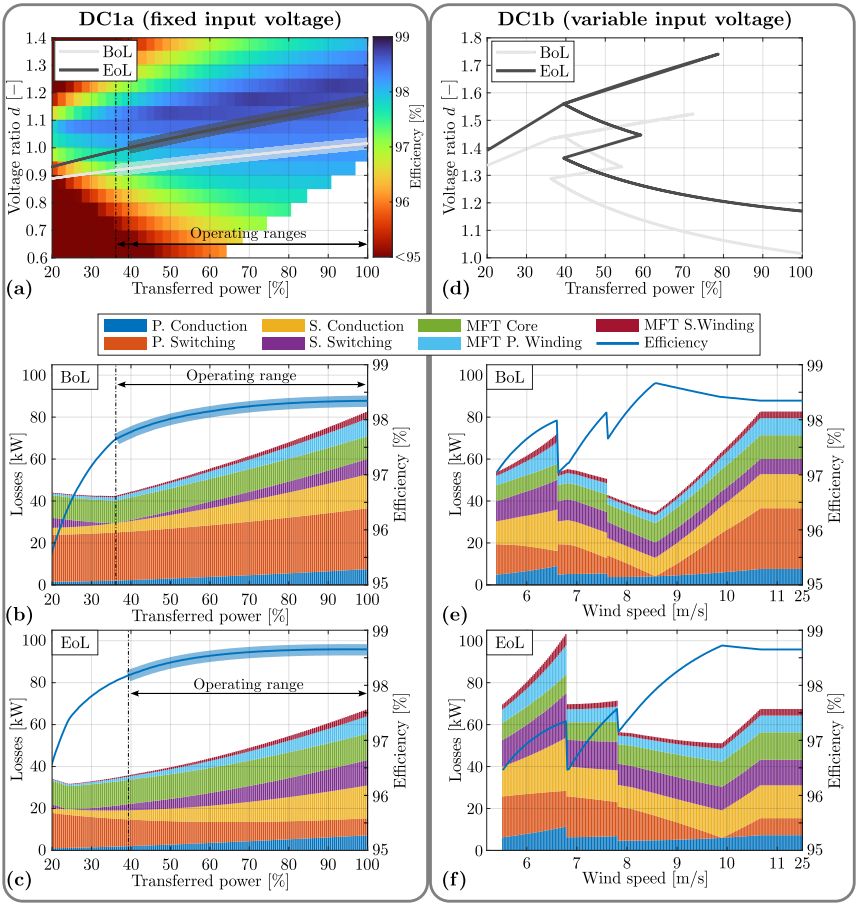


Figure 5.5: (a) DABCS efficiency map for different transferred power and voltage ratio d under SPS modulation, along with the voltage ratio curves of the electrolyzer and corresponding power losses at (b) BoL and (c) EoL operation of the electrolyzer cells in the DC1a configuration. (d) Voltage ratio curve across the DABCS and corresponding power losses at (e) BoL and (f) EoL operation of the electrolyzer cells in the DC1b configuration.

the DC1b EDS, but in this case according to the wind speed, as input voltage is variable and the transferred power is cycled according to the power allocation strategy. While in the DC1a variant, the fixed input voltage of the DABCS results in a relatively constant DABCS efficiency over the operating ranges, remaining above 97.5 % in the operating ranges, the DC1b variant on the contrary results in efficiency as low as 96.5% at low wind speed, with efficiency converging to that of the DC1a variant above the rated wind speed.

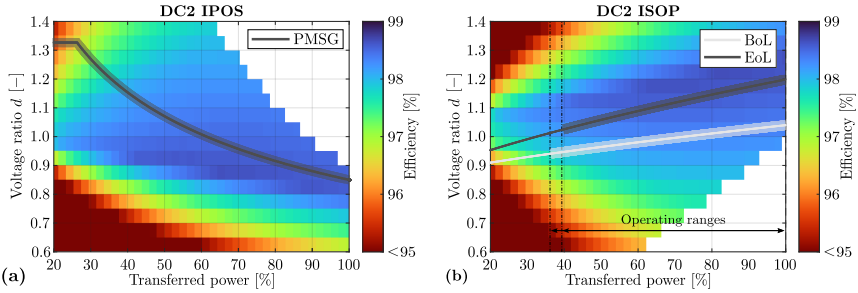


Figure 5.6: Efficiency map along with the respective voltage ratio curves of (a) the IPOS DABCS and (b) of the ISOP DABCS in the DC2 configuration.

The DC2 configuration features two separate DABCSs, one DABCS, connected in IPOS or ISOS based on the PMSG voltage rating, that steps up the variable rectified PMSG voltage to 10 kV and a second one in ISOP connection that steps down the 10 kV to the electrolyzer voltage. Their efficiency maps, along with the voltage ratio curves across the respective DABCSs, are illustrated in Fig. 5.6a and Fig. 5.6b, respectively.

Considering the efficiency curves of each individual component in the EDS, the overall efficiency curve for every configuration can be derived for both BoL and EoL conditions, as shown in Fig. 5.7. The components directly supplying the electrolyzer are influenced by the operational strategies employed. Notably, reducing the number of conversion steps in the DC1 EDS significantly enhances the overall efficiency. Furthermore, most EDS configurations exhibit a relatively flat efficiency plateau above 50 % of the rated load.

To account for the variability of the power source and load conditions during the operation of the plant, the load cycle efficiency (LCE) is computed for each year of the plant lifespan, by weighting the efficiency for all load conditions and the total number of hours per year at each load level, as follows

$$\eta_{\mathrm{LCE}} = \frac{\sum_{i=1}^{u} \eta_{\mathrm{i}} \cdot t_{\mathrm{i}}}{\sum_{i=1}^{u} t_{\mathrm{i}}} \tag{5.2}$$

with u the number of load levels i, η_{i} the efficiency at load level i and t_{i} the total number of hours per year the plant operates at that load level. Based on the efficiency curves presented, the LCE of each component in the distribution system is then yearly determined as shown in Fig. 5.8.

The increase of the cell voltage with aging results in relatively large variation over the years in LCE of the converters directly supplying the electrolyzer. The comparatively lower variation in LCE for the other components is only due to the variation in the minimum load with aging of the cells. While the LCE of AFE rectifier decreases as the cells age due to higher voltage ratio r, the LCE of DABCS connected in ISOP supplying the electrolyzer unit increases as explained by the variation in switching losses from the primary to the secondary side. It should be noted that this effect does not apply for the DABCS connected in IPOP as LV IGBT modules is considered on both sides. In addition, it can be observed that the large variation in voltage ratio d in DC1b results in lower LCE compared to DC1a, especially at EoL of the cells.

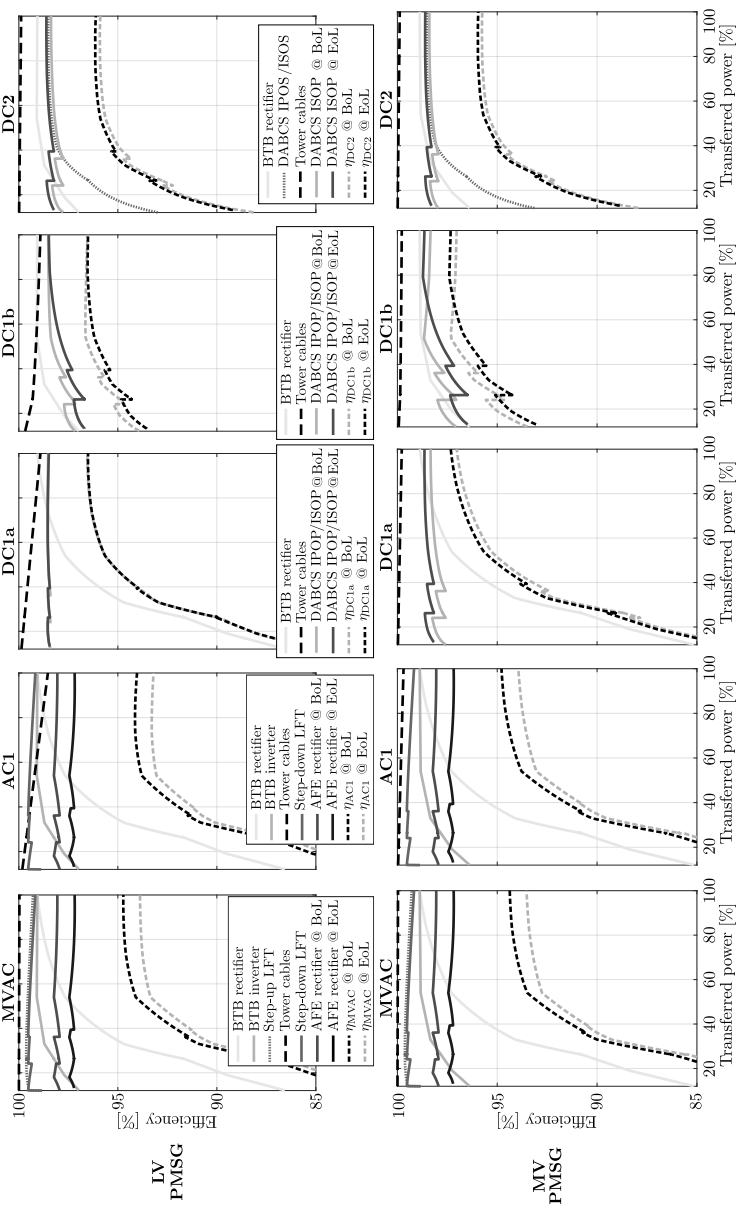


Figure 5.7: Efficiency curves of the different EDS according to transferred power for different PMSG rated voltage.

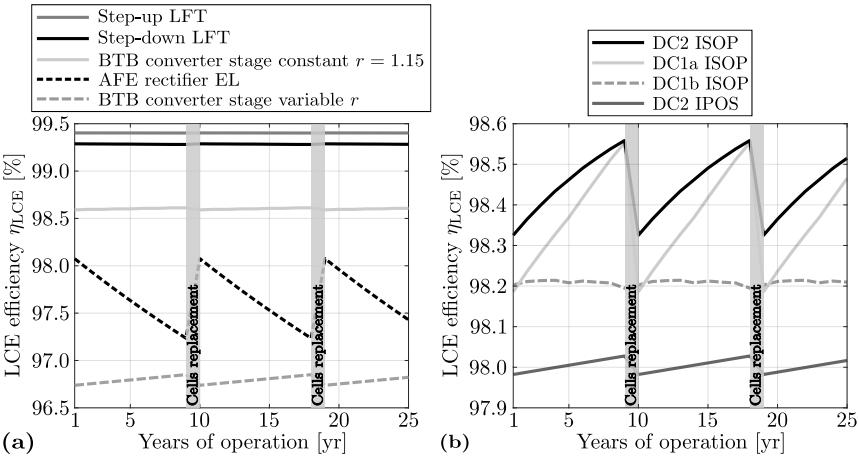


Figure 5.8: LCE variation with year of operation of (a) standard components and (b) DABCS considered in various EDS. Note that in this work, electrolyzer cells are assumed to be replaced with cells of identical performances.

5.2.2 Cost, Volume, Mass and Availability of EDS Components

When comparing different EDS, efficiency is not the only factor to consider. The cost of the EDS, which can be a significant portion of the total cost of a wind-to-hydrogen plant, along with its mass, volume, and availability, are also crucial, especially for offshore applications.

Table 5.4 lists the specific cost, mass, volume, and reliability parameters of the conventional components. For a similar power rating, LV converters have typically lower power density than MV converters due to the need for larger cross section in cables and/or busbars. While the values for standard components follow literature or market prices, the parameters for DABCS are determined in Section 4.2.7 and listed in Table 5.3.

The repair time, often approximated by the mean time to repair (MTTR), of a component includes the time for failure discovery, diagnosis, replacement part acquisition, travel to site and repair completion [210]. The relatively long repair times are often due to the transportation of technicians and equipment to offshore locations, which can be affected by weather conditions, as discussed in Section 2.1.4. The repair time for a DABCS is assumed to be 30 days, similar to that of a wind turbine BTB converter, as commonly assumed in the literature [211].

Table 5.4: Parameters of the Standard Components in the EDS.

Component	Specific cost [€/kW]	Gravimetric p. density [kW/kg]	Volumetric p. density [kW/dm^3]	Failure rate [yr^{-1}]	Repair time [h]
MV BTB converter	180 [213]	1.64 [131]	0.64 [131]	0.37	720
LV BTB converter	120 [213]	0.89 [214]	0.31 [214]	0.37 [201]	720 [211]
Electrolyzer rectifier	60 [213]	1.78	0.62	0.19	720
LFT	18 [213]	0.42 [174]	0.36 [174]	0.025 [204]	3000 [204]

The availability of an EDS component on a period t can be calculated as follows [212]

$$A_{\mathrm{i}}(t) = \frac{\mu_{\mathrm{i}}}{\mu_{\mathrm{i}} + \lambda_{\mathrm{i}}} + \frac{\lambda_{\mathrm{i}}}{\mu_{\mathrm{i}} + \lambda_{\mathrm{i}}} \cdot \exp\left(-\left(\mu_{\mathrm{i}} + \lambda_{\mathrm{i}}\right) \cdot t\right) \tag{5.3}$$

with $\mu_{\mathrm{i}} = 1/\mathrm{MTTR}$ the repair rate and λ_{i} the failure rate per year of the component. The overall availability of the EDS depends on the availability of each individual component between the generator and an electrolyzer unit and is determined by multiplying their respective availabilities as follows

$$A_{\mathrm{EDS}} = \prod_{i=1}^{N} A_{\mathrm{i}} \tag{5.4}$$

with N the number of components within the EDS. Since the three different parallel paths for the three electrolyzer units are assumed to be identical, with similar component failure rates, the expected energy not supplied (EENS) to the three electrolyzer units due to the failure and the repair of each component in the EDS can be approximated by

$$\mathrm{EENS} = \left(1 - A_{\mathrm{EDS}}\right) \cdot 15\ [\mathrm{MW}] \cdot 8760\ [\mathrm{h}] \cdot C_{\mathrm{F,WT}}. \tag{5.5}$$

5.3 LCOH Calculation

The LCOH is widely employed in techno-economic analyses to evaluate the economic viability of electrolysis plants. The LCOH is determined by dividing the expected total lifetime costs incurring during the plant lifetime by the total amount of hydrogen produced during its operational life. For an offshore decentralized wind-to-hydrogen plant, these costs typically include the CapEx and OpEx of both the offshore wind turbine and the electrolysis plant, along with desalination expenses, stack replacement costs and the expense of constructing a pipeline to shore. The annual hydrogen production is estimated based on the wind turbine capacity factor, overall plant availability, and the efficiencies of the electrolyzer units, auxiliaries and the EDS. Since the LCOH calculation takes into account such key performance metrics of the plant, it enables to holistically compare different EDS configurations with only one comprehensive indicator.

The LCOH of the hydrogen collected onshore over the plant lifetime L is computed as

follows [18]

$$\mathrm{LCOH} = \frac{\sum_{n=1}^{L} \frac{C_{\mathrm{plant},n} + O_{\mathrm{plant},n} + R_{\mathrm{stack},n}}{(1+i_r)^n}}{\sum_{n=1}^{L} \frac{M_{\mathrm{H_2},n}}{(1+i_r)^n}} \tag{5.6}$$

with $C_{\mathrm{plant},n}$ the CapEx and $O_{\mathrm{plant},n}$ the OpEx of the wind-to-hydrogen plant in year n respectively, $R_{\mathrm{stack},n}$ the stack replacement costs adjusted in year n and i_r the real interest rate. $M_{\mathrm{H_2},n}$ is the total mass of hydrogen produced in year n and is expressed as,

$$M_{\mathrm{H_2},n} = \frac{P_{\mathrm{WT}} \cdot 8760 \cdot C_{\mathrm{F,plant},n} \cdot A_{\mathrm{EDS}} \cdot \bar{\eta}_{\mathrm{EDS},n}}{\bar{E}_{\mathrm{SEC},n}} \tag{5.7}$$

with P_{WT} the wind turbine electrical rated power (kW), $C_{\mathrm{F,plant},n}$ the capacity factor of the plant in year n (considering minimum load requirement, plant downtime and maintenance window), $\bar{\eta}_{\mathrm{EDS},n}$ the LCE efficiency of the EDS and $\bar{E}_{\mathrm{SEC},n}$ the load cycle SEC of the electrolysis plant (kWh/kg) in year n.

As the power allocation strategy leverages the advantage of the higher efficiency of the electrolysis at partial loads, although the EDSs exhibit lower efficiencies at reduced power levels, the electrolysis plant efficiency combined with the EDS efficiency still results in higher overall efficiencies under partial load conditions, as illustrated in Fig. 5.9a for BoL and Fig. 5.9b for EoL.

Due to the minimum load requirement of the electrolyzer cells, the capacity factor decreases as the cells age, resulting in a capacity factor that is approximately 1 % below the theoretical maximum capacity factor of the wind turbine of 60.5 %, as shown in Fig. 5.9c. The product of the EDS availability and the capacity factor of the plant, gives a representation of the energy delivered to the electrolysis plant according to the EDS employed.

Figure 5.9d shows the annual hydrogen production for each EDS, taking into account the capacity factor, availability, and the combined efficiencies of both the EDS and the plant. Over time, hydrogen production declines by approximately 13 % from BoL to EoL, primarily due to decreases in both electrolysis efficiency and capacity factor. Among the configurations, DC1b achieves the highest hydrogen output, about 9 % more than the MVAC configuration, which yields the lowest production.

Table 5.5 lists all relevant cost parameters employed for the LCOH computation. The CapEx of the wind turbine is based on literature and takes into consideration the estimated costs for studies, commissioning, installation, hardware and decommissioning. The data, adapted from [26], deliberately excludes the costs associated with electrical equipment, grid connection and substation, since these are not required for stand-alone plants.

In [76], a comprehensive overview of the CapEx for the different subsystems of PEM water electrolysis plants of varying sizes in 2020 and 2030 was provided and is shown in Fig. 5.10. The cost breakdown includes the electrolysis stacks, BoS, BoP, water purification, cooling, housing, instrumentation, and engineering. The CapEx breakdowns show that although the cell stack is the most expensive individual component, it does

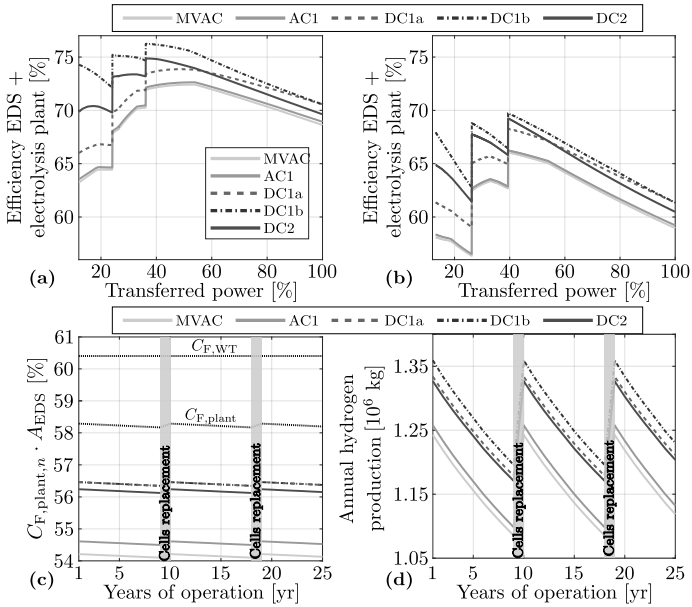


Figure 5.9: Combined efficiency of the EDS and of the electrolysis plant (cells + auxiliaries) at (a) BoL and (b) EoL considering an MV PMSG. (c) Capacity factor and (d) corresponding annual amount of hydrogen produced according to the employed EDS.

not dominate the overall system CapEx. Moreover, as plant size increases, the specific costs for all subsystems decrease due to economies of scale. This reduction is particularly notable for peripheral components such as gas and water purification, BoP, cooling, and instrumentation, which benefit from optimized and centralized configurations in larger plants. Additionally, ongoing technological advancements are expected to further reduce the specific costs of all electrolysis plant subsystems over time.

As the considered electrolysis plant (cf. Fig. 1.6) is made of three electrolyzer units and only one auxiliary unit centralizing the BoP (e.g. water purification, gas treatment, cooling), two separate cost functions are used in this work. The first one approximates the system costs for the equipment specific to the electrolyzer unit, sized at the unit rated power $P_{\mathrm{EL,unit}}$ (kW), while the second one estimates the costs for the centralized equipment sized at the plant rated power $P_{\mathrm{EL,plant}}$ (kW). This approach is likely to be valid for a 15 MW plant, where sharing of BoP equipment is feasible, however, for larger plants, scalability may plateau beyond a certain rating. Additionally, the OpEx for the electrolysis plant, which includes maintenance, repairs and labor, is assumed to be 4 % of the CapEx. The stack replacement cost R_{stack} is assumed as half of the electrolyzer unit CapEx and is dependent on the capacity factor of the plant [215].

Although onshore the weight of an electrolysis plant is usually not critical, offshore installations require additional considerations for support structures, installation, and

Table 5.5: Cost Parameters for the LCOH computation.

Parameters	Value	Unit	Source
Wind turbine CapEx function			
in 2020	2500	€/kW	adapted from [26]
in 2030	2050	€/kW	adapted from [26]
Wind turbine OpEx	2.5 % of CapEx	€/kW	[26]
Electrolyzer unit CapEx function			
in 2020	$827 \cdot {P_{\mathrm{EL,unit}}}^{-0.083}$	€/kW	adapted from [76]
in 2030	$639 \cdot {P_{\mathrm{EL,unit}}}^{-0.092}$	€/kW	adapted from [76]
Auxiliary unit CapEx function			
in 2020	$3188 \cdot {P_{\mathrm{EL,plant}}}^{-0.250}$	€/kW	adapted from [76]
in 2030	$3717 \cdot {P_{\mathrm{EL,plant}}}^{-0.290}$	€/kW	adapted from [76]
Electrolysis plant OpEx	4 % of CapEx	€/kW	[215]
Electrolysis installation cost	41	€/kW	[216]
Water consumption	10	$\mathrm{dm^3/kg_{H_2}}$	[217]
Desalination CapEx	5000	$€/\mathrm{m^3 d}$	adapted from [218]
Desalination requirement	10	$\mathrm{kWh/m^3}$	adapted from [217]
Desalination maintenance costs	2 % of CapEx	$€/\mathrm{m^3 d}$	[217]
Overall auxiliary consumption	1 % of overall plant	kWh	[–]
Electrolyzer unit weight function	$1642 \cdot {P_{\mathrm{EL,unit}}}^{-0.629}$	tons/MW	[219]
Cost adder for offshore weight	10	€/kg	[220]
Cost of pipeline	0.18	$€/\mathrm{kg_{H_2}}$	[27]
Copper cost	9	€/kg	[221]
EDS components OpEx	2 % of CapEx	€/kW	[–]
Yearly maintenance window	7	days	[–]
Interest rate	5	%	[–]
Inflation rate	2	%	[–]
Plant lifetime	25	years	[–]

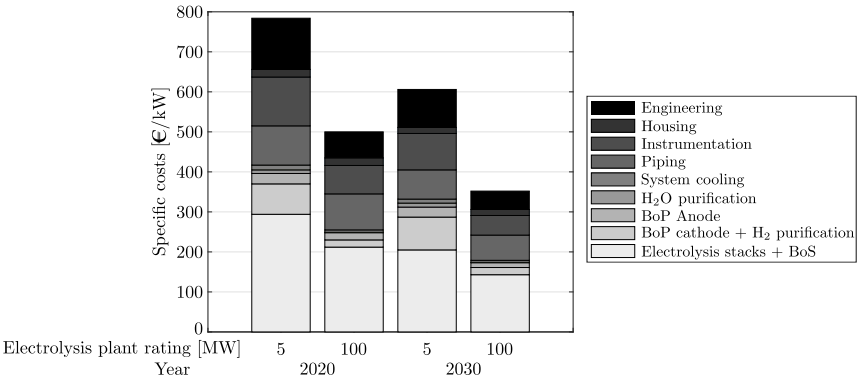


Figure 5.10: Overall PEM electrolysis system cost for different ratings in 2020 and in 2030 adapted from [76].

maintenance logistics. This requires the consideration of the extra mass caused by locating the electrolysis plant on the wind turbine's platform. To address this, a specific

weight function, as listed in Table 5.5, is employed. The weight function captures the weight reductions achieved with larger electrolyzer units, reflecting savings in equipment, piping, and structural steel. Moreover, an additional 15 tons per MW is taken into account for the auxiliary unit, thereby bringing the total weight of the electrolysis plant to approximately 300 tons for the configuration under consideration [219].

The installation, material and maintenance costs incurred by the pipeline for transmission to shore is computed according to the hydrogen output and is no more than 0.18 €/kg_{H_2} as suggested in [27].

After calculating the costs associated with the wind-to-hydrogen plant and determining the hydrogen output, based on power distribution and the EDS efficiency curve, the LCOH for each EDS can be estimated. For instance, in Fig. 5.11 is illustrated the LCOH breakdown for the MVAC EDS when employing an MV PMSG. As can be seen, the wind turbine contributes nearly half of the LCOH, while more than a quarter comes from the electrolysis plant. The combined OpEx of the wind turbine and the electrolysis plant represent the largest share of the LCOH, underscoring the importance of effective offshore maintenance.

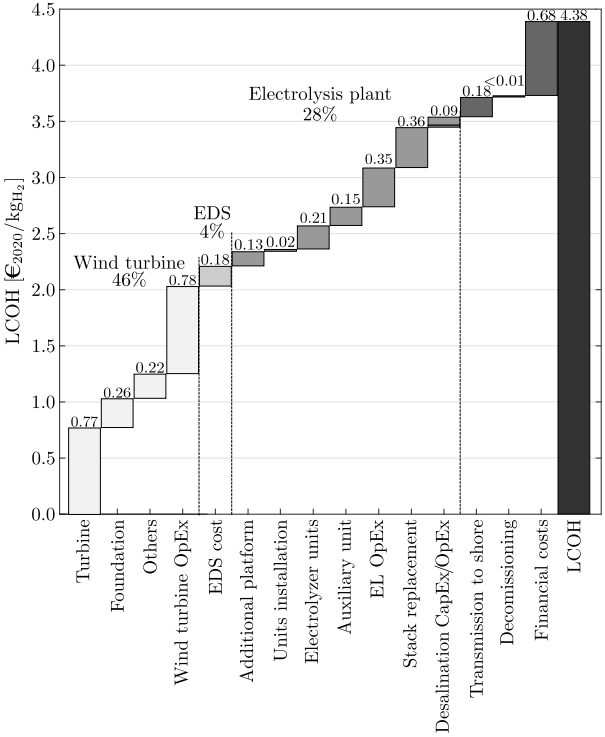


Figure 5.11: Breakdown of the LCOH in the MVAC EDS with costs parameters following 2020 cost functions.

5.4 Comparative Analysis of EDS

Figure 5.12 illustrates the characteristics of the different EDS and the corresponding LCCA results, depending on whether an LV or an MV PMSG is employed. The losses are determined by averaging the LCE over the plant's lifetime and the LCOH is estimated using cost functions that reflect 2020 cost levels.

Due to the high number of conversion steps, the MVAC configuration results in an unavailability in a year of 6.1 % and EDS losses ranging from 7.6 % to 8.3 %, depending on the rated voltage of the PMSG. Removing the step-up LFT in the nacelle, as done in the AC1 EDS, yields different outcomes based on the PMSG voltage.

For an LV PMSG:

- the elimination of the step-up LFT increases conduction losses in the tower cables (+1.1 % compared to the MVAC configuration) due to the relatively low distribution voltage. These additional losses counterbalance the savings gained from removing the step-up LFT losses, resulting in overall higher losses than the MVAC EDS,
- the removal of the LFT results in an overall mass increase due to the substantial mass of copper required for the tower cables,
- consequently, the LCOH is increased by 0.7 % compared to the MVAC configuration with the same PMSG voltage class.

Conversely, for an MV PMSG:

- the efficiency gain achieved by removing the step-up LFT is maintained due to the relatively high 3.3 kV distribution voltage, resulting in overall losses of 7.9 %,
- the removal of such a bulky and heavy component significantly reduces the weight (-30 %) and space requirements (-31 %) of the distribution system,
- as a result, the LCOH is reduced by 1.1 % compared to the MVAC configuration.

The reduced number of conversion steps in the DC1 EDS, achieved by removing the AC stages, leads to the lowest losses and unavailability among all EDSs, regardless of the rated voltage of the PMSG. Although using a DC distribution system reduces copper utilization compared to the AC1 configuration, both the DC1a and DC1b variants still exhibit relatively high conduction losses in the tower cables when a LV PMSG is employed. The constant DC input voltage of the DABCS in the DC1a EDS yields lower DABCS losses than in the DC1b variant (1.5 % versus 1.8 %). However, in the DC1b configuration, the variable DC link voltage operation despite causing slightly higher conduction losses in the tower cables (1.0 % in DC1b versus 0.8 % in DC1a), substantially reduces losses in the BTB rectifier. This results in lower overall EDS losses compared to the DC1a variant (3.4 % versus 5.0 % when an MV PMSG is used).

Moreover, the DC1 configuration has the lowest weight requirement of all EDSs (-68 % compared to the MVAC configuration with a MV PMSG). The combination of the highest efficiency and availability makes the DC1b configuration the most competitive in terms

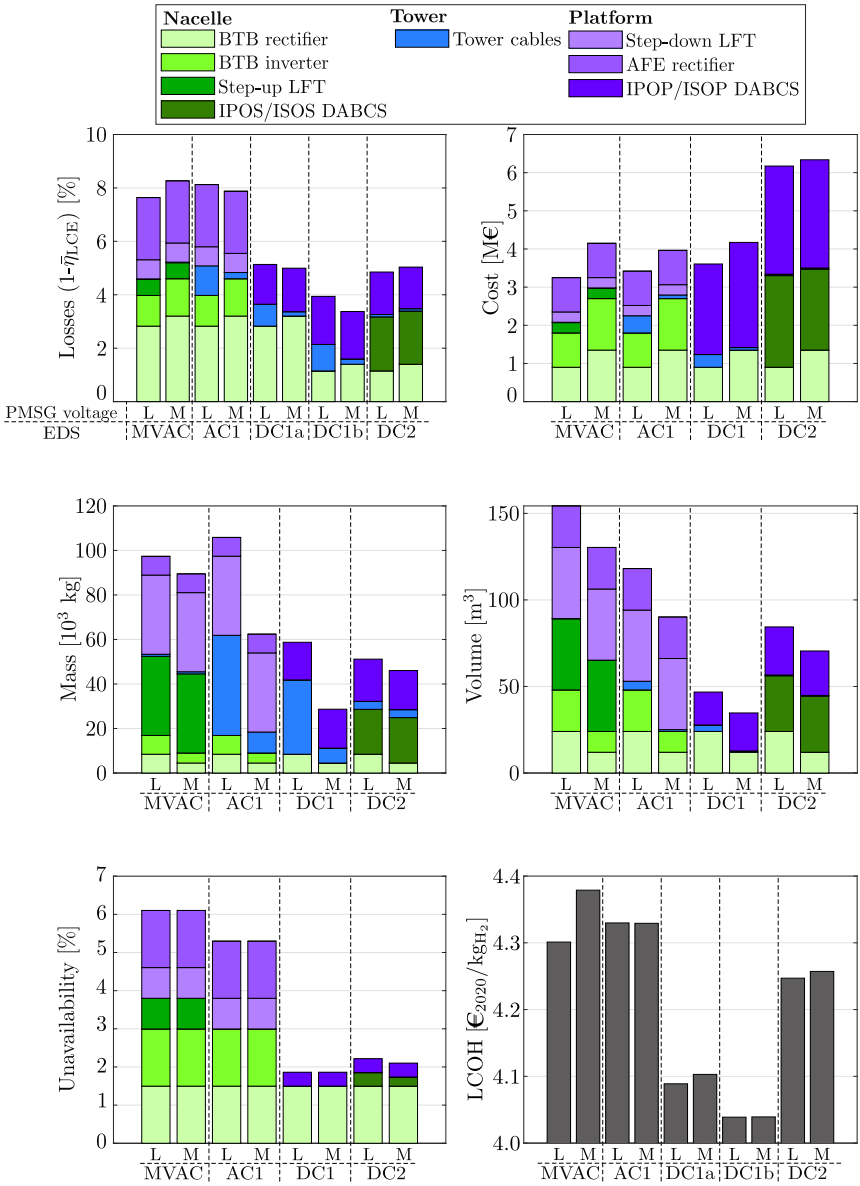


Figure 5.12: Results of the comparative analysis of the different EDSs according to whether an LV (L) or an MV (M) PMSG is employed.

of LCOH (-7.7 % lower than the MVAC configuration).

In the DC2 configuration, the addition of a step-up IPOS or ISOS DABCS in the nacelle, according to the PMSG rated voltage, enables the segmentation of the voltage conversion across the nacelle and platform DABCSs, leading to lower losses per DABCS. The higher DC distribution voltage reduces copper usage and losses in the tower cables. However, the higher number of conversion stages leads to higher losses and unavailability than for the DC1 configuration and results in the most expensive option among EDSs. Ultimately, for stand-alone wind-to-hydrogen plants where the distance between the PMSG and the electrolyzer units is relatively short, the DC2 configuration is not competitive in terms of LCOH.

Overall, the DC1b variant stands out as the most competitive EDS thanks to a combination of a low number of conversion steps and a variable DC-link voltage. Given the minimal difference in LCOH between LV and MV PMSG configurations, the DC1b variant with the MV option is preferred due to its significantly lower copper requirements for the tower cables. Moreover, this configuration occupies a volume of only about 20 m^3 on the platform, potentially fitting into a 20 ft container.

6 Comprehensive Parametric Analysis

This chapter aims to explore the impact of a wide range of parameters on plant performance by focusing on the LCOH of the DC1b configuration employing an MV PMSG. As demonstrated in the previous section, this configuration is expected to be the most competitive, achieving an estimated LCOH of 4.04 $€_{2020}/kg_{H_2}$ under the assumptions used in the LCCA. In the following, firstly, a sensitivity analysis is carried out to investigate the relative importance of the parameters considered in the hydrogen production cost calculation. The sensitivity analysis is widely used in techno-economic analysis because it shows how sensitive the results of a model are to changes in the input parameters, helping decision-makers to identify key parameters. Next, an in-depth analysis of various approaches to enhance the efficiency of the DABCS is performed. Finally, an optimization study is conducted to assess the electrolysis plant modularity and sizing relative to the wind turbine rated power. This aims to identify an optimal sizing of the plant configuration by thoroughly assessing both energetic and economic aspects of the plant.

6.1 Sensitivity Analysis

The sensitivity analysis is performed by increasing and decreasing each parameter by 20 % from its baseline value while holding all other variables constant. For every case, the complete LCCA, as shown in Fig. 5.1, is computed, resulting in a potential different DABCS design to better align with the plant conditions if required.

6.1.1 Economical Parameters

First, the sensitivity analysis examines economic parameters, such as project lifetime and the CapEx of both the wind turbine and the electrolysis plant. Hydrogen production costs are determined by aggregating the CapEx associated with each individual component. Given that wind-to-hydrogen plants are not yet mature, these cost parameters are subject to significant uncertainties.

Figure 6.1 shows the sensitivity of the LCOH to variations in the considered CapEx for the offshore wind turbine, the electrolysis plant and the EDS. Reductions in the cost of offshore wind turbines offer the greatest potential for lowering the LCOH. This can be explained by Fig. 5.11, since the wind turbine represents one of the larger shares of the LCOH. For instance, a 20 % reduction in wind turbine cost would decrease the LCOH by 11.6 %. In contrast, changes in the CapEx of the electrolysis plant and the EDS have a

relatively smaller effect on the LCOH. These results are expected due to the mentioned elements having a smaller cost contribution to the LCOH.

Assuming cost functions that estimate CapEx for 2030 results in a reduction in the specific cost of the wind turbine (-18 % compared to 2020 specific cost cf. Table 5.5) as well as a lower average specific cost of the electrolysis plant from 700 €/kW to 520 €/kW (-26%). This lowers the LCOH to 3.34 $€_{2030}/kg_{H_2}$, i.e. 17 % lower than if 2020 cost functions are used. Note that this does not include potential improvements in cell or EDS efficiency, or wind turbine power coefficient that may result from further technological advancements.

Lastly, the plant lifetime is a key parameter in determining the LCOH because it not only defines the period over which costs are amortized but also extends the operational duration, enabling the same equipment to produce more hydrogen over time. Operating the plant 20 % longer than the considered 25 years, decreases the LCOH by 6 %, while decreasing the plant lifetime by 20 % increases the LCOH by 9 %. This nonlinearity arises because the LCOH calculations spread costs over time and discount future values. Extending the plant's lifetime means that later costs (discounted more heavily) are spread out and the fixed, front-loaded CapEx are amortized over more years. In contrast, a shorter lifetime concentrates those front-loaded CapEx into fewer years, sharply increasing the annualized expenses.

6.1.2 Plant Conditions

Besides the uncertainties associated with investment costs for offshore hydrogen plants, several other factors can significantly influence the LCOH. By varying these parameters, designers can better identify key areas where targeted improvements will yield the greatest benefits.

Definition of EoL of the Cells

In the previous chapters of this work, the cells were assumed to have reached their EoL when their efficiency at rated load decreased by 10 % relative to their initial value. However, the allowable maximum degradation level can significantly affect the plant conditions. The lower efficiency at EoL results in a higher maximum electrolyzer voltage and an increase in the amount of heat to be dissipated, consequently requiring larger cooling systems, as outlined in Section 2.2.1.

For instance, an increase in the permissible efficiency reduction by 20 %, i.e. resulting in a BoL to EoL efficiency delta of 12 %, yields an EoL voltage of 1200 V at rated load. This higher voltage enables the continued use of LV devices, such as the 1.7 kV IGBT module on the secondary side of the DABCS. Under these conditions, the cell lifetime extends to 93000 operating hours and the LCOH is reduced by 0.7 %. Conversely, if the permissible EoL efficiency is only 8 % from the efficiency at BoL, the cell lifetime falls to 55000 hours and the LCOH increases by 1.9 %. Note that these calculations do not account for potential variations in the BoP CapEx that might arise from changes in the heat dissipation requirements.

Cell Degradation Rate

The degradation rate of the electrolyzer is a crucial factor, especially for offshore applications. A higher degradation rate means more frequent replacement of electrolyzer cells, leading to increased overall CapEx and maintenance costs. Conversely, a slower degradation rate extends the cells lifespan before replacement is needed. For instance, increasing the degradation rate by 20 % results in a cell lifetime of approximately 55000 operating hours, requiring three replacements over 25 years of operation and raises the LCOH by 2.7 %. On the other hand, decreasing the degradation rate by 20 % extends the cell lifetime to roughly 85000 operating hours, necessitating only two replacements during the plant lifetime and reduces the LCOH by 2.0 %.

Plant Capacity Factor

Hydrogen production is directly affected by the plant capacity factor, which largely depends on the average wind speed at the turbine site. For example, if the average wind speed increases by 20 % over the base case of 10 m/s, the wind turbine operates at its rated load 60 % of the time (producing 77 % of the hydrogen at rated capacity), yielding a plant capacity factor of 74 %. This results in a higher average load on the electrolyzer units and a 29 % increase in hydrogen production over the plant's lifetime, which in turn reduces the LCOH by 18 %. However, operating at this higher load also leads to more frequent cell replacements and higher SEC of the cells. Conversely, if the average wind speed drops by 20 % from the base case to 8 m/s, the turbine operates more often at partial load, only 25 % of the time at rated capacity (producing just 54 % of the hydrogen at rated load), yielding a plant capacity factor of 43 %. This scenario results in a

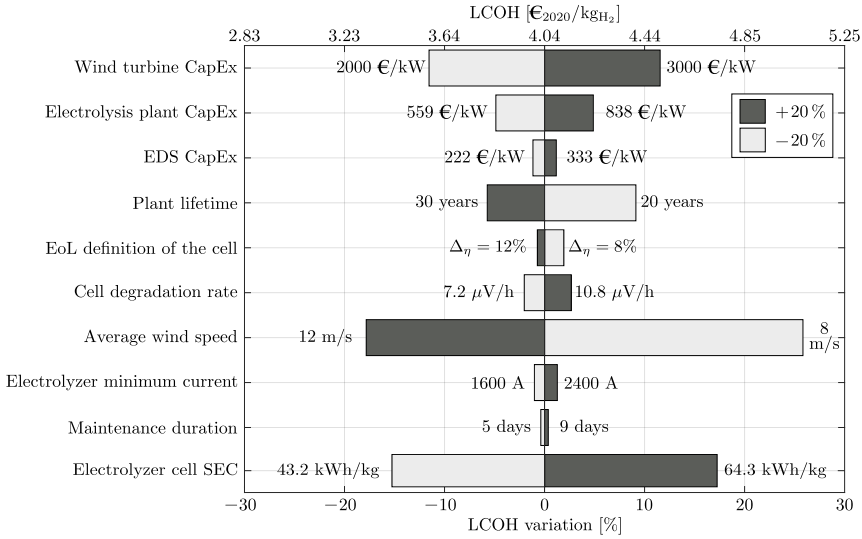


Figure 6.1: Tornado chart illustrating the variation in LCOH when key parameters are increased or decreased by 20 %.

24 % decrease in hydrogen production over the plant's lifetime and a 26 % increase in the LCOH, despite the reduced load extending cell lifetime and lowering SEC. Generally, higher wind speeds can be obtained by locating the plant farther offshore, but there is also an increase in deployment, maintenance and transmission costs as the distance from the shore increases and should be considered. Nevertheless, the significant variation in LCOH with wind speeds underscores the importance of accurately estimating the capacity factor at the start of a project.

Another key factor affecting the plant capacity factor is the minimum allowable operating current of the electrolyzer cell. For example, reducing the minimum current density requirement by 20 % from its base value of 0.80 to 0.64 A/cm², lowers the minimum load to 1.4 MW. With this lower load requirement, the wind turbine can supply power to the electrolyzer unit at lower wind speeds, increasing the plant's capacity factor by 0.3 percentage points to 57.7 %. Over the plant's lifetime, this adjustment results in about 1 % higher hydrogen production and a 1.0 % reduction in LCOH. Conversely, if the minimum current density requirement is increased by 20 %, to 0.93 A/cm², the minimum load raises to 2.2 MW, which reduces the capacity factor to 57.3 % and ultimately leads to a 1.3 % higher LCOH.

The plant capacity factor is also affected by downtime due to maintenance windows. However, this impact is relatively minor as an increase in downtime by 20 % results in only a 0.4 % rise in the LCOH.

Another parameter affecting the plant's capacity factor is the availability of the EDS. For example, in the DC1b EDS, the DABCS incorporates one extra redundant submodule to ensure a reliability in a year above 95 %. While this additional submodule enhances availability, it also increases costs and reduces the power density of the converter. Figure 6.2 illustrates how the DABCS specific cost, reliability in a year and LCOH vary according to the additionally installed converter power for the various DABCS configurations listed in Table 4.3 that employ different IGBT modules on the primary side. For configuration with LV devices, the combination of a relatively high number of submodules results in a high specific cost and a low reliability without redundancy. An optimal LCOH is obtained by adding between one and two redundant submodules depending on $N_{\mathrm{SM,min}}$. In contrast, DABCS with a low number of submodules, i.e. employing HV devices on the primary side, already have a relatively high reliability without redundant submodules, making it unnecessary in terms of LCOH to require additional redundant submodules. Figure 6.2 confirms that, for this plant, using the fewest number of submodules in the DABCS is the most optimal configuration as it achieves an LCOH that is approximately 5 % lower than that of a DABCS with a high submodule count, e.g. the one using 1.2 kV IGBT modules on the primary side.

Electrolyzer Cell Efficiency

Another important parameter of the plant is the electrolyzer cell efficiency, since it has a direct impact on the amount of hydrogen produced. For instance, as shown in Fig. 6.3, if the cell specific consumption energy decreases by 20 % from 53.7 kWh/kg at rated load at BoL to 43.2 kWh/kg, the electrolyzer voltage will be lower, specifically 800 V at BoL and 970 V at EoL at rated load. The improved cell efficiency leads to a 20 % increase in hydrogen production over the plant lifetime, which in turn lowers the LCOH by 15 %.

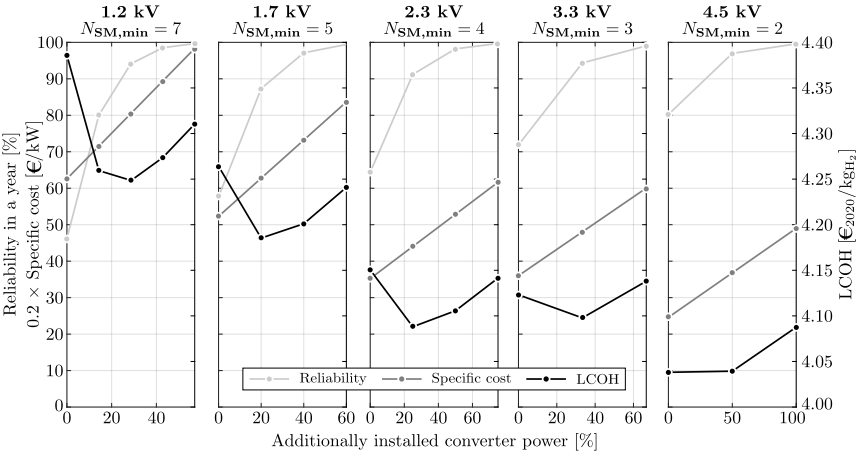


Figure 6.2: DABCS specific cost, reliability in a year and LCOH according to the additionally installed converter power for DABCS configurations employing different IGBT modules on the primary side. Note that the specific cost is scaled by a factor 0.2 for better visibility.

Conversely, if the cell SEC increases by 20 % to 64.3 kWh/kg at BoL at rated load, the electrolyzer voltage rises to 1200 V at BoL and 1350 V at EoL at rated load, increasing the LCOH by 17 %. Note that the higher electrolyzer voltage at EoL restricts the use of LV devices on the secondary side of the DABCS. Therefore, an optimal converter configuration is determined by employing a minimum of two submodules ($N_{SM,min}$ = 2) composed of the 4.5 kV IGBT module on the primary side and the 3.3 kV IGBT module on the secondary side. Due to the higher inherent switching losses of the 3.3 kV device, the converter is designed at a lower switching frequency of 550 Hz to achieve a DABCS efficiency of 98.5 % at rated load.

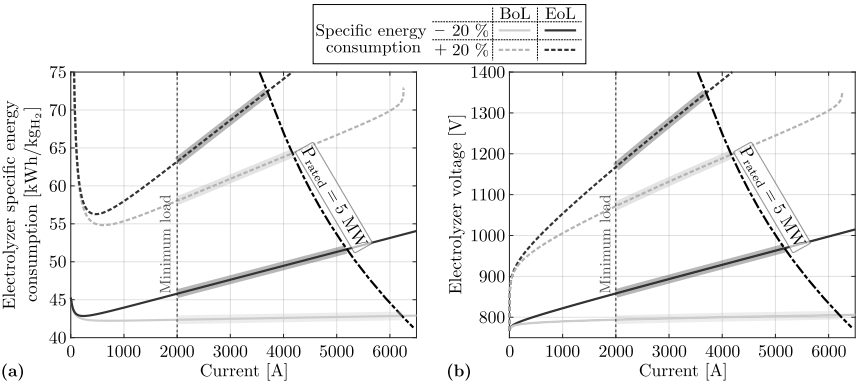


Figure 6.3: (a) Electrolyzer SEC and (b) corresponding polarization curves at BoL and EoL for ± 20 % variation in SEC of the cells.

6.2 DABCS Efficiency

The amount of hydrogen produced is directly affected by the efficiency of the conversion process between the PMSG terminals and the hydrogen output. The DABCS is an integral element of the EDS in the wind-to-hydrogen conversion chain and can significantly impact the LCOH. So far in this work, a DABCS efficiency of 98.5 % at rated load at the MoL of the cells has been considered. However, higher DABCS efficiencies are feasible and are explored in the following.

6.2.1 Operation at Lower Switching Frequencies

One approach is to design and operate the DABCS at a lower switching frequency. In this analysis, the same configuration, i.e. two submodules with one additional redundant submodule composed of the 4.5 kV IGBT module on the primary side and the 1.7 kV IGBT module on the secondary side, is investigated across a range of switching frequencies. The methodology introduced in Fig. 4.2 is repeated for various switching frequencies below 890 Hz. As shown in Fig. 6.4a, reducing the switching frequency decreases the transformer losses and even more notably the switching losses of the semiconductors. The decrease in transformer losses can be attributed to the transformer designs maintaining the same peak flux density across frequencies, which requires larger core sizes at lower switching frequencies, thereby reducing core losses. Consequently, the overall efficiency of the DABCS at rated load under MoL of the cells improves with a lower switching frequency. However, operating at a lower switching frequency requires larger passive components, e.g. a larger transformer due to increased magnetic flux and higher series inductance requirements. This, in turn, increases material usage and results in a more expensive converter. As depicted in Fig. 6.4b, the three DABCSs can tolerate a switching frequency reduction to approximately 800 Hz if housed in a 20 ft container, or even down to 300 Hz when housed in a 40 ft container. Because lowering the switching frequency simultaneously leads to enhanced efficiency, reduced power density and increased cost, an

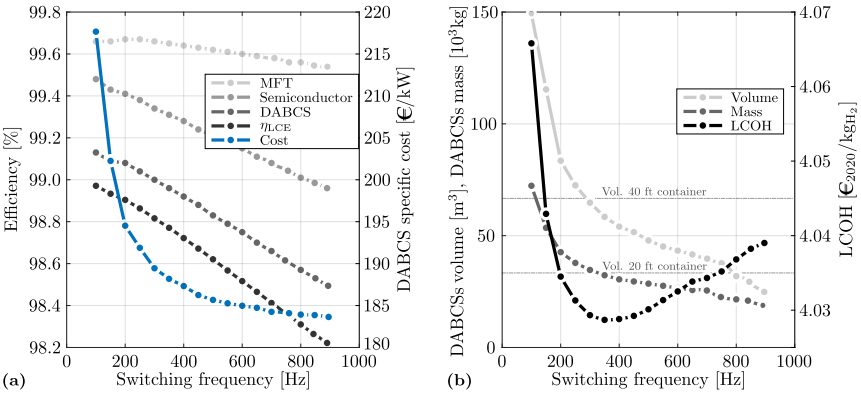


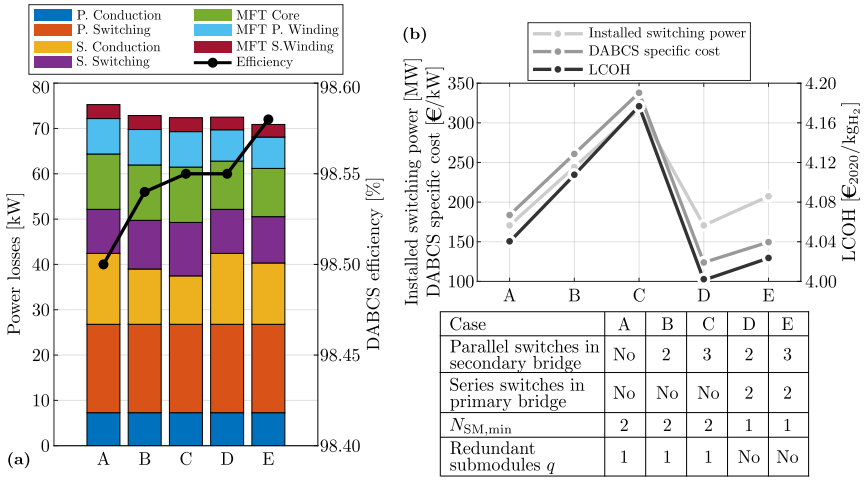
Figure 6.4: (a) MFT, semiconductor and DABCS efficiency at rated load MoL of the cells, DABCS LCE and specific cost according to the switching frequency. (b) Corresponding DABCSs volume and mass, and LCOH according to the switching frequency.

optimum in terms of LCOH is reached at a switching frequency of 350 Hz. Nevertheless, the LCOH is reduced by only 0.3 % compared to the base switching frequency of 890 Hz. Given this marginal improvement and the increased volume requirements, reducing the switching frequency should not be justified, especially since at this reduced frequency the three DABCSs cannot fit within a 20 ft container and would require more space on the platform.

6.2.2 Parallel and Series Connection of Semiconductors

Another way to enhance the efficiency of the DABCS is by increasing the amount of silicon employed in the DABCS. In this analysis, the employment of the 4.5 kV IGBT module on the primary side and the 1.7 kV IGBT module on the secondary side is again considered. As shown in Fig. 6.5a, paralleling two IGBT modules on the secondary side (case B) lowers overall power losses, by reducing the secondary-side conduction losses, even though it increases switching losses compared to case A. Extending this approach to three parallel IGBT modules on the secondary side (case C) further reduces conduction losses. However, as shown in Fig. 6.5b, the additional semiconductors lead to a higher installed switching power and increased specific cost. The efficiency gains do not offset the increased converter cost, ultimately raising the LCOH.

Additionally, the IGBT modules can be connected in series within the primary side bridges (case D). This configuration requires only a single DAB submodule sized for the rated load. The use of one MFT enhances efficiency and reduces material usage, thereby lowering the specific cost of the DABCS. When no redundant submodules are used, this method lowers the LCOH by 1.0 % compared to base case A. If in addition three parallel IGBTs on the secondary side are employed (case E), the specific cost increases and the



Case	A	B	C	D	E
Parallel switches in secondary bridge	No	2	3	2	3
Series switches in primary bridge	No	No	No	2	2
$N_{\mathrm{SM,min}}$	2	2	2	1	1
Redundant submodules q	1	1	1	No	No

Figure 6.5: (a) DABCS power losses at rated load at MoL of the electrolyzer and (b) DABCS installed switching power, specific cost and LCOH according to the different cases of IGBT modules connection in the DABCS brigdes.

reduced power losses are insufficient to counterbalance, leading to a higher LCOH overall. Although case D appears promising in terms of efficiency and cost, the combined parallel and series connections introduces additional complexity that may increase the failure rate of the submodule.

6.2.3 Employment of Wide-Bandgap Semiconductors

The last approach investigated in this work to improve the DABCS efficiency is the use of wide bandgap devices. For example, silicon carbide (SiC) metal oxide semiconductor field-effect transistors (MOSFET) offer numerous advantages over conventional silicon (Si)-based devices. Due to their higher critical electric fields, SiC devices can have thinner and more highly doped voltage-blocking layers, resulting in reduced on-resistance compared to their Si counterparts. The smaller form factor leads to lower device capacitances and combined with higher electron mobility, faster switching speeds are possible, ultimately resulting in lower switching losses compared to Si devices.

The potential benefits of integrating SiC devices into the ISOP configuration are investigated in the following. Specifically, two different SiC MOSFET devices from Infineon, as listed in Table 6.1, are evaluated. The same methodology, illustrated in Fig. 4.2, that was applied previously with IGBT modules is now repeated with the two additional SiC MOSFETs at a switching frequency of 890 Hz.

Figure 6.6 shows that, at this relatively low switching frequency, the employment of SiC devices on both sides of the DABCS without parallelizing several modules does not provide significant improvements in semiconductor efficiency compared to configurations using IGBT modules. This is primarily because, despite exhibiting relatively low switching losses, the SiC MOSFETs have higher on-state voltages at the device-rated current (cf. Appendix A). For instance, the 2.3 kV SiC device should operate below a drain current of approximately 1000 A to maintain a lower on-state voltage than a comparable IGBT, while the 3.3 kV SiC device should operate roughly below 400 A to achieve a similar on-state voltage than the 3.3 kV IGBT module.

To fully leverage the advantages of SiC devices it would require operating at higher switching frequencies. In DABCS configuration employing SiC devices, switching losses are less sensitive to frequency increases than in those based on IGBT modules. This would potentially allow denser designs with reduced material usage while only marginally increasing switching losses. However, as shown in Fig 6.4a, although the specific cost drops significantly between 100 and 600 Hz, little additional cost reduction is achieved at even higher frequencies. In addition, the higher switching frequency would not result in higher DABCS efficiencies, which is the primary objective of this section.

Table 6.1: Commercially Available SiC MOSFET Modules Considered.

Description	DC voltage [V]	Current ratings [A]	Thermal resistance [K/kW]
2.3 kV SiC (FF1000UXTR23T2M1)	1500	2000	37.6
3.3 kV SiC (FF2000UXTR33T2M1)	2100	1000	47.8

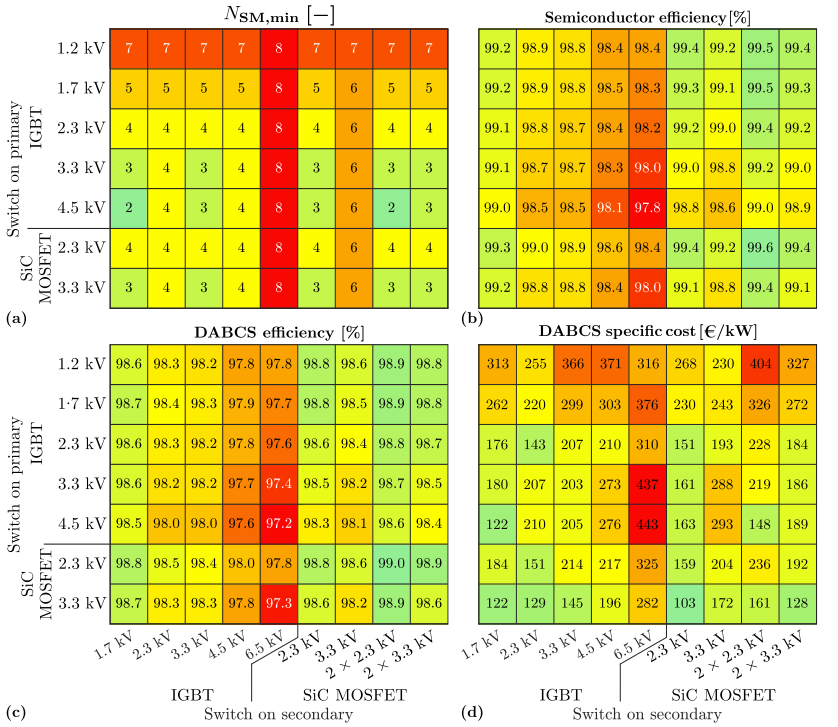


Figure 6.6: DABCS (a) minimum number of submodules employed (b) semiconductor efficiency (c) overall efficiency at MoL and (d) specific cost at a switching frequency of 890 Hz according to the switching devices employed on the primary and secondary side. Note that the specific cost here does not consider the use of redundant submodules.

Thus, at this relatively low switching frequency of 890 Hz, SiC MOSFET modules should be parallelized within bridges to leverage their advantages. For instance, parallelizing two SiC MOSFET modules on the secondary side reduces conduction losses, thereby improving semiconductor efficiency as illustrated in Fig. 6.6. Moreover, parallelizing the 3.3 kV SiC MOSFET on the secondary side enables a reduction in the number of modules in the ISOP connection from six to three, which in turn, lowers the number of MFTs and the specific cost of the converter. Table 6.2 summarizes several DABCS configurations that achieve higher converter efficiencies than full IGBT-based DABCS. Some configurations (F and G) combine IGBT with SiC MOSFET modules (hybrid setup), while others (H, I, J, K) are fully based on SiC MOSFET modules.

As discuss previously, each configuration has an optimal redundant submodule count. A similar analysis is conducted for the configurations listed in Table 6.2, assuming that SiC MOSFET modules have a failure rate equivalent to that of IGBT modules and that the same cost function (4.20) applies irrespective of the semiconductor technology. The results illustrated in Fig. 6.7 indicate that, for all considered configurations, employing a single redundant submodule minimizes LCOH, by striking an optimal balance between

availability and converter cost. Figure 6.7 also shows that, although fully SiC-based configurations with multiple parallelized SiC MOSFETs on the secondary (configuration J and K) achieve higher efficiencies, the increased number of semiconductor and the associated high installed switching power lead to a higher LCOH compared to other designs. Configurations G and I perform the best primarly because they employ semiconductor devices that minimize semiconductor oversizing in respect to the electrical requirements of the application and simultaneously require fewer number of submodules, both of which contribute to lowering the DABCS specific cost. The most optimal configuration appears to be configuration I, namely using a full SiC MOSFET-based arrangement using the 3.3 kV SiC MOSFET module on the primary side and the 2.3 kV SiC MOSFET module on the secondary side. This configuration then achieves an LCOH reduction of 0.9 % relative to the base configuration employing 4.5 kV IGBT modules on the primary side and 1.7 kV IGBT modules on the secondary side without redundant submodules (see Fig. 6.2).

Table 6.2: DABCS Configuration Variants Employing SiC MOSFET Modules.

Configuration	**Switch on on primary**	**Switch on on secondary**	$N_{\mathbf{SM,min}}$ [–]	**Semiconductor efficiency** [%]	**DABCS efficiency** [%]
F	2.3 kV SiC	1.7 kV IGBT	4	99.3	98.8
G	3.3 kV SiC	1.7 kV IGBT	3	99.2	98.7
H	2.3 kV SiC	2.3 kV SiC	4	99.4	98.8
I	3.3 kV SiC	2.3 kV SiC	3	99.1	98.6
J	2.3 kV SiC	2 × 2.3 kV SiC	4	99.6	99.0
K	3.3 kV SiC	2 × 2.3 kV SiC	3	99.4	98.9

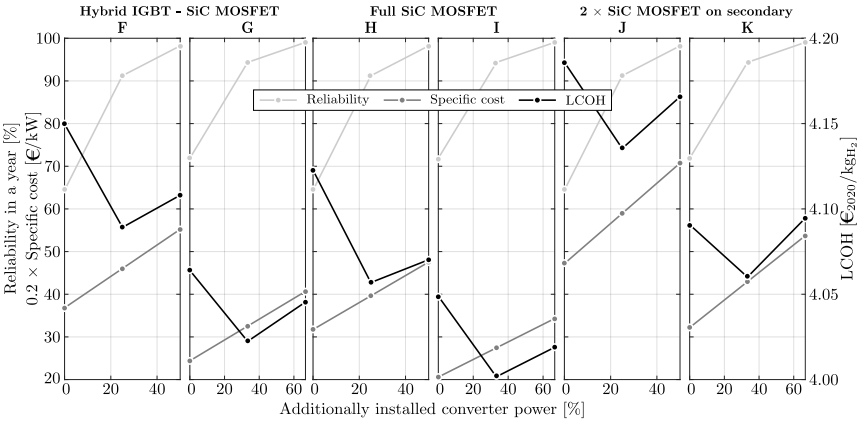


Figure 6.7: DABCS specific cost, reliability in a year and LCOH according to the additionally installed converter power for the different DABCS configurations.

6.3 Plant Sizing Optimization[1]

In this work, three electrolyzer units of 5 MW have been considered for the electrolysis plant configuration. However, the sizing of the electrolysis plant according to the rated power of the wind turbine and the modularity of the plant can significantly impact several key factors. Therefore, a thorough optimization is performed in the following to determine the optimal sizing and modularity of the plant by assessing both energetic and economic aspects.

The ratio k_{size} is defined as the ratio of the rated power of the electrolysis plant $P_{\text{EL, plant}}$ to the rated power of the wind turbine P_{WT}. An undersized electrolysis plant relative to the wind turbine rated power is represented by $k_{\text{size}} < 1$, while an oversized plant is represented by $k_{\text{size}} > 1$. The plant's modularity is expressed by the number of independent electrolyzer units N_{units} within the plant. Increasing N_{units} means that the overall capacity is distributed among a greater number of lower-rated units. The variation in the electrolyzer unit rated power can be achieved in two ways:

1. By varying only the number of cells in series per electrolyzer unit.
   Here, the cell area and operating conditions remain constant while the number of cells in series is reduced. This approach lowers the rated voltage of the unit without affecting the current. For instance, an electrolysis plant of 15 MW and $N_{\text{units}} = 3$ has an electrolyzer unit rated voltage of 1000 V at BoL, whereas for $N_{\text{units}} = 5$, the rated voltage is reduced to 600 V, while the rated current remains at 5000 A at BoL.

2. By varying only the cell area while keeping all other parameters identical.
   This approach maintains the unit rated voltage but reduces the rated current. For instance, for $N_{\text{units}} = 5$ and $k_{\text{size}} = 1$, the unit rated voltage remains at 1000 V but the rated current is reduced to 3000 A at BoL.

Option 1 imposes more stringent requirements on the electrolyzer power supply (specifically the DABCSs in the DC1 EDS) as N_{units} increases. With more electrolyzer units carrying the same current, there is a significant increase in DABCSs semiconductor conduction losses and MFT winding losses. Additionally, when N_{units} is low (e.g., 1 or 2), having many cells in series per unit may result in a voltage that exceeds the 1500 V DC threshold of the LV class. In contrast, while option 2 may also experience increased challenges with higher modularity due to more components, this effect is less severe because the current per unit decreases as more units are added. For these reasons, option 2 is adopted for the variation in modularity in this analysis.

6.3.1 Plant Capacity Factor

As illustrated in Fig. 6.8a, an undersized plant, i.e. $k_{\text{size}} < 1$, exhibits a lower minimum operating load, which allows hydrogen production to start at lower wind speeds. Nevertheless, as the wind turbine has to operate below its rated power, the potential hydrogen output is significantly reduced, adversely affecting the plant capacity factor. Conversely, an oversized plant, i.e. $k_{\text{size}} > 1$, can on one side capture the wind turbine rated power

[1] Parts of this section have been published in Runser *et al.* [222]

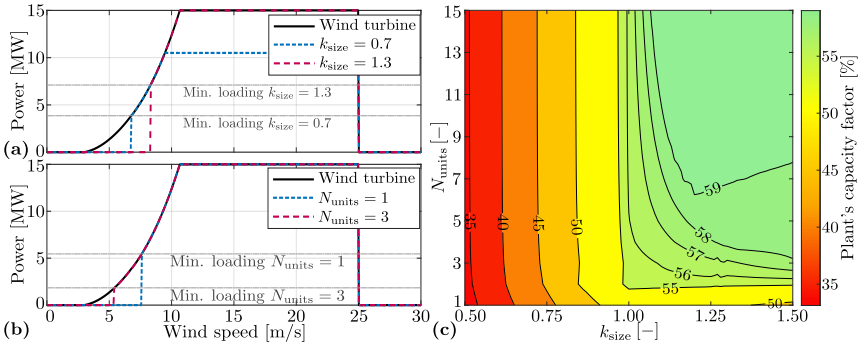


Figure 6.8: (a) Power curves for $N_{\text{units}} = 1$ of the wind turbine along with a 30 % oversized ($k_{\text{size}} = 1.3$) and a 30 % undersized ($k_{\text{size}} = 0.7$) electrolysis plant. (b) Power curves for $k_{\text{size}} = 1.0$ of the wind turbine along with an electrolysis plant composed of $N_{\text{units}} = 1$ and $N_{\text{units}} = 3$. (c) Plant capacity factor averaged over its lifetime according to the plant sizing ratio and modularity.

but requires a higher minimum operating load and on the other side reduce the EENS when one or more units are unavailable due to a failure or downtime.

Moreover, as depicted in Fig. 6.8b, a plant with higher modularity, i.e. higher N_{units}, can substantially reduce the overall minimum load, thereby enhancing the plant capacity factor. However, an upper limit to the capacity factor increment can be identified in cases where the electrolysis plant is capable of absorbing power across almost the entire power curve of the wind turbine. Conversely, a smaller N_{units} increases the overall minimum load plant, reducing the operating window of the plant. Ultimately, as shown in Fig. 6.8c, from a capacity factor perspective, it is preferable to have more independent units (high N_{units}) and oversize the plant.

6.3.2 Electrolyzer Specific Energy Consumption

As discussed in Section 2.2.1, the higher the load on an electrolyzer, the greater the SEC of the cells. Consequently, as illustrated in Fig. 6.9a, an electrolysis plant with oversized electrolyzer units will operate at a relatively lower load compared to an undersized one, resulting in lower SEC at the rated power of the wind turbine. Additionally, modularity plays a role on the SEC, albeit to a lesser extent. As mentioned in Section 3.2, a plant with a high number of units allows more electrolyzer units to operate at lower loads (cf. Fig. 6.9b), thereby reducing the overall plant SEC.

Figure 6.9c illustrates the SEC of the electrolysis plant averaged over the plant lifetime, considering different sizing and modularity configurations. Ultimately, similar to the capacity factor, it is preferable to oversize the plant and have a high number of independent rows to achieve optimal SEC of the electrolyzer units.

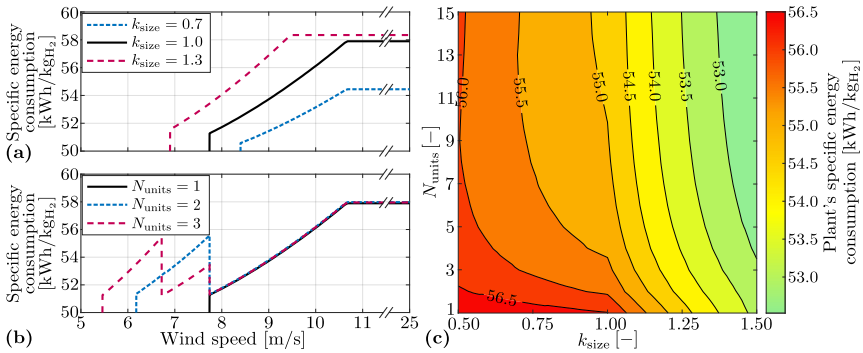


Figure 6.9: (a) Plant SEC at MoL according to the wind speed for N_{units} = 1 and different plant sizing k_{size}. (b) Plant SEC at MoL according to the wind speed for k_{size} = 1 and different plant modularity. (c) Plant SEC averaged over its lifetime according to the plant's sizing ratio and modularity.

6.3.3 Power Electronics Efficiency

For each modularity and sizing of the plant considered, a DABCS for each electrolyzer unit is designed with the minimum number of submodules at a switching frequency of 890 Hz. The number of redundant submodules is selected to achieve the minimum LCOH as discussed in Section 6.1.2. As shown in Fig. 6.10, the sizing and modularity also affect the LCE of the EDS. The decrease in efficiency as N_{units} increases can be explained by several factors.

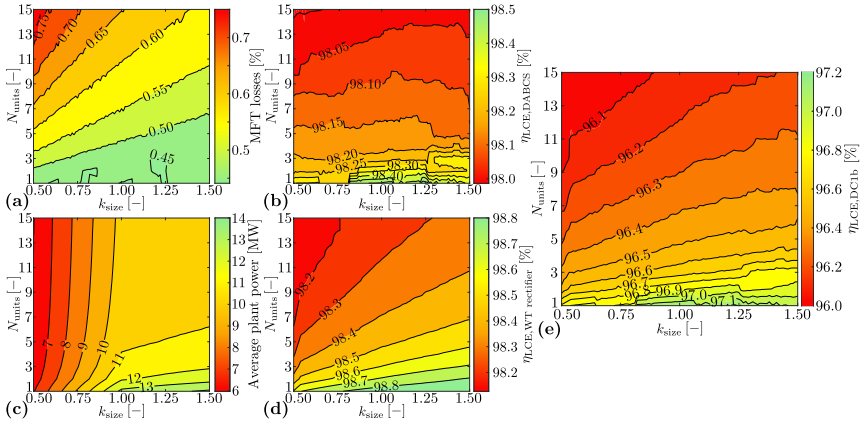


Figure 6.10: (a) MFT losses at rated load MoL. (b) DABCS LCE, (c) average plant power (d) wind turbine rectifier LCE and (e) EDS LCE averaged over the plant lifetime according to the plant's sizing ratio and modularity.

As demonstrated for the plant SEC, a more modular plant enables the electrolysis plant to operate at a lower load on average over its operating lifetime (cf. Fig. 6.10c). However, as illustrated in Fig. 5.7, the EDS efficiency decreases as the operating power decreases. Moreover, the high number of units results in a higher number of DABCS and therefore a higher number of semiconductors and MFTs sized for the same amount of power. This means more components carrying the same power, increasing conduction losses as illustrated in Fig. 6.10a.

Ultimately, the variables k_{size} and N_{units} have a non-negligible impact on the efficiency of the EDS, with the lowest efficiency of the investigated range being about 1 % lower than the highest. One might consider compensating for the decline in efficiency by designing DABCS for lower operating frequency as N_{units} increases, but the increase in components count limits the use of larger individual DABCS.

6.3.4 Plant CapEx

Figure 6.11a illustrates that both increasing the rated power of the plant and the number of units with smaller rated power lead to higher electrolysis plant CapEx. This is due to the economies of scale observed in larger electrolysis plants, as outlined by the cost functions in Table 5.5. Additionally, an increase in N_{units} results in higher EDS CapEx as shown in Fig. 6.11b, particularly for the DABCS, since a higher number of DABCSs with smaller rated power are needed.

The lowest EDS cost is achieved when N_{units} is equal to three. This outcome arises because, with three electrolyzer units, the optimal DABCS configuration in terms of LCOH does not require additional redundant submodules, as the loss of one DABCS only affects one-third of the plant production. In contrast, if the plant features only one electrolyzer unit, the optimal DABCS configuration in terms of LCOH is the one with the minimum number of submodules, which is six (driven by the high DC current requirement), with two additional redundant submodules. This can be explained by the greater importance of maintaining high availability when only one electrolyzer unit operates in the plant, as any failure of the DABCS results in a complete halt in production.

Ultimately, as illustrated in Fig. 6.11c, the larger and more modular the plant, the higher the overall CapEx.

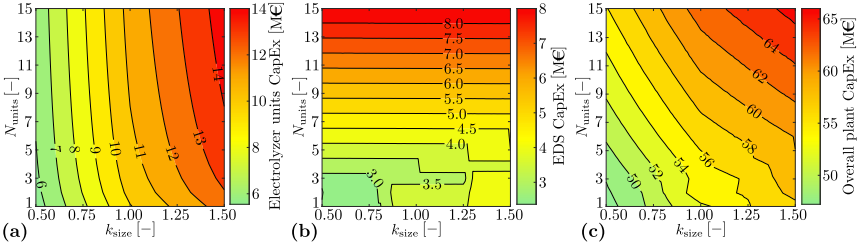


Figure 6.11: (a) Electrolyzer units CapEx, (b) EDS CapEx and (c) overall plant CapEx according to the plant's sizing ratio and modularity with cost functions that estimate CapEx for 2020.

6.3.5 LCOH

Figure 6.12a shows the total amount of hydrogen produced over the plant lifetime, while Fig. 6.12b and 6.12c, represent the LCOH collected onshore for various plant configurations in 2020 and 2030, respectively. When the size factor k_{size} is below 1, the reduction in plant CapEx is offset by a lower capacity factor and higher SEC, which together raise the LCOH. In contrast, when k_{size} exceeds 1, the benefits of reduced SEC and an improved capacity factor outweigh the increased CapEx, thereby lowering the LCOH.

Likewise, with a low number of units N_{units} (e.g. one or two), the LCOH slightly increases because the disadvantages of a lower capacity factor and higher SEC outweigh the savings in CapEx. However, as N_{units} increases, the LCOH decreases owing to a higher capacity factor and lower SEC, even though the plant CapEx and EDS losses are higher. This improvement continues only up to a threshold, beyond which escalating CapEx and EDS losses begin to dominate, indicating that an optimal balance between plant sizing and modularity exists to minimize the LCOH.

Considering cost functions estimating CapEx for 2020, a minimal LCOH of 3.84 €$_{2020}$/kg$_{H_2}$ is achieved with an optimal plant configuration of k_{size} = 1.33 and N_{units} = 4. This corresponds to an electrolysis plant comprising four electrolyzer units of roughly 5 MW, totaling 20 MW for a 15 MW wind turbine. Under the CapEx assumptions for 2030, the lowest LCOH of 3.17 €$_{2030}$/kg$_{H_2}$ is obtained with a k_{size} = 1.42 and N_{units} = 4, which translates into an electrolysis plant of four electrolyzer units of 5.33 MW, totaling 21.3 MW for the same 15 MW wind turbine.

The shift towards higher oversizing for the 2030 scenario reflects the reduced relative impact of CapEx in the future, thus allowing more extensive oversizing at a lower cost. Note that this analysis does not account for possible improvements in electrolysis efficiency, which could further favor larger, oversized electrolysis plant designs. Overall, achieving the lowest LCOH requires significant oversizing (approximately 33 to 42 %), resulting in a roughly 5 % reduction in LCOH compared to the baseline configuration of three units of 5 MW. Note that this optimal sizing is specific to the parameters and boundary conditions considered. Furthermore, oversizing necessitates a larger footprint, ranging from 700 to 1000 m^2, to accommodate the entire electrolysis plant on the wind turbine platform [135], with an anticipated increase in weight of roughly 40 to 50 tons on the platform compared to the base case.

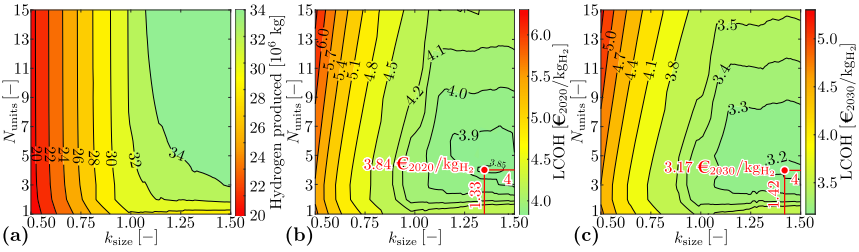


Figure 6.12: (a) Hydrogen produced over the plant lifetime and LCOH assuming cost functions that estimate CapEx for (b) 2020 and (c) 2030.

6.4 Achieving Competitive LCOH

After a detailed parametric analysis, where the key variables were adjusted by up to 20 %, the results show that the LCOH remains consistently above the 2 €/kg_{H_2} threshold, a cost level comparable to conventional hydrogen production methods. This underscores that while progress has been made in technology and cost optimization, achieving economically attractive conditions for wind-to-hydrogen plants requires further comprehensive improvement, considering both direct costs and broader environmental and societal impacts.

Figure 6.13 illustrates an exemplary scenario in which a combination of technological advancements and cost reductions could yield an LCOH close to 2 €/kg_{H_2}. Specifically, the figure depicts the effects of oversizing the plant by 40 %, enhancing the efficiency of the electrolysis process by 20 %, increasing the number of operational hours at full load by operating at a higher annual average wind speed, and reducing the CapEx for both wind turbine and the electrolysis plant by 30 %. Although these modifications represent ambitious improvements, they clearly illustrate the scale and scope of the progress necessary to make hydrogen production from stand-alone wind-to-hydrogen plants a credible competitor in the hydrogen market, particularly under current market and policy conditions where external environmental costs are not accounted for.

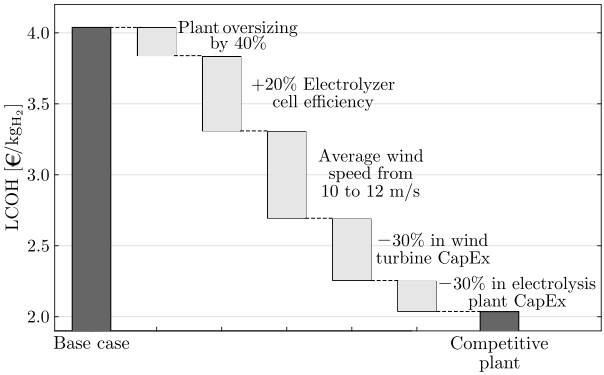


Figure 6.13: Exemplary combination of technological and economic enhancements on the LCOH.

7 Conclusions and Outlook

The integration of electrolysis plants with decentralized stand-alone offshore wind turbines offers a promising pathway to more efficient and cost-effective hydrogen production compared to grid-connected electrolysis plants. Such an approach, often referred to as wind-to-hydrogen plants, can potentially reduce transmission and conversion losses as well as investments in grid infrastructure. Despite the promise of bypassing extensive grid infrastructures while enabling scalable hydrogen production, wind-to-hydrogen plants remained underexplored in several critical aspects. While the electrolysis process and the capture of offshore wind energy are two mature technologies, their close integration demands a more detailed examination of the requirements for both systems in combination. The sole coupling of electrolysis with offshore wind power introduces a range of new challenges due to constrained environments, variable power supply, rapid power ramp rates and changing operational conditions over the lifetime of the plant. Electrical components located between the wind turbine generator and the electrolyzer units—collectively referred to as the EDS—and operation strategies are key factors of the electrical integration of electrolysis plants with decentralized stand-alone offshore wind turbines. Previous studies have either analyzed characteristics such as efficiency, reliability and cost, separately or have not adequately considered all relevant key parameters.

This thesis focuses on establishing a methodology to comprehensively compare different electrical connection schemes and operating strategies, thereby providing robust insights for the design and optimization of decentralized wind-to-hydrogen plants. The proposed methodology considers technical challenges arising from fluctuating renewable power and variable operating conditions, with the goals of maximizing operational performance, enhancing reliability, and minimizing overall costs. Particular attention is paid to emerging topologies such as modular isolated DC-DC converters, which offer significant advantages in efficiency, power density and dynamic response for connecting large-scale electrolyzers to DC buses. To primarily overcome the current limitations of individual semiconductor switches and to share the load, these converters consist of multiple submodules connected in parallel. The potential modularity of these converters makes them subject to optimization in their modularity to enhance key performance parameters such as converter efficiency, power density, reliability and cost.

7.1 Contributions

The main contributions of this dissertation are summarized in the following.

Specification of the Requirement for the EDS in Wind-to-Hydrogen Plants

The thesis describes the modeling of both electrolysis and wind turbine systems and extracts their electrical characteristics. These extracted characteristics, together with insights gained from an extensive literature review, form the basis for determining the specific technical requirements of the EDS. Ultimately, the work emphasizes that a thorough, integrated approach is essential to ensure the efficient, reliable, safe and stable operation of both systems.

Development of EDS Concepts and Comparison of Plant Operation Strategies

The thesis introduces and explores methods to prevent the wind turbine from exceeding the ramp rate limitation of the electrolysis plant. The selected method uses the wind turbine rotor as an energy buffer, by operating at a higher rotational speed than nominal, extra energy can be released when required. For the exemplary 15 MW wind turbine with relatively large rotor inertia considered in this work, the analysis shows that fulfilling the dynamics requirement while maintaining the nominal power extraction requires only a 3 % increase in rotor speed. The thesis evaluates three different plant operation strategies. The most promising one minimizes the load on each unit by evenly distributing the wind turbine output power. This approach leverages the higher efficiency of PEM electrolyzers at lower loads and ensures that each unit frequently runs under these conditions, which ultimately results in the highest overall electrolysis efficiency. Several EDS architectures are presented, detailing both AC-based and DC-based approaches, considering single-stage and double-stage conversion to accommodate either LV or MV PMSG configurations.

Configuration Optimization of High Power Isolated DC-DC Converters

The thesis focuses on the optimization and analysis of high-power isolated DC-DC converters, specifically on the configuration of DABCS. The thesis outlines the methodology for optimizing the modular connection of DABCS by designing the main components based on the switching devices used on the primary and secondary sides. A detailed analysis of semiconductor losses and MFT losses is conducted. The analysis shows that configurations employing LV IGBT modules on both sides of the DABCS exhibit superior semiconductor efficiency compared to any other configurations. However, the semiconductor efficiency advantage is counterbalanced by a decrease in MFT efficiency when a higher number of submodules is used. A Pareto optimization analysis of efficiency versus power density is conducted to identify the most suitable configuration. Among the various modular connections examined (ISOP, IPOP, IPOS) the results indicated that employing the minimum number of submodules results in the optimal balance of DABCS efficiency, power density and cost.

Development of a Holistic Methodology to Compare Different EDS

The proposed LCCA methodology offers a comprehensive methodology for comparing different EDS configurations. This holistic approach takes into account the variability of the power source and the evolving operating conditions of the electrolyzer over the lifetime of the plant. It evaluates the total cost of ownership, including initial CapEx, OpEx, replacement costs, energy losses, and downtime, to deliver a detailed assessment of long-term cost-effectiveness. The LCOH is employed as a comprehensive indicator, integrating these performance metrics into a single figure that enables a straightforward

comparison of different EDS configurations. The key findings underscore the significant influence of EDS design on overall plant performance. Implementing a single-stage DC-based distribution system reduces the number of conversion steps, thereby increasing both efficiency and availability of the plant. Additionally, it considerably reduces weight and size requirements, which is especially beneficial for offshore applications where the weight and size of installations pose substantial challenges and contribute to high transportation, installation and maintenance costs. Overall, such a configuration may reduce the LCOH by roughly 8 % compared to distribution systems based on standard AC components, further enhancing the competitiveness of green hydrogen production plants.

Comprehensive Parametric Analysis

The thesis provides a comprehensive parametric analysis of the plant performances, focusing on attaining a competitive LCOH. A sensitivity analysis is conducted on various economic parameters and plant conditions to understand their impact on the LCOH. The sensitivity analysis reveals that LCOH is primarily driven by three factors: the cost of the wind turbine, the annual number of full load hours, and the overall efficiency of the plant. Methods to enhance the efficiency of the DABCS are explored, including parallel and series connections of semiconductors devices. While these configurations can reduce power losses, they must be balanced against additional system complexity and cost. Furthermore, a sizing optimization is performed for the electrolysis plant by considering capacity and modularity. It suggests that significant oversizing, by 33 to 42 %, can lead to a notable reduction in LCOH, though this comes at the expense of a larger physical footprint and increased weight on the wind turbine platform. Despite these technological and economic optimizations, the LCOH of wind-to-hydrogen plants remains above that of conventional hydrogen production methods. This persistent challenge highlights the need for further advancements in technology and cost optimization and sets the stage for future research and innovation in the sector.

7.2 Future Work

To further deepen the analysis of integrating electrolysis plants with decentralized standalone offshore wind turbines and further enhance the competitiveness of green hydrogen production, the following research topics are summarized and suggested as future work.

Optimization of Electrolyzer Cell Design for RES Profiles

Since the electrolyzer cell design significantly influences plant operating limits, its design should be optimized according to different RES load profiles. For RES that can result in operation with relatively high hours at full load, a cell design that minimizes resistance and achieves higher efficiency at rated load, even if it comes with more stringent minimum load requirements, may be most effective. Conversely, for RES that frequently result in operation under partial load, a thicker cell design may offer lower efficiency but a wider operating window, thereby improving overall plant performance. Therefore, the optimal electrolyzer cell design must be tailored to the specific RES load profile.

Further Improvement of the DABCS Optimization Methodology

Future work should incorporate the impact of lossless snubber capacitance on DABCS optimization. Implementing snubber capacitors in parallel with each switching device, combined with the introduction of dead time during the commutation, can effectively reduce hard turn-off switching losses by damping voltage transients. However, accurately accounting for snubber effects is challenging because it demands precise knowledge of the turn-off waveform and the influence of passive circuit components, including parasitics. Accordingly, experimental measurements will be necessary to calibrate the model for turn-off loss reduction per turned-off current and per switching device. Moreover, experimental validation of the DABCS design methodologies will ensure that the theoretical optimization is effectively accurate to practical system performance.

Methodology Extension to Other Converter Topologies

Unidirectional topologies, such as the Single-Active Bridge, may offer benefits by reducing the number of active semiconductors, potentially lowering converter costs. However, it is essential to conduct a comprehensive analysis to evaluate the overall impact of implementing such a topology, including the effects on phase currents and the specific requirements for the MFTs is necessary.

Converter Control Architecture of the Plant

Evaluate and implement a robust control strategy by considering both centralized and decentralized approaches for managing the various converters in the EDS. Given the stand-alone operation, the control architecture must adopt tailored control methods and ensure rapid and precise converter management to avoid power mismatches and potential frequent shutdowns of the plant. In addition, proactive measures to prevent the system from entering a dead state by maintaining sufficient UPS charge levels at all times have to be considered. Lastly, optimizing startup procedures, including integrated black-start capabilities, will ensure smooth and reliable plant operation and enable recovery after a total shutdown.

Thorough Analysis of Different Electrolyzer Modularities

Future work should include a detailed evaluation of the electrolysis process under various electrolyzer modularities. The in-depth effects of varying the number of cells in series and adjusting cell sizes on overall electrolysis performance could be considered. Key factors to assess include thermal management, current distribution, reduction of crossover phenomena, cell imbalances, stray currents and stack reliability. Additionally, a comprehensive cost analysis is essential to determine the optimal modularity strategy for the plant.

A Characteristics of Considered Semiconductors

Figure A.1 details the output characteristics and switching losses of the IGBT and SiC MOSFET modules of different voltage classes considered in this study.

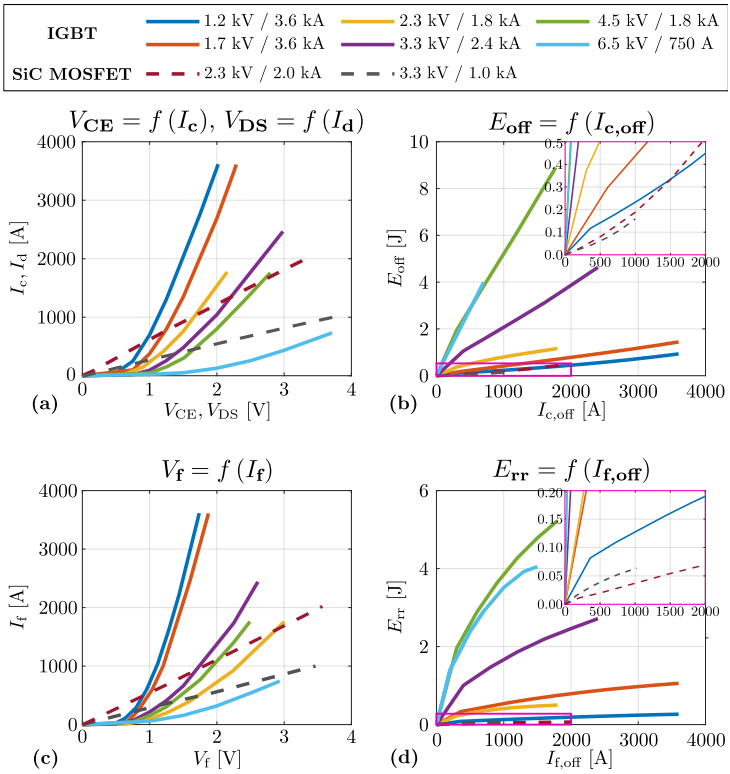


Figure A.1: (a) Output characteristics, (b) turn-off characteristics, (c) anti-parallel diode output characteristics and (d) recovery losses characteristics.

B Calculation of Semiconductor Junction Temperature Under DAB Operation

Considering a BTB converter with a rated power P_{rated} of 1.66 MW and a semiconductor efficiency η of 98 %, the losses each semiconductor needs to dissipate are as follow

$$\begin{aligned} P_{\text{loss,BTB}} &= \frac{P_{\text{rated}}}{12} \cdot (1-\eta) \\ &= \frac{1666}{12} * (1-0.98) = 2.8 \text{ kW}. \end{aligned} \tag{B.1}$$

The denominator 12 comes from the number of semiconductor in the three-phase topology. Assuming that each semiconductor of the three-phase BTB converter is equipped with a liquid-cooled plate supplied by cooling medium temperature T_{cooling} of 40 °C, the thermal resistance of the cooled plates can be assessed such as

$$R_{\text{th,CP}} = \frac{T_{\text{j,BTB}} - T_{\text{cooling}} - P_{\text{loss,BTB}} \cdot R_{\text{th,JH}}}{P_{\text{loss,BTB}}} \tag{B.2}$$

with $T_{\text{j,BTB}}$ the semiconductor junction temperature and $R_{\text{th,JH}}$ the semiconductor junction to heatsink thermal resistance.

Therefore, if the bridges from this BTB converter are operated under DAB operation, the junction temperature of the semiconductor can be computed as follow

$$\begin{aligned} T_{\text{j,DAB}} &= T_{\text{cooling}} + (R_{\text{th,CP}} + R_{\text{th,JH}}) \cdot P_{\text{loss,DAB}} \\ &= T_{\text{cooling}} + \left(\frac{T_{\text{j,BTB}} - T_{\text{cooling}}}{P_{\text{loss,BTB}}} \right) \cdot P_{\text{loss,DAB}} \end{aligned} \tag{B.3}$$

A DAB converter with a semiconductor efficiency of 99 % requires each semiconductor to dissipate only $P_{\text{loss,DAB}} = 1.4$ kW of losses. Considering that the semiconductors of the BTB converter operate at a junction temperature $T_{\text{j,BTB}}$ of 125 °C under rated conditions, according to (B.3) the operation under DAB would result in a junction temperature of $T_{\text{j,DAB}} = 40 + \left(\frac{125-40}{2.8}\right) \cdot 1.4 = 82.5\,^{\circ}\text{C}$ only.

List of Abbreviations and Acronyms

2L	Two-Level
3L	Three-Level
AC	Alternating Current
AC1	Single-transformer configuration
AFE	Active Front End
B6	Three-Phase Bridge
BoL	Beginning-of-Life
BoP	Balance-of-Plant
BoS	Balance-of-Stack
BTB	Back-To-Back
CapEx	Capital Expenditures
CCUS	Carbon Capture Utilization and Storage
CSPI	Cooling System Performance Index
DAB	Dual Active Bridge
DABCS	Dual Active Bridge Converter System
DC	Direct Current
DC1	Single-stage DC
DC2	Double-stage DC
EDS	Electrical Distribution System
EENS	Expected Energy Not Supplied
EMF	Electromotive Force
EoL	End-of-Life
ESS	Energy Storage Systems
EU	European Union
GHG	Greenhouse Gases
HV	High Voltage
HVAC	High Voltage Alternating Current
HVDC	High Voltage Direct Current
HWRT	High Wind Ride Through

IGBT	Insulated Gate Bipolar Transistor
IGCT	Integrated Gate Commutated Thyristor
IPOP	Input-Parallel Output-Parallel
IPOS	Input-Parallel Output-Series
ISOP	Input Series Output Parallel
ISOS	Input-Series Output-Series
LCCA	Life Cycle Cost Analysis
LCE	Load Cycle Efficiency
LCOH	Levelized Cost Of Hydrogen
LFT	Line-Frequency Transformer
LSC	Line-Side Converter
LV	Low Voltage
MFT	Medium Frequency Transformer
MoL	Middle-of-Life
MOSFET	Metal-Oxide-Semiconductor Field-Effect Transistor
MPPT	Maximum Power Point Tracking
MSC	Machine-Side Converter
MTTR	Mean Time To Repair
MV	Medium Voltage
MVAC	Medium-Voltage Alternating Current
OLTC	On-Load Tap Changer
OpEx	Operating Expenditures
PEM	Proton Exchange Membrane
PI	Proportional Integral
PMSG	Permanent Magnet Synchronous Generator
PV	Photovoltaic
RES	Renewable Energy Sources
rms	Root Mean Square
SEC	Specific Energy Consumption
Si	Silicon
SiC	Silicon Carbide
SPS	Single-Phase-Shift
STATCOM	Static Compensator
SVPWM	Space Vector Pulse Width Modulation
TSR	Tip-Speed Ratio
UPS	Uninterruptible Power Supply
ZVS	Zero-Voltage Switching

List of Symbols

$\alpha_{\mathrm{an}},\ \alpha_{\mathrm{ca}}$	Anode and cathode charge transfer coefficients
$\bar{\eta}_{\mathrm{EDS},n}$	LCE of the EDS in year n
$\bar{E}_{\mathrm{SEC},n}$	Load cycle SEC of the electrolysis plant in year n
β	Pitch angle of the blades
ΔG	Gibbs free energy
ΔV	DC-link voltage ripple requirement
$\Delta_{\mathrm{V}_{n+1}}$	Cell voltage degradation for year $n+1$
$\dot{M}_{\mathrm{H_2}}$	Amount of hydrogen gas produced in one hour
$\dot{n}_{\mathrm{H_2}}$	Hydrogen production rate
$\dot{n}_{\mathrm{H_2}}^{\mathrm{perm}}$	Permeation rate of hydrogen
$\dot{n}_{\mathrm{O_2}}^{\mathrm{evo}}$	Evolved oxygen flow
η_{cell}	Cell efficiency
η_{F}	Faraday efficiency
η_{LCE}	LCE efficiency
η_{V}	Voltage efficiency
η_{i}	Efficiency at load level i
λ	Tip-speed ratio
λ_{BTB}	Failure rate of a conventional BTB wind converter
λ_{i}	Failure rate per year of a component
λ_{LFT}	Failure rate of a conventional LFT
λ_{m}	Membrane humidity ratio
λ_{SM}	Failure rate of a single DAB submodule
μ_{i}	Repair rate per year of a component
ω_{e}	Generator electric angular speed
ω_{m}	Angular rotor speed
ϕ_{m}	Membrane thickness
π_{T}	Temperature-dependent stress factor
ψ_{m}	Constant magnet flux-linkage

ρ	air density
σ_m	Ionic conductivity
τ	DC-link hold-up time requirement
θ_l	Line voltage phase
φ	DAB load angle
A	Wind turbine cross-sectional area
A_EDS	Availability of the EDS
A_i	Availability of a component
A_m	Active cell area
A_p	MFT area product
B	Total rotation friction
c	Scale parameter of Weibull distribution function
C_dl	Double-layer capacitance
$C_\mathrm{F,WT}$	Capacity factor of the wind turbine
C_f	Line filter capacitance
C_p	Power coefficient of the wind turbine
$C_\mathrm{F,plant,n}$	Capacity factor of the plant in year n
$C_{\mathrm{H_2/O_2}}$	Concentration of hydrogen in oxygen
C_mag	Cost of magnetic components
C_min	Minimum required capacitance
$C_\mathrm{plant,n}$	CapEx of the plant in year n
d	DABCS voltage ratio
$d_\mathrm{fl},\ d_\mathrm{pl}$	Degradation rates under full and partial load
D_p	Droop coefficient
d_foil	Foil thickness
$d_{\mathrm{H_2}}$	Hydrogen density
d_w	Inter-winding distance
E_A	Cell activation energy
E_SEC	Specific energy consumption of the cells
E_a1	Activation energy
$E_\mathrm{on}, E_\mathrm{off}$	Turn-on and turn-off energy losses per pulse
E_rr	Reverse recovery energy
E_sw	Switching energy losses per pulse
F	Faraday constant
f_sw	DAB switching frequency
f_Weibull	Weibull distribution function

$h_{\mathrm{fl,n}},\ h_{\mathrm{pl,n}}$	Numbers of hours under full load and partial load in the year n
I_{cell}	Cell current
i_{c}	Instantaneous collector current
$i_{\mathrm{d,l}},\ i_{\mathrm{q,l}}$	Line currents in the d- and q-axis
$i_{\mathrm{d,s}},\ i_{\mathrm{q,s}}$	Stator current in the d- and q-axis
i_{f}	Instantaneous forward current
I_{loss}	Portion of the cell current not contributing to hydrogen production
i_r	Inflation rate
$I_{\mathrm{c,off}}$	Collector current at turn-off
$I_{\mathrm{c,on}}$	Collector current at turn-on
$I_{\mathrm{f,off}}$	Forward current at turn-off
I_{nom}	Rated current of semiconductor device
$i_{\mathrm{S1}},\ i_{\mathrm{S2}}$	Currents flowing through the switching devices S1 and S2
J	Cell current density
$J_{0,\mathrm{an}},\ J_{0,\mathrm{ca}}$	Anode and cathode exchange current densities
J_{lim}	Maximum cell current density
J_{m}	Total moment of inertia of the wind turbine drive train
J_{w}	Winding current density
k	Shape parameter of Weibull distribution function
k_0	Boltzmann constant
$K_{\mathrm{p}}^{\mathrm{T_{ref}}}$	Permeability coefficient at the reference temperature
k_{size}	Sizing ratio of the electrolysis plant compared to the wind turbine
L	Lifetime of the plant
$L_{\mathrm{d,s}},\ L_{\mathrm{q,s}}$	Stator inductance in the d- and q-axis
L_{e}	AFE phase inductance
L_{f}	Line filter inductance
$L_{\mathrm{s,DABCS}}$	DABCS series inductance
$L_{\mathrm{s,SM}}$	Submodule's series inductance
L_{s}	DAB series inductance
L_{σ}	MFT leakage inductance
m	Number of layers
$M_{\mathrm{H_2},n}$	Total mass of hydrogen produced in year n
N	Number of components in the EDS
n	Year of operation

n_p	Generator's number of poles
$n_\mathrm{tr,DABCS}$	DABCS transformer turns ratio
$n_\mathrm{tr,SM}$	Submodule's transformer turns ratio
n_tr	DAB transformer turns ratio
N_t	Total number of submodules in the DABCS
$N_1,\ N_2$	Primary and secondary windings number of turns
N_semi	Number of semiconductor devices
$N_\mathrm{SM,min}$	Minimum number of submodules required in the DABCS
$N_\mathrm{SM,p},\ N_\mathrm{SM,s}$	Number of submodules required on the primary and secondary side of the DABCS
$O_\mathrm{plant,n}$	OpEx of the plant in year n
P_m	Wind turbine mechanical power
P_w	Wind power
$P_\mathrm{cond,p,DABCS},\ P_\mathrm{cond,s,DABCS}$	Primary and secondary side conduction losses of the DABCS
$P_\mathrm{cond,p,SM},\ P_\mathrm{cond,s,SM}$	Primary and secondary side conduction losses per submodule
$P_\mathrm{EL,plant}$	Rated power of the electrolysis plant
$P_\mathrm{EL,unit}$	Rated power of a single electrolyzer unit
$p_\mathrm{H_2O}$	Water partial pressure
$p_\mathrm{H_2}$	Hydrogen partial pressure
P_i	Power at load level i
$P_\mathrm{loss,BTB}$	Overall semiconductor losses in a BTB converter
$P_\mathrm{loss,DAB}$	Overall semiconductor losses in a DAB submodule
$p_\mathrm{O_2}$	Oxygen partial pressure
$P_\mathrm{p,DABCS},\ P_\mathrm{s,DABCS}$	Primary and secondary side semiconductor losses of the DABCS
$P_\mathrm{sw,p,DABCS},\ P_\mathrm{sw,s,DABCS}$	Primary and secondary side switching losses of the DABCS
$P_\mathrm{sw,p,SM},\ P_\mathrm{sw,s,SM}$	Primary and secondary side switching losses per submodule
P_switch	Installed converter switching power
P_WT	Wind turbine electrical rated power
q	Number of redundant submodules employed in the DABCS
R	Universal gas constant
r	Voltage ratio between peak AC voltage and DC-link voltage
R_blade	Turbine blade length
R_s	Stator resistance
R_DABCS	Reliability of the overall DABCS
R_ion	Proton resistance
R_SM	Reliability of one DAB submodule

$R_{\text{stack,n}}$	Stack replacement costs in year n
$R_{\text{th,CP}}$	Thermal resistance between of the cold plate
$R_{\text{th,JH}}$	Thermal resistance between junction and cold plate
$S1,\ S2$	Upper switching device on primary and secondary side phase u of the DAB
t	Period of time
T_{cell}	Cell temperature
T_{e}	Electromagnetic torque
T_{j}	Junction temperature
T_{m}	Turbine mechanical torque
T_{ref}	Cell reference temperature
T_{cooling}	Temperature of the cooling medium
$T_{\text{CP,max}}$	Cold plate allowable maximum temperature
t_{i}	Total number of hours per year at load level i
$T_{\text{j,BTB}}$	Junction temperature of semiconductors in a BTB converter
$T_{\text{j,DAB}}$	Junction temperature of semiconductors in a DAB converter
T_{op}	Actual junction temperature
T_{ref}	Reference junction temperature
T_{rise}	MFT maximal winding temperature rise
T_{sw}	Switching period
u	Number of load levels
U_{block}	Blocking voltage of semiconductor device
v	Wind speed
V_{act}	Activation overpotential
V_{cell}	Cell voltage
v_{ce}	Instantaneous collector-emitter voltage
$v_{\text{d,l}},\ v_{\text{q,l}}$	Line voltages in the d- and q-axis
v_{d}	Stator voltage in the d-axis
v_{f}	Instantaneous forward voltage
V_{l}	Line voltage amplitude
v_{m}	Molar volume of hydrogen
V_{oc}	Open circuit voltage
V_{PMSG}	Rated voltage of the PMSG
$V_{\text{p}},\ V_{\text{s}}$	DAB primary and secondary bridge voltages
v_{q}	Stator voltage in the q-axis
V_{rev}^{0}	Reversible voltage

V_{th}^{0}	Thermoneutral voltage
V_{trans}	Mass transport overpotential
V_{Ω}	Ohmic overpotential
$V_{\mathrm{AC,pk}}$	Peak AC voltage
V_{B}	Voltage at which switching energies are measured in the datasheet
V_{CS}	Volume of the cooling system
$V_{\mathrm{DC,IGBT}}$	IGBT DC voltage rating
V_{DC}	DC-link voltage
V_{MVDC}	DABCS input voltage

List of Figures

1.1 Simplified representation of an electrolysis plant. 1
1.2 Breakdown of global production and demand for 97 Mt of hydrogen in 2023 [6]. 2
1.3 Three different connection schemes of coupling of electrolysis to stand-alone offshore wind energy. 5
1.4 Thyristor rectifier topologies commonly used in industrial-scale electrolyzer power supplies. 12
1.5 IGBT rectifier topologies commonly used in industrial-scale electrolyzer power supplies. 13
1.6 Simplified representation of a decentralized wind-to-hydrogen plant comprising three independent electrolyzer units. 13
1.7 Modular connection of isolated DC-DC converter submodules. 15
1.8 Modular connection of electrolyzer stacks. 15
1.9 Evolution of the minimum load requirement from a plant perspective for different number of units[1]. 17
1.10 Schematic structure of the thesis. 18

2.1 (a) Power coefficient C_p for variable TSR and different pitch angles β. (b) Wind turbine mechanical power P_m for different wind speed. 20
2.2 Power curve of the considered wind turbine and evolution of the power coefficient, blade pitch angle, rotor speed and TSR with wind speed. 22
2.3 (a) Probability density function of wind speed and (b) corresponding hours per year at different wind turbine output power. 23
2.4 Standard full-scale converter and its control scheme typically used in offshore wind turbines connected to the grid [118]. 24
2.5 Passive and active rectification in wind turbine electrical drivetrain. 27
2.6 Examples of common topologies used in the wind turbine electrical drivetrain, depending on the voltage level [88]. 29
2.7 (a) Wind speed variation with negative gradient, (b) corresponding response in wind turbine output power according to the rotor inertia and (c) the instantaneous rate of change in output power. 32
2.8 Schematic of the basic operating principle of a PEM electrolysis cell. 33
2.9 Breakdown of the voltage of a generic PEM electrolysis cell operating at a pressure of 35 bar and $T_{cell} = 60\,°C$ (adapted from [143]). 36
2.10 PEM cell polarization curves under variant operating conditions. 37
2.11 Different cell efficiencies at 35 bar and $T_{cell} = 60\,°C$ of an exemplary PEM cell (adapted from [143]). 38

2.12 Concentration of hydrogen in oxygen on the anode side for different operating conditions in an exemplary PEM cell design (adapted from [147]). . . 40
2.13 Generated characteristic curves of the considered 5 MW PEM electrolyzer. 43
2.14 Simplified representation of a PEM electrolysis plant [75, 157]. 44
2.15 Distribution of the possibly theoretical amount of hydrogen produced during the first year of operation at different wind turbine output power (considering no power losses in the EDS) and no downtime in the plant. 47

3.1 Power coefficient C_p for variable TSR and different pitch angles β. 49
3.2 (a) Wind speed variation with negative gradient, (b) corresponding response in wind turbine output power according to the wind turbine TSR and (c) the instantaneous rate of change in output power. 50
3.3 Power extracted from the wind according to rotor speed and for different wind speed v. 51
3.4 Power allocation strategies according to the wind turbine output power represented at BoL. Note that in this figure, the auxiliaries consumption and the losses in the EDS are not considered. 53
3.5 Overall electrolysis efficiency at BoL for different power allocation strategies. Note that in this figure, the auxiliaries consumption and the losses in the EDS are not considered. 54
3.6 Output power and voltage according to the rotational speed of the wind turbine PMSG, as well as the power and voltage of the electrolyzer units under different cell aging. The base electrolyzer voltage is defined at BoL rated load such that it is 1000 V, while the base rms PMSG voltage is set at full load, which is equal to 690 V when LV is considered, or 3300 V when MV is considered for the PMSG. 55
3.7 EDS considered in this work. 56
3.8 Wind turbine electrical drivetrain and its control scheme employed in the MVAC configuration [118]. 57
3.9 Electrolyzer power supply and its control scheme employed in the MVAC configuration (adapted from [173]). 58
3.10 Operating ranges of the isolated DC-DC converter in DC1a and DC1b configurations. 60
3.11 Modular connection of isolated DC-DC converter submodules employed in the DC2 EDS to increase the rectified generator voltage to 10 kV. 61

4.1 Topology and typical waveforms of the three-phase DAB [185]. 64
4.2 Flowchart of the employed design procedure of the DABCS for different switch combinations. 65
4.3 Normalized soft-switching area of the DABCS and the polarization curves of the electrolyzer at different cells aging. An additional operating condition, denoted as middle-of-life (MoL), is introduced by assuming a linear degradation of the electrolyzer throughout its lifetime. 66
4.4 (a) Number of submodules employed in the DABCS, (b) submodules' turns ratio, (c) submodules' phase inductance. 68

4.5 DABCS losses at switching frequency of 1 kHz under full load operation at MoL of the electrolyzer according to the pair of IGBT modules employed on the primary and secondary side: (a) Submodule conduction losses on the primary side, DABCS primary side (b) conduction losses, (c) switching losses, and (d) overall semiconductor losses. DABCS secondary side (e) conduction losses, (f) switching losses, and (g) overall semiconductor losses. (h) DABCS overall semiconductor efficiency. 70
4.6 Liquid-cooled cold plate maximum temperature allowed on the cold plate (a) on the primary and (b) on the secondary side. The volume of the liquid cooling system for the semiconductor in the entire DABCS (c) on the primary and (d) secondary side. 72
4.7 (a) Minimum required capacitance on the primary side submodules, (b) minimum required capacitance on the secondary side of the DABCS, and (c) the total capacitor volume of the DABCS according to the different switches combinations and for a switching frequency of 1 kHz. 73
4.8 (a) Flowchart of the employed design procedure of the MFT design procedure (based on [197, 198]). (b) Three-phase transformer core shape geometry and winding schematics. (c) Comparison of Pareto-optimal MFT designs for various DABCS configurations and an operating frequency of 1 kHz. For the case of 8 submodules of 625 kW, all sets of designs and the Pareto front are represented, while other configurations are represented only by their Pareto fronts. The selected efficiency-optimized designs are represented with yellow stars. 74
4.9 Characteristic of the selected efficiency-optimized MFT designs. 76
4.10 Temperature-dependent stress factor π_{T} according to actual junction temperature T_{op} for different reference junction temperature T_{ref}. 77
4.11 DABCS (a) reliability in a year and (b) power density according to the additional installed converter power for different minimum number of submodules required $N_{\mathrm{SM,min}}$. 78
4.12 DABCS efficiency under full load operation at MoL of the electrolyzer, (b) DABCS power density and (c) specific cost according to the employed switch combination for a switching frequency of 1 kHz. 79
4.13 Results of the efficiency versus power density Pareto optimization considering the use of the 1.7 kV IGBT module on the secondary side and different IGBT modules on the primary side. 80
4.14 Single MFT volume versus switching frequency for different IGBT modules on the primary side. 80
4.15 (a) Results of the Pareto optimization and (b) number of submodules of the different DABCS configurations employing 1.7 kV IGBT modules on the secondary side and various voltage class IGBT modules on the primary side for different input voltages. 82
4.16 (a) Number of submodules employed in the DABCS in IPOP connection. (b) DABCS overall semiconductor efficiency. (c) Comparison of Pareto-optimal MFT designs for various number of submodules. DABCS (d) efficiency under full load operation at MoL of the electrolyzer and (e) power density according to the employed switch combination for a switching frequency of 1 kHz. 83

4.17 Normalized soft-switching area of the step-up DABCS considered in the DC2 EDS and the voltage ratio across the DABCS in relation to the transferred power. 85
4.18 (a) Number of submodules employed, (b) overall semiconductor efficiency, (c) DABCS efficiency under rated load operation at MoL and (d) power density according to the employed switch combination in IPOS connection for a switching frequency of 1 kHz. 86

5.1 Methodology employed for evaluating and comparing the different EDS. . . 88
5.2 (a) Electrolyzer polarization curves over the nine years of operation and (b) the corresponding SEC of the electrolyzer according to the considered power allocation strategy. 89
5.3 Efficiency curves of (a) BTB converter based on the voltage ratio r and (b) corresponding efficiency curves of the BTB converter stage (rectifier or inverter) according to the PMSG variable voltage versus operation at a constant voltage ratio $r = 1.15$. 90
5.4 (a) Voltage ratio curves across the electrolyzer rectifier for different aging conditions and (b) corresponding electrolyzer rectifier efficiency. (c) Efficiency curves of LFT according to its ratings. 91
5.5 (a) DABCS efficiency map for different transferred power and voltage ratio d under SPS modulation, along with the voltage ratio curves of the electrolyzer and corresponding power losses at (b) BoL and (c) EoL operation of the electrolyzer cells in the DC1a configuration. (d) Voltage ratio curve across the DABCS and corresponding power losses at (e) BoL and (f) EoL operation of the electrolyzer cells in the DC1b configuration. 93
5.6 Efficiency map along with the respective voltage ratio curves of (a) the IPOS DABCS and (b) of the ISOP DABCS in the DC2 configuration. . . . 94
5.7 Efficiency curves of the different EDS according to transferred power for different PMSG rated voltage. 95
5.8 LCE variation with year of operation of (a) standard components and (b) DABCS considered in various EDS. Note that in this work, electrolyzer cells are assumed to be replaced with cells of identical performances. 96
5.9 Combined efficiency of the EDS and of the electrolysis plant (cells + auxiliaries) at (a) BoL and (b) EoL considering an MV PMSG. (c) Capacity factor and (d) corresponding annual amount of hydrogen produced according to the employed EDS. 99
5.10 Overall PEM electrolysis system cost for different ratings in 2020 and in 2030 adapted from [76]. 100
5.11 Breakdown of the LCOH in the MVAC EDS with costs parameters following 2020 cost functions. 101
5.12 Results of the comparative analysis of the different EDSs according to whether an LV (L) or an MV (M) PMSG is employed. 103

6.1 Tornado chart illustrating the variation in LCOH when key parameters are increased or decreased by 20 %. 107
6.2 DABCS specific cost, reliability in a year and LCOH according to the additionally installed converter power for DABCS configurations employing different IGBT modules on the primary side. Note that the specific cost is scaled by a factor 0.2 for better visibility. 109

6.3 (a) Electrolyzer SEC and (b) corresponding polarization curves at BoL and EoL for ± 20 % variation in SEC of the cells. 109
6.4 (a) MFT, semiconductor and DABCS efficiency at rated load MoL of the cells, DABCS LCE and specific cost according to the switching frequency. (b) Corresponding DABCSs volume and mass, and LCOH according to the switching frequency. 110
6.5 (a) DABCS power losses at rated load at MoL of the electrolyzer and (b) DABCS installed switching power, specific cost and LCOH according to the different cases of IGBT modules connection in the DABCS brigdes. . . 111
6.6 DABCS (a) minimum number of submodules employed (b) semiconductor efficiency (c) overall efficiency at MoL and (d) specific cost at a switching frequency of 890 Hz according to the switching devices employed on the primary and secondary side. Note that the specific cost here does not consider the use of redundant submodules. 113
6.7 DABCS specific cost, reliability in a year and LCOH according to the additionally installed converter power for the different DABCS configurations. 114
6.8 (a) Power curves for $N_{\text{units}} = 1$ of the wind turbine along with a 30 % oversized ($k_{\text{size}} = 1.3$) and a 30 % undersized ($k_{\text{size}} = 0.7$) electrolysis plant. (b) Power curves for $k_{\text{size}} = 1.0$ of the wind turbine along with an electrolysis plant composed of $N_{\text{units}} = 1$ and $N_{\text{units}} = 3$. (c) Plant capacity factor averaged over its lifetime according to the plant sizing ratio and modularity. 116
6.9 (a) Plant SEC at MoL according to the wind speed for $N_{\text{units}} = 1$ and different plant sizing k_{size}. (b) Plant SEC at MoL according to the wind speed for $k_{\text{size}} = 1$ and different plant modularity. (c) Plant SEC averaged over its lifetime according to the plant's sizing ratio and modularity. 117
6.10 (a) MFT losses at rated load MoL. (b) DABCS LCE, (c) average plant power (d) wind turbine rectifier LCE and (e) EDS LCE averaged over the plant lifetime according to the plant's sizing ratio and modularity. 117
6.11 (a) Electrolyzer units CapEx, (b) EDS CapEx and (c) overall plant CapEx according to the plant's sizing ratio and modularity with cost functions that estimate CapEx for 2020. 118
6.12 (a) Hydrogen produced over the plant lifetime and LCOH assuming cost functions that estimate CapEx for (b) 2020 and (c) 2030. 119
6.13 Exemplary combination of technological and economic enhancements on the LCOH. 120

A.1 (a) Output characteristics, (b) turn-off characteristics, (c) anti-parallel diode output characteristics and (d) recovery losses characteristics. 125

List of Tables

1.1 Summary of most relevant offshore hydrogen production projects around the world. 7

2.1 Parameters of the 15 MW Wind Turbine [109]. 21
2.2 Characteristics Considered for the 5 MW PEM Electrolyzer Units Depending on Cell Aging. 42

3.1 Impact of TSR on Rotor Speed, Power Extraction, and Maximum Instantaneous Rate of Change of Power. 51
3.2 Maximum theoretical plant capacity factor and averaged electrolysis efficiency for different power allocation strategies at BoL[1]. 54

4.1 Commercially Available IGBT Power Modules Considered. 67
4.2 Range Sweep of Design Variables in the MFT Design Procedure. 75
4.3 Comparative Analysis of Different DABCS Configuration Achieving an Efficiency of 98.5 %. 80

5.1 Degradation rates. 89
5.2 Tower Cables Characteristics. 91
5.3 DABCSs Specifications. 92
5.4 Parameters of the Standard Components in the EDS. 97
5.5 Cost Parameters for the LCOH computation. 100

6.1 Commercially Available SiC MOSFET Modules Considered. 112
6.2 DABCS Configuration Variants Employing SiC MOSFET Modules. 114

Bibliography

[1] C. Acar and I. Dincer, "3.1 Hydrogen Production," in *Comprehensive Energy Systems*. Elsevier, 2018, pp. 1–40.

[2] R. Leroy, "Industrial water electrolysis: Present and future," *International Journal of Hydrogen Energy*, vol. 8, no. 6, pp. 401–417, 1983.

[3] A. Buttler and H. Spliethoff, "Current status of water electrolysis for energy storage, grid balancing and sector coupling via power-to-gas and power-to-liquids: A review," *Renewable and Sustainable Energy Reviews*, vol. 82, pp. 2440–2454, Feb. 2018.

[4] D. Niblett, M. Delpisheh, S. Ramakrishnan, and M. Mamlouk, "Review of next generation hydrogen production from offshore wind using water electrolysis," *Journal of Power Sources*, vol. 592, p. 233904, Feb. 2024.

[5] A. Ursua, L. M. Gandia, and P. Sanchis, "Hydrogen Production From Water Electrolysis: Current Status and Future Trends," *Proceedings of the IEEE*, vol. 100, no. 2, pp. 410–426, Feb. 2012.

[6] IEA, "Global hydrogen review 2024," IEA, Paris, Tech. Rep., 2024, accessed February 23, 2025. [Online]. Available: https://www.iea.org/reports/global-hydrogen-review-2024

[7] ——, "Global hydrogen review 2023," IEA, Paris, Tech. Rep., 2023, accessed May 18, 2024. [Online]. Available: https://www.iea.org/reports/global-hydrogen-review-2023

[8] ——, "Renewables 2023," IEA, Paris, Tech. Rep., 2024, accessed June 10, 2024. [Online]. Available: https://www.iea.org/reports/renewables-2023

[9] ——, "Net Zero by 2050," IEA, Paris, Tech. Rep., 2021, accessed June 10, 2024. [Online]. Available: https://www.iea.org/reports/net-zero-by-2050

[10] ——, "Electricity Grids and Secure Energy Transitions," IEA, Paris, Tech. Rep., 2023, accessed June 10, 2024. [Online]. Available: https://www.iea.org/reports/electricity-grids-and-secure-energy-transitions

[11] A. Mohammadi and M. Mehrpooya, "A comprehensive review on coupling different types of electrolyzer to renewable energy sources," *Energy*, vol. 158, pp. 632–655, Sep. 2018.

[12] M. Khan and M. Iqbal, "Analysis of a small wind-hydrogen stand-alone hybrid energy system," *Applied Energy*, vol. 86, no. 11, pp. 2429–2442, Nov. 2009.

[13] I. Firtina-Ertis, C. Acar, and E. Erturk, "Optimal sizing design of an isolated stand-alone hybrid wind-hydrogen system for a zero-energy house," *Applied Energy*, vol. 274, p. 115244, Sep. 2020.

[14] T. Maeda, H. Ito, Y. Hasegawa, Z. Zhou, and M. Ishida, "Study on control method of the stand-alone direct-coupling photovoltaic – Water electrolyzer," *International Journal of Hydrogen Energy*, vol. 37, no. 6, pp. 4819–4828, Mar. 2012.

[15] D. Concha, H. Renaudineau, M. S. Hernández, A. M. Llor, and S. Kouro, "Evaluation of DCX converters for off-grid photovoltaic-based green hydrogen production," *International Journal of Hydrogen Energy*, vol. 46, no. 38, pp. 19 861–19 870, Jun. 2021.

[16] A. Rogeau, J. Vieubled, M. De Coatpont, P. Affonso Nobrega, G. Erbs, and R. Girard, "Techno-economic evaluation and resource assessment of hydrogen production through offshore wind farms: A European perspective," *Renewable and Sustainable Energy Reviews*, vol. 187, p. 113699, Nov. 2023.

[17] A. Ioannou and F. Brennan, "A preliminary techno-economic comparison between a grid-connected and non-grid connected offshore floating wind farm," in *2019 Offshore Energy and Storage Summit (OSES)*. BREST, France: IEEE, Jul. 2019, pp. 1–6.

[18] B. A. Franco, P. Baptista, R. C. Neto, and S. Ganilha, "Assessment of offloading pathways for wind-powered offshore hydrogen production: Energy and economic analysis," *Applied Energy*, vol. 286, p. 116553, Mar. 2021.

[19] G. Calado and R. Castro, "Hydrogen Production from Offshore Wind Parks: Current Situation and Future Perspectives," *Applied Sciences*, vol. 11, no. 12, p. 5561, Jun. 2021.

[20] C. Tries, F. Hofmann, and T. Brown, "Benefits from islanding hydrogen production in renewable energy systems," in *21st Wind & Solar Integration Workshop (WIW 2022)*. Hybrid Conference, The Hague, Netherlands: Institution of Engineering and Technology, 2022, pp. 294–301. [Online]. Available: https://digital-library.theiet.org/content/conferences/10.1049/icp.2022.2767

[21] Q. Hassan, S. Algburi, A. Z. Sameen, H. M. Salman, and A. K. Al-Jiboory, "A review of green hydrogen production by renewable resources," *Energy Harvesting and Systems*, vol. 11, no. 1, p. 20220127, Jan. 2024.

[22] H. Renaudineau, A. M. Llor, R. Cortes D., C. A. Rojas, C. Restrepo, and S. Kouro, "Photovoltaic Green Hydrogen Challenges and Opportunities: A Power Electronics Perspective," *IEEE Industrial Electronics Magazine*, vol. 16, no. 1, pp. 31–41, Mar. 2022.

[23] K. Mohammedi, "Environmental Impact of Seawater Desalination Plants: Case Study in Algeria," *American Journal of Environmental Protection*, vol. 2, no. 6, p. 141, 2013.

[24] R. S. El-Emam and H. Özcan, "Comprehensive review on the techno-economics of sustainable large-scale clean hydrogen production," *Journal of Cleaner Production*, vol. 220, pp. 593–609, May 2019.

[25] European Commission. Joint Research Centre. Institute for Energy and Transport., *HVDC submarine power cables in the world: state of the art knowledge.* LU: Publications Office, 2015. [Online]. Available: https://data.europa.eu/doi/10.2790/023689

[26] L. Sens, U. Neuling, and M. Kaltschmitt, "Capital expenditure and levelized cost of electricity of photovoltaic plants and wind turbines – Development by 2050," *Renewable Energy*, vol. 185, pp. 525–537, Feb. 2022.

[27] D. DeSantis, B. D. James, C. Houchins, G. Saur, and M. Lyubovsky, "Cost of long-distance energy transmission by different carriers," *iScience*, vol. 24, no. 12, p. 103495, Dec. 2021.

[28] B. Miao, L. Giordano, and S. H. Chan, "Long-distance renewable hydrogen transmission via cables and pipelines," *International Journal of Hydrogen Energy*, vol. 46, no. 36, pp. 18 699–18 718, May 2021.

[29] S. McDonagh, S. Ahmed, C. Desmond, and J. D. Murphy, "Hydrogen from offshore wind: Investor perspective on the profitability of a hybrid system including for curtailment," *Applied Energy*, vol. 265, p. 114732, May 2020.

[30] J. G. García Clúa, R. J. Mantz, and H. De Battista, "Evaluation of hydrogen production capabilities of a grid-assisted wind–H2 system," *Applied Energy*, vol. 88, no. 5, pp. 1857–1863, May 2011.

[31] R. Takahashi, H. Kinoshita, T. Murata, J. Tamura, M. Sugimasa, A. Komura, M. Futami, M. Ichinose, and K. Ide, "Output Power Smoothing and Hydrogen Production by Using Variable Speed Wind Generators," *IEEE Transactions on Industrial Electronics*, vol. 57, no. 2, pp. 485–493, Feb. 2010.

[32] M. G. Dozein, A. M. De Corato, and P. Mancarella, "Virtual Inertia Response and Frequency Control Ancillary Services From Hydrogen Electrolyzers," *IEEE Transactions on Power Systems*, vol. 38, no. 3, pp. 2447–2459, May 2023.

[33] S. D. Tavakoli, M. G. Dozein, V. A. Lacerda, M. C. Mañe, E. Prieto-Araujo, P. Mancarella, and O. Gomis-Bellmunt, "Grid-Forming Services From Hydrogen Electrolyzers," *IEEE Transactions on Sustainable Energy*, vol. 14, no. 4, pp. 2205–2219, Oct. 2023.

[34] V. Aryai, N. Abdussamie, R. Abbassi, I. Penesis, C.-M. Wang, and V. Garaniya, "A Feasibility Study on Green Energy Production at the Location of Offshore Oil and Gas Platforms in Australia," in *Volume 10: Professor Ian Young Honouring Symposium on Global Ocean Wind and Wave Climate; Blue Economy Symposium; Small Maritime Nations Symposium.* Melbourne, Australia: American Society of Mechanical Engineers, Jun. 2023, p. V010T13A009.

[35] A. Panagopoulos and K.-J. Haralambous, "Environmental impacts of desalination and brine treatment - Challenges and mitigation measures," *Marine Pollution Bulletin*, vol. 161, p. 111773, Dec. 2020.

[36] O. S. Ibrahim, A. Singlitico, R. Proskovics, S. McDonagh, C. Desmond, and J. D. Murphy, "Dedicated large-scale floating offshore wind to hydrogen: Assessing design variables in proposed typologies," *Renewable and Sustainable Energy Reviews*, vol. 160, p. 112310, May 2022.

[37] A. Singlitico, J. Østergaard, and S. Chatzivasileiadis, "Onshore, offshore or in-turbine electrolysis? Techno-economic overview of alternative integration designs for green hydrogen production into Offshore Wind Power Hubs," *Renewable and Sustainable Energy Transition*, vol. 1, p. 100005, Aug. 2021.

[38] D. Jang, K. Kim, K.-H. Kim, and S. Kang, "Techno-economic analysis and Monte Carlo simulation for green hydrogen production using offshore wind power plant," *Energy Conversion and Management*, vol. 263, p. 115695, Jul. 2022.

[39] Nikkei Asia, "Offshore wind to power Japan's biggest green hydrogen plant," Jul. 2021, accessed June 27, 2024. [Online]. Available: https://asia.nikkei.com/Business/Energy/Offshore-wind-to-power-Japan-s-biggest-green-hydrogen-plant2

[40] Port of Rotterdam, "Shell to start building Europe's biggest green hydrogen plant," Jul. 2022, accessed June 27, 2024. [Online]. Available: https://www.portofrotterdam.com/en/news-and-press-releases/shell-to-start-building-europes-biggest-green-hydrogen-plant

[41] SeaH2land, "Summary," accessed June 27, 2024. [Online]. Available: https://seah2land.nl/en/summary

[42] NortH2, "Kickstarting the green hydrogen economy," accessed June 27, 2024. [Online]. Available: https://www.north2.eu/

[43] Lhyfe, "Lhyfe announces that Sealhyfe, the world's first offshore hydrogen production pilot, produces its first kilos of green hydrogen in the Atlantic Ocean!" Jun. 2023, accessed June 27, 2024. [Online]. Available: https://perma.cc/9S6T-9LSA

[44] Hope, "Offshore green hydrogen at a new scale," accessed June 27, 2024. [Online]. Available: https://hope-h2.eu/

[45] PosHYdon, "About PosHYdon," accessed June 27, 2024. [Online]. Available: https://poshydon.com/en/home-en/about-poshydon/

[46] OYSTER, "Project," accessed June 27, 2024. [Online]. Available: https://oysterh2.eu/about/project/

[47] AquaVentus, "The green energy revolution starts in the NorthSea," accessed June 27, 2024. [Online]. Available: https://aquaventus.org/en/

[48] Dolphyn hydrogen, "Producing Ultra Low Carbon Hydrogen Economically and at Scale," accessed June 27, 2024. [Online]. Available: https://www.dolphynhydrogen.com/

[49] X. Guo, H. Zhu, and S. Zhang, "Overview of electrolyser and hydrogen production power supply from industrial perspective," *International Journal of Hydrogen Energy*, vol. 49, pp. 1048–1059, Jan. 2024.

[50] A. Ursúa, E. L. Barrios, J. Pascual, I. San Martín, and P. Sanchis, "Integration of commercial alkaline water electrolysers with renewable energies: Limitations and improvements," *International Journal of Hydrogen Energy*, vol. 41, no. 30, pp. 12 852–12 861, Aug. 2016.

[51] Y. Cai and F.-M. Bréon, "Wind power potential and intermittency issues in the context of climate change," *Energy Conversion and Management*, vol. 240, p. 114276, Jul. 2021.

[52] V. Martinez Lopez, H. Ziar, J. Haverkort, M. Zeman, and O. Isabella, "Dynamic operation of water electrolyzers: A review for applications in photovoltaic systems integration," *Renewable and Sustainable Energy Reviews*, vol. 182, p. 113407, Aug. 2023.

[53] A. H. El-Kady, M. T. Amin, F. Khan, and M. M. El-Halwagi, "Identification and assessment of risk factors in offshore wind-integrated hydrogen production system," *International Journal of Hydrogen Energy*, vol. 52, pp. 1312–1332, Jan. 2024.

[54] S. Sherif, F. Barbir, and T. Veziroglu, "Wind energy and the hydrogen economy—review of the technology," *Solar Energy*, vol. 78, no. 5, pp. 647–660, May 2005.

[55] R. Fang and Y. Liang, "Control strategy of electrolyzer in a wind-hydrogen system considering the constraints of switching times," *International Journal of Hydrogen Energy*, vol. 44, no. 46, pp. 25 104–25 111, Sep. 2019.

[56] F. Gambou, D. Guilbert, M. Zasadzinski, and H. Rafaralahy, "A Comprehensive Survey of Alkaline Electrolyzer Modeling: Electrical Domain and Specific Electrolyte Conductivity," *Energies*, vol. 15, no. 9, p. 3452, May 2022.

[57] H. Sayed-Ahmed, A. Toldy, and A. Santasalo-Aarnio, "Dynamic operation of proton exchange membrane electrolyzers—Critical review," *Renewable and Sustainable Energy Reviews*, vol. 189, p. 113883, Jan. 2024.

[58] J. Gu, B. Guo, S. Hu, S. Ding, T. Zhang, Z. Tian, F. Yang, and M. Ouyang, "Experimental studies on dynamic performance of 250-kW alkaline electrolytic system," *Journal of Power Sources*, vol. 592, p. 233920, Feb. 2024.

[59] Hans van't Noordende and Peter Ripson, "A One-GigaWatt Green-Hydrogen Plant," Institute for Sustainable Process Technology, Amersfoort, The Netherlands, Tech. Rep., Jan. 2022, accessed October 4, 2024. [Online]. Available: https://ispt.eu/media/Public-report-gigawatt-advanced-green-electrolyser-design.pdf

[60] C. Rakousky, G. P. Keeley, K. Wippermann, M. Carmo, and D. Stolten, "The stability challenge on the pathway to high-current-density polymer electrolyte membrane water electrolyzers," *Electrochimica Acta*, vol. 278, pp. 324–331, Jul. 2018.

[61] C. Rakousky, U. Reimer, K. Wippermann, S. Kuhri, M. Carmo, W. Lueke, and D. Stolten, "Polymer electrolyte membrane water electrolysis: Restraining degradation in the presence of fluctuating power," *Journal of Power Sources*, vol. 342, pp. 38–47, Feb. 2017.

[62] G. Papakonstantinou, G. Algara-Siller, D. Teschner, T. Vidaković-Koch, R. Schlögl, and K. Sundmacher, "Degradation study of a proton exchange membrane water electrolyzer under dynamic operation conditions," *Applied Energy*, vol. 280, p. 115911, Dec. 2020.

[63] S. H. Frensch, F. Fouda-Onana, G. Serre, D. Thoby, S. S. Araya, and S. K. Kær, "Influence of the operation mode on PEM water electrolysis degradation," *International Journal of Hydrogen Energy*, vol. 44, no. 57, pp. 29 889–29 898, Nov. 2019.

[64] H. Ito, N. Miyazaki, M. Ishida, and A. Nakano, "Cross-permeation and consumption of hydrogen during proton exchange membrane electrolysis," *International Journal of Hydrogen Energy*, vol. 41, no. 45, pp. 20 439–20 446, Dec. 2016.

[65] J. Brauns and T. Turek, "Alkaline Water Electrolysis Powered by Renewable Energy: A Review," *Processes*, vol. 8, no. 2, p. 248, Feb. 2020.

[66] A. Dutton, "Experience in the design, sizing, economics, and implementation of autonomous wind-powered hydrogen production systems," *International Journal of Hydrogen Energy*, vol. 25, no. 8, pp. 705–722, Aug. 2000.

[67] H. De Battista, R. J. Mantz, and F. Garelli, "Power conditioning for a wind–hydrogen energy system," *Journal of Power Sources*, vol. 155, no. 2, pp. 478–486, Apr. 2006.

[68] V. Timmers, A. Egea-Àlvarez, A. Gkountaras, and L. Xu, "Control and Power Balancing of an Off-Grid Wind Turbine With Co-Located Electrolyzer," *IEEE Transactions on Sustainable Energy*, pp. 1–12, 2024.

[69] A. M. O. Haruni, M. Negnevitsky, M. E. Haque, and A. Gargoom, "A Novel Operation and Control Strategy for a Standalone Hybrid Renewable Power System," *IEEE Transactions on Sustainable Energy*, vol. 4, no. 2, pp. 402–413, Apr. 2013.

[70] S. Muyeen, R. Takahashi, and J. Tamura, "Electrolyzer switching strategy for hydrogen generation from variable speed wind generator," *Electric Power Systems Research*, vol. 81, no. 5, pp. 1171–1179, May 2011.

[71] B. Yodwong, D. Guilbert, M. Phattanasak, W. Kaewmanee, M. Hinaje, and G. Vitale, "AC-DC Converters for Electrolyzer Applications: State of the Art and Future Challenges," *Electronics*, vol. 9, no. 6, p. 912, May 2020.

[72] M. Chen, S.-F. Chou, F. Blaabjerg, and P. Davari, "Overview of Power Electronic Converter Topologies Enabling Large-Scale Hydrogen Production via Water Electrolysis," *Applied Sciences*, vol. 12, no. 4, p. 1906, Feb. 2022.

[73] J. Koponen, A. Poluektov, V. Ruuskanen, A. Kosonen, M. Niemelä, and J. Ahola, "Comparison of thyristor and insulated-gate bipolar transistor -based power supply topologies in industrial water electrolysis applications," *Journal of Power Sources*, vol. 491, p. 229443, Apr. 2021.

[74] J. Solanki, N. Fröhleke, J. Böcker, A. Averberg, and P. Wallmeier, "High-current variable-voltage rectifiers: state of the art topologies," *IET Power Electronics*, vol. 8, no. 6, pp. 1068–1080, Jun. 2015.

[75] IRENA, *Green hydrogen cost reduction: scaling up electrolysers to meet the 1.5°C climate goal*. Abu Dhabi: Irena, 2020.

[76] M. Holst, S. Aschbrenner, T. Smolinka, C. Voglstätter, and G. Grimm, "Cost Forecast for Low Temperature Electrolysis - Technology Driven Bottom-Up Prognosis for PEM and Alkaline Water Electrolysis Systems," Fraunhofer-Gesellschaft, Tech. Rep., 2021, accessed July 31, 2024. [Online]. Available: https://publica.fraunhofer.de/handle/publica/441376

[77] V. Scaini and T. Ma, "High-current DC choppers in the metals industry," *IEEE Industry Applications Magazine*, vol. 8, no. 2, pp. 26–33, Apr. 2002.

[78] J. Solanki, N. Fröhleke, J. Böcker, and P. Wallmeier, "Comparison of Thyristor-Rectifier with Hybrid Filter and Chopper-Rectifier for High-Power, High-Current Application," in *PCIM Europe 2013*. Berlin: VDE-Verl, 2013, pp. 1391–1398.

[79] S. Bintz, D. Hafele, V. Ketchedjian, and J. Roth-Stielow, "Parallel-Serial-Rectifier for Power-to-Hydrogen Applications," in *2019 21st European Conference on Power Electronics and Applications (EPE '19 ECCE Europe)*. Genova, Italy: IEEE, Sep. 2019, pp. P.1–P.11.

[80] F.-W. Speckmann, S. Bintz, and K. P. Birke, "Influence of rectifiers on the energy demand and gas quality of alkaline electrolysis systems in dynamic operation," *Applied Energy*, vol. 250, pp. 855–863, Sep. 2019.

[81] A. Ursúa, L. Marroyo, E. Gubía, L. M. Gandía, P. M. Diéguez, and P. Sanchis, "Influence of the power supply on the energy efficiency of an alkaline water electrolyser," *International Journal of Hydrogen Energy*, vol. 34, no. 8, pp. 3221–3233, May 2009.

[82] J. Koponen, V. Ruuskanen, A. Kosonen, M. Niemela, and J. Ahola, "Effect of Converter Topology on the Specific Energy Consumption of Alkaline Water Electrolyzers," *IEEE Transactions on Power Electronics*, vol. 34, no. 7, pp. 6171–6182, Jul. 2019.

[83] H. P. Buitendach, R. Gouws, C. A. Martinson, C. Minnaar, and D. Bessarabov, "Effect of a ripple current on the efficiency of a PEM electrolyser," *Results in Engineering*, vol. 10, p. 100216, Jun. 2021.

[84] F. Parache, H. Schneider, C. Turpin, N. Richet, O. Debellemaniere, E. Bru, A. T. Thieu, C. Bertail, and C. Marot, "Impact of Power Converter Current Ripple on the Degradation of PEM Electrolyzer Performances," *Membranes*, vol. 12, no. 2, p. 109, Jan. 2022.

[85] M. Keddar, Z. Zhang, C. Periasamy, and M. L. Doumbia, "Power quality improvement for 20 MW PEM water electrolysis system," *International Journal of Hydrogen Energy*, vol. 47, no. 95, pp. 40 184–40 195, Dec. 2022.

[86] J. Rodriguez, J. Pontt, C. Silva, E. Wiechmann, P. Hammond, F. Santucci, R. Alvarez, R. Musalem, S. Kouro, and P. Lezana, "Large Current Rectifiers: State of the Art and Future Trends," *IEEE Transactions on Industrial Electronics*, vol. 52, no. 3, pp. 738–746, Jun. 2005.

[87] P. Catalán, Y. Wang, J. Arza, and Z. Chen, "A Comprehensive Overview of Power Converter Applied in High-Power Wind Turbine: Key Challenges and Potential Solutions," *IEEE Transactions on Power Electronics*, vol. 38, no. 5, pp. 6169–6195, May 2023.

[88] V. Yaramasu, B. Wu, P. C. Sen, S. Kouro, and M. Narimani, "High-power wind energy conversion systems: State-of-the-art and emerging technologies," *Proceedings of the IEEE*, vol. 103, no. 5, pp. 740–788, May 2015.

[89] C. Meyer, M. Hoing, A. Peterson, and R. W. De Doncker, "Control and Design of DC Grids for Offshore Wind Farms," *IEEE Transactions on Industry Applications*, vol. 43, no. 6, pp. 1475–1482, 2007.

[90] M. Stieneker, B. J. Mortimer, N. R. Averous, H. Stagge, and R. W. De Doncker, "Optimum design of medium-voltage DC collector grids depending on the offshore-wind-park power," in *2014 IEEE Symposium on Power Electronics and Machines for Wind and Water Applications*. Milwaukee, WI, USA: IEEE, Jul. 2014, pp. 1–8.

[91] D. Guilbert, B. Yodwong, W. Kaewmanee, and M. Phattanasak, "Power converters for hybrid renewable energy systems with hydrogen buffer storage: A short review," in *2018 International Conference on Smart Grid (icSmartGrid)*. Nagasaki, Japan: IEEE, Dec. 2018, pp. 28–33.

[92] D. Guilbert, S. M. Collura, and A. Scipioni, "DC/DC converter topologies for electrolyzers: State-of-the-art and remaining key issues," *International Journal of Hydrogen Energy*, vol. 42, no. 38, pp. 23 966–23 985, Sep. 2017.

[93] P. Zumel, L. Ortega, A. Lazaro, C. Fernandez, A. Barrado, A. Rodriguez, and M. M. Hernando, "Modular Dual-Active Bridge Converter Architecture," *IEEE Transactions on Industry Applications*, vol. 52, no. 3, pp. 2444–2455, May 2016.

[94] J. E. Huber and J. W. Kolar, "Optimum Number of Cascaded Cells for High-Power Medium-Voltage AC–DC Converters," *IEEE Journal of Emerging and Selected Topics in Power Electronics*, vol. 5, no. 1, pp. 213–232, Mar. 2017.

[95] R. S. Deshmukh, A. Shekhar, and P. Bauer, "Adaptive Modularity for Power Electronics Based Electrolysis Systems for Green Hydrogen," in *2022 IEEE 20th International Power Electronics and Motion Control Conference (PEMC)*. Brasov, Romania: IEEE, Sep. 2022, pp. 508–515.

[96] C. Pascalau, T. B. Soeiro, N. H. Van Der Blij, and P. Bauer, "Electrical Energy Conversion for Low Temperature Electrolysis - Challenges and Future Trends," in *2021 IEEE 19th International Power Electronics and Motion Control Conference (PEMC)*. Gliwice, Poland: IEEE, Apr. 2021, pp. 349–356.

[97] J. G. García Clúa, R. J. Mantz, and H. De Battista, "Optimal sizing of a grid-assisted wind-hydrogen system," *Energy Conversion and Management*, vol. 166, pp. 402–408, Jun. 2018.

[98] C. N. Bonacina, N. B. Gaskare, and G. Valenti, "Assessment of offshore liquid hydrogen production from wind power for ship refueling," *International Journal of Hydrogen Energy*, vol. 47, no. 2, pp. 1279–1291, Jan. 2022.

[99] L. Phan-Van, V. N. Dinh, R. Felici, and T. N. Duc, "New models for feasibility assessment and electrolyser optimal sizing of hydrogen production from dedicated wind farms and solar photovoltaic farms, and case studies for Scotland and Vietnam," *Energy Conversion and Management*, vol. 295, p. 117597, Nov. 2023.

[100] J. Park, K. Hwan Ryu, C.-H. Kim, W. Chul Cho, M. Kim, J. Hun Lee, H.-S. Cho, and J. H. Lee, "Green hydrogen to tackle the power curtailment: Meteorological data-based capacity factor and techno-economic analysis," *Applied Energy*, vol. 340, p. 121016, Jun. 2023.

[101] A. Hofrichter, D. Rank, M. Heberl, and M. Sterner, "Determination of the optimal power ratio between electrolysis and renewable energy to investigate the effects on the hydrogen production costs," *International Journal of Hydrogen Energy*, vol. 48, no. 5, pp. 1651–1663, Jan. 2023.

[102] N. Cooper, C. Horend, F. Röben, A. Bardow, and N. Shah, "A framework for the design & operation of a large-scale wind-powered hydrogen electrolyzer hub," *International Journal of Hydrogen Energy*, vol. 47, no. 14, pp. 8671–8686, Feb. 2022.

[103] D. Guilbert and G. Vitale, "Improved Hydrogen-Production-Based Power Management Control of a Wind Turbine Conversion System Coupled with Multistack Proton Exchange Membrane Electrolyzers," *Energies*, vol. 13, no. 5, p. 1239, Mar. 2020.

[104] A. Makhsoos, M. Kandidayeni, L. Boulon, and B. G. Pollet, "A comparative analysis of single and modular proton exchange membrane water electrolyzers for green hydrogen production- a case study in Trois-Rivières," *Energy*, vol. 282, p. 128911, Nov. 2023.

[105] X. Lu, B. Du, S. Zhou, W. Zhu, Y. Li, Y. Yang, C. Xie, B. Zhao, L. Zhang, J. Song, and Z. Deng, "Optimization of power allocation for wind-hydrogen system multi-stack PEM water electrolyzer considering degradation conditions," *International Journal of Hydrogen Energy*, vol. 48, no. 15, pp. 5850–5872, Feb. 2023.

[106] S. S. Queiroz and L. Costa, "Green Hydrogen Power Supply: Challenges and Opportunities," in *2023 8th IEEE Workshop on the Electronic Grid (eGRID)*. Karlsruhe, Germany: IEEE, Oct. 2023, pp. 1–6.

[107] Z. Zarkov and B. Demirkov, "Power control of PMSG for wind turbine using maximum torque per ampere strategy," in *2017 15th International Conference on Electrical Machines, Drives and Power Systems (ELMA)*. Sofia, Bulgaria: IEEE, Jun. 2017, pp. 292–297.

[108] Søren Gundtoft, "Wind Turbines." University College of Aarhus, Jan. 2012.

[109] E. Gaertner, "Definition of the IEA wind 15-megawatt offshore reference wind turbine technical report," NREL, Golden, CO, Tech. Rep. NREL/TP-5000-75698, Mar. 2020, accessed November 28, 2023. [Online]. Available: https://www.nrel.gov/docs/fy20osti/75698.pdf

[110] David Caine, "Dolphyn Hydrogen Phase 1 - Final Report," ERM, Tech. Rep., Oct. 2019, accessed August 24, 2024. [Online]. Available: https://assets.publishing.service.gov.uk/media/5e4ab9be40f0b677c1344ec8/Phase_1_-_ERM_-_Dolphyn.pdf

[111] J. G. Njiri and D. Söffker, "State-of-the-art in wind turbine control: Trends and challenges," *Renewable and Sustainable Energy Reviews*, vol. 60, pp. 377–393, Jul. 2016.

[112] Siemens AG, "Siemens D6 platform – 6.0-MW direct drive wind turbine – The new standard for offshore," Siemens AG, Erlangen, Germany, Tech. Rep., 2014, accessed August 26, 2024. [Online]. Available: https://assets.new.siemens.com/siemens/assets/api/uuid:1c690d9444b15f1a542d0e3166f43a90814743f2/d6-offshore-brochure-en.pdf

[113] A. R. Nejad, J. Keller, Y. Guo, S. Sheng, H. Polinder, S. Watson, J. Dong, Z. Qin, A. Ebrahimi, R. Schelenz, F. Gutiérrez Guzmán, D. Cornel, R. Golafshan, G. Jacobs, B. Blockmans, J. Bosmans, B. Pluymers, J. Carroll, S. Koukoura, E. Hart, A. McDonald, A. Natarajan, J. Torsvik, F. K. Moghadam, P.-J. Daems, T. Verstraeten, C. Peeters, and J. Helsen, "Wind turbine drivetrains: state-of-the-art technologies and future development trends," *Wind Energy Science*, vol. 7, no. 1, pp. 387–411, Feb. 2022.

[114] T. Telsnig, A. Georgakaki, and S. Letout, "Clean Energy Technology Observatory, Wind energy in the European Union - 2022 Status Report on Technology Development, Trends, Value Chains and Markets," Publications Office of the European Union, Luxembourg, Tech. Rep., 2022, accessed September 10, 2024. [Online]. Available: https://data.europa.eu/doi/10.2760/855840

[115] L. Sethuraman, M. Maness, and K. Dykes, "Optimized Generator Designs for the DTU 10-MW Offshore Wind Turbine using *GeneratorSE*," in *35th Wind Energy Symposium*. Grapevine, Texas: American Institute of Aeronautics and Astronautics, Jan. 2017.

[116] F. K. Moghadam and N. Desch, "Life Cycle Assessment of Various PMSG-Based Drivetrain Concepts for 15 MW Offshore Wind Turbines Applications," *Energies*, vol. 16, no. 3, p. 1499, Feb. 2023.

[117] F. Blaabjerg and Ke Ma, "Future on Power Electronics for Wind Turbine Systems," *IEEE Journal of Emerging and Selected Topics in Power Electronics*, vol. 1, no. 3, pp. 139–152, Sep. 2013.

[118] B. Wu, Y. Lang, N. Zargari, and S. Kouro, *Power Conversion and Control of Wind Energy Systems*, 1st ed. Wiley, Jul. 2011.

[119] F. Sevilmis and H. Karaca, "Simulation and analysis of SVPWM based VSI for wind energy systems," in *Proceedings of the 2014 6th International Conference on Electronics, Computers and Artificial Intelligence (ECAI)*. Bucharest, Romania: IEEE, Oct. 2014, pp. 73–78.

[120] G. Jose and R. Chacko, "A review on wind turbine transformers," in *2014 Annual International Conference on Emerging Research Areas: Magnetics, Machines and Drives (AICERA/iCMMD)*. Kottayam, India, India: IEEE, Jul. 2014, pp. 1–7.

[121] P. Sarajcev, A. Meglic, and R. Goic, "Lightning Overvoltage Protection of Step-Up Transformer Inside a Nacelle of Onshore New-Generation Wind Turbines," *Energies*, vol. 14, no. 2, p. 322, Jan. 2021, publisher: MDPI AG.

[122] Anders Grauers, "Design of Direct-driven Permanent-magnet Generators for Wind Turbines," Ph.D. dissertation, Chalmers University of Technology, Göteborg, Oct. 1996.

[123] A. Faulstich, J. Stinke, and F. Wittwer, "Medium voltage converter for permanent magnet wind power generators up to 5 MW," in *2005 European Conference on Power Electronics and Applications*. Dresden, Germany: IEEE, 2005, pp. 9 pp.–P.9.

[124] A. Di Gerlando, G. Foglia, M. F. Iacchetti, and R. Perini, "Analysis and Test of Diode Rectifier Solutions in Grid-Connected Wind Energy Conversion Systems Employing Modular Permanent-Magnet Synchronous Generators," *IEEE Transactions on Industrial Electronics*, vol. 59, no. 5, pp. 2135–2146, May 2012.

[125] A. Bensalah, G. Barakat, and Y. Amara, "Electrical Generators for Large Wind Turbine: Trends and Challenges," *Energies*, vol. 15, no. 18, p. 6700, Sep. 2022.

[126] J. Birk and B. Andresen, "Parallel-connected converters for optimizing efficiency, reliability and grid harmonics in a wind turbine," in *2007 European Conference on Power Electronics and Applications*. Aalborg, Denmark: IEEE, 2007, pp. 1–7.

[127] G. Gohil, L. Bede, R. Maheshwari, R. Teodorescu, T. Kerekes, and F. Blaabjerg, "Parallel interleaved VSCs: Influence of the PWM scheme on the design of the coupled inductor," in *IECON 2014 - 40th Annual Conference of the IEEE Industrial Electronics Society*. Dallas, TX, USA: IEEE, Oct. 2014, pp. 1693–1699.

[128] D. Zhang, F. Wang, R. Burgos, R. Lai, and D. Boroyevich, "Interleaving Impact on AC Passive Components of Paralleled Three-Phase Voltage-Source Converters," in *2008 IEEE Industry Applications Society Annual Meeting*. Edmonton, Alberta, Canada: IEEE, Oct. 2008, pp. 1–7.

[129] W. Erdman and M. Behnke, "Low Wind Speed Turbine Project Phase II: The Application of Medium-Voltage Electrical Apparatus to the Class of Variable Speed Multi-Megawatt Low Wind Speed Turbines," National Renewable Energy Laboratory (N.R.E.L.), Golden, CO, USA, Tech. Rep., 2005, accessed September 9, 2024.

[130] P. Ladoux, N. Serbia, and E. I. Carroll, "On the Potential of IGCTs in HVDC," *IEEE Journal of Emerging and Selected Topics in Power Electronics*, vol. 3, no. 3, pp. 780–793, Sep. 2015, publisher: Institute of Electrical and Electronics Engineers (IEEE).

[131] ABB, "ABB wind turbine converters PCS6000," Mar. 2023, accessed May 21, 2024. [Online]. Available: https://new.abb.com/power-converters-inverters/wind-turbines/utility-scale/pcs6000

[132] Bengt Frankén, "Analysis of Electrical Systems within Offshore Wind Parks," Elforsk, Stockholm, Tech. Rep., Nov. 2007, accessed September 13, 2024. [Online]. Available: https://www.neplan.ch/wp-content/uploads/2015/01/V-118-R-07-65-Reliability-Windpark.pdf

[133] H. Polinder, J. A. Ferreira, B. B. Jensen, A. B. Abrahamsen, K. Atallah, and R. A. McMahon, "Trends in Wind Turbine Generator Systems," *IEEE Journal of Emerging and Selected Topics in Power Electronics*, vol. 1, no. 3, pp. 174–185, Sep. 2013.

[134] Zhou Junwei, Qiu Yingning, Feng Yanhui, and Feng Kai, "Fault Tolerance for Wind Turbine Power Converter," in *2nd IET Renewable Power Generation Conference (RPG 2013)*. Beijing, China: Institution of Engineering and Technology, 2013, pp. 3.24–3.24.

[135] S. Ramakrishnan, M. Delpisheh, C. Convery, D. Niblett, M. Vinothkannan, and M. Mamlouk, "Offshore green hydrogen production from wind energy: Critical review and perspective," *Renewable and Sustainable Energy Reviews*, vol. 195, p. 114320, May 2024.

[136] N. Ohlendorf and W.-P. Schill, "Frequency and duration of low-wind-power events in Germany," *Environmental Research Letters*, vol. 15, no. 8, p. 084045, Aug. 2020.

[137] N. R. Averous, "Analysis of the application of a grid emulator to conduct grid compliance tests for multi-megawatt Wind turbines : a contribution towards ground testing of wind turbines," Ph.D. dissertation, RWTH Aachen University, 2020.

[138] R. Jones and P. Waite, "Optimised power converter for multi-MW direct drive permanent magnet wind turbines," in *Proceedings of the 2011 14th European Conference on Power Electronics and Applications*. Birmingham, UK: IEEE, Sep. 2011.

[139] C. Lamy and P. Millet, "A critical review on the definitions used to calculate the energy efficiency coefficients of water electrolysis cells working under near ambient temperature conditions," *Journal of Power Sources*, vol. 447, p. 227350, Jan. 2020.

[140] D. Falcão and A. Pinto, "A review on PEM electrolyzer modelling: Guidelines for beginners," *Journal of Cleaner Production*, vol. 261, p. 121184, Jul. 2020.

[141] Z. Abdin, C. Webb, and E. Gray, "Modelling and simulation of a proton exchange membrane (PEM) electrolyser cell," *International Journal of Hydrogen Energy*, vol. 40, no. 39, pp. 13 243–13 257, Oct. 2015.

[142] A. S. Tijani, N. A. Binti Kamarudin, and F. A. Binti Mazlan, "Investigation of the effect of charge transfer coefficient (CTC) on the operating voltage of polymer electrolyte membrane (PEM) electrolyzer," *International Journal of Hydrogen Energy*, vol. 43, no. 19, pp. 9119–9132, May 2018.

[143] Tarik Dervišić and Carina Engström, "Electric infrastructure for electrolyser systems," Master's thesis, Chalmers University of Technology, Gothenburg, 2021.

[144] M. Schalenbach, M. Carmo, D. L. Fritz, J. Mergel, and D. Stolten, "Pressurized PEM water electrolysis: Efficiency and gas crossover," *International Journal of Hydrogen Energy*, vol. 38, no. 35, pp. 14 921–14 933, Nov. 2013.

[145] F. Scheepers, M. Stähler, A. Stähler, E. Rauls, M. Müller, M. Carmo, and W. Lehnert, "Temperature optimization for improving polymer electrolyte membrane-water electrolysis system efficiency," *Applied Energy*, vol. 283, p. 116270, Feb. 2021.

[146] A. Hernandez-Gomez, V. Ramirez, and D. Guilbert, "Investigation of PEM electrolyzer modeling: Electrical domain, efficiency, and specific energy consumption," *International Journal of Hydrogen Energy*, vol. 45, no. 29, pp. 14 625–14 639, May 2020.

[147] P. Trinke, B. Bensmann, and R. Hanke-Rauschenbach, "Current density effect on hydrogen permeation in PEM water electrolyzers," *International Journal of Hydrogen Energy*, vol. 42, no. 21, pp. 14 355–14 366, May 2017.

[148] C. Rakousky, U. Reimer, K. Wippermann, M. Carmo, W. Lueke, and D. Stolten, "An analysis of degradation phenomena in polymer electrolyte membrane water electrolysis," *Journal of Power Sources*, vol. 326, pp. 120–128, Sep. 2016.

[149] E. Kuhnert, V. Hacker, and M. Bodner, "A Review of Accelerated Stress Tests for Enhancing MEA Durability in PEM Water Electrolysis Cells," *International Journal of Energy Research*, vol. 2023, pp. 1–23, Feb. 2023.

[150] C. Rozain, E. Mayousse, N. Guillet, and P. Millet, "Influence of iridium oxide loadings on the performance of PEM water electrolysis cells: Part II – Advanced oxygen electrodes," *Applied Catalysis B: Environmental*, vol. 182, pp. 123–131, Mar. 2016.

[151] S. Sun, Z. Shao, H. Yu, G. Li, and B. Yi, "Investigations on degradation of the long-term proton exchange membrane water electrolysis stack," *Journal of Power Sources*, vol. 267, pp. 515–520, Dec. 2014.

[152] E. Kuhnert, K. Mayer, M. Heidinger, C. Rienessel, V. Hacker, and M. Bodner, "Impact of intermittent operation on photovoltaic-PEM electrolyzer systems: A degradation study based on accelerated stress testing," *International Journal of Hydrogen Energy*, vol. 55, pp. 683–695, Feb. 2024.

[153] A. Weiß, A. Siebel, M. Bernt, T.-H. Shen, V. Tileli, and H. A. Gasteiger, "Impact of Intermittent Operation on Lifetime and Performance of a PEM Water Electrolyzer," *Journal of The Electrochemical Society*, vol. 166, no. 8, pp. F487–F497, 2019.

[154] "IEC 61140:2016, Protection against electric shock - Common aspects for installation and equipment," Jan. 2016. [Online]. Available: https://webstore.iec.ch/publication/23997

[155] G. Sakas, A. Ibáñez-Rioja, V. Ruuskanen, A. Kosonen, J. Ahola, and O. Bergmann, "Dynamic energy and mass balance model for an industrial alkaline water electrolyzer plant process," *International Journal of Hydrogen Energy*, vol. 47, no. 7, pp. 4328–4345, Jan. 2022.

[156] B. Endrődi, C. A. Trapp, I. Szén, I. Bakos, M. Lukovics, and C. Janáky, "Challenges and Opportunities of the Dynamic Operation of PEM Water Electrolyzers," *Energies*, vol. 18, no. 9, p. 2154, Apr. 2025, publisher: MDPI AG.

[157] J. J. Caparrós Mancera, F. Segura Manzano, J. M. Andújar, F. J. Vivas, and A. J. Calderón, "An Optimized Balance of Plant for a Medium-Size PEM Electrolyzer: Design, Control and Physical Implementation," *Electronics*, vol. 9, no. 5, p. 871, May 2020.

[158] X. Jin, S. You, M. Petersen, J. Riofrio, S. Thakur, C. Træholt, and Z. Feng, "Exploring commercial water electrolyser systems: a data-based analysis of product characteristics," *Clean Energy*, vol. 8, no. 1, pp. 126–133, Feb. 2024.

[159] B. W. Tuinema, E. Adabi, P. K. Ayivor, V. García Suárez, L. Liu, A. Perilla, Z. Ahmad, J. L. Rueda Torres, M. A. Meijden, and P. Palensky, "Modelling of large-sized electrolysers for real-time simulation and study of the possibility of frequency support by electrolysers," *IET Generation, Transmission & Distribution*, vol. 14, no. 10, pp. 1985–1992, May 2020.

[160] J. Eichman, K. Harrison, and M. Peters, "Novel Electrolyzer Applications: Providing More Than Just Hydrogen," National Renewable Energy Laboratory (N.R.E.L.), Tech. Rep. NREL/TP-5400-61758, 1159377, Sep. 2014, accessed July 10, 2024. [Online]. Available: http://www.osti.gov/servlets/purl/1159377/

[161] Luca Bertuccioli, Alvin Chan, David Hart, Franz Lehner, Ben Madden, and Eleanor Standen, "Development of Water Electrolysis in the European Union," Fuel Cells and Hydrogen Joint Undertaking, Lausanne, Tech. Rep., Feb. 2014, accessed September 26, 2024. [Online]. Available: https://refman.energytransitionmodel.com/publications/2020

[162] T. Runser and R. W. De Doncker, "Comparative Analysis of Distribution Systems in Stand-Alone Wind-to-Hydrogen Plants," in *2024 IEEE Energy Conversion Congress and Exposition (ECCE)*. Phoenix, AZ, USA: IEEE, Oct. 2024, pp. 378–385.

[163] S. Liu, R. G. Cirstea, H. Wu, T. Bosma, and X. Wang, "Comparative Evaluation of Converter Control Impact on Torsional Dynamics of Type-IV Grid-Forming Wind Turbines," *IEEE Transactions on Sustainable Energy*, vol. 15, no. 4, pp. 2803–2814, Oct. 2024, publisher: Institute of Electrical and Electronics Engineers (IEEE).

[164] J. Kim, S. H. Lee, and J.-W. Park, "Inertia-Free Stand-Alone Microgrid—Part II: Inertia Control for Stabilizing DC-Link Capacitor Voltage of PMSG Wind Turbine System," *IEEE Transactions on Industry Applications*, vol. 54, no. 5, pp. 4060–4068, Sep. 2018.

[165] Z. Gao, W. Du, and H. Wang, "Transient stability analysis of a grid-connected type-4 wind turbine with grid-forming control during the fault," *International Journal of Electrical Power & Energy Systems*, vol. 155, p. 109514, Jan. 2024, publisher: Elsevier BV.

[166] Y. Zhuang, R. Menzies, O. Nayak, and H. Turanli, "Dynamic performance of a STATCON at an HVDC inverter feeding a very weak AC system," *IEEE Transactions on Power Delivery*, vol. 11, no. 2, pp. 958–964, Apr. 1996.

[167] Leonard Azimoh, "Investigation into voltage and angle stability of a hybrid HVAC-HVDC power network," Ph.D. dissertation, University of Cape Town, South Africa, 2010.

[168] M. Nawir, "Integration of Wind Farms into Weak AC Grids," Ph.D. dissertation, School of Engineering - Cardiff University, Cardiff, UK, 2017.

[169] Matthew J. Korytowski, "Effects of the Phase Locked Loop on the Stability of a Voltage Source Converter in a Weak Grid Environment," Ph.D. dissertation, University of Pittsburgh, Pittsburgh, PA, USA, 2014.

[170] Terry Chi Young Ho, "AC Voltage Control of a Future Large Offshore Wind Farm Network Connected by HVDC," Ph.D. dissertation, Durham University, United Kingdom, 2015.

[171] M. Hong, H. Xin, W. Liu, Q. Xu, T. Zheng, and D. Gan, "Critical Short Circuit Ratio Analysis on DFIG Wind Farm with Vector Power Control and Synchronized Control," *Journal of Electrical Engineering and Technology*, vol. 11, no. 2, pp. 320–328, Mar. 2016.

[172] U. Shipurkar, E. Lyrakis, K. Ma, H. Polinder, and J. A. Ferreira, "Lifetime Comparison of Power Semiconductors in Three-Level Converters for 10-MW Wind Turbine Systems," *IEEE Journal of Emerging and Selected Topics in Power Electronics*, vol. 6, no. 3, pp. 1366–1377, Sep. 2018.

[173] R. W. De Doncker, *Lecture notes - power electronics: control, synthesis, application ; [winter semester 2013/14]*, 3rd ed. Aachen: RWTH Aachen, ISEA, 2013.

[174] J. E. Huber and J. W. Kolar, "Volume/weight/cost comparison of a 1MVA 10 kV/400 V solid-state against a conventional low-frequency distribution transformer," in *2014 IEEE Energy Conversion Congress and Exposition (ECCE)*, Pittsburgh, PA, USA, Sep. 2014, pp. 4545–4552.

[175] M. Liserre, F. Blaabjerg, and A. Dell'Aquila, "Step-by-step design procedure for a grid-connected three-phase PWM voltage source converter," *International Journal of Electronics*, vol. 91, no. 8, pp. 445–460, Aug. 2004.

[176] W. Chen, X. Ruan, H. Yan, and C. K. Tse, "DC/DC Conversion Systems Consisting of Multiple Converter Modules: Stability, Control, and Experimental Verifications," *IEEE Transactions on Power Electronics*, vol. 24, no. 6, pp. 1463–1474, Jun. 2009.

[177] Xinbo Ruan, Wu Chen, Lulu Cheng, C. Tse, Hong Yan, and Tao Zhang, "Control Strategy for Input-Series–Output-Parallel Converters," *IEEE Transactions on Industrial Electronics*, vol. 56, no. 4, pp. 1174–1185, Apr. 2009.

[178] A. Bach, J. Mathé, B. J. Mortimer, T. Karsten, and R. W. D. Doncker, "Impedance-Based Modeling and Stability Analysis of the Input-Series Output-Parallel DAB3 Converter with Decentralized Control," in *2023 IEEE 24th Workshop on Control and Modeling for Power Electronics (COMPEL)*. Ann Arbor, MI, USA: IEEE, Jun. 2023, pp. 1–8.

[179] Gayan Abeynayake, "DC collection systems for offshore wind farms," Ph.D. dissertation, Cardiff University, United Kingdom, 2021.

[180] T. Runser, S. Arend, T. Karsten, A. Bach, and R. W. De Doncker, "Configuration Optimization of Dual Active Bridge Converter Systems for Interfacing Large-Scale Water Electrolyzer with Stand-Alone Renewables," in *2024 13th International Conference on Renewable Energy Research and Applications (ICRERA)*. Nagasaki, Japan: IEEE, Nov. 2024, pp. 270–277.

[181] N. Soltau, "High-power medium-voltage DC-DC converters : design, control and demonstration," Ph.D. dissertation, RWTH Aachen University, Germany, 2017.

[182] R. De Doncker, D. Divan, and M. Kheraluwala, "A three-phase soft-switched high-power-density DC/DC converter for high-power applications," *IEEE Transactions on Industry Applications*, vol. 27, no. 1, pp. 63–73, Feb. 1991.

[183] D. O. Neacsu, M. N. Cirstea, and D. Butnicu, "Comparative Reliability Analysis for Resonant Converter Operation Under Component Ageing," *IEEE Journal of Emerging and Selected Topics in Industrial Electronics*, vol. 2, no. 2, pp. 142–154, Apr. 2021.

[184] R. De Doncker, D. Divan, and M. Kheraluwala, "A three-phase soft-switched high power density DC/DC converter for high power applications," in *Conference Record of the 1988 IEEE Industry Applications Society Annual Meeting*. Pittsburgh, PA, USA: IEEE, 1988, pp. 796–805.

[185] S. P. Engel, N. Soltau, H. Stagge, and R. W. De Doncker, "Improved Instantaneous Current Control for High-Power Three-Phase Dual-Active Bridge DC–DC Converters," *IEEE Transactions on Power Electronics*, vol. 29, no. 8, pp. 4067–4077, Aug. 2014, publisher: Institute of Electrical and Electronics Engineers (IEEE).

[186] H. v. Hoek, "Design and operation considerations of three-phase dual active bridge converters for low-power applications with wide voltage ranges," Ph.D. dissertation, RWTH Aachen University, Germany, 2017.

[187] M. Stieneker and R. W. De Doncker, "Dual-active bridge dc-dc converter systems for medium-voltage DC distribution grids," in *2015 IEEE 13th Brazilian Power Electronics Conference and 1st Southern Power Electronics Conference (COBEP/SPEC)*. Fortaleza, Brazil: IEEE, Nov. 2015, pp. 1–6.

[188] J. Hu, Z. Yang, S. Cui, and R. W. De Doncker, "Closed-form asymmetrical duty-cycle control to extend the soft-switching range of three-phase dual-active-bridge converters," *IEEE Transactions on Power Electronics*, vol. 36, no. 8, pp. 9609–9622, Aug. 2021.

[189] P. Maniscalco, V. Scaini, and W. Veerkamp, "Specifying DC chopper systems for electrochemical applications," *IEEE Transactions on Industry Applications*, vol. 37, no. 3, pp. 941–948, Jun. 2001.

[190] R. U. Lenke, "A contribution to the design of isolated DC-DC converters for utility applications," Ph.D. dissertation, RWTH Aachen University, Aachen, 2012.

[191] Hempenius, Ate, "Techno-economic comparison between the reduction of iron-oxide using hydrogen or electrowinning, powered by sustainable energy from the grid," Bachelor's Thesis, Eindhoven University of Technology, Netherlands, 2021.

[192] U. Drofenik, G. Laimer, and J. W. Kolar, "Theoretical Converter Power Density Limits for Forced Convection Cooling," in *Official proceedings of the International Conference Power Electronics, Intelligent Motion, Power Quality*, Nuremberg, Germany, Jun. 2005, pp. 608–619.

[193] Z. Yang, J. Hu, G. C. Pasupuleti, and R. W. De Doncker, "Operation-Oriented Design Procedure of a Three-Phase Dual-Active Bridge Converter for a Wide Operation Range," in *2018 IEEE Energy Conversion Congress and Exposition (ECCE)*. Portland, OR, USA: IEEE, Sep. 2018, pp. 2835–2842.

[194] D. Guilbert and G. Vitale, "Dynamic Emulation of a PEM Electrolyzer by Time Constant Based Exponential Model," *Energies*, vol. 12, no. 4, p. 750, Feb. 2019.

[195] N. Soltau, D. Eggers, K. Hameyer, and R. W. De Doncker, "Iron Losses in a Medium-Frequency Transformer Operated in a High-Power DC–DC Converter," *IEEE Transactions on Magnetics*, vol. 50, no. 2, pp. 953–956, Feb. 2014.

[196] N. Soltau, H. Stagge, R. W. De Doncker, and O. Apeldoorn, "Development and demonstration of a medium-voltage high-power DC-DC converter for DC distribution systems," in *2014 IEEE 5th International Symposium on Power Electronics for Distributed Generation Systems (PEDG)*. Galway, Ireland: IEEE, Jun. 2014, pp. 1–8.

[197] A. Garcia-Bediaga, I. Villar, A. Rujas, L. Mir, and A. Rufer, "Multiobjective Optimization of Medium-Frequency Transformers for Isolated Soft-Switching Converters Using a Genetic Algorithm," *IEEE Transactions on Power Electronics*, vol. 32, no. 4, pp. 2995–3006, Apr. 2017.

[198] M. A. Bahmani, T. Thiringer, and M. Kharezy, "Design Methodology and Optimization of a Medium-Frequency Transformer for High-Power DC–DC Applications," *IEEE Transactions on Industry Applications*, vol. 52, no. 5, pp. 4225–4233, Sep. 2016.

[199] "IEC 60085:2007, Electrical insulation - Thermal evaluation and designation," Nov. 2007. [Online]. Available: https://webstore.iec.ch/publication/666

[200] S. P. Engel, M. Stieneker, N. Soltau, S. Rabiee, H. Stagge, and R. W. De Doncker, "Comparison of the Modular Multilevel DC Converter and the Dual-Active Bridge Converter for Power Conversion in HVDC and MVDC Grids," *IEEE Transactions on Power Electronics*, vol. 30, no. 1, pp. 124–137, Jan. 2015.

[201] K. Fischer, K. Pelka, and J. Walgern, "Trends and influencing factors in power-converter reliability of wind turbines," in *PCIM Europe 2023; International Exhibition and Conference for Power Electronics, Intelligent Motion, Renewable Energy and Energy Management*, Nuremberg, Germany, Jun. 2023.

[202] K. Fischer, K. Pelka, A. Bartschat, B. Tegtmeier, D. Coronado, C. Broer, and J. Wenske, "Reliability of power converters in wind turbines: exploratory analysis of failure and operating data from a worldwide turbine fleet," *IEEE Transactions on Power Electronics*, vol. 34, no. 7, pp. 6332–6344, Jul. 2019.

[203] International Electrotechnical Commission, "IEC 61709:2017, electric components - Reliability - Reference conditions for failure rates and stress models for conversion," Feb. 2017. [Online]. Available: https://webstore.iec.ch/publication/28554

[204] C. MacIver, "A Reliability Evaluation of Offshore HVDC Transmission Network Options," Ph.D. dissertation, University of Strathclyde, Strathclyde, 2015.

[205] E. De Jong, J. Popovic, and J. Ferreira, "Design Towards Higher Integration Levels in Power Electronics," in *Twenty-First Annual IEEE Applied Power Electronics Conference and Exposition, 2006. APEC '06.* USA: IEEE, Mar. 2006, pp. 878–884.

[206] J. Kolar, J. Biela, and J. Minibock, "Exploring the pareto front of multi-objective single-phase PFC rectifier design optimization - 99.2% efficiency vs. 7kW/din^3 power density," in *2009 IEEE 6th International Power Electronics and Motion Control Conference*. Wuhan: IEEE, May 2009, pp. 1–21.

[207] European Commission. Joint Research Centre., "Historical analysis of FCH 2 JU electrolyser projects: evaluation of contributions towards advancing the state of the art." Publications Office, LU, Tech. Rep., 2021, accessed January 24, 2025. [Online]. Available: https://data.europa.eu/doi/10.2760/951902

[208] European Commission, "Commission regulation no. 548/2014," 2014. [Online]. Available: http://data.europa.eu/eli/reg/2014/548/oj

[209] M. Stieneker, "Analysis of medium-voltage direct-current collector grids in offshore wind parks; 1. Auflage," Ph.D. dissertation, RWTH Aachen University, Germany, 2017.

[210] E. Camm, M. R. Behnke, O. Bolado, M. Bollen, M. Bradt, C. Brooks, W. Dilling, M. Edds, W. J. Hejdak, D. Houseman, S. Klein, F. Li, J. Li, P. Maibach, T. Nicolai, J. Patino, S. V. Pasupulati, N. Samaan, S. Saylors, T. Siebert, T. Smith, M. Starke, and R. Walling, "Wind power plant substation and collector system redundancy, reliability, and economics," in *2009 IEEE Power & Energy Society General Meeting*. Calgary, Canada: IEEE, Jul. 2009, pp. 1–6.

[211] V. Timmers, A. Egea-Àlvarez, A. Gkountaras, R. Li, and L. Xu, "All-DC offshore wind farms: When are they more cost-effective than AC designs?" *IET Renewable Power Generation*, vol. 17, no. 10, pp. 2458–2470, Jul. 2023.

[212] InnoDC, "Report on the evaluation of DC/DC converters, submarine cables and offshore substations on losses, cost, economy and reliability," InnoDC, Tech. Rep., Aug. 2018, accessed July 31, 2024. [Online]. Available: https://innodc.org/

[213] J. E. Huber and J. W. Kolar, "Applicability of solid-state transformers in today's and future distribution grids," *IEEE Transactions on Smart Grid*, vol. 10, no. 1, pp. 317–326, Jan. 2019.

[214] ABB, "ABB wind turbine converters ACS880," Sep. 2018, accessed February 2, 2025. [Online]. Available: https://new.abb.com/power-converters-inverters/wind-turbines/utility-scale/acs880

[215] T. R. Lucas, A. F. Ferreira, R. Santos Pereira, and M. Alves, "Hydrogen production from the WindFloat Atlantic offshore wind farm: A techno-economic analysis," *Applied Energy*, vol. 310, p. 118481, Mar. 2022.

[216] M. Woznicki, G. Le Solliec, and R. Loisel, "Far off-shore wind energy-based hydrogen production: Technological assessment and market valuation designs," *Journal of Physics: Conference Series*, vol. 1669, no. 1, p. 012004, Oct. 2020.

[217] L. Mika, K. Sztekler, T. Bujok, P. Boruta, and E. Radomska, "Seawater Treatment Technologies for Hydrogen Production by Electrolysis—A Review," *Energies*, vol. 17, no. 24, p. 6255, Dec. 2024.

[218] S. Bhojwani, K. Topolski, R. Mukherjee, D. Sengupta, and M. M. El-Halwagi, "Technology review and data analysis for cost assessment of water treatment systems," *Science of The Total Environment*, vol. 651, pp. 2749–2761, Feb. 2019.

[219] Fabian David Chico Moreno, "Design of an Electrolyzer Integrated in an Offshore Wind Turbine System," Ph.D. dissertation, University of Twente, Netherlands, Oct. 2021.

[220] Catrinus Jepma, Gert-Jan Kok, Malte Renz, Miralda van Schot, and Kees Wouters, "North Sea Energy D 3 . 6 Towards sustainable energy production on the North Sea-Green hydrogen production and CO 2 storage : onshore or offshore ?" Topsector Energy: TKI Offshore Wind & TKI New Gas, Groningen, Tech. Rep. NSE1-D3.6, Mar. 2018, accessed February 15, 2025. [Online]. Available: https://north-sea-energy.eu/static/fc2fba594593abe1330f8b80eeaad756/NSE1_D3.6-Towards-sustainable-energy-production-on-the-North-Sea_final-public.pdf

[221] Market Insider, "Copper price in Euro," Feb. 2025, accessed February 2, 2025. [Online]. Available: https://markets.businessinsider.com/commodities/copper-price/euro

[222] T. Runser, S. Arend, and R. W. De Doncker, "Stand-Alone Offshore Wind Energy and Water Electrolysis: A Study on Optimal Electrolyzer Sizing," in *2023 25th European Conference on Power Electronics and Applications (EPE'23 ECCE Europe)*. Aalborg, Denmark: IEEE, Sep. 2023, pp. 1–9.

Curriculum Vitae

Thibaut Runser

Personal Information

Date of birth	27 August 1998
Place of birth	Mulhouse, France
Nationality	French

Education

2022–2026	PhD in Electrical Engineering and Information Technology RWTH Aachen University, Aachen Supervisor: Prof. Rik W. De Doncker Co-Supervisor: Prof. Damien Guilbert
2016–2021	Electrical Engineering (Dipl.-Ing.) Université de Technologie de Belfort-Montbéliard, France
2018–2018	Semester abroad at the Hochschule für Technik und Architektur Freiburg, Switzerland
2013–2016	General Higher Education Entrance Qualification (Baccalauréat) Don Bosco Landser High School, Landser, France

Work Experience

Since 01/2025	Specialist Converter Systems Siemens Energy, Erlangen, Germany
2022–2024	Industrial PhD Student Siemens Energy, Erlangen, Germany
02/2021–09/2021	Master's Thesis Huawei Nürnberg Research Center, Nürnberg, Germany
09/2019–02/2020	R&D Internship SuperGrid Institute, Lyon, France

E.ON ERC Band 1
Streblow, R.
Thermal Sensation and Comfort Model for Inhomogeneous Indoor Environments
1. Auflage 2011
ISBN 978-3-942789-00-4

E.ON ERC Band 2
Naderi, A.
Multi-phase, multi-species reactive transport modeling as a tool for system analysis in geological carbon dioxide storage
1. Auflage 2011
ISBN 978-3-942789-01-1

E.ON ERC Band 3
Westner, G.
Four Essays related to Energy Economic Aspects of Combined Heat and Power Generation
1. Auflage 2012
ISBN 978-3-942789-02-8

E.ON ERC Band 4
Lohwasser, R.
Impact of Carbon Capture and Storage (CCS) on the European Electricity Market
1. Auflage 2012
ISBN 978-3-942789-03-5

E.ON ERC Band 5
Dick, C.
Multi-Resonant Converters as Photovoltaic Module-Integrated Maximum Power Point Tracker
1. Auflage 2012
ISBN 978-3-942789-04-2

E.ON ERC Band 6
Lenke, R.
A Contribution to the Design of Isolated DC-DC Converters for Utility Applications
1. Auflage 2012
ISBN 978-3-942789-05-9

E.ON ERC Band 7
Brännström, F.
Einsatz hybrider RANS-LES-Turbulenzmodelle in der Fahrzeugklimatisierung
1. Auflage 2012
ISBN 978-3-942789-06-6

E.ON ERC Band 8
Bragard, M.
The Integrated Emitter Turn-Off Thyristor - An Innovative MOS-Gated High-Power Device
1. Auflage 2012
ISBN 978-3-942789-07-3

E.ON ERC Band 9
Hoh, A.
Exergiebasierte Bewertung gebäudetechnischer Anlagen
1. Auflage 2013
ISBN 978-3-942789-08-0

E.ON ERC Band 10
Köllensperger, P.
The Internally Commutated Thyristor - Concept, Design and Application
1. Auflage 2013
ISBN 978-3-942789-09-7

E.ON ERC Band 11
Achtnicht, M.
Essays on Consumer Choices Relevant to Climate Change: Stated Preference Evidence from Germany
1. Auflage 2013
ISBN 978-3-942789-10-3

E.ON ERC Band 12
Panašková, J.
Olfaktorische Bewertung von Emissionen aus Bauprodukten
1. Auflage 2013
ISBN 978-3-942789-11-0

E.ON ERC Band 13
Vogt, C.
Optimization of Geothermal Energy Reservoir Modeling using Advanced Numerical Tools for Stochastic Parameter Estimation and Quantifying Uncertainties
1. Auflage 2013
ISBN 978-3-942789-12-7

E.ON ERC Band 14
Benigni, A.
Latency exploitation for parallelization of power systems simulation
1. Auflage 2013
ISBN 978-3-942789-13-4

E.ON ERC Band 15
Butschen, T.
Dual-ICT – A Clever Way to Unite Conduction and Switching Optimized Properties in a Single Wafer
1. Auflage 2013
ISBN 978-3-942789-14-1

E.ON ERC Band 16
Li, W.
Fault Detection and Protection inMedium Voltage DC Shipboard Power Systems
1. Auflage 2013
ISBN 978-3-942789-15-8

E.ON ERC Band 17
Shen, J.
Modeling Methodologies for Analysis and Synthesis of Controls and Modulation Schemes for High-Power Converters with Low Pulse Ratios
1. Auflage 2014
ISBN 978-3-942789-16-5

E.ON ERC Band 18
Flieger, B.
Innenraummodellierung einer Fahrzeugkabine in der Programmiersprache Modelica
1. Auflage 2014
ISBN 978-3-942789-17-2

E.ON ERC Band 19
Liu, J.
Measurement System and Technique for Future Active Distribution Grids
1. Auflage 2014
ISBN 978-3-942789-18-9

E.ON ERC Band 20
Kandzia, C.
Experimentelle Untersuchung der Strömungsstrukturen in einer Mischlüftung
1. Auflage 2014
ISBN 978-3-942789-19-6

E.ON ERC Band 21
Thomas, S.
A Medium-Voltage Multi-Level DC/DC Converter with High Voltage Transformation Ratio
1. Auflage 2014
ISBN 978-3-942789-20-2

E.ON ERC Band 22
Tang, J.
Probabilistic Analysis and Stability Assessment for Power Systems with Integration of Wind Generation and Synchrophasor Measurement
1. Auflage 2014
ISBN 978-3-942789-21-9

E.ON ERC Band 23
Sorda, G.
The Diffusion of Selected Renewable Energy Technologies: Modeling, Economic Impacts, and Policy Implications
1. Auflage 2014
ISBN 978-3-942789-22-6

E.ON ERC Band 24
Rosen, C.
Design considerations and functional analysis of local reserve energy markets for distributed generation
1. Auflage 2014
ISBN 978-3-942789-23-3

E.ON ERC Band 25
Ni, F.
Applications of Arbitrary Polynomial Chaos in Electrical Systems
1. Auflage 2015
ISBN 978-3-942789-24-0

E.ON ERC Band 26
Michelsen, C. C.
The *Energiewende* in the German Residential Sector: Empirical Essays on Homeowners' Choices of Space Heating Technologies
1. Auflage 2015
ISBN 978-3-942789-25-7

E.ON ERC Band 27
Rohlfs, W.
Decision-Making under Multi-Dimensional Price Uncertainty for Long-Lived Energy Investments
1. Auflage 2015
ISBN 978-3-942789-26-4

E.ON ERC Band 28
Wang, J.
Design of Novel Control algorithms of Power Converters for Distributed Generation
1. Auflage 2015
ISBN 978-3-942789-27-1

E.ON ERC Band 29
Helmedag, A.
System-Level Multi-Physics Power Hardware in the Loop Testing for Wind Energy Converters
1. Auflage 2015
ISBN 978-3-942789-28-8

E.ON ERC Band 30
Togawa, K.
Stochastics-based Methods Enabling Testing of Grid-related Algorithms through Simulation
1. Auflage 2015
ISBN 978-3-942789-29-5

E.ON ERC Band 31
Huchtemann, K.
Supply Temperature Control Concepts in Heat Pump Heating Systems
1. Auflage 2015
ISBN 978-3-942789-30-1

E.ON ERC Band 32
Molitor, C.
Residential City Districts as Flexibility Resource: Analysis, Simulation, and Decentralized Coordination Algorithms
1. Auflage 2015
ISBN 978-3-942789-31-8

E.ON ERC Band 33
Sunak, Y.
Spatial Perspectives on the Economics of Renewable Energy Technologies
1. Auflage 2015
ISBN 978-3-942789-32-5

E.ON ERC Band 34
Cupelli, M.
Advanced Control Methods for Robust Stability of MVDC Systems
1. Auflage 2015
ISBN 978-3-942789-33-2

E.ON ERC Band 35
Chen, K.
Active Thermal Management for Residential Air Source Heat Pump Systems
1. Auflage 2015
ISBN 978-3-942789-34-9

E.ON ERC Band 36
Pâques, G.
Development of SiC GTO Thyristors with Etched Junction Termination
1. Auflage 2016
ISBN 978-3-942789-35-6

E.ON ERC Band 37
Garnier, E.
Distributed Energy Resources and Virtual Power Plants: Economics of Investment and Operation
1. Auflage 2016
ISBN 978-3-942789-37-0

E.ON ERC Band 38
Calì, D.
Occupants' Behavior and its Impact upon the Energy Performance of Buildings
1. Auflage 2016
ISBN 978-3-942789-36-3

E.ON ERC Band 39
Isermann, T.
A Multi-Agent-based Component Control and Energy Management System for Electric Vehicles
1. Auflage 2016
ISBN 978-3-942789-38-7

E.ON ERC Band 40
Wu, X.
New Approaches to Dynamic Equivalent of Active Distribution Network for Transient Analysis
1. Auflage 2016
ISBN 978-3-942789-39-4

E.ON ERC Band 41
Garbuzova-Schiftler, M.
The Growing ESCO Market for Energy Efficiency in Russia: A Business and Risk Analysis
1. Auflage 2016
ISBN 978-3-942789-40-0

E.ON ERC Band 42
Huber, M.
Agentenbasierte Gebäudeautomation für raumlufttechnische Anlagen
1. Auflage 2016
ISBN 978-3-942789-41-7

E.ON ERC Band 43
Soltau, N.
High-Power Medium-Voltage DC-DC Converters: Design, Control and Demonstration
1. Auflage 2017
ISBN 978-3-942789-42-4

E.ON ERC Band 44
Stieneker, M.
Analysis of Medium-Voltage Direct-Current Collector Grids in Offshore Wind Parks
1. Auflage 2017
ISBN 978-3-942789-43-1

E.ON ERC Band 45
Bader, A.
Entwicklung eines Verfahrens zur Strompreisvorhersage im kurzfristigen Intraday-Handelszeitraum
1. Auflage 2017
ISBN 978-3-942789-44-8

E.ON ERC Band 46
Chen, T.
Upscaling Permeability for Fractured Porous Rocks and Modeling Anisotropic Flow and Heat Transport
1. Auflage 2017
ISBN 978-3-942789-45-5

E.ON ERC Band 47
Ferdowsi, M.
Data-Driven Approaches for Monitoring of Distribution Grids
1. Auflage 2017
ISBN 978-3-942789-46-2

E.ON ERC Band 48
Kopmann, N.
Betriebsverhalten freier Heizflächen unter zeitlich variablen Randbedingungen
1. Auflage 2017
ISBN 978-3-942789-47-9

E.ON ERC Band 49
Fütterer, J.
Tuning of PID Controllers within Building Energy Systems
1. Auflage 2017
ISBN 978-3-942789-48-6

E.ON ERC Band 50
Adler, F.
A Digital Hardware Platform for Distributed Real-Time Simulation of Power Electronic Systems
1. Auflage 2017
ISBN 978-3-942789-49-3

E.ON ERC Band 51
Harb, H.
Predictive Demand Side Management Strategies for Residential Building Energy Systems
1. Auflage 2017
ISBN 978-3-942789-50-9

E.ON ERC Band 52
Jahangiri, P.
Applications of Paraffin-Water Dispersions in Energy Distribution Systems
1. Auflage 2017
ISBN 978-3-942789-51-6

E.ON ERC Band 53
Adolph, M.
Identification of Characteristic User Behavior with a Simple User Interface in the Context of Space Heating
1. Auflage 2018
ISBN 978-3-942789-52-3

E.ON ERC Band 54
Galassi, V.
Experimental evidence of private energy consumer and prosumer preferences in the sustainable energy transition
1. Auflage 2017
ISBN 978-3-942789-53-0

E.ON ERC Band 55
Sangi, R.
Development of Exergy-based Control Strategies for Building Energy Systems
1. Auflage 2018
ISBN 978-3-942789-54-7

E.ON ERC Band 56
Stinner, S.
Quantifying and Aggregating the Flexibility of Building Energy Systems
1. Auflage 2018
ISBN 978-3-942789-55-4

E.ON ERC Band 57
Fuchs, M.
Graph Framework for Automated Urban Energy System Modeling
1. Auflage 2018
ISBN 978-3-942789-56-1

E.ON ERC Band 58
Osterhage, T.
Messdatengestützte Analyse und Interpretation sanierungsbedingter Effizienzsteigerungen im Wohnungsbau
1. Auflage 2018
ISBN 978-3-942789-57-8

E.ON ERC Band 59
Frieling, J.
Quantifying the Role of Energy in Aggregate Production Functions for Industrialized Countries
1. Auflage 2018
ISBN 978-3-942789-58-5

E.ON ERC Band 60
Lauster, M.
Parametrierbare Gebäudemodelle für dynamische Energiebedarfsrechnungen von Stadtquartieren
1. Auflage 2018
ISBN 978-3-942789-59-2

E.ON ERC Band 61
Zhu, L.
Modeling, Control and Hardware in the Loop in Medium Voltage DC Shipboard Power Systems
1. Auflage 2018
ISBN 978-3-942789-60-8

E.ON ERC Band 62
Feron, B.
An optimality assessment methodology for Home Energy Management System approaches based on uncertainty analysis
1. Auflage 2018
ISBN 978-3-942789-61-5

E.ON ERC Band 63
Diekerhof, M.
Distributed Optimization for the Exploitation of Multi-Energy Flexibility under Uncertainty in City Districts
1. Auflage 2018
ISBN 978-3-942789-62-2

E.ON ERC Band 64
Wolisz, H.
Transient Thermal Comfort Constraints for Model Predictive Heating Control
1. Auflage 2018
ISBN 978-3-942789-63-9

E.ON ERC Band 65
Pickartz, S.
Virtualization as an Enabler for Dynamic Resource Allocation in HPC
1. Auflage 2019
ISBN 978-3-942789-64-6

E.ON ERC Band 66
Khayyamim, S.
Centralized-decentralized Energy Management in Railway System
1. Auflage 2019
ISBN 978-3-942789-65-3

E.ON ERC Band 67
Schlösser, T.
Methodology for Holistic Evaluation of Building Energy Systems under Dynamic Boundary Conditions
1. Auflage 2019
ISBN 978-3-942789-66-0

E.ON ERC Band 68
Cui, S.
Modular Multilevel DC-DC Converters Interconnecting High-Voltage and Medium-Voltage DC Grids
1. Auflage 2019
ISBN 978-3-942789-67-7

E.ON ERC Band 69
Hu, J.
Modulation and Dynamic Control of Intelligent Dual-Active-Bridge Converter Based Substations for Flexible DC Grids
1. Auflage 2019
ISBN 978-3-942789-68-4

E.ON ERC Band 70
Schiefelbein, J.
Optimized Placement of Thermo-Electric Energy Systems in City Districts under Uncertainty
1. Auflage 2019
ISBN 978-3-942789-69-1

E.ON ERC Band 71
Ferdinand, R.
Grid Operation of HVDC-Connected Offshore Wind Farms: Power Quality and Switching Strategies
1. Auflage 2019
ISBN 978-3-942789-70-7

E.ON ERC Band 72
Musa, A.
Advanced Control Strategies for Stability Enhancement of Future Hybrid AC/DC Networks
1. Auflage 2019
ISBN 978-3-942789-71-4

E.ON ERC Band 73
Angioni, A.
Uncertainty modeling for analysis and design of monitoring systems for dynamic electrical distribution grids
1. Auflage 2019
ISBN 978-3-942789-72-1

E.ON ERC Band 74
Möhlenkamp, M.
Thermischer Komfort bei Quellluftströmungen
1. Auflage 2019
ISBN 978-3-942789-73-8

E.ON ERC Band 75
Voss, J.
Multi-Megawatt Three-Phase Dual-Active Bridge DC-DC Converter
1. Auflage 2019
ISBN 978-3-942789-74-5

E.ON ERC Band 76
Siddique, H.
The Three-Phase Dual-Active Bridge Converter Family: Modeling, Analysis, Optimization and Comparison of Two-Level and Three-Level Converter Variants
1. Auflage 2019
ISBN 978-3-942789-75-2

E.ON ERC Band 77
Heesen, F.
An Interdisciplinary Analysis of Heat Energy Consumption in Energy-Efficient Homes: Essays on Economic, Technical and Behavioral Aspects
1. Auflage 2019
ISBN 978-3-942789-76-9

E.ON ERC Band 78
Möller, R.
Untersuchung der Durchschlagspannung von Mineral-, Silikonölen und synthetischen Estern bei mittelfrequenten Spannungen
1. Auflage 2020
ISBN 978-3-942789-77-6

E.ON ERC Band 79
Höfer, T.
Transition Towards a Renewable Energy Infrastructure: Spatial Interdependencies and Stakeholder Preferences
1. Auflage 2020
ISBN 978-3-942789-78-3

E.ON ERC Band 80
Freitag, H.
Investigation of the Internal Flow Behavior in Active Chilled Beams
1. Auflage 2020
ISBN 978-3-942789-79-0

E.ON ERC Band 81
Razik, L.
High-Performance Computing Methods in Large-Scale Power System Simulation
1. Auflage 2020
ISBN 978-3-942789-80-6

E.ON ERC Band 82
Mirz, M.
A Dynamic Phasor Real-Time Simulation Based Digital Twin for Power Systems
1. Auflage 2020
ISBN 978-3-942789-81-3

E.ON ERC Band 83
Schmitz, H.
Energy Consumption Behavior of Private Households: Heterogeneity, Prosuming, and Rebound
1. Auflage 2020
ISBN 978-3-942789-82-0

E.ON ERC Band 84
Cupelli, L.
Data-driven Methods for Voltage Control in Distribution Networks: A Bottom-Up Approach
1. Auflage 2020
ISBN 978-3-942789-83-7

E.ON ERC Band 85
Happ, S.
A Scalable Simulation Method for Cyber-Physical Power Systems
1. Auflage 2020
ISBN 978-3-942789-84-4

E.ON ERC Band 86
Rewitz, K.
Modellierung des thermischen Komforts in Kabinen-innenräumen
1. Auflage 2021
ISBN 978-3-948234-00-3

E.ON ERC Band 87
Wesseling, M.
Probabilistische Bewertung von Entrauchungsanlagen
1. Auflage 2021
ISBN 978-3-948234-01-0

E.ON ERC Band 88
Stoyanova, I.
Cooperative Energy Management and Cross-Domain Optimization for Electro-Thermal Devices at City-District and City-Level
1. Auflage 2021
ISBN 978-3-948234-02-7

E.ON ERC Band 89
Tran, T.
Advanced hierarchical control structure for Virtual Oscillator-based distributed generation in multi-bus microgrids under different grid dynamics and disturbances
1. Auflage 2021
ISBN 978-3-948234-03-4

E.ON ERC Band 90
Yang, Z.
On the Stability of Three-Phase Grid-Tied Photovoltaic Inverter Systems
1. Auflage 2021
ISBN 978-3-948234-04-1

E.ON ERC Band 91
Wang, T.
Fault Detection and Isolation in DC Distribution Grids
1. Auflage 2021
ISBN 978-3-948234-05-8

E.ON ERC Band 92
Beushausen, S.
A GaN-Based Switched-Mode Gate-Drive Unit for Medium-Voltage IGBTs
1. Auflage 2021
ISBN 978-3-948234-06-5

E.ON ERC Band 93
Schumacher, M.
Design and Assessment of Grid-driven Distributed Cogeneration
1. Auflage 2021
ISBN 978-3-948234-07-2

E.ON ERC Band 94
Joebges, P.
Distributed Real-Time Simulation of Modular Bidirectional DC-DC Converters for Control-Hardware-in-the-Loop
1. Auflage 2021
ISBN 978-3-948234-08-9

E.ON ERC Band 95
Averous, R.
Analysis of the Application of a Grid Emulator to Conduct Grid Compliance Tests for Multi-Megawatt Wind Turbines A Contribution towards Ground Testing of Wind Turbines
1. Auflage 2021
ISBN 978-3-948234-09-6

E.ON ERC Band 96
Virdag, A.
Design, Implementation and Analysis of DC Circuit-breaker for Low-Voltage DC Grids with Counter-current Injection Principle
1. Auflage 2021
ISBN 978-3-948234-10-2

E.ON ERC Band 97
Dähling, S.
Cloud-based Multi-Agent Systems for Flexibility Management in Future Distribution Grids
1. Auflage 2021
ISBN 978-3-948234-11-9

E.ON ERC Band 98
Qawasmi, A.
Fault Current Interruption Analysis and Development of a Power Semiconductor Switch for a Medium-Voltage DC Hybrid Circuit Breaker
1. Auflage 2021
ISBN 978-3-948234-12-6

E.ON ERC Band 99
Nolting, L.
Die Versorgungssicherheit mit Elektrizität im Kontext von Liberalisierung und Energiewende
1. Auflage 2021
ISBN 978-3-948234-13-3

E.ON ERC Band 100
Mathis, P.
Heat Transfer Enhancement in Natural Convective Channel Flows by Vortex Streets
1. Auflage 2022
ISBN 978-3-948234-14-0

E.ON ERC Band 101
Wolff, S.
Stated Preferences Concerning Private Passenger and Light-Duty Electric Vehicles in Germany
1. Auflage 2022
ISBN 978-3-948234-15-7

E.ON ERC Band 102
Hackbarth, A.
Private Households' Preferences for Alternative Fuel Vehicles in Germany – An Empirically Founded Analysis of Adoption Decisions, Willingness-to-Pay, and Policy Scenarios
1. Auflage 2022
ISBN 978-3-948234-16-4

E.ON ERC Band 103
Ge, L.
Performance Enhancement of Switched Reluctance Machines for High-speed Backup Generators: Design, Measurement and Control
1. Auflage 2022
ISBN 978-3-948234-17-1

E.ON ERC Band 104
Atasoy, T.
Strategic and Behavioral Responses of Consumers and Producers to Energy and Environmental Policies
1. Auflage 2022
ISBN 978-3-948234-18-8

E.ON ERC Band 105
Remmen, P.
Automated Calibration of Non-Residential Urban Building Energy Modeling
1. Auflage 2022
ISBN 978-3-948234-19-5

E.ON ERC Band 106
Schild, T.
Systematische Entwicklung strukturierter Steuerungs-algorithmen für die Gebäude- und Anlagentechnik
1. Auflage 2022
ISBN 978-3-948234-20-1

E.ON ERC Band 107
Sidik, Y.
Modeling, Control, and Dynamic Stability Analysis of Two-Stage DC Collector Grids in Offshore Wind Park Clusters
1. Auflage 2022
ISBN 978-3-948234-21-8

E.ON ERC Band 108
Sadu, A.
Towards resilient design of distribution grid automation system: An evaluation of its reliability against random failures and susceptibility to targeted attacks
1. Auflage 2022
ISBN 978-3-948234-22-5

E.ON ERC Band 109
Hinz, A.
Electrical Propulsion Systems for Civil Transportation Aircraft
1. Auflage 2022
ISBN 978-3-948234-23-2

E.ON ERC Band 110
Mehrfeld, P.
Evaluation of Heat Pump Systems Under Dynamic Operating Conditions
1. Auflage 2022
ISBN 978-3-948234-24-9

E.ON ERC Band 111
Teichrib, J.
A Hybrid Semiconductor Device for Medium-Voltage DC-DC Converters - The Combination of Thyris-tor and Transistor Technologies
1. Auflage 2022
ISBN 978-3-948234-25-6

E.ON ERC Band 112
Frehn, A.
Under voltage ride through tests on nacelle test benches equipped with a power hardware in the loop setup
1. Auflage 2023
ISBN 978-3-948234-26-3

E.ON ERC Band 113
Bode, G.
Generation of Training Data for Fault Detection and Diagnosis Algorithms Using Fault Simulation and Parameter Uncertainty
1. Auflage 2023
ISBN 978-3-948234-27-0

E.ON ERC Band 114
Vering, C.
Optimale Auslegung von Wärmepumpensystemen für Bestandsgebäude
1. Auflage 2023
ISBN 978-3-948234-28-7

E.ON ERC Band 115
Bogdanović, M.
Towards model partitioning automation of distributed real-time power systems simulations of distribution networks
1. Auflage 2023
ISBN 978-3-948234-29-4

E.ON ERC Band 116
Hering, D.
Optimization of district heating networks using mixed integer quadratically constrained programs
1. Auflage 2023
ISBN 978-3-948234-30-0

E.ON ERC Band 117
De Din, E.
Multi-Timescale Framework for the Voltage Control of Active Distribution Grids
1. Auflage 2023
ISBN 978-3-948234-31-7

E.ON ERC Band 118
Specht, J.
The Energy Supplier 2.0 – Activating Private Households' Flexibility Potential for Value Creation and Services Supply
1. Auflage 2023
ISBN 978-3-948234-32-4

E.ON ERC Band 119
Teichmann, J.
Auswirkungen der Hydraulik auf das Betriebsverhalten von raumlufttechnischen Anlagen
1. Auflage 2023
ISBN 978-3-948234-33-1

E.ON ERC Band 120
Haghgoo, M.
Semantic Interoperability as a Service for the Smart Energy System
1. Auflage 2023
ISBN 978-3-948234-34-8

E.ON ERC Band 121
Roy, G.
Automation Architectures for hybrid ac-dc grid
1. Auflage 2023
ISBN 978-3-948234-35-5

E.ON ERC Band 122
Mork, M.
Model Predictive Control of Building Energy Systems
1. Auflage 2023
ISBN 978-3-948234-36-2

E.ON ERC Band 123
Zargar, B.
Data-Driven Distribution System State Estimation Using Synchrophasor Measurements
1. Auflage 2023
ISBN 978-3-948234-37-9

E.ON ERC Band 124
Rohn, M.
Einseitiges Induktionsverhalten von multiplen Luftstrahlen unterschiedlicher Düsengeometrien
1. Auflage 2024
ISBN 978-3-948234-38-6

E.ON ERC Band 125
Sheykhha, S.
Four essays on the sustainable energy transition: Model-based analyses of regional energy market structures and regulations
1. Auflage 2024
ISBN 978-3-948234-39-3

E.ON ERC Band 126
Warmuz, J.
Current Interruption Capability and Feasibility Assessment for a Medium-Voltage Direct Current Hybrid Circuit Breaker Application
1. Auflage 2024
ISBN 978-3-948234-40-9

E.ON ERC Band 127
Gürses, G.
Machine learning techniques for time series forecasting in power systems operation
1. Auflage 2024
ISBN 978-3-948234-41-6

E.ON ERC Band 128
Baranski, M.
Design of Distributed Model-based Control Agents for Building Automation Systems
1. Auflage 2024
ISBN 978-3-948234-42-3

E.ON ERC Band 129
Karami, M.
Driving Sustainability Through Business Model Innovation in the Energy Industry and Related Sectors
1. Auflage 2024
ISBN 978-3-948234-43-0

E.ON ERC Band 130
Hoffmann, M.
Entwicklung eines Simulationsmodells zur Vorhersage und Optimierung eines Luftwäschers mittels 3-dimensionaler Mehrphasen-Strömungssimulation
1. Auflage 2024
ISBN 978-3-948234-44-7

E.ON ERC Band 131
Stoffel, P.
Learning Strategies for Data-Driven Model Predictive Control of Building Energy Systems
1. Auflage 2024
ISBN 978-3-948234-45-4

E.ON ERC Band 132
Dognini, A.
Multi-criteria service restoration methods for AC and AC/DC distribution grids
1. Auflage 2024
ISBN 978-3-948234-46-1

E.ON ERC Band 133
Schreiner, L.
International Public-Private Strategies in Sustainable Investment and Finance
1. Auflage 2024
ISBN 978-3-948234-47-8

E.ON ERC Band 134
Priesmann, J.
Verteilungseffekte im Kontext der Energiewende: Herausforderungen und regulatorische Lösungsansätze
1. Auflage 2024
ISBN 978-3-948234-48-5

E.ON ERC Band 135
Mortimer, B.
Horizontal Network Coupling for Charging Infrastructure Based on Three-Phase Solid-State Transformers
1. Auflage 2024
ISBN 978-3-948234-49-2

E.ON ERC Band 136
Gümrükcü, E.
A Versatile Strategy for Optimizing Electric Vehicles' Charging Spot Selections in Distribution Grids
1. Auflage 2024
ISBN 978-3-948234-50-8

E.ON ERC Band 137
Pan, Z.
Large Language Model Based Semantic Interoperability Enhancement for Energy Data Management
1. Auflage 2025
ISBN 978-3-948234-51-5

E.ON ERC Band 138
Korompili, A.
Two-Level Control for Multi-Terminal DC Distribution Grids
1. Auflage 2025
ISBN 978-3-948234-52-2

E.ON ERC Band 139
Dinkelbach, J.
Enabling the Real-Time Simulation of Low-Inertia Power Systems by Dynamic Phasor Modelling and Efficient Computing Methods
1. Auflage 2025
ISBN 978-3-948234-53-9

E.ON ERC Band 140
Kümpel, A.
Adaptive agentenbasierte modellprädiktive Regelung für Gebäudeenergiesysteme
1. Auflage 2025
ISBN 978-3-948234-54-6

E.ON ERC Band 141
Gurumurthy, S.
Advanced Harmonic Stability Monitoring and Control of Power-Electronics Dominated Grids
1. Auflage 2025
ISBN 978-3-948234-55-3

E.ON ERC Band 142
Sowa, I.
Distributed Consensus Control Supported by High Reporting Rate Meters in Cyber-Physical Microgrids
1. Auflage 2025
ISBN 978-3-948234-56-0

E.ON ERC Band 143
Klingebiel, J.
Bedarfsgesteuerte Abtauung von Luft-Wärmepumpen durch Reinforcement Learning
1. Auflage 2025
ISBN 978-3-948234-57-7

E.ON ERC Band 144
Ginocchi, M.
Sensitivity Analysis for Power System Applications
1. Auflage 2025
ISBN 978-3-948234-58-4

E.ON ERC Band 145
Ahmadifar, A.
Resilient Microgrid Management in Active Distribution Systems for Normal and Contingency Operations
1. Auflage 2025
ISBN 978-3-948234-59-1

E.ON ERC Band 146
Höges, C.
Kältemittelkreislaufkonfigurationen von Wärmepumpen für die Gebäudebeheizung
1. Auflage 2025
ISBN 978-3-948234-60-7

E.ON ERC Band 147
Stock, J.
Separation of Existing District Heating Networks for Optimal Utilisation of Sustainable Heat Sources
1. Auflage 2025
ISBN 978-3-948234-61-4

E.ON ERC Band 148
Penthong, T.
Towards Automatization of Distance Protection Coordination and Interoperability Testing for Digital Substations
1. Auflage 2026
ISBN 978-3-948234-62-1

E.ON ERC Band 149
Holtwerth, A.
Model Predictive Control of Hybrid Battery-Hydrogen Energy Storage Systems Using Mixed Integer Linear Programming
1. Auflage 2026
ISBN 978-3-948234-63-8

E.ON ERC Band 150
Ostmann, P.
Aeroakustische Emissionen von Luftdurchlässen
1. Auflage 2026
ISBN 978-3-948234-64-5

E.ON ERC Band 151
Kockel, C.
Globale Wasserstoff-wertschöpfungsketten für die Energiewende in Deutschland: Umweltauswirkungen und Kosten unter Unsicherheiten
1. Auflage 2026
ISBN 978-3-948234-65-2

E.ON ERC Band 152
Herzog, F.
Common-Mode Currents in Low-Voltage DC Underlay Grids with AC-Side Grounding
1. Auflage 2026
ISBN 978-3-948234-66-9

E.ON ERC Band 153
Hetzenecker, K.
Optimizing Three-Phase DC-DC Converters for MVDC Grids
1. Auflage 2026
ISBN 978-3-948234-67-6

E.ON ERC Band 154
Heins, T.
Model Predictive Control for Frequency Stability Enhancement of Converter-driven Power Systems
1. Auflage 2026
ISBN 978-3-948234-68-3

The thesis investigates the electrical integration of electrolysis plants with decentralized stand-alone offshore wind turbines for hydrogen production. Such wind-to-hydrogen systems have the potential to reduce transmission losses, conversion stages and grid infrastructure compared to conventional grid-connected electrolysis plants. However, the close coupling of electrolysis plant with stand-alone wind turbine raises significant challenges, including highly variable wind power, constrained offshore environments and altering electrolyzer operating conditions over the plant's lifetime.

The research addresses the lack of a holistic methodology for designing and comparing electrical distribution systems for these plants. To fill this gap, a comprehensive framework is developed that combines technical requirement analysis, converter design optimization, plant operation strategies and life-cycle cost evaluation. Particular emphasis is placed on isolated DC-DC converters, whose modularity can be optimized to improve key converter parameters. Key findings show that the single-stage DC-based distribution system is the most promising architecture, reducing the number of conversion steps and potentially lowering the Levelized Cost of Hydrogen by about 8 % compared to conventional AC-based systems. In addition, a sensitivity analysis reveals the relative impact of economic parameters and plant conditions on competitiveness, while a plant sizing optimization suggests that oversizing of the electrolyzer can further improve plant competitiveness.

ISBN 978-3-948234-69-0

Thinking the Future
Zukunft denken